

GRAPHENE-BASED METAL/METAL SULPHIDE  
NANOCOMPOSITES: FABRICATION, CHARACTERIZATION AND  
ITS APPLICATIONS

AMIR MORADI GOLSHEIKH

THESIS SUBMITTED IN FULFILLMENT OF  
THE REQUIREMENT FOR THE DEGREE  
OF DOCTOR OF PHILOSOPHY

DEPARTMENT OF PHYSICS  
THE FACULTY OF SCIENCE  
UNIVERSITY OF MALAYA  
KUALA LUMPUR

2014



UNIVERSITI MALAYA

**ORIGINAL LITERARY WORK DECLARATION**

Name of Candidate: **Amir Moradi Golsheikh**

(Passport No: **J16606716**)

Registration/Matric No: **SHC100053**

Name of Degree: **Doctor of Philosophy**

Title of Thesis: **Graphene-based Metal/Metal Sulphide Nanocomposites: Fabrication, Characterization and its Applications**

Field of Study: **Nanophysics**

I do solemnly and sincerely declare that:

- (1) I am the sole author/writer of this Work;
- (2) This Work is original;
- (3) Any use of any work in which copyright exists was done by way of fair dealing and for permitted purposes and any excerpt or extract from, or reference to or reproduction of any copyright work has been disclosed expressly and sufficiently and the title of the Work and its authorship have been acknowledged in this Work;
- (4) I do not have any actual knowledge nor do I ought reasonably to know that the making of this work constitutes an infringement of any copyright work;
- (5) I hereby assign all and every rights in the copyright to this Work to the University of Malaya ("UM"), who henceforth shall be owner of the copyright in this Work and that any reproduction or use in any form or by any means whatsoever is prohibited without the written consent of UM having been first had and obtained;
- (6) I am fully aware that if in the course of making this Work I have infringed any copyright whether intentionally or otherwise, I may be subject to legal action or any other action as may be determined by UM.

Candidate's Signature

Date

Subscribed and solemnly declared before,

Witness's Signature

Date

Name:

Designation:

**To my wife and my daughter with love**

## ABSTRACT

Graphene, a one-atom-thick planar sheet of  $sp^2$ -bonded carbon atoms, has attracted tremendous attention due to its unique electronic, mechanical, thermal, and optical properties. Graphene's high electrical conductivity, large surface-to-volume ratio, and excellent chemical tolerance make it a distinguishable matrix for nanocomposites. Therefore, incorporation of graphene with inorganic materials such as metal, metal oxides and metal sulfides has been the focus of research in recent years for their multifunctional abilities. In order to obtain some graphene-based nanocomposites with controlling the morphology of composite and properties, several synthesis approaches have been designed and carried out.

First, silver-nanoparticles-decorated reduced graphene oxide (rGO) have been electrodeposited on indium tin oxide (ITO) by a cyclic voltammetry method. It was established that the silver ammonia complex ( $\text{Ag}(\text{NH}_3)_2\text{OH}$ ) was the key component to achieving well-distributed AgNPs with small and narrow size distribution decorated on reduced graphene sheets. The composite deposited on ITO exhibited notable electrocatalytic activity for the reduction of  $\text{H}_2\text{O}_2$ , leading to an enzymeless electrochemical sensor with a fast amperometric response time less than 2s. The corresponding calibration curve of the current response showed a linear detection range of 0.1 mM to 100 mM (with regression value of  $R^2 = 0.9992$ ) while the limit of detection was estimated to be 5  $\mu\text{M}$ .

Second, reduced graphene oxide (rGO) uniformly decorated with silver nanoparticles (AgNPs) have been synthesized through a simple ultrasonic irradiation of the aqueous solution containing silver ammonia complex ( $\text{Ag}(\text{NH}_3)_2\text{OH}$ ) and graphene oxide (GO). The size of the nanoparticles could be tuned by adjusting the volume ratio of the precursors and the ultrasonic irradiation time. The average particle size of the silver with the narrowest size distribution was 4.57 nm. The prepared AgNPs-rGO

modified glassy carbon electrode exhibited notable electrocatalytic activity toward the non-enzymatic detection of  $\text{H}_2\text{O}_2$  with a wide linear range of 0.1–70 mM ( $R^2 = 0.9984$ ) and a detection limit of 4.3  $\mu\text{M}$ . Furthermore, the prepared AgNPs-rGO composite was employed for the spectral detection of  $\text{Hg}^{2+}$  ions and showed a detection limit of 20 nM.

Third, the hydrothermal conditions such as reaction temperature, reaction time, pH of the solution and the amount of gelatin have been optimized for preparing  $\text{FeS}_2$  nanoparticles and subsequently the optimum hydrothermal conditions have been utilized for preparation of  $\text{FeS}_2$ /graphene nanocomposites with different loading amount of graphene. At the optimum concentration of GO (1 mg/mL), a photocurrent intensity of about 1.01  $\mu\text{A}$  is obtained, which is about 2.6 time higher than that obtained on the pure  $\text{FeS}_2$  electrode.

Finally, reduced graphene oxide decorated with hierarchical ZnS nanoparticles have been synthesized by one-pot sonochemical method. The resultant composites have been characterized by x-ray diffraction (XRD), fourier transform infrared spectroscopy (FTIR), raman spectroscopy, field emission scanning electron microscope (FESEM), transmission electron microscope (TEM) and photoluminescence spectroscopy. A significant enhancement in the photocatalytic degradation of methylene blue (MB) was observed with ZnS/rGO nanocomposite as compared to that of the bare ZnS particles.

It is worth to notice that all the samples were synthesized for the first time by the mentioned methods. The samples AgNPs/rGO/ITO, AgNPs/rGO and ZnS/rGO were prepared without using any reducing or stabilizing agents and  $\text{FeS}_2$ /rGO was prepared for the first time by using gelatin as a nontoxic reducing and capping agent.

## ABSTRAK

Graphene terdiri daripada atom-atom karbon yang terikat secara  $sp^2$  dan membentuk satu satah yang mempunyai ketebalan bersamaan dengan saiz satu atom. Ia telah menarik banyak perhatian kerana memiliki ciri-ciri elektronik, mekanikal, terma dan optikal yang unik. Konduktiviti elektrik yang tinggi, nisbah permukaan kepada isipadu yang besar, dan toleransi kimia yang sangat baik yang dimiliki oleh graphene membolehkan ia menjadi matrik pembezaan bagi komposit nano. Oleh itu, perpadanan graphene dengan bahan-bahan bukan organik seperti logam, oksida logam dan sulfida logam telah menjadi fokus penyelidikan sejak beberapa tahun kebelakangan ini kerana kebolehan ia digunakan dalam pelbagai fungsi. Bagi memperolehi beberapa komposit nano berasaskan graphene dengan mengawal morfologi komposit dan ciri-cirinya, beberapa pendekatan sintesis telah direka dan dilaksanakan.

Pertama, zarah-zarah perak berskala nano (AgNPs) menghiasi penurunan graphene oksida (rGO) telah dimendapkan pada oksida timah indium (ITO) dengan kaedah voltammetri berkitar. Secara umum telah, diketahui bahawa kompleks ammonia perak ( $\text{Ag}(\text{NH}_3)_2\text{OH}$ ) merupakan komponen penting untuk memperoleh AgNPs yang bersaiz kecil serta bertaburan secara sekata pada permukaan helaian rGO. Komposit yang termendap pada ITO telah menunjukkan aktiviti elektromangkin yang penting bagi penurunan  $\text{H}_2\text{O}_2$ , seterusnya membawa kepada pengesanan elektrokimia kurang berenzim dengan masa tindakbalas amperometrik yang pantas iaitu kurang daripada 2 s. Keluk penentukuran yang sepadan bagi tindak balas semasa menunjukkan jarak pengesanan linear di antara 0.1 mM kepada 100 mM (dengan nilai regresi  $R^2 = 0.9992$ ) manakala had pengesanan dianggarkan sebanyak 5  $\mu\text{M}$ .

Kedua, sintesis rGO yang dihiasi taburan sekata zarah-zarah perak berskala nano (AgNPs) telah dilakukan melalui sinaran ultrasonic mudah terhadap larutan ammonia perak kompleks ( $\text{Ag}(\text{NH}_3)_2\text{OH}$ ) dan graphene oksida (GO). Saiz zarah ini boleh diubah

dengan menetapkan nisbah isipadu pelopor larutan dan masa sinaran. Purata saiz zarah perak dengan saiz taburan yang sempit adalah 4.57 nm. Elektrod karbon berkaca yang diubahsuai dengan menggunakan AgNPs-rGO mempamerkan aktiviti elektrokatalitik yang ketara terhadap pengesanan bahan bukan enzim iaitu  $\text{H}_2\text{O}_2$  dengan julat linear yang luas, diantara 0.1 hingga 70 mM (dengan nilai regresi  $R_2 = 0.9984$ ) dan had pengesanan sebanyak 4.3  $\mu\text{M}$ . Tambahan pula, komposit AgNPs-rGO yang disintesis telah digunakan untuk mengesan spektrum bagi ion  $\text{Hg}^{2+}$  dan ia telah menunjukkan had pengesanan sebanyak 20 nM.

Ketiga, beberapa parameter hidroterma seperti suhu tindakbalas, masa tindakbalas, pH bagi larutan dan jumlah gelatin telah dioptimumkan untuk menghasilkan zarah-zarah  $\text{FeS}_2$  dan kemudiannya parameter yang telah optimum ini digunakan untuk penyediaan  $\text{FeS}_2$ /graphene komposit nano dengan jumlah graphene yang berbeza. Pada kepekatan GO yang optimum (1 mg/mL), keamatan fotoarus sebanyak  $\sim 1.01 \mu\text{A}$  telah diperolehi, iaitu 2.6 kali lebih tinggi berbanding nilai yang diperolehi daripada elektrod  $\text{FeS}_2$  tulen.

Akhir sekali, penurunan oksida graphene dengan taburan ZnS berhierarki nanosfera telah disintesis melalui kaedah *1-pot sonochemical*. Hasil perpaduan komposit ini, telah dianalisis melalui kaedah belauan sinar-X (XRD), spektroskopi penghantar inframerah jelmaan fourier (FTIR), spektroskopi raman, mikroskop pengimbas pancaran medan elektron (FESEM), mikroskop pancaranelektron (TEM) dan spektroskopi fotoluminasi.

Adalah amat penting untuk dinyatakan disini bahawa semua sampel telah disintesis untuk pertama kalinya dengan kaedah yang dinyatakan sebelum ini. Sampel AgNPs/rGO/ITO, AgNPs/rGO dan ZnS/rGO telah disediakan tanpa menggunakan mana-mana ejen penurun atau penstabil, dan  $\text{FeS}_2$ /rGO telah disediakan untuk pertama



kalinya dengan menggunakan gelatin sebagai ejen penurun dan pengikat yang tidak bertoksik.

## ACKNOWLEDGEMENTS

This thesis would not have been possible without the opportunity given to me by the University of Malaya and the inspiration and constant support bestowed to me by the following people:

First of all, I would like to express my gratitude to my supervisor Dr. Huang Nay Ming and my co-supervisor Dr. Rozalina Zakaria for their supervision, advice and guidance. I appreciate all their contributions of time, ideas, and funding to make my Ph.D. program productive and exciting. I would also like to thank Department of Physics for providing me support and facilities, University of Malaya for PPP Grant (PV039-2011A), and Ministry of Higher Education of Malaysia for High Impact Research Grant (UM.C/625/1/HIR/MOHE/SC/05, UM.C/625/1/HIR/MOHE/SC/06 and UM.C/625/1/HIR/MOHE/SC/21).

I want to thank Prof. Wan Jeffrey Basirun and Dr. Reza Mahmoudian for allowing me to use their lab in Department of Chemistry and for their valuable discussions.

I would like to thank my best friend (Dr. Ali Khorsand Zak), who had suggested and helped me to enroll my study in University of Malaya, and also my good friends Mr. Siamak Pilban, Dr. Ahmad Kamalianfar, Dr. Majid Darroudi, Mr. Majid Azarang, Mr. Mehran Sookhakian, Dr. Nadia Mahmoudi, Dr. Maryam Banihashemian, and Mr. shahid Mehmood for their kind supports.

Finally, I would like to thank all of my family for their support, especially my parents and my parents-in-law. Words fail me to express my appreciation to my wife, whose love and encouragement allowed me to finish this journey.

## TABLE OF CONTENTS

ABSTRACT.....	ii
ABSTRAK.....	iv
ACKNOWLEDGEMENTS.....	vii
TABLE OF CONTENTS.....	viii
LIST OF TABLES.....	xi
LIST OF FIGURES.....	xii
LIST OF SYMBOLS AND ABBREVIATIONS.....	xviii
CHAPTER I: INTRODUCTION.....	1
1.1 Background of study.....	1
1.2 Aim and objectives.....	3
1.3 Hypothesis.....	4
1.4 Thesis structure.....	5
CHAPTER II: REVIEW OF RELATED LITERATURE.....	7
2.1 Graphene.....	7
2.2 Synthesis of graphene.....	9
2.2.1 Mechanical exfoliation.....	9
2.2.2 Epitaxial growth.....	10
2.2.3 Chemical vapor deposition.....	11
2.2.4 Graphene from graphene oxide.....	15
2.3 Graphene oxide: preparation methods and structure.....	21
2.4 Graphene-based nanocomposites.....	25
2.4.1 Graphene-based polymer nanocomposites.....	25
2.4.2 Graphene-based inorganic nanocomposites.....	27
2.5 Synthesis of graphene-inorganic nanocomposites.....	29
2.5.1 <i>Ex situ</i> hybridization.....	29
2.5.2 <i>In situ</i> formation or crystallization on the surface of graphene.....	30
2.6 Application of graphene-inorganic nanocomposites.....	37
2.6.1 Photocatalysis.....	37
2.6.2 Energy storage and conversion.....	41
2.6.3 Sensing.....	46
2.6.4 Other applications.....	49
CHAPTER III: DESIGN, METHODS AND PROCEDURE.....	50
3.1 Chemicals and Materials.....	50
3.2 Synthesis of graphene oxide.....	50
3.3 Electrodeposition synthesis of silver-nanoparticle-decorated graphene on indium-tin-oxide for enzymeless hydrogen peroxide detection.....	51
3.3.1 Fabrication of AgNPs-rGO/ITO.....	51

3.3.2	Electrochemical sensing measurements.....	52
3.4	One-pot sonochemical synthesis of reduced graphene oxide uniformly decorated with ultrafine silver nanoparticles for non-enzymatic detection of H <sub>2</sub> O <sub>2</sub> and optical detection of mercury ions .....	53
3.4.1	Preparation of Ag-rGO composite .....	53
3.4.2	Preparation of modified electrode.....	54
3.4.3	Spectral detection of Hg <sup>2+</sup> ions .....	55
3.5	One-pot hydrothermal synthesis and characterization of FeS <sub>2</sub> (Pyrite)/Graphene nanocomposite .....	55
3.5.1	Preparation of FeS <sub>2</sub> (pyrite) .....	55
3.5.2	Preparation of FeS <sub>2</sub> (pyrite)/graphene nanocomposite .....	57
3.5.3	Photocurrent measurement.....	57
3.5.4	EIS measurement .....	58
3.6	Sonochemical synthesis of reduced graphene oxide decorated with hierarchical ZnS nanospheres.....	59
3.6.1	Preparation of ZnS-rGO nanocomposite.....	59
3.6.2	Photocatalytic measurements .....	60
3.7	Characterization.....	60
3.7.1	X-Ray Diffraction .....	60
3.7.2	Fourier transform infrared spectroscopy .....	61
3.7.3	Raman spectroscopy .....	62
3.7.4	Field emission scanning electron microscope.....	64
3.7.5	High resolution transmission electron microscope .....	66
CHAPTER IV: RESULTS AND DISCUSSIONS .....		67
4.1	One-step electrodeposition synthesis of silver-nanoparticle-decorated graphene on indium-tin-oxide for enzymeless hydrogen peroxide detection .....	67
4.1.1	Electrodeposition of AgNPs-rGO on ITO via cyclic voltammetry technique .....	67
4.1.2	X-ray diffraction analysis.....	69
4.1.3	FTIR spectroscopy .....	70
4.1.4	Raman spectroscopy .....	71
4.1.5	Morphology.....	72
4.1.6	Formation mechanism.....	75
4.1.7	Electrochemical sensing of H <sub>2</sub> O <sub>2</sub> .....	76
4.2	One-pot sonochemical synthesis of reduced graphene oxide uniformly decorated with ultrafine silver nanoparticles for non-enzymatic detection of H <sub>2</sub> O <sub>2</sub> and optical detection of mercury ions .....	79
4.2.1	X-ray diffraction analysis.....	79
4.2.2	UV-Vis absorption spectra.....	80
4.2.3	FTIR spectroscopy .....	82

4.2.4	X-ray photoelectron spectroscopy .....	83
4.2.5	Raman spectroscopy .....	83
4.2.6	Morphology .....	85
4.2.7	Formation mechanism .....	89
4.2.8	Electrochemical sensing of H <sub>2</sub> O <sub>2</sub> .....	90
4.2.9	Optical detection of Hg <sup>2+</sup> ions .....	93
4.3	One-pot hydrothermal synthesis and characterization of FeS <sub>2</sub> (Pyrite)/Graphene nanocomposite .....	96
4.3.1	Optimization of the hydrothermal conditions .....	96
4.3.2	X-ray diffraction .....	102
4.3.3	FTIR spectroscopy .....	103
4.3.4	Raman spectroscopy .....	104
4.3.5	Morphology .....	105
4.3.6	Formation mechanism .....	108
4.3.7	EIS measurment .....	109
4.3.8	Photocurrent measurement .....	113
4.4	Sonochemical synthesis of reduced graphene oxide decorated with hierarchical ZnS nanoparticles .....	114
4.4.1	X-ray diffraction analysis .....	115
4.4.2	FTIR spectroscopy .....	116
4.4.3	Raman spectroscopy .....	117
4.4.4	Morphology study .....	118
4.4.5	Photoluminescence study .....	121
4.4.6	Photocatalytic activity .....	122
CHAPTER V: CONCLUSIONS .....		126
REFERENCES .....		128

## LIST OF TABLES

Table 3.1 Experimental conditions for the preparation of FeS <sub>2</sub> . .....	57
Table 4.1 A comparison of this work with works in the literature regarding the performance of the H <sub>2</sub> O <sub>2</sub> assays.....	78
Table 4.2 D and G peak positions, and intensity ratio of I (D) /I (G) (obtained by Raman analysis) of GO and AgNPs-rGO composites that were prepared at different ultrasonic irradiation times.....	85
Table 4.3 Comparison of results from this work and literature regarding performance of H <sub>2</sub> O <sub>2</sub> assays.....	93
Table 4.4 Electrochemical parameters obtained by simulation of the EIS results of FeS <sub>2</sub> particles and FeS <sub>2</sub> /rGO nanocompoaites with different GO concentrations; 0.5, 1, and 2 mg/mL in 0.1 M KCl solution containing 1 mM Fe(CN) <sub>6</sub> <sup>3-/4-</sup> (1:1).....	113

## LIST OF FIGURES

Figure 1.1 Number of publications per year on graphene. The data was extracted on December 24, 2013 through the Institute of Scientific Information (ISI) database using graphene as a keyword that appeared in topic.....	1
Figure 2.1 2-dimensional graphene is a basic building-block material for graphitic materials such as fullerene, carbon nanotube and graphite. (Source: Geim and Novoselov, 2007).....	7
Figure 2.2 Schematic $sp^2$ -hybridized C-C bond structure of graphene containing in-plane $\sigma$ -bonds and perpendicular $\pi$ -bonds. (Source: Hass et al., 2008). ....	8
Figure 2.3 Mechanical exfoliation of monolayer and few-layer graphene from HOPG. (Source: Van Noorden, 2012). ....	10
Figure 2.4 Schematic of the decomposition of a-Si <sub>1-x</sub> C <sub>x</sub> alloys into graphene. (Source: Peng et al., 2013). ....	11
Figure 2.5 Schematic growth mechanism of graphene on Ni substrate by chemical vapor deposition. (Source: Yu et al., 2008). ....	13
Figure 2.6 Schematic illustration of the possible C isotopes distribution in graphene films proposed for different growth mechanism for sequential input of C isotopes. a) C isotopes randomly distributed in graphene film such as might occur by surface segregation and/or precipitation. b) C isotopes seperately distributed in graphene film such as might occur by surface adsorption. (Source: Li et al., 2009c). ...	14
Figure 2.7 a) Schematic illustration of the roll-based production of graphene films grown on copper foil. b) Copper foil wrapping around a 7.5-inch quartz tube to be inserted into an 8-inch quartz reactor. The lower image shows the stage in which the copper foil reacts with CH <sub>4</sub> and H <sub>2</sub> gases at high temperatures c) Roll-to-roll transfer of graphene film from thermal release tape to PET film at 120 °C. d) A transparent graphene film transferred on a 35-inch PET sheet. e) An assembled graphene/PET touch panel showing outstanding flexibility. (Source: Bae et al., 2010). ....	15
Figure 2.8 a) During oxidization of graphite, linear clusters of epoxy groups are formed through cooperative binding that lead to a bent sheet. b) Carbon dioxide is released during thermal treatment and c) leaves vacancies and topological defects on the carbon grid that remains bent after reduction. (Source: Schniepp et al., 2006). ....	17
Figure 2.9 The average electrical conductivity of reduced GO films annealed at different temperatures. (Source: Wang et al., 2007). ....	18
Figure 2.10 Schematic illustration of the chemical approach to synthesis of aqueous graphene dispersion. 1) Oxidization of graphite (black blocks) to graphite oxide (gray blocks) and increasing the interlayer distance of sheets. 2) Sonication of graphite oxide to exfoliate and obtain colloidal GO. 3) Chemical reduction of GO colloids to obtain a conductive graphene colloids. (Source: Li et al., 2008). ....	19
Figure 2.11 Schematic illustration of the electrophoretic deposition process and b) Cross-sectional SEM image of electrophoretic deposited GO film. (Source: An et al., 2010). ....	21

Figure 2.12 Procedure comparison of different methods to produce GO. The very small amount of under-oxidized graphite which retained on the sieve indicates the increased efficiency of the improved GO method. (Source: Marcano et al., 2010). .....	23
Figure 2.13 (a) Lerf and Klinowski model for GO (Lerf et al., 1998). (b) STM image of a GO monolayer, which shows the oxidized and unoxidized regions (Gómez-Navarro et al., 2007). (c) New structural model for GO, which suggests five- and six-membered lactol rings (Gao et al., 2009). .....	24
Figure 2.14 Thermal conductivity enhancement of epoxy-based composites at 30 °C. Utilized graphitic fillers: graphitic microparticles (GMP), graphite nanoplatelets GNPs exfoliated at 200 °C (GNP-200) and 800 °C (GNP-800), carbon black (CB), and purified single-wall carbon nanotubes (SWNTs). (Source: Yu et al., 2007). .....	26
Figure 2.15 Schematic illustration of the fabrication of GO-Fe <sub>3</sub> O <sub>4</sub> . (Source: He et al., 2010a). .....	30
Figure 2.16 (a) Schematic illustration of the synthesis of rGO-GNDs. (b and c) TEM images of rGO uniformly decorated with Au nanodots. (Source: Yang et al., 2011c). .....	32
Figure 2.17 (a) Schematic illustration of the fabrication procedures of Pt/EGS nanocomposite film, (b) Photograph of EGO colloid solution and the setup of electrophoretic deposition process, (c) Photograph of the electrodeposited samples of Expandable graphene oxide (EGO), Expandable graphene sheets (EGS) and Pt/EGS, and (d and e) FESEM images of Pt/EGS nanocomposite at increasing magnifications. (Source: Liu et al., 2010c). .....	35
Figure 2.18 Schematic structure of P25-GR and tentative processes of the photodegradation of methylene blue (MB) over P25-GR. (Source: Zhang et al., 2009a). .....	39
Figure 2.19 (a) The energy level diagram for N-graphene/CdS nanocomposites in relation to the redox potentials for water spitting process in Na <sub>2</sub> S/Na <sub>2</sub> SO <sub>3</sub> aqueous solution, and (b) H <sub>2</sub> evolution of CdS, N-graphene/CdS composites with different contents of N-graphene. (Source: Jia et al., 2011). .....	40
Figure 2.20 (a) Gas response of WO <sub>3</sub> and WO <sub>3</sub> nanorods/graphene versus NO <sub>2</sub> concentration at 300 °C; (b) gas sensing to 1 ppm NO <sub>2</sub> , 100 ppm SO <sub>2</sub> , 100 ppm Cl <sub>2</sub> and 1 mL NH <sub>3</sub> .H <sub>2</sub> O, acetone, propanol, cyclohexane, methanol, ethanol, toluene and butanol. (Source: An et al., 2012). .....	47
Figure 3.1 Potentiostat/galvanostat (Versastat 3 Applied Research Princeton, USA). .....	52
Figure 3.2 Photograph of Misonix Sonicator S-4000, USA, 20 kHz. ....	54
Figure 3.3 Photograph of stainless steel autoclave and its teflon used for hydrothermal reaction. ....	56
Figure 3.4 Schematic illustration of the sandwich-type device for photocurrent measurements. ....	58



Figure 3.5 Schematic illustration of the X-ray diffraction by parallel atomic planes in a crystallite material.....	61
Figure 3.6 Schematic diagram of the FTIR machine.....	62
Figure 3.7 Energy-level diagram shows the states involved in Raman signal. The thickness of lines is proportional to the strength of signal from the different transitions. ....	63
Figure 3.8 The resulting Raman lines from different transitions.....	64
Figure 3.9 Schematic illustration of Scanning electron microscope. ....	65
Figure 4.1 Photo image of AgNPs/rGO composites on ITO with different volume ratios of GO (1.0 mg/mL) to Ag(NH <sub>3</sub> ) <sub>2</sub> OH (0.04 M): 12 (AgNPs-rGO-1), 6 (AgNPs-rGO-2) and 3 (AgNPs-rGO-3). ....	68
Figure 4.2 The first cycle of the CV profile of ITO in the solution of GO (1.0 mg/mL) and Ag(NH <sub>3</sub> ) <sub>2</sub> OH (0.04 M) with different volume ratios of 12, 6, and 3 (a–c), respectively, and in the solution of GO (1.0 mg/mL) and AgNO <sub>3</sub> (0.04 M) with a volume ratio of 12 (d). The inset highlights the CV profile of the solutions containing Ag(NH <sub>3</sub> ) <sub>2</sub> OH (a) and AgNO <sub>3</sub> (d). ....	69
Figure 4.3 XRD patterns of pristine GO (a), ITO (b), and AgNPs-rGO deposited on ITO that prepared by using the solution with different volume ratios of GO (1.0 mg/mL) to Ag(NH <sub>3</sub> ) <sub>2</sub> OH (0.04 M) of 12, 6, and 3, respectively (c–e).....	70
Figure 4.4 FTIR spectra of pristine GO (a) and AgNPs-rGO composite using the solution with the volume ratio of GO (1.0 mg/mL) to Ag(NH <sub>3</sub> ) <sub>2</sub> OH (0.04 M) of 6 (b). ....	71
Figure 4.5 Raman spectra of pristine GO (a) and the AgNPs-rGO composites using the solution with the volume ratio of GO (1.0 mg/mL) to Ag(NH <sub>3</sub> ) <sub>2</sub> OH (0.04 M) of 6 (b). The inset highlights the peaks of pristine GO. ....	72
Figure 4.6 FESEM images and size distribution diagram of AgNPs-rGO prepared by using the solution with GO (1.0 mg/mL) to Ag(NH <sub>3</sub> ) <sub>2</sub> OH (0.04 M) volume ratios of 12 (a and b), 6 (c and d), and 3 (e and f) and using the solution with a GO (1.0 mg/mL) to AgNO <sub>3</sub> (0.04 M) volume ratio of 12 (g and h). ....	74
Figure 4.7 Schematic illustration of the formation mechanism of AgNPs-rGO via electrodeposition. ....	75
Figure 4.8 CVs of various electrodes in 0.2 M PBS (pH 6.5) in the presence of 1.0 mM H <sub>2</sub> O <sub>2</sub> : bare ITO (a), AgNPs-rGO/ITO prepared by using different volume ratios of GO (1.0 mg/mL) to Ag(NH <sub>3</sub> ) <sub>2</sub> OH (0.04 M) of 12, 6, and 3, respectively (b–d), and AgNPs-rGO/ITO prepared by using the solution with GO (1.0 mg/mL) to AgNO <sub>3</sub> (0.04 M) volume ratio of 12 (e).....	77
Figure 4.9 Steady-state response of the AgNPs-rGO-2/ITO electrode to successive injection of H <sub>2</sub> O <sub>2</sub> into the stirred 0.2 M PBS (pH 6.5) with an applied potential of –0.3 V. The inset is the corresponding calibration curve. ....	78

Figure 4.10 XRD patterns of pristine GO (a), sample holder (b), and AgNPs-rGO that were prepared at different ultrasonic irradiation time: 5 min (c), 15 min (d) and 30 min (e). .....	80
Figure 4.11 (A) UV-vis absorption spectra of GO and AgNPs-rGO (the inset shows the photograph of the solution of GO and $\text{Ag}(\text{NH}_3)_2\text{OH}$ before and after ultrasonic irradiation), (B) time evolution of UV-vis absorption spectra of AgNPs-rGO. ....	81
Figure 4.12 FTIR spectra of pristine GO (a), and AgNPs-rGO that were prepared at different ultrasonic irradiation time: 5 min (b), 15 min (c) and 30 min (d). ....	82
Figure 4.13 XPS spectra of pristine GO (a), and AgNPs-rGO that were prepared at different ultrasonic irradiation time: 5 min (b), 15 min (c) and 30 min (d). ....	83
Figure 4.14 Raman spectra of pristine GO (a), and AgNPs-rGO that were prepared at different ultrasonic irradiation time: 5 min (b), 15 min (c) and 30 min (d). ....	85
Figure 4.15 TEM images and size distribution diagrams of AgNPs-rGO prepared by using the solution with GO (1.0 mg/mL) to $\text{Ag}(\text{NH}_3)_2\text{OH}$ (0.04 M) volume ratio of 8 (a and b), 4 (c and d), 2 (e and f) as well as the solution with GO (1.0 mg/mL) to $\text{AgNO}_3$ (0.04 M) volume ratio of 4 (g and h) with the same ultrasonic irradiation time of 5 min. ....	87
Figure 4.16 TEM images and size distribution diagrams of AgNPs-rGO prepared by using the solution with GO (1.0 mg/mL) to $\text{Ag}(\text{NH}_3)_2\text{OH}$ (0.04 M) volume ratio of 4 at different ultrasonic irradiation times 15 min (a and b) and 30 min (c and d), and HRTEM image of silver nanoparticles anchored on the surface of rGO sheet (e). ....	88
Figure 4.17 Schematic illustration of the formation mechanism of AgNPs-rGO composite via ultrasonic irradiation. ....	90
Figure 4.18 CV values of various electrodes in 0.2 M PBS (pH 6.5) in presence of 1.0 mM $\text{H}_2\text{O}_2$ : (a) bare GCE and AgNPs-rGO/GCE prepared by using different ultrasonication times of (b) 5 min, (c) 15 min and (d) 30 min. ....	92
Figure 4.19 Steady-state response of AgNPs-rGO-4/GCE to successive injections of $\text{H}_2\text{O}_2$ into stirred 0.2 M PBS (pH 6.5) with applied potential of -0.4 V. The inset is the corresponding calibration curve. ....	93
Figure 4.20 (a) Absorbance responses of AgNPs-rGO composite for different concentrations of $\text{Hg}^{2+}$ ions from 0.1 to 100 $\mu\text{M}$ . The inset shows the gradual colour change of the AgNPs-rGO solution with the increase in the $\text{Hg}^{2+}$ ion concentration. (b) The corresponding calibration curve for the $\text{Hg}^{2+}$ ion detection. (c) The relative absorbance change in AgNPs-rGO in the presence of $\text{Hg}^{2+}$ ions and some other common metal ions. ....	95
Figure 4.21 XRD patterns of samples A, B and C prepared at 180 °C with different reaction times; (a) 12 h, (b) 24 h and (c) 36 h. ....	97
Figure 4.22 XRD patterns of samples D, E and F prepared at 200 °C with different reaction times; (a) 12 h, (b) 24 h and (c) 36 h. ....	98

Figure 4.23 XRD patterns of samples G, E and H prepared at 200 °C for 24 h under different pH conditions; (a) 10, (b) 11 and (c) 12.....	99
Figure 4.24 FESEM images of samples E and H prepared at 200 °C for 24 h under different pH conditions; (a) 11, (b) 12. ....	99
Figure 4.25 TEM images of samples I, J, E and K prepared with different concentrations of gelatin; (a) 0, (b) 0.8, (c) 1.5 and (d) 2% wt/v.....	100
Figure 4.26 XRD pattern of samples I, J, E and K prepared with different concentrations of gelatin; (a) 0, (b) 0.8, (c) 1.5 and (d) 2% wt/v.....	101
Figure 4.27 XRD pattern of (a) pristine GO, (b) sample holder and samples prepared with different concentrations of GO: (c) without GO (sample E), (d) 0.5, (e) 1 and (f) 2 mg/mL. ....	103
Figure 4.28 FTIR spectra of (a) pristine GO and (b) FeS <sub>2</sub> /rGO nanocomposite (with 1 mg/mL of GO concentration). ....	104
Figure 4.29 Raman spectra of (a) pristine GO and (b) FeS <sub>2</sub> /rGO nanocomposite (with 1 mg/mL of GO concentration). The inset highlights the miniature peaks of the nanocomposite.....	105
Figure 4.30 FESEM images of samples prepared at the optimum hydrothermal conditions with different concentrations of GO: (a) without GO (sample E), (b) 0.5, (c) 1 and (d) 2 mg/mL. (e) FESEM image of sample prepared at 200 °C for 24 h under pH 11 with 2 mg/mL of GO concentration in the absence of gelatin. ....	107
Figure 4.31 Size distribution diagram of FeS <sub>2</sub> /rGO nanocomposites with different concentration of GO: (a) 0.5, (b) 1 and (c) 2 mg/mL.....	107
Figure 4.32 Schematic illustration of the formation mechanism of FeS <sub>2</sub> /rGO nanocomposite.....	109
Figure 4.33 Nyquist plots of different electrodes: FeS <sub>2</sub> (a), FeS <sub>2</sub> /rGO nanocomposites with different GO concentrations; (b) 0.5, (c) 1, (d) 2 mg/mL and together (e) in a 0.1 M KCl containing 1 mM Fe(CN) <sub>6</sub> <sup>3-/4-</sup> (1:1).....	112
Figure 4.34 Bode plots of different electrodes and the equivalent circuit models of the electrodes that prepared using: (1) FeS <sub>2</sub> particles and (2) FeS <sub>2</sub> /rGO nanocompoaites with different GO concentrations; 0.5, 1, and 2 mg/mL where the chi-squared ( $\chi^2$ ) is minimised at 10 <sup>-4</sup> . ....	113
Figure 4.35 Photocurrent response of FeS <sub>2</sub> particles (a) and FeS <sub>2</sub> /rGO nanocomposites with different concentration of GO: (b) 0.5, (c) 1 and (d) 2 mg/mL..	114
Figure 4.36 XRD patterns of pristine GO (a), sample holder (b), and ZnS/rGO nanocomposites that prepared at different ultrasonic irradiation time: 5 min (c), 15 min (d) and 30 min (e).....	116
Figure 4.37 FTIR spectra of pristine GO (a), and ZnS/rGO nanocomposite (b). ....	117

Figure 4.38 Raman spectra of pristine GO (a), and ZnS/rGO nanocomposite (b). .....	118
Figure 4.39 FESEM images and size distribution diagrams of ZnS/rGO nanocomposites prepared by using the solution with GO (1.0 mg/mL) and different amount of zinc acetate dehydrate 0.4 mM (a and b), 0.8 mM (c and d), 1.2 mM (e and f) and 1.6 mM (g and h), and ZnS particles (i and j). ....	120
Figure 4.40 TEM mages of ZnS/rGO nanocomposite at different magnifications. .....	121
Figure 4.41 Room temperature photoluminescence spectra of pure ZnS (a), and ZnS/rGO nanocomposite (b). ....	122
Figure 4.42 Photocatalytic activity: (a) UV-vis absorption spectra of MB aqueous solution at different time in the presence of ZnS/rGO-1.2 as photocatalyst and (b) photodegradation rate of MB at different interval times in the presence of varius photocatalysts. ....	125
Figure 4.43 Adsorption-desorption equilibrium rate of MB in dark condition versus time in the presence of varius photocatalysts. ....	125

## LIST OF SYMBOLS AND ABBREVIATIONS

Atomic force microscopy	(AFM)
Chemical vapor deposition	(CVD)
Constance phase element	(CPE)
Counter electrode	(CE)
Cyclic voltammetry	(CV)
Dye-sensitized solar cells	(DSSCs)
Electrochemical double-layer capacitors	(EDLCs)
Electrochemical impedance spectroscopy	(EIS)
Field emission scanning electron microscope	(FESEM)
Fourier transform infrared spectroscopy	(FTIR)
Glassy carbon electrode	(GCE)
Graphene oxide	(GO)
Highly oriented pyrolytic graphite	(HOPG)
Indium tin oxide	(ITO)
Methylene blue	(MB)
Nanoparticles	(NPs)
Phosphate buffer solution	(PBS)
Quantum dot-sensitized solar cells	(QDSSCs)
Reduced graphene oxide	(rGO)
Saturated calomel electrode	(SCE)
Silicon carbide	(SiC)
Single-wall carbon nanotubes	(SWNTs)
Scanning tunneling microscopy	(STM)
Surface-enhanced Raman scattering	(SERS)
Thioacetamide	(TAA)
Transmission electron microscope	(TEM)
Ultraviolet	(UV)
Working electrode	(WE)
X-ray diffraction	(XRD)

## CHAPTER I: INTRODUCTION

### 1.1 Background of study

Graphene is a one-atom-thick planar sheet of  $sp^2$ -bonded carbon atoms in form of a honeycomb lattice. Graphene exhibits unique electrical (Novoselov et al., 2004), thermal (Balandin et al., 2008), mechanical (Lee et al., 2008), and optical properties (Rao et al., 2009). These unique properties hold great promise for potential applications in many advanced technologies such as nanoelectronics (Gilje et al., 2007, Sharma and Ahn, 2013, Yung et al., 2013), sensors (Zhou et al., 2009b, Wu et al., 2013, Yuan and Shi, 2013, Yavari and Koratkar, 2012), capacitors (Liu et al., 2010a, Xu et al., 2013a, Dong et al., 2013, Huang et al., 2012) and composites (Stankovich et al., 2006a, Bai and Shen, 2012, Potts et al., 2011). So, according to the published papers in web of science, graphene has been extensively studied (Figure 1.1).

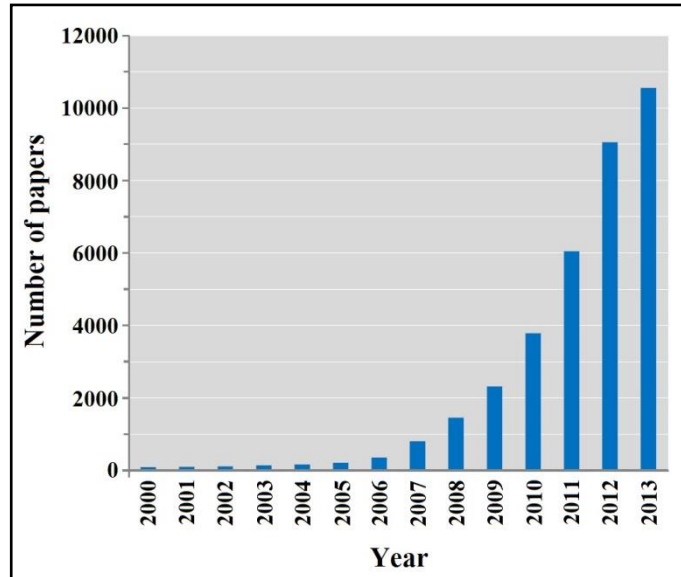


Figure 1.1 Number of publications per year on graphene. The data was extracted on December 24, 2013 through the Institute of Scientific Information (ISI) database using graphene as a keyword that appeared in topic.

In 2006, Professor Rodney S. Ruoff and his group reported the first graphene-based nanocomposite, a graphene-polystyrene composite (Stankovich et al., 2006a).

According to their results, incorporation of the reduced graphene oxide or chemically modified graphene sheets with polystyrene enhanced the electrical conductivity of the composite. This achievement opened a broad new class of graphene-based composite materials. In addition, graphene oxide has attracted attention as a precursor for the low-cost and large-scale production of graphene-based nanocomposite materials. So, graphene has been incorporated with a variety of materials for various applications.

In recent years, graphene-based nanocomposites have been widely reported and explored for various applications. According to the second component in the composites, graphene-based nanocomposite can be classified into two main categories. The first category is graphene-based polymer composites. The superior electrical (Novoselov et al., 2004), mechanical (Lee et al., 2008), thermal (Balandin et al., 2008) and optical (Bae et al., 2010) properties of graphene hold great promise for improving the properties of graphene-based polymer nanocomposites (Stankovich et al., 2006a, Ramanathan et al., 2008, Xu et al., 2009, Quan et al., 2009), compared to the neat polymers.

The second category is graphene-based inorganic nanocomposites. Graphene has been decorated with a variety of inorganic materials such as metals (Au (Vinodgopal et al., 2010, Huang et al., 2010a), Ag (Shen et al., 2010, Zhang et al., 2012b), Pt (Yoo et al., 2009, Li et al., 2010c), Cu (Luechinger et al., 2008, Li et al., 2013a), etc.), metal oxides (ZnO (Li and Cao, 2011, Luo et al., 2012), TiO<sub>2</sub> (Guo et al., 2011), SnO<sub>2</sub> (Huang et al., 2011b), Fe<sub>3</sub>O<sub>4</sub> (Wang et al., 2011d), Fe<sub>2</sub>O<sub>3</sub> (Wang et al., 2011b), NiO (Xia et al., 2011), MnO<sub>2</sub> (Cheng et al., 2011), etc.), metal sulphides (CdS (Cao et al., 2010, Jia et al., 2011), ZnS (Wang et al., 2010i, Zhang et al., 2012c), MoS<sub>2</sub> (Li et al., 2011d, Chang and Chen, 2011b), PbS (Zhang et al., 2012a), etc.). Such composites have great potentials for various applications such as electrochemical sensing, surface-enhanced

Raman scattering, various catalytic activity, supercapacitors, solar cells and lithium ion batteries.

## 1.2 Aim and objectives

As mentioned, superior properties of graphene make it an attractive matrix for composites. It is found that decoration of graphene sheets with nanoparticles not only enhances the performance of graphene and nanoparticles, but also displays additional novel properties resulting from the interaction between nanoparticles and graphene sheets. Developing the method that is fast, low-cost, environmentally friendly and nontoxic for preparing graphene-based composites is very important and challenging. The morphology, size and distribution of nanoparticles on the surface of graphene affect the performance of the composite, which are difficult to control. Compared to metal oxides, few literatures have reported on the synthesis of metal sulfide-graphene nanocomposites such as ZnS and even there is no report on the synthesis of graphene-FeS<sub>2</sub> nanocomposite.

In order to achieve the mentioned objectives, we designed and carried out the following researches:

1) Electrodeposition of silver nanoparticles on the graphene surface and simultaneously on the surface of indium tin oxide (ITO) as an electrode by a cyclic voltammetry method in an aqueous solution mixture of graphene oxide (GO) and silver ammonia complex ( $\text{Ag}(\text{NH}_3)_2\text{OH}$ ) as an electrolyte. The resultant electrode can be used for enzymeless electrochemical detection of hydrogen peroxide.

2) Synthesis of reduced graphene oxide (rGO) uniformly decorated with silver nanoparticles (AgNPs) through a simple ultrasonic irradiation of the aqueous solution containing silver ammonia complex ( $\text{Ag}(\text{NH}_3)_2\text{OH}$ ) and graphene oxide (GO). The size of nanoparticles could be tuned by adjusting the volume ratio of precursors and



ultrasonic irradiation time. The resultant composite can be investigated for electrochemical sensing.

3) Optimization of the hydrothermal conditions such as reaction temperature, reaction time, pH of the solution and the amount of gelatin for preparing FeS<sub>2</sub> nanoparticles and subsequently utilizing the optimum hydrothermal conditions for preparation of FeS<sub>2</sub>/graphene nanocomposites with different loading amount of graphene. The resultant composites can be evaluated for potential application in energy conversion by photocurrent measurement.

4) Synthesis of reduced graphene oxide (rGO) decorated with hierarchical ZnS nanospheres by a one-pot sonochemical strategy. The size and number density of nanospheres could be tuned by adjusting the volume ratio of precursors. The resultant composite can be used for photocatalytic degradation of methylene blue (MB) under ultraviolet (UV) light irradiation.

### **1.3 Hypothesis**

Before doing the experiments, the following hypotheses have been considered:

1) Electrochemical approach for deposition of variety of inorganic crystals on different substrates is a very attractive method to produce thin-films due to its fast, easy and environmental friendly. On the other hand, it was found that GO can be deposited on the surface of different substrates such as glassy carbon electrode (GCE) and indium tin oxide (ITO), and simultaneously reduced by electrochemical techniques. Similarly, silver nanoparticles and GO sheets could be electrodeposited on ITO substrate.

2) FeS<sub>2</sub>, also known as pyrite, displays interesting electronic and optical properties and has a narrow band gap of 0.95 eV, and a high optical absorption coefficient ( $\alpha > 10^5 \text{ cm}^{-1}$ ). Due to these interesting properties, FeS<sub>2</sub> has been investigated for applications in photovoltaic devices. Hydrothermal is a powerful synthesis approach for the formation of a variety of inorganic nanostructures with high

crystallinity without the need of post-synthetic annealing and calcination, and simultaneously reduction of GO to rGO. Gelatin is known as a green capping and reducing agent for preparation of nanoparticles. Incorporation of graphene with FeS<sub>2</sub> can enhance the performance of the composite for energy conversion.

3) Sonochemical method has been proven to be a versatile and promising technique in the synthesis of a variety of nanostructures such as metals, metal oxides and metal sulfides. The adsorbed metal ions such as Ag ions onto the surface of GO sheets could be easily reduced into the metallic form of Ag by applying ultrasonic irradiation. Also, the adsorbed zinc ions onto the surface of GO sheets could be reduced in the presence of sulfur precursor such as thioacetamide (TAA) to form ZnS particles by applying ultrasonic irradiation.

#### **1.4 Thesis structure**

The thesis was written in five chapters. Chapter One presents the history of study, aim and objectives, and hypothesis. Chapter Two includes a literature review on two main parts: first, graphene and graphene oxide, their structures and synthesis methods, and second, graphene-based nanocomposites, their synthesis methods and applications. Chapter Three deals with the experimental details of the four main projects:

1. Electrodeposition synthesis of silver-nanoparticle-decorated graphene on indium-tin-oxide for enzymeless hydrogen peroxide detection
2. One-pot sonochemical synthesis of reduced graphene oxide uniformly decorated with ultrafine silver nanoparticles for non-enzymatic detection of H<sub>2</sub>O<sub>2</sub> and optical detection of mercury ions
3. One-pot hydrothermal synthesis and characterization of FeS<sub>2</sub> (Pyrite)/Graphene nanocomposite

#### 4. Sonochemical synthesis of reduced graphene oxide decorated with hierarchical ZnS nanospheres

The techniques, which used in this thesis, were explained in the end of this chapter. Chapter Four presents the results and discussion of each project. Chapter Five provides the conclusion of the thesis.

## CHAPTER II: REVIEW OF RELATED LITERATURE

### 2.1 Graphene

Graphene is a one-atom-thick planar sheet of  $sp^2$ -bonded carbon atoms in form of a honeycomb lattice, and it is essentially building-block material for graphitic materials such as fullerene, carbon nanotube and graphite (Figure 2.1).

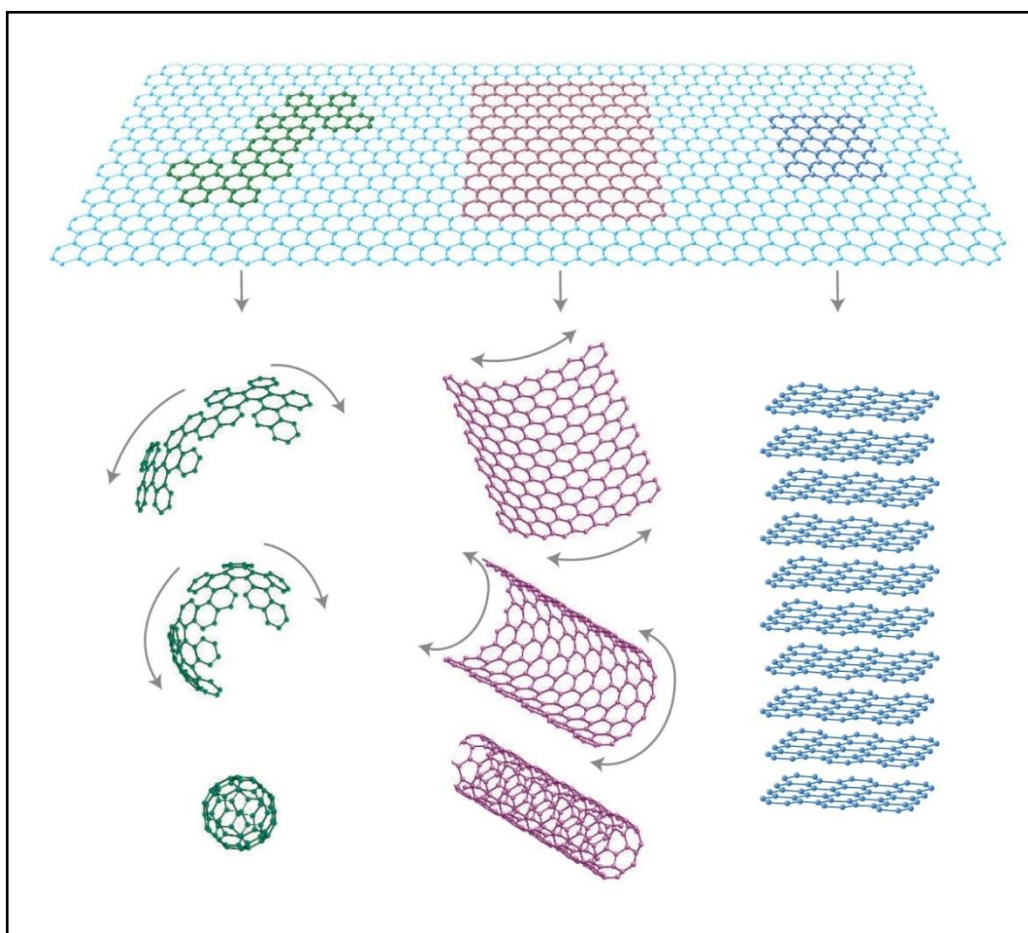


Figure 2.1 2-dimensional graphene is a basic building-block material for graphitic materials such as fullerene, carbon nanotube and graphite. (Source: Geim and Novoselov, 2007)

The  $2s$ ,  $2p_x$  and  $2p_y$  orbitals in each carbon atom of graphene are mixed with together to form three  $sp^2$ -hybrid orbitals. Three  $sp^2$ -hybrid orbital electrons form extremely strong in-plane  $\sigma$ -bonds with three nearest neighbor atoms in the basal plane of graphene (Figure 2.2). The fourth valence electron lies in the  $2p_z$  orbital that is

oriented perpendicular to the graphene plane and forms the delocalized  $\pi$ -bond, which is responsible for the electron conduction.

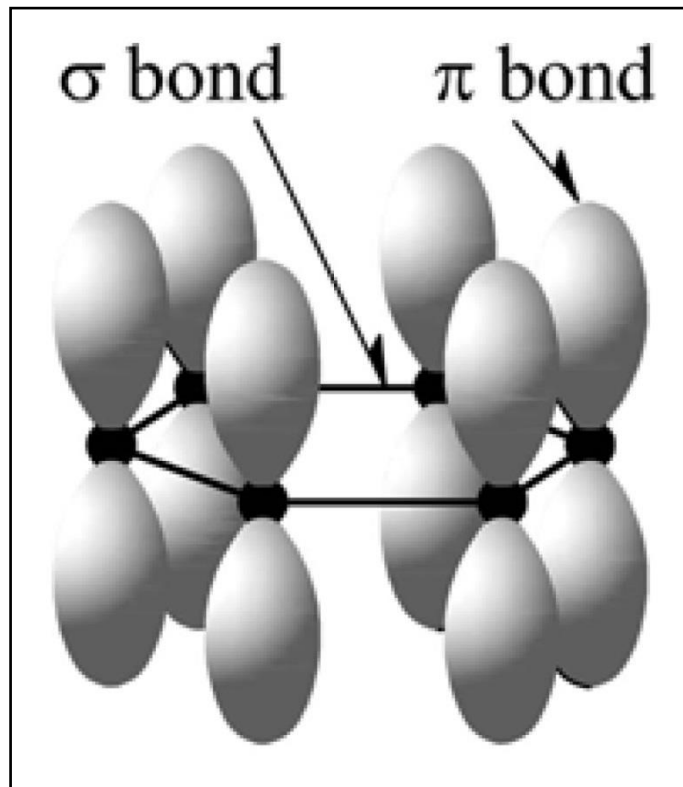


Figure 2.2 Schematic  $sp^2$ -hybridized C-C bond structure of graphene containing in-plane  $\sigma$ -bonds and perpendicular  $\pi$ -bonds. (Source: Hass et al., 2008).

Graphene was first isolated from graphite by Geim and Novoselov at the University of Manchester in 2004. According to their study, graphene demonstrated ambipolar electric-field effect with a high value of charge carrier mobility ( $\sim 10\,000\text{ cm}^2\text{ V}^{-1}\text{ s}^{-1}$ ) at ambient temperature (Novoselov et al., 2004). Du et al. reported superior charge carrier mobility of  $200\,000\text{ cm}^2\text{ V}^{-1}\text{ s}^{-1}$  at low-temperature for charge carrier density below  $5 \times 10^9\text{ cm}^{-2}$ , which cannot be obtained in semiconductors or non-suspended graphene (Du et al., 2008). It has been found that the charge carrier mobility decreases with the increase of layer of graphene (Nagashio et al., 2009). The thermal conductivity measurements have shown that the suspended single-layer graphene sheet exhibits extremely high thermal conductivity value of  $5000\text{ W m}^{-1}\text{ K}^{-1}$  (Balandin et al., 2008). The measurements have shown that the white light opacity of a suspended single-layer graphene sheet is  $2.3 \pm 0.1\%$  with a negligible reflectance ( $< 0.1\%$ ),

whereas the opacity is independent of wavelength and increases linearly with the increase of the number of layers from 1 to 5 (Nair et al., 2008). Besides, graphene exhibits other superior properties such as fracture strength (125 GPa) (Lee et al., 2008), Young's modulus ( $\sim 1100$  GPa) (Lee et al., 2008), and large specific surface area (theoretical value of  $2630 \text{ m}^2 \text{ g}^{-1}$ ) (Rao et al., 2009).

## **2.2 Synthesis of graphene**

Four most common routes for synthesis of graphene are mechanical exfoliation, epitaxial growth, chemical vapor deposition and reduction of graphene oxide, which are either top-down or bottom-up strategy. The top-down strategy is the breaking down of graphite into graphene and bottom-up strategy is the building up of graphene using carbon atoms.

### **2.2.1 Mechanical exfoliation**

In 2004, Geim's group reported the exfoliation of monolayer graphene and transferring it onto a 300 nm silicon dioxide substrate using mechanical exfoliation technique (Novoselov et al., 2004). In this method, an isolated graphene can be produced by peeling it off from highly oriented pyrolytic graphite (HOPG) using a Scotch tape (Figure 2.3). Although few layer graphene sheets are transparent for visible light but can be easily identified by optical microscopy on the  $\text{SiO}_2$  surface because of the optical contrast of graphene sheet and  $\text{SiO}_2$  substrate. The thickness of few layer graphene sheets on  $\text{SiO}_2$  surface can measure by using Atomic force microscopy (AFM). The advantage with this technique is that the individual graphene sheet prepared by this technique has high quality, while the disadvantage is that this technique is not suitable for large-scale production.



Figure 2.3 Mechanical exfoliation of monolayer and few-layer graphene from HOPG. (Source: Van Noorden, 2012).

### 2.2.2 Epitaxial growth

Epitaxial growth technique is one of the bottom-up strategies to produce graphene sheets. Generally, a silicon carbide (SiC) is heated to the temperature higher than 1000 °C under ultra-high vacuum. In these conditions, the silicon atoms desorb from the surface of silicon carbide, and the carbon atoms left behind rearrange to create few layers of graphene (Figure 2.4). Back to history, monolayer graphene on silicon

carbide has been prepared by A. J. Van Bommel et al. in 1975 (Van Bommel et al., 1975). In recent years, the epitaxial growth of graphene on silicon carbide has been highly promoted by a lot of scientists, which include Professor de Heer from Georgia Institute of Technology (Berger et al., 2006, de Heer et al., 2007, Hass et al., 2008, Kedzierski et al., 2008). De Heer and his group comprehensively investigated the growth mechanism and electronic properties of the graphene on SiC prepared by epitaxial growth technique (Hass et al., 2008). Recently, some developments were reported on the epitaxial growth of graphene. Juang et al. improved this process and grew the epitaxial graphene on SiC substrate at low temperature (750 °C) (Juang et al., 2009) and Emtsev et al. has reported the epitaxial growth of graphene on SiC substrate in an argon atmosphere close to atmospheric pressure (Emtsev et al., 2009). The major

advantages with this method are that it has potential to use for large-scale production, and the epitaxial graphene on SiC can be used for immediate implementation in electronic devices. The epitaxial few-layer graphene grown on SiC substrate is not uniform on thickness and the electronic properties of the epitaxial graphene depend upon its thickness. However, a way of growing to achieve wide and uniform few-layer graphene with a desired thickness should be established.

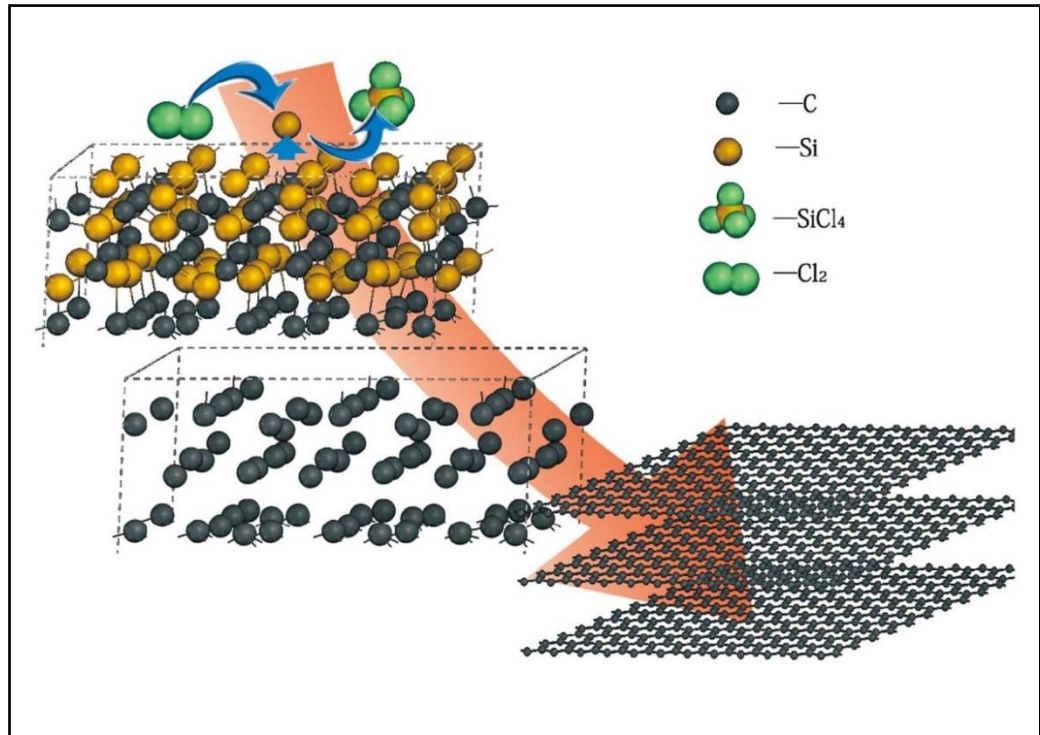


Figure 2.4 Schematic of the decomposition of a-Si<sub>1-x</sub>C<sub>x</sub> alloys into graphene. (Source: Peng et al., 2013).

### 2.2.3 Chemical vapor deposition

Chemical vapor deposition (CVD) technique is another bottom-up strategy to produce monolayer or few-layer graphene. CVD has attracted attention due to its ability to the fabrication of large continuous graphene sheets and transferring from metal substrate onto the surface of other substrates. Generally, carbon atoms can be segregated from hydrocarbon gas (for example, CH<sub>4</sub> or C<sub>2</sub>H<sub>2</sub>) and adsorbed on the surface of a metal catalytic substrate (such as nickel (Kim et al., 2009, Reina et al., 2008), cobalt (Blake et al., 2008) and copper (Li et al., 2009b, Bae et al., 2010)), and



create monolayer or few-layer graphene under high temperature and high vacuum. Back to history, the growth of “monolayer graphite” on metal single crystal was reported in early CVD studies (May, 1969, Shelton et al., 1974, Eizenberg and Blakely, 1979). Recently, researchers have been trying to obtain monolayer and few-layer graphene on several kinds of metal substrate with controlled quality and thickness. The mechanism of growth in CVD technique depends on the carbon solubility of the metal substrate. For the metal substrate with mediate and high carbon solubility such as Ni and Co, the segregated carbon atoms diffuse into the surface of metal substrate while increasing temperature to form a solid solution. Then, the carbon atoms come out from inside of the metal substrate and precipitate as a graphene layer on the surface of metal during the cooling process (Kim et al., 2009, Reina et al., 2008). The thickness and quality of graphene layers can be controlled by varying the cooling rate, and the concentration of carbon atoms diffused into the metal substrate. Figure 2.5 shows the effect of cooling rate process on the thickness and quality of graphene on the surface of nickel substrate (Yu et al., 2008). By using a low cooling rate ( $0.1\text{ }^{\circ}\text{C/s}$ ) gives nothing because the carbon atoms have enough time to diffuse into the nickel substrate. With medium or fast cooling rate ( $\sim 10\text{ }^{\circ}\text{C/s}$ ), few-layer graphene with different thickness and quality can be formed. With very fast cooling rate ( $\sim 20\text{ }^{\circ}\text{C/s}$ ), few-layer graphene with several defects can be formed on the surface of nickel substrate. The concentration of carbon atoms diffused into the metal substrate can be determined by the type and concentration of hydrocarbon gas as well as the thickness of metal substrate.

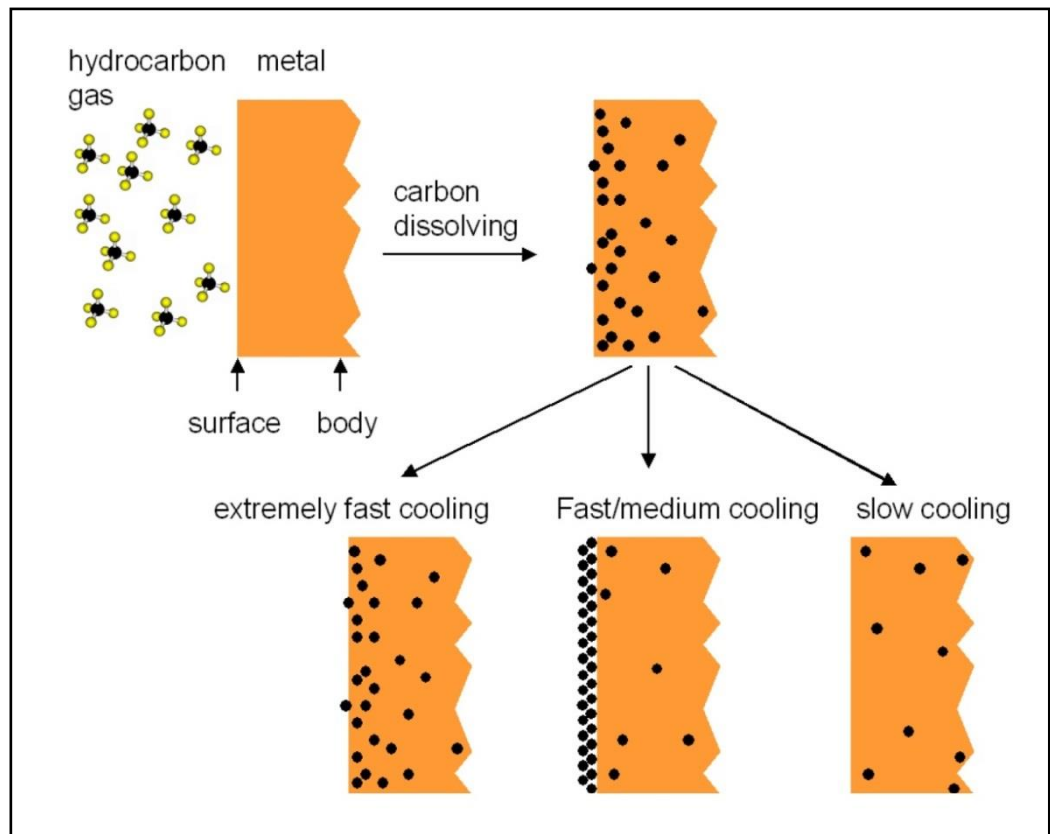


Figure 2.5 Schematic growth mechanism of graphene on Ni substrate by chemical vapor deposition. (Source: Yu et al., 2008).

In contrast, Ruoff et al. demonstrated that the growth mechanism of graphene on metal with low carbon solubility such as copper (Cu) is based on the surface absorption of carbon atoms whereas on Ni is based on the segregation and precipitation of carbon atoms (Li et al., 2009b, Li et al., 2009c) (Figure 2.6). When a copper foil is heated up from room temperature to 1000 °C under a mixture of methane and hydrogen gas, methane molecules are decomposed (Cu acts as a catalyst to promote the decomposition of methane), and the carbon atoms are adsorbed onto the surface of Cu substrate. In the early growth process, the carbon atoms adsorbed onto the surface of Cu acting as nucleation sites of graphene and growth to form monolayer graphene islands uniformly distributed on the surface of Cu substrate. These graphene islands grow outward and join to the neighboring graphene islands to make a continuous graphene layer, which fully covers the Cu substrate under the optimum conditions such as annealing temperature, hydrogen/methane flow rate and partial pressure. After fully coverage of

the Cu substrate with monolayer graphene, the growth process is terminated, which means the process is “self-limiting” (Li et al., 2009c).

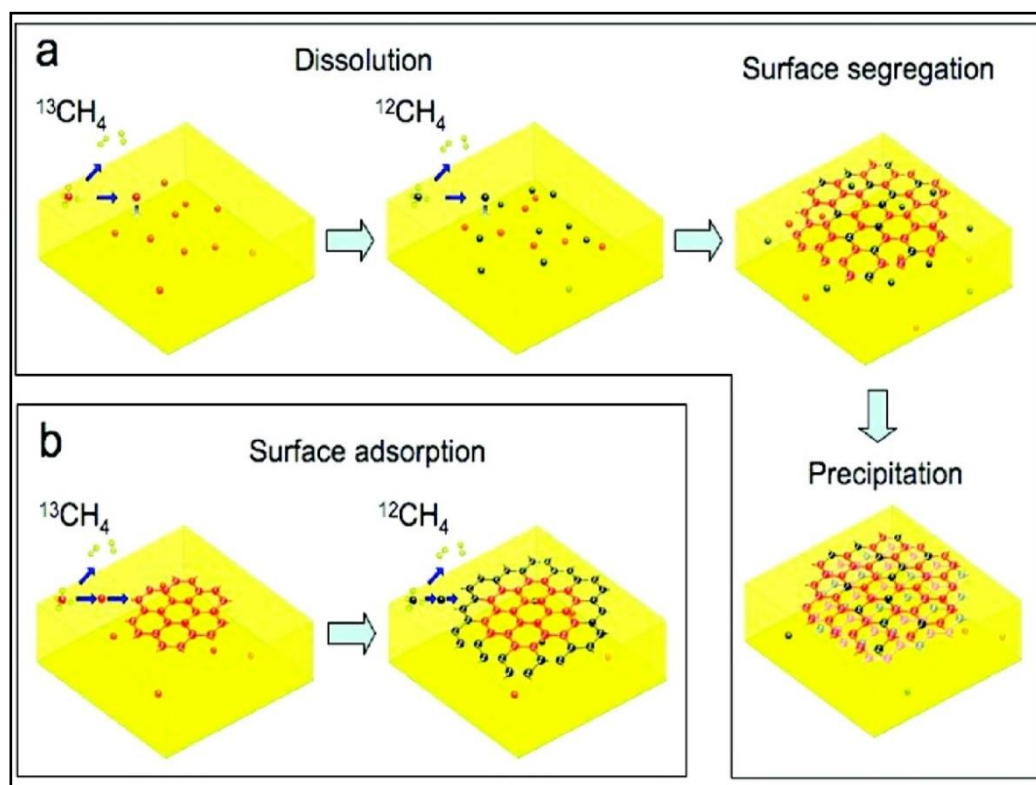


Figure 2.6 Schematic illustration of the possible C isotopes distribution in graphene films proposed for different growth mechanism for sequential input of C isotopes. a) C isotopes randomly distributed in graphene film such as might occur by surface segregation and/or precipitation. b) C isotopes seperately distributed in graphene film such as might occur by surface adsorption. (Source: Li et al., 2009c).

As mentioned, the graphene grown on metal by CVD can be transferred to the other substrate (Li et al., 2009b, Bae et al., 2010). Recently, Bae et al. reported the production of 30 inches predominantly monolayer graphene on a roll of copper foil by using CVD technique (Bae et al., 2010) (Figure 2.7). They transferred their production onto the other substrate by three steps: 1) supporting with a layer of polymer (polyethylene terephthalate (PET)), 2) chemical etching of the copper foil and 3) releasing the graphene layers and transfer onto the other substrates.

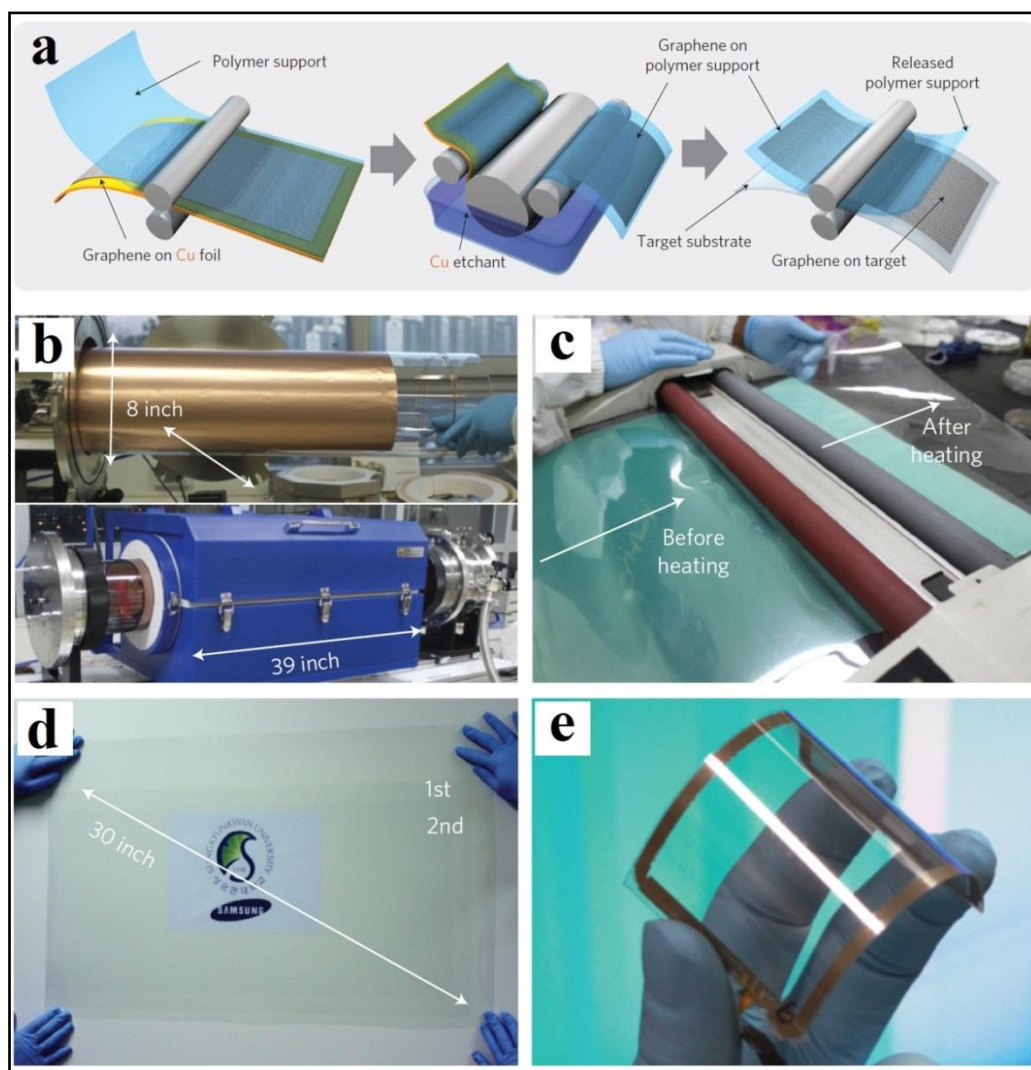


Figure 2.7 a) Schematic illustration of the roll-based production of graphene films grown on copper foil. b) Copper foil wrapping around a 7.5-inch quartz tube to be inserted into an 8-inch quartz reactor. The lower image shows the stage in which the copper foil reacts with  $\text{CH}_4$  and  $\text{H}_2$  gases at high temperatures c) Roll-to-roll transfer of graphene film from thermal release tape to PET film at  $120^\circ\text{C}$ . d) A transparent graphene film transferred on a 35-inch PET sheet. e) An assembled graphene/PET touch panel showing outstanding flexibility. (Source: Bae et al., 2010).

#### 2.2.4 Graphene from graphene oxide

As mentioned, graphite flakes can be oxidized in the presence of strong acids and oxidizing agents. The carbon planes of graphite oxide are heavily functionalized with oxygen-containing groups. Due to these oxygen-containing groups, graphite oxide can be easily exfoliated to individual graphene oxide sheets by sonication in water or rapid heating process. Graphene is conductive, mainly due to the long-range  $sp^2$  bonding network of the graphitic lattice (B, 2001, Kopelevich and Esquinazi, 2007). GO is

electrically insulating due to the disruption of  $sp^2$  bonding network by the oxygen-containing groups during the oxidation process. The conductivity of GO can be returned by removing oxygen-containing groups and restoring the  $sp^2$  bonding network in the process named reduction. The obtained product is usually called reduced graphene oxide (rGO), chemically modified graphene, or chemically converted graphene. The complete removing of the oxygen-containing groups has not yet been achieved, resulting in only partially restoration of the  $sp^2$  bonding network. Thus, the rGO has lower electrical conductivity compared to the pristine graphene. There are a number of strategies for the reduction of GO such as thermal annealing reduction, chemical reduction by using reducing agents, electrochemical reduction, etc.

#### *2.2.4.1 Thermal annealing reduction*

GO is thermally unstable and can be reduced by heat treatment, and the process is called thermal annealing reduction. Rapid heating ( $>2000$  °C/min) can exfoliate and reduce graphite oxide, yielding a black powder (Schniepp et al., 2006, Wu et al., 2009a, McAllister et al., 2007, Wu et al., 2009b). The exfoliation and reduction of graphite oxide are mainly due to the decomposition of oxygen-containing groups at high temperature and the sudden generation of CO or CO<sub>2</sub> gases within the space between graphite oxide sheets, which generates a high pressure (130 MPa at 1000 °C) to separate the graphene sheets from each other (McAllister et al., 2007). Although, the dual-role of rapid heating makes this method a good way to produce large-scale graphene, but the rGO produced by this method has small lateral size with defects. The main reason is that carbon atoms can be removed from the carbon plane during the thermal reduction process (by releasing carbon dioxide), which splits the carbon plane of graphene into the pieces with small size, and makes vacancies and topological defects (Schniepp et al., 2006, Kudin et al., 2007) (Figure 2.8). As a result, the electrical conductivity of the

products has a value range from 10 to 23 S/cm, which is lower than that of pristine graphene ( $10^4$  S/cm) (Schniepp et al., 2006, Cuong et al., 2010).

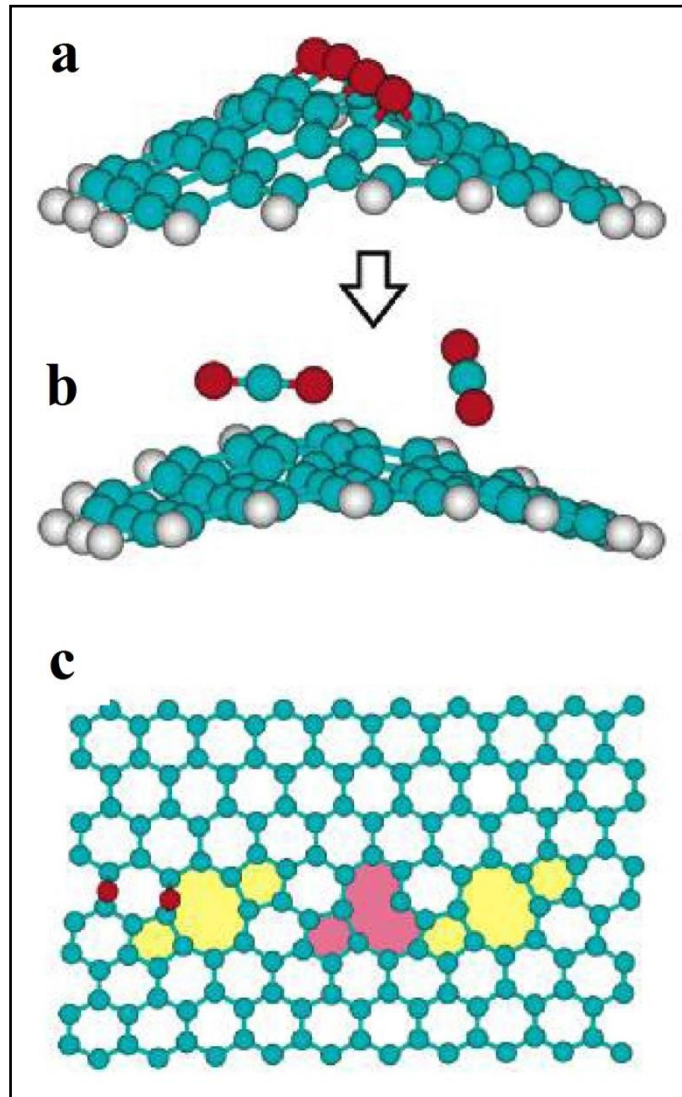


Figure 2.8 a) During oxidization of graphite, linear clusters of epoxy groups are formed through cooperative binding that lead to a bent sheet. b) Carbon dioxide is released during thermal treatment and c) leaves vacancies and topological defects on the carbon grid that remains bent after reduction. (Source: Schniepp et al., 2006).

Another strategy is the reduction of GO film by thermal annealing with slow heating in vacuum, or in the presence of inert or reducing gas. In this route, the electrical conductivity of the reduced GO film depends on the annealing temperature. Wang and coworkers showed the electrical conductivity of the reduced GO film increases with the increase of the annealing temperature (Wang et al., 2007) (Figure 2.9). In addition to the annealing temperature, the annealing atmosphere affects the quality of reduced GO film. Therefore, thermal annealing reduction has been carried out

in vacuum (Becerril et al., 2008), inert gas (Wang et al., 2007) or reducing atmosphere (Wu et al., 2009a, Wang et al., 2007, Wu et al., 2009b, Li et al., 2009d).

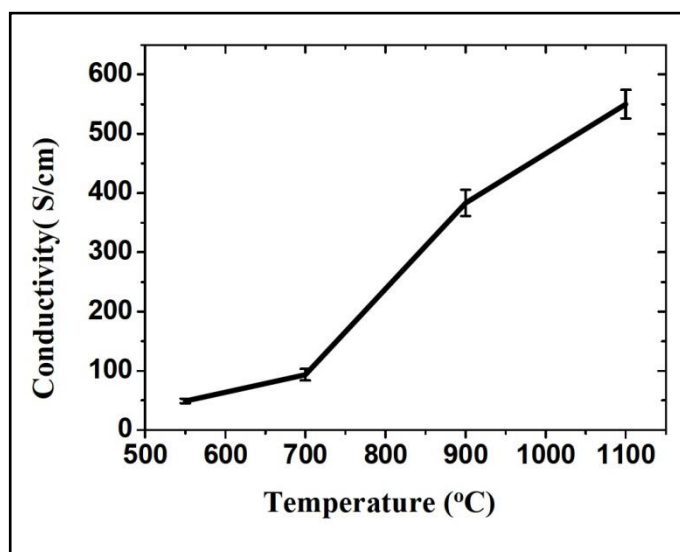


Figure 2.9 The average electrical conductivity of reduced GO films annealed at different temperatures. (Source: Wang et al., 2007).

#### 2.2.4.2 Chemical reduction

The solution-based process to produce monolayer graphene sheets was firstly demonstrated by Ruoff and his group (Stankovich et al., 2006b, Stankovich et al., 2007). In this way, the hydrophilic nature of graphite oxide sheets leads water molecules to intercalate between the graphite sheets, which increases the interlayer distance of the sheets. Increasing the interlayer distance of the sheets weakens the van der Waals forces between the sheets. In addition, the graphite oxide sheets are negatively charged when dispersed in water. Weakening of the van der Waals forces, and electrostatic repulsion between the sheets lead to the exfoliation of graphite oxide sheets and make a stable monolayer, bilayer or few-layer GO sheets solution by sonication treatment. Chemically converted graphene sheets can be obtained by chemical reduction of these graphene oxide sheets (Li et al., 2008) (Figure 2.10).



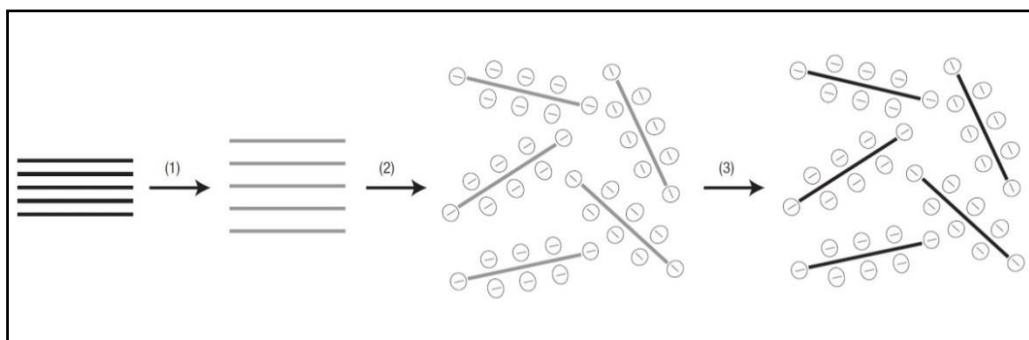


Figure 2.10 Schematic illustration of the chemical approach to synthesis of aqueous graphene dispersion. 1) Oxidization of graphite (black blocks) to graphite oxide (gray blocks) and increasing the interlayer distance of sheets. 2) Sonication of graphite oxide to exfoliate and obtain colloidal GO. 3) Chemical reduction of GO colloids to obtain a conductive graphene colloids. (Source: Li et al., 2008).

Several reducing agents have been used for the reduction of graphene oxide such as hydrazine hydrate (Stankovich et al., 2006b, Stankovich et al., 2007), sodium borohydride (Bourlinos et al., 2003, Shin et al., 2009) and hydroiodic acid (Pei et al., 2010, Moon et al., 2010). Chemical reduction is usually carried out at ambient temperature or by using moderate heating, which makes it a low-cost and easy way to produce large-scale graphene compared with thermal annealing reduction. Ruoff and his group, firstly, used hydrazine hydrate as reducing agent to produce very thin layer of graphene-like sheets (Stankovich et al., 2007). During the reduction of GO, The brown colored of GO dispersed in water turns black and the reduced graphene oxide sheets aggregate and finally precipitate. The presumable reason for the precipitation of the rGO sheets is that the rGO sheets become less hydrophilic due to removal of oxygen-containing groups. To improve the stability of rGO, Li and coworkers added ammonia into the reaction solution to increase the pH during the reduction with hydrazine, which provides the maximal surface charge density on the rGO sheets (Li et al., 2008). In 2009, Shin et al. showed the rGO film prepared using  $\text{NaBH}_4$  as a reductant of GO has resistance much lower (59  $\text{k}\Omega/\text{square}$ ) than that of prepared using hydrazine for reduction of GO (780  $\text{k}\Omega/\text{square}$ ) (Shin et al., 2009). It demonstrates  $\text{NaBH}_4$  is more effective than hydrazine for reduction of GO although it is slowly hydrolyzed by water.



In 2010, Pei et al. and Moon et al. reported independently another reducing route in producing GO, in which hydroiodic acid used as a strong reductant of GO (Pei et al., 2010, Moon et al., 2010). Both independent studies show that the conductivity of afforded rGO film is around 300 S/cm. GO can be reduced in the form of colloidal, powder or film by hydroiodic acid in the form of solution or vapor. Some efforts have been made to use green and natural reducing agents such as vitamin C (Fernández-Merino et al., 2010), sugar (Zhu et al., 2010a) or gelatin (Liu et al., 2011b).

#### 2.2.4.3 *Electrochemical reduction*

Electrochemical methods have been reported in the reduction of GO (Zhou et al., 2009a, Wang et al., 2009b, Ramesha and Sampath, 2009, Guo et al., 2009). Electrochemical reduction of GO is a very attractive method to produce a graphene-film due to its fast, easy, green nature and does not require the use of any toxic reducing agents (such as  $\text{NaBH}_4$  and  $\text{N}_2\text{H}_4$ ). The pre-deposited GO film on a substrate (gold, glassy carbon electrode, ITO, etc.) can be reduced by applying a constant DC voltage (Guo et al., 2009) or a DC bias using cyclic voltammetry technique (Ramesha and Sampath, 2009). Ramesh and Sampath reported the reduction of GO by using cyclic voltammetry technique in the range of 0 to -1 V with respect to a saturated calomel electrode (SCE) in an aqueous 0.1M  $\text{KNO}_3$  solution, in which the reduction of GO in the first scan starts from -0.6 V and reaches to a maximum at -0.87 V. In the second scan, the reduction peak was not observed, indicating the reduction of GO in this scanning potential range is an electrochemically irreversible process. Guo et al. reported the reduction of GO by applying a DC voltage of -1.3 or -1.5 V with respect to SCE in 10 mmol/L pH 5.0 phosphate buffer solution (PBS) ( $\text{K}_2\text{HPO}_4/\text{KH}_2\text{PO}_4$ ) as an electrolyte. In cyclic voltammetry study, Guo et al. found the reduction of GO can be started at -0.75 V and reached to the maximum at -1.2 V, and the reduction of GO is an electrochemically irreversible process. Furthermore, the electrochemically reduction

methods can be used for the deposition of GO sheets on the substrate in addition to direct production through reduction. In the year of 2010, An et al. reported the electrophoretic deposition of GO platelets on the different conductive substrate by applying a DC voltage of 10 V to the substrate in an aqueous solution of GO, in which the electrodeposited GO sheets can be reduced during the deposition process (Figure 2.11) (An et al., 2010). In 2011, Chen et al. reported the electrodeposition of GO sheets on glassy carbon electrode (GCE) and simultaneous reduction of them by using cyclic voltammetry technique. In this method, cyclic voltammetry technique performs in the range of +0.6 to -1.5 V on a GCE in a phosphate buffer solution of GO sheets with the pH of around 9 (Chen et al., 2011b).

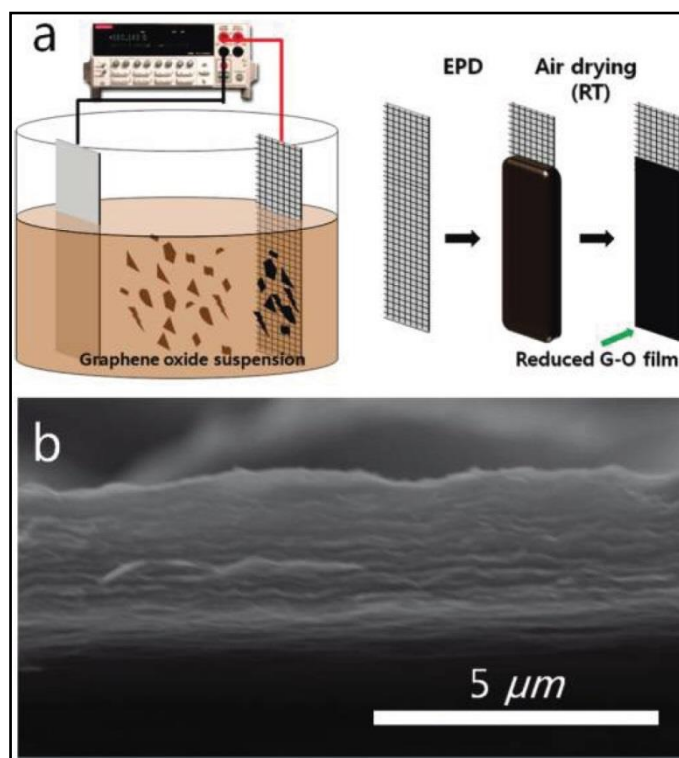


Figure 2.11 Schematic illustration of the electrophoretic deposition process and b) Cross-sectional SEM image of electrophoretic deposited GO film. (Source: An et al., 2010).

### 2.3 Graphene oxide: preparation methods and structure

Back to the history, Brodie reported the preparation of graphite oxide by oxidizing graphite with potassium chlorate ( $\text{KClO}_3$ ) in fuming nitric acid ( $\text{HNO}_3$ ) in 1859 (Brodie, 1859). After 40 years, L. Staudenmaier improved the Brodie's method by

modification, in which adding a concentrated sulfuric acid to the reaction that increases the acidity of the reaction mixture. They also add potassium chlorate in multiple aliquots in the reaction mixture over the course of the reaction (Staudenmaier, 1898). In 1957, Hummers and Offeman developed a rapid and relatively safe method where graphite is oxidized by reacting with an anhydrous mixture of potassium permanganate ( $\text{KMnO}_4$ ), sodium nitrate ( $\text{NaNO}_3$ ) and concentrated sulfuric acid ( $\text{H}_2\text{SO}_4$ ) (Hummers and Offeman, 1958). It was found that the products prepared by using Hummer's method usually contain incompletely oxidized graphite-core/GO-shell particles. To reduce the amount of these particles and achieve a higher degree of oxidation, Kovtyukhova and coworkers propose the pretreatment of graphite powder in a mixture of concentrated  $\text{H}_2\text{SO}_4$ ,  $\text{K}_2\text{S}_2\text{O}_8$ , and  $\text{P}_2\text{O}_5$  at 80 °C before using Hummer's method. All these methods generate toxic gases such as  $\text{NO}_2$ ,  $\text{N}_2\text{O}_4$  and/or  $\text{ClO}_2$  including the Hummer's method. Furthermore, these methods may cause explosion if reaction is not carried out carefully. Since graphene was first isolated by Geim and Novoselov at the University of Manchester in 2004, graphite oxide has attracted attention as a precursor for the low-cost and large-scale production of graphene-based materials and a lot of publications have been reported about its synthesis, structure, reduction and applications. To improve the preparation procedure of GO, Tour and coworkers reported a new recipe for the preparation of GO in 2010 (Marcano et al., 2010). They excluded sodium nitrate ( $\text{NaNO}_3$ ) from the reaction, increased the amount of potassium permanganate ( $\text{KMnO}_4$ ) and introduced phosphoric acid ( $\text{H}_3\text{PO}_4$ ) into the reaction in a 9:1 mixture of  $\text{H}_2\text{SO}_4/\text{H}_3\text{PO}_4$  (Figure 2.12). It is believed GO prepared by this method has higher level of oxidation with more intact graphitic basal planes compare to GO prepared by Hummer's method. When graphite flakes are oxidized by using strong oxidizing agents, the carbon atoms' layer of graphite is decorated by oxygen-functional groups to form graphite oxide. These oxygen-functional groups can expand the

interlayer space of graphite planes 0.34 nm to 0.8 nm and make the planes hydrophilic. As a result, graphite oxide can be easily dispersed and exfoliated in water by using moderate sonication or stirring for a long time. After exfoliation, the solution contains monolayer, bilayer or few-layer sheets of carbon atoms, which are named graphene oxide (GO). The surface charge measurement of GO sheets shows that the GO sheets are negatively charged when dispersed in water. As a result, electrostatic repulsion between GO sheets form stable suspension (Li et al., 2008).

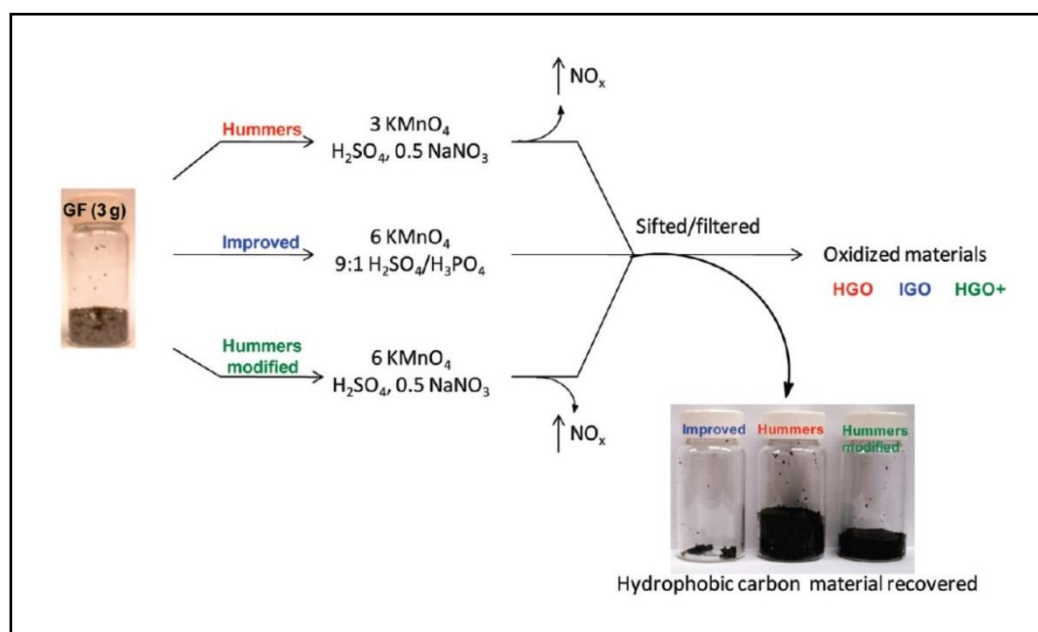


Figure 2.12 Procedure comparison of different methods to produce GO. The very small amount of under-oxidized graphite which retained on the sieve indicates the increased efficiency of the improved GO method. (Source: Marcano et al., 2010).

Although, it has been investigated over a century, the precise chemical structure of GO is still the subject for considerable debate and there is no unambiguous model. It is related to the complexity of GO due to its amorphous character. In 1998, Lerf and Klinowski proposed a nonstoichiometric model for GO (Lerf et al., 1998) (Figure 2.13a). In this model, the carbon plane of graphite is decorated with epoxy (1, 2-ether instead of 1, 3-ether, which suggested by Mermoux) and hydroxyl groups, which they are very close to one another. Carbonyl groups can be found on the edge of the plane most likely as carboxylic acids and within the plane as organic carbonyl defects. These

functional groups decorate both sides of the surface of GO. Recently, Gao et al. showed the presence of five- and six-member-ring lactols on the periphery of GO plane by interpreting nuclear magnetic resonance (NMR) spectroscopy data (Gao et al., 2009) (Figure 2.13b). According to the Lerf and Klinowski model, GO contains two kinds of regions consisted of aromatic regions with unoxidized benzene rings and regions contain oxidized six-member rings, which are distributed randomly on the surface of GO. The degree of oxidation affects the size of both regions. The scanning tunneling microscopy (STM) study on the surface of GO confirmed the presence of both regions with a few nanometer sizes (Gómez-Navarro et al., 2007) (Figure 2.13c).

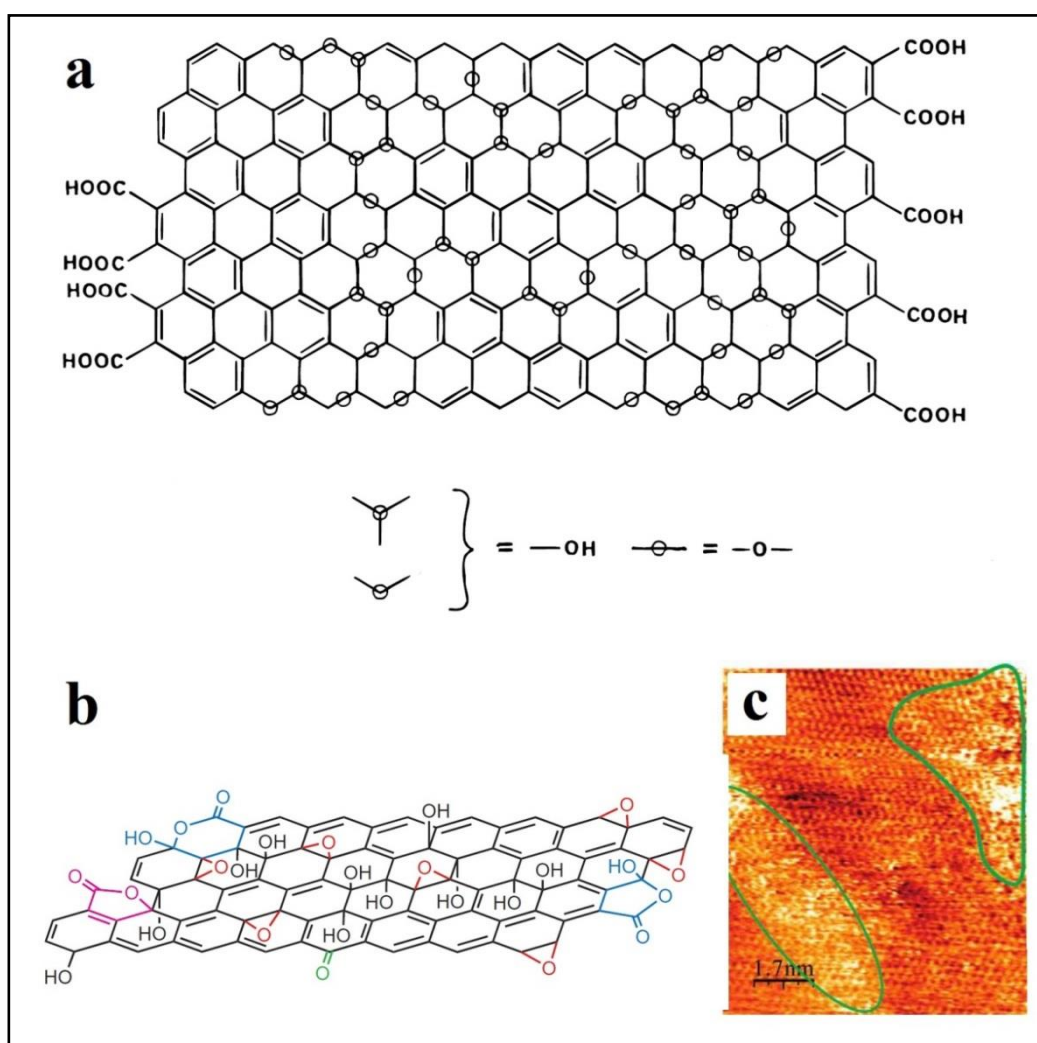


Figure 2.13 (a) Lerf and Klinowski model for GO (Lerf et al., 1998). (b) STM image of a GO monolayer, which shows the oxidized and unoxidized regions (Gómez-Navarro et al., 2007). (c) New structural model for GO, which suggests five- and six-membered lactol rings (Gao et al., 2009).

## **2.4 Graphene-based nanocomposites**

Graphene's high electrical conductivity, large surface-to-volume ratio, and excellent chemical tolerance make it an attractive matrix for composites. In 2006, Ruoff et al. reported the first graphene-based nanocomposite, a graphene-polystyrene composite (Stankovich et al., 2006a). According to their results, incorporation of the graphene sheets with polystyrene enhanced the electrical conductivity of the composite. This achievement has introduced a new class of graphene-based composite materials. According to the second component in the composites, graphene-based nanocomposite can be classified into two main categories: 1) graphene-based polymer nanocomposites and 2) graphene-based inorganic nanocomposites.

### **2.4.1 Graphene-based polymer nanocomposites**

The superior electrical (Novoselov et al., 2004), mechanical (Lee et al., 2008), thermal (Balandin et al., 2008) and optical (Bae et al., 2010) properties of graphene hold great promise for improving the properties of graphene-based polymer nanocomposites (Stankovich et al., 2006a, RamanathanT et al., 2008, Xu et al., 2009, Quan et al., 2009), compared to the neat polymers. Compared with carbon nanotubes (CNTs), graphene is inexpensive and has a higher surface-to-volume ratio. To achieve the full advantage of graphene's properties and homogeneously distributed in composite, incorporation of individual graphene sheets is the important key. The distribution of graphene sheets in the nanocomposite and the interfacial bonding of graphene sheets with polymers affect the properties of nanocomposite (Potts et al., 2011). As mentioned, graphite oxide has hydrophilic nature and it can be nature to the individual graphene oxide (GO) sheets in water (Stankovich et al., 2007, Li et al., 2008), which makes it incompatible with most of organic polymers. By chemical functionalization of graphene oxide sheets, the hydrophilic character of graphene oxide sheets reduces and makes it compatible with many organic polymers (Stankovich et al., 2006a, RamanathanT et al., 2008).

According to these characters, graphite oxide has attracted attention to use as a nanofiller for production of graphene-based polymer nanocomposites. Compared to the other carbon materials, including carbon nanotubes (CNTs), graphene provides very efficient mechanical, electrical and thermal conductivity enhancement. For example, in 2007, Yu et al. reported the enhancement of thermal conductivity of epoxy resin by mixing with thermally exfoliated and reduced graphite platelets (few graphene layer with the thickness of 1 to 15 nm and diameters ranging from sub-micrometre to 100  $\mu\text{m}$ ) (Yu et al., 2007). They showed that few-layer graphene (four layers) with the thickness of  $\sim 2$  nm enhances the thermal conductivity of epoxy more than 3000% (in loading of  $\sim 25$  vol %) and the thermal conductivity of composite reaches to the amount of 6.44 W/mK (in loading of  $\sim 25$  vol %), which surpasses the performance of the other carbon material as a filler such as single-wall carbon nanotubes (SWNTs) (Figure 2.14).

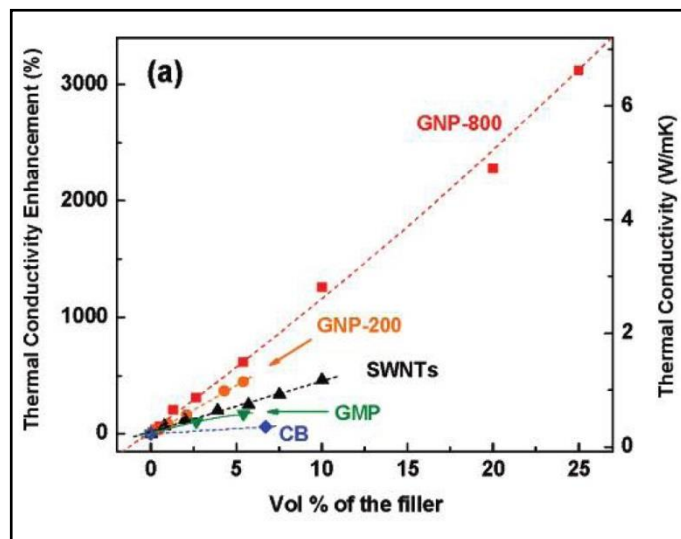


Figure 2.14 Thermal conductivity enhancement of epoxy-based composites at 30 °C. Utilized graphitic fillers: graphitic microparticles (GMP), graphite nanoplatelets GNPs exfoliated at 200 °C (GNP-200) and 800 °C (GNP-800), carbon black (CB), and purified single-wall carbon nanotubes (SWNTs). (Source: Yu et al., 2007).

#### 2.4.2 Graphene-based inorganic nanocomposites

According to the kind of inorganic component, graphene-based inorganic nanocomposites can be classified into four categories:

- 1) graphene-based metal nanocomposites
- 2) graphene-based metal compound nanocomposites
- 3) graphene-based nonmetal nanocomposites
- 4) graphene-based carbon material nanocomposites

Among graphene-based metal nanocomposites, the noble metals such as silver (Ag) (Pasricha et al., 2009, Shen et al., 2011b, Zhang et al., 2011f, Shen et al., 2010, Vijay Kumar et al., 2013), gold (Au) (Huang et al., 2010b, Zhou et al., 2010b, Li et al., 2012a, Zhang et al., 2011e), platinum (Pt) (Yoo et al., 2009, Li et al., 2009e, Li et al., 2010c, Huang et al., 2013) are the most reported in literatures as second component because of their optical and catalytic properties. Incorporation of the intriguing two-dimensional graphene nanosheets with noble metals is expected not only enhances the performance of noble metals and graphene, but also to display additional novel functionalities resulting from the interaction between the materials. For instance, Lu et al. reported on the assembling of Ag or Au nanoparticles on the surface of graphene nanosheets, which were supported on flat silicon (Si) wafer or Si nanowells. This incorporation dramatically enhanced the surface enhanced raman scattering (SERS) effect of Ag or Au NPs, which were used to detect various aromatic molecules (such as rhodamine 6G (R6G), rhodamine B (RB), methyl violet (MV) and methylene blue (MB) ) (Lu et al., 2011a).

Besides noble metals, other metals such as tin (Sn) (Li et al., 2013b, Wang et al., 2013a, Qin et al., 2012, Wang et al., 2009a), copper (Cu) (Luechinger et al., 2008, Bin et al., 2009, Bai et al., 2011, Li et al., 2013a), cobalt (Co) (Li et al., 2013a, Wang et al., 2013b, Warner et al., 2009), alloys (Bai et al., 2011, Vinayan and Ramaprabhu, 2013),



and bimetals (Anandan et al., 2012, Wang et al., 2013b) have been also reported to incorporate with graphene nanosheets.

Graphene has been extensively integrated with different metal compounds such as metal oxides (such as ZnO (Li and Cao, 2011, Luo et al., 2012), TiO<sub>2</sub> (Guo et al., 2011), SnO<sub>2</sub> (Huang et al., 2011b), Fe<sub>3</sub>O<sub>4</sub> (Wang et al., 2011d), Fe<sub>2</sub>O<sub>3</sub> (Wang et al., 2011b), NiO (Xia et al., 2011), MnO<sub>2</sub> (Cheng et al., 2011), etc.), metal sulphides (such as CdS (Cao et al., 2010, Jia et al., 2011), ZnS (Wang et al., 2010i, Zhang et al., 2012c), MoS<sub>2</sub> (Li et al., 2011d, Chang and Chen, 2011b), PbS (Zhang et al., 2012a), etc.), metal selenides (such as CdSe (Wang et al., 2011h)) metal hydroxides (such as MnOOH (Chen et al., 2010a), Co(OH)<sub>2</sub> (He et al., 2010b), Ni(OH)<sub>2</sub> (Wang et al., 2010f)), etc.). It has been demonstrated that the charge-transferring, and magnetic and electronic interactions between graphene sheets and the attached metal compound nanostructures can improve their performance in various applications.

Besides metals and metal compounds, non-metallic materials such as S (Wang et al., 2011c, Cao et al., 2011), Si (Chou et al., 2010, Wang et al., 2010g), SiO<sub>2</sub> (Kou and Gao, 2011), Si<sub>3</sub>N<sub>4</sub> (Walker et al., 2011), SiOC (Ji et al., 2009), CN (Yang et al., 2011b, Sun et al., 2010b), C<sub>3</sub>N<sub>4</sub> (Li et al., 2011c, Xiang et al., 2011) have also been used as second component in the graphene-based nanocomposites. Graphene-based non-metal nanocomposites have been explored for various applications such as lithium-ion batteries, catalysis activities. Some of the graphene-based non-metal nanocomposites were used as metal-free catalysts to replace metal catalysts (Li et al., 2011c).

Graphene has also been combined with other carbon materials such as carbon nanotube (Wassei et al., 2011, Das et al., 2011b, Dong et al., 2011), fullerene (Yu et al., 2011), carbon black (Yan et al., 2010c), carbon sphere (Lei et al., 2011) and carbon nanofibers (Fan et al., 2011b) to design new carbon materials. Among them, carbon nanotubes have attracted attention to incorporate with graphene because of its

remarkable electrical, mechanical, thermal and structural properties. The combination of carbon nanotubes with graphene sheets produces carbon materials with high electrical conductivity, large specific surface area, and unique thermal and mechanical properties.

## **2.5 Synthesis of graphene-inorganic nanocomposites**

The graphene-based inorganic nanocomposites are usually prepared by using different strategies: 1) hybridization of pre-synthesized nanomaterials with graphene oxide or reduced graphene oxide, which is called the *ex situ* hybridization, and 2) formation or crystallization of nanomaterials in the presence of graphene oxide, reduced graphene oxide or functionalized graphene nanosheets, and growing on the surface of them, which is called the *in situ* formation or crystallization.

### **2.5.1 *Ex situ* hybridization**

In this strategy, first, nanomaterials (such as nanoparticles, nanowires, nanorods or, etc.) are synthesized before mixing with graphene-based nanosheets. The surface of graphene and/or nanomaterials is usually modified, which can bind with together through either covalent bonding (He et al., 2010a, Zhang et al., 2011d) or non-covalent interactions (such as  $\pi$ - $\pi$  stacking (Huang et al., 2010a), or electrostatic interactions (Zhu et al., 2010b)). For example, He et al. reported the attachment of  $\text{Fe}_3\text{O}_4$  nanoparticles onto the surface of graphene oxide by covalent bonding. Firstly, for introducing amino groups on the surface of  $\text{Fe}_3\text{O}_4$  nanoparticles, they modified  $\text{Fe}_3\text{O}_4$  nanoparticles with tetraethyl orthosilicate (TEOS) and (3-aminopropyl) triethoxysilane (APTES). These amino groups on the surface of  $\text{Fe}_3\text{O}_4$  nanoparticles can be reacted with the carboxylic groups of GO with the aid of 1-ethyl-3-(3-dimethylaminopropyl)carbodiimide (EDC) and N-hydroxysuccinimide (NHS) to form a GO- $\text{Fe}_3\text{O}_4$  hybrid (Figure 2.15).

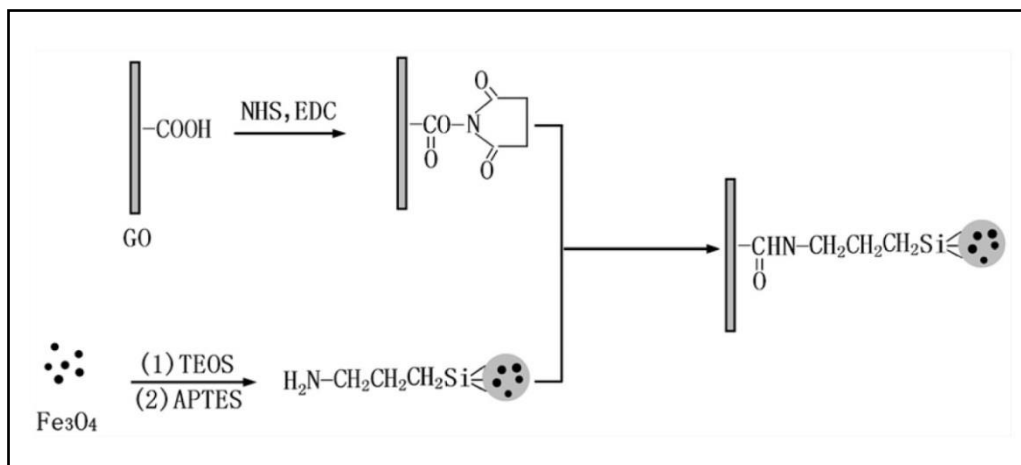


Figure 2.15 Schematic illustration of the fabrication of GO-Fe<sub>3</sub>O<sub>4</sub>. (Source: He et al., 2010a).

## 2.5.2 *In situ* formation or crystallization on the surface of graphene

*Ex situ* hybridization strategy involves multiple steps, which results in the complexity of the preparation process. Compared to the *ex situ* hybridization strategy, *in situ* formation or crystallization strategy is a simple and usually one-step process. Another advantage of this strategy is that the using surfactants or polymer for modification of graphene and/or nanomaterials could be eliminated, which may influence the performance of the nanocomposites. In addition, in this strategy, a variety of techniques can be utilized, including chemical reduction methods, sol-gel techniques, solvothermal/hydrothermal routes, electrochemical deposition techniques, sonochemical method.

### 2.5.2.1 *Chemical reduction method*

The *in situ* chemical reduction method is the most common way to the synthesis of graphene-based inorganic nanocomposites. The attraction of noble metal ions onto the surface of graphene oxide is the initial step for the nucleation of the nanostructures on the surface of graphene, which can prepare by mixing a precursor of noble metal such as HAuCl<sub>4</sub>, AgNO<sub>3</sub>, K<sub>2</sub>PtCl<sub>4</sub> or H<sub>2</sub>PdCl<sub>6</sub> with a solution of GO. These attracted

noble metal ions can be easily reduced by common reducing agents such as  $\text{NaBH}_4$ , amines and ascorbic acid, in which GO could also be reduced simultaneously. For example, synthesis of rGO-Ag nanocomposite has been reported using  $\text{AgNO}_3$  as a precursor of Ag and  $\text{NaBH}_4$  as reducing agent (Li and Liu, 2010, Tien et al., 2011, Das et al., 2011a). Sometimes, GO may not reduce during the reduction of noble metal ions on the surface of GO. There are two ways to address this problem, 1) using additional reducing agents for reducing GO, 2) using rGO instead of GO. For the second option, since rGO has less hydrophilicity nature compared to GO due to less oxygen-containing groups on its surface, which is restricted for use in aqueous solution based processes, and the resultant composite is not uniformly decorated and densely covered with nanoparticles. To address this problem, rGO sheets should be modified before mixing with noble metal ions. For example, Chen et al. modified GO nanosheets by adhering a perylene thiol derivative (ETPTCDI) on the basal plane of GO nanosheets with a non-covalent interaction. They reduced the resultant modified GO into the well-dispersed modified rGO nanosheets, which can serve as an excellent two-dimensional stabilizer and template for in situ nucleation and growth of Au nanodots (GNDs) via thiol-Au bonding. By this strategy, reduced graphene oxide uniformly decorated with Au nanodots was achieved (Yang et al., 2011c) (Figure 2.16).

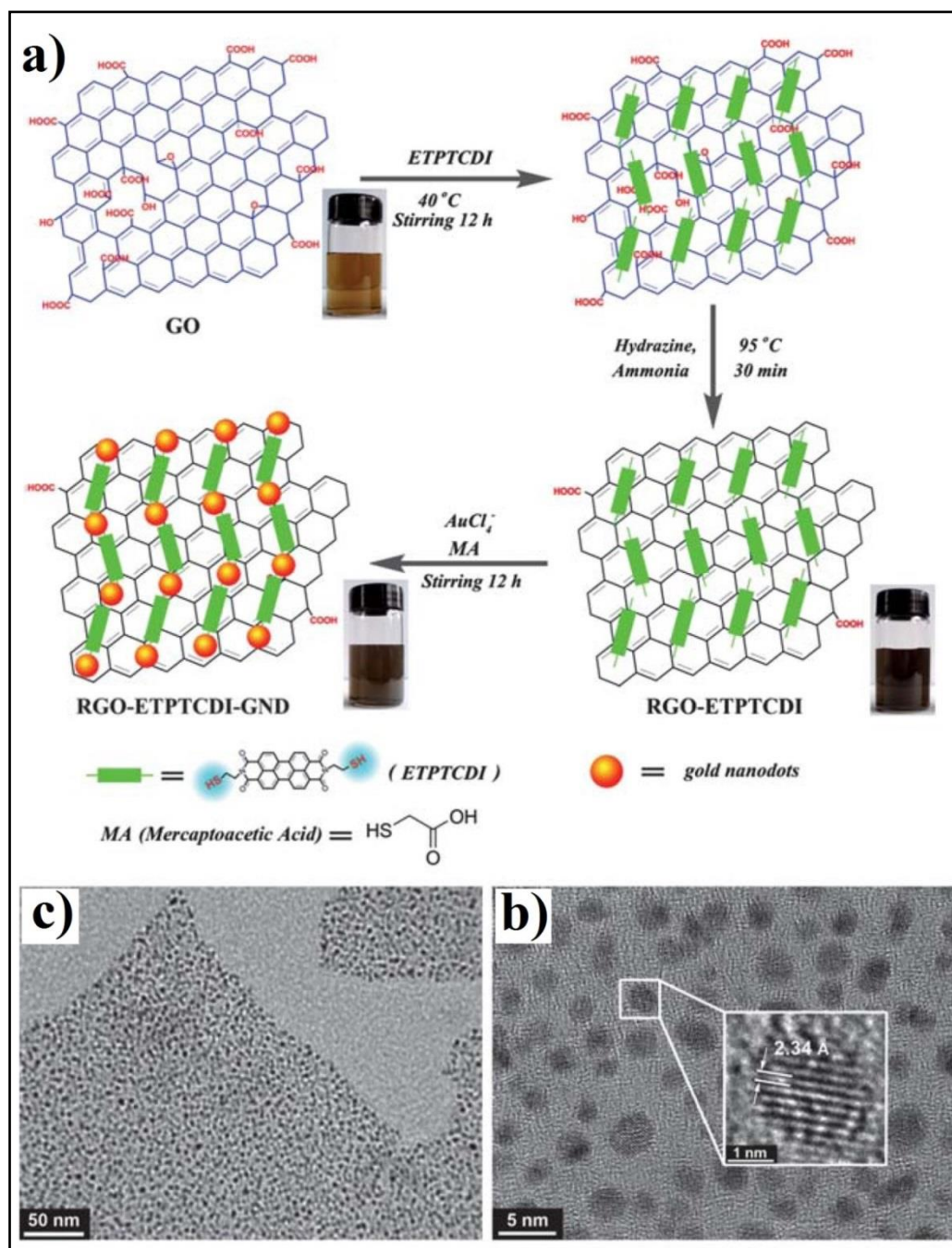


Figure 2.16 (a) Schematic illustration of the synthesis of rGO-GNDs. (b and c) TEM images of rGO uniformly decorated with Au nanodots. (Source: Yang et al., 2011c).

#### 2.5.2.2 Hydrothermal/Solvothermal routes

Hydrothermal and solvothermal are powerful synthesis approaches for the formation of a variety of inorganic nanostructures. Recently, these methods have been frequently used for the synthesis of graphene-based inorganic nanocomposites such as metal oxides (ZnO (Marlinda et al., 2012, Zou et al., 2011b, Wu et al., 2010a), TiO<sub>2</sub> (Shen et al., 2011a, Shen et al., 2011c, Zhou et al., 2011b), Fe<sub>3</sub>O<sub>4</sub> (Wang et al., 2011d,

Shi et al., 2011, Zhou et al., 2011c), SnO<sub>2</sub> (Lim et al., 2013, Huang et al., 2011b)), metal hydroxides (MnOOH (Chen et al., 2010a), Co(OH)<sub>2</sub> (He et al., 2010b), Ni(OH)<sub>2</sub> (Wang et al., 2010f)) and chalcogenides (ZnS (Wang et al., 2010i, Xue et al., 2011), CdS (Cao et al., 2010, Wang et al., 2010i), MoS<sub>2</sub> (Chang and Chen, 2011a), CdTe (Lu et al., 2011e)). These routes were usually operated at elevated temperature of solutions (aqueous solution for hydrothermal and non-aqueous solution for solvothermal) with high vapor pressure in a sealed vessel called the autoclave. As mentioned, the reaction carried out in a sealed autoclave with a confined volume, so the elevated temperature increases the vapor pressure above the critical pressure, which facilitates the crystal growth of initial nucleation sites. The main advantage of hydrothermal synthesis is feasible in producing desired nanostructures such as nanoparticles, nanowires and nanorods with high crystallinity without the need of post-synthetic annealing and calcination. Concurrently, it enables the reduction of GO to rGO (Zhou et al., 2009c). For synthesis of graphene-supported chalcogenides, besides metal salts and GO, the source of sulfur (S) or tellurium (Te) were also needed. In the synthesis of graphene-based metal sulfide nanocomposites, sources of sulfur may act as a reducing agent of GO. For the synthesis of CdS/rGO, Cao et al. utilized a solvothermal process, in which a mixture of Cd(CH<sub>3</sub>COO)<sub>2</sub> and GO in dimethyl sulfoxide (DMSO) was heated in a sealed autoclave at 180 °C for 12 h (Cao et al., 2010). In this reaction, DMSO not only acted as a source of sulfur and solvent but also acted as a reducing agent for GO.

#### 2.5.2.3 *Electrochemical deposition*

Electrochemical approach for deposition of variety of inorganic crystals on different substrates is a very attractive method to produce thin-films due to its fast, easy and green nature. Recently, different electrochemical deposition techniques have been utilized for the fabrication of graphene-based noble metal nanocomposites such as Au (Du et al., 2010, Hu et al., 2010, Fu et al., 2010), Pt (Liu et al., 2010c), however, the

process involves multi-step. For example, Liu et al. used electrophoretic technique for deposition of GO on indium tin oxide (ITO) by applying a constant potential of 150 V for 45 s, followed by electrochemical reduction of the resultant EGO/ITO film by a cyclic voltammetry method in the potential range of 0 to -1.0 V. Then, Pt nanoparticles were electrodeposited on the reduced GO film by applying a constant potential of -0.25 V for 1800 s in a mixed electrolyte of 3mM  $\text{H}_2\text{PtCl}_6$  and 0.5M  $\text{H}_2\text{SO}_4$  (Liu et al., 2010c) (Figure 2.17). Field emission scanning electron microscope (FESEM) images indicate that Pt nanoparticles are uniformly distributed on the surface of reduced GO film (Figure 2.17). Zhou et al. proposed three different strategies to electrodeposition of Pt nanoparticles on the surface of rGO sheets, including two-step and one-step process (Zhou et al., 2010c). In the first strategy, pre-assembled GO on a glassy carbon electrode (GCE) is reduced at a constant potential of -1.5 V, and Pt nanoparticles are electrodeposited on rGO/GCE at -0.25 V. The second strategy is electrodeposition of Pt nanoparticles on pre-assembled GO/GCE at -0.25 V, followed by reduction of GO at -1.5 V. While, the third strategy is one-step electrochemical reduction of Pt nanoparticles and GO at a constant potential of -1.5 V. It is realized that highly dispersed Pt nanoparticles on rGO nanosheets with small sizes could be achieved only by using the third strategy. Another one-step strategy for fabrication of graphene-Au nanocomposite film was developed by Liu et al., in which Au ions and GO nanosheets are electrochemically reduced via a cyclic voltammetry technique in the potential range of 0.6 to -1.5 V with respect to a saturated calomel electrode (SCE) (Liu et al., 2011a).

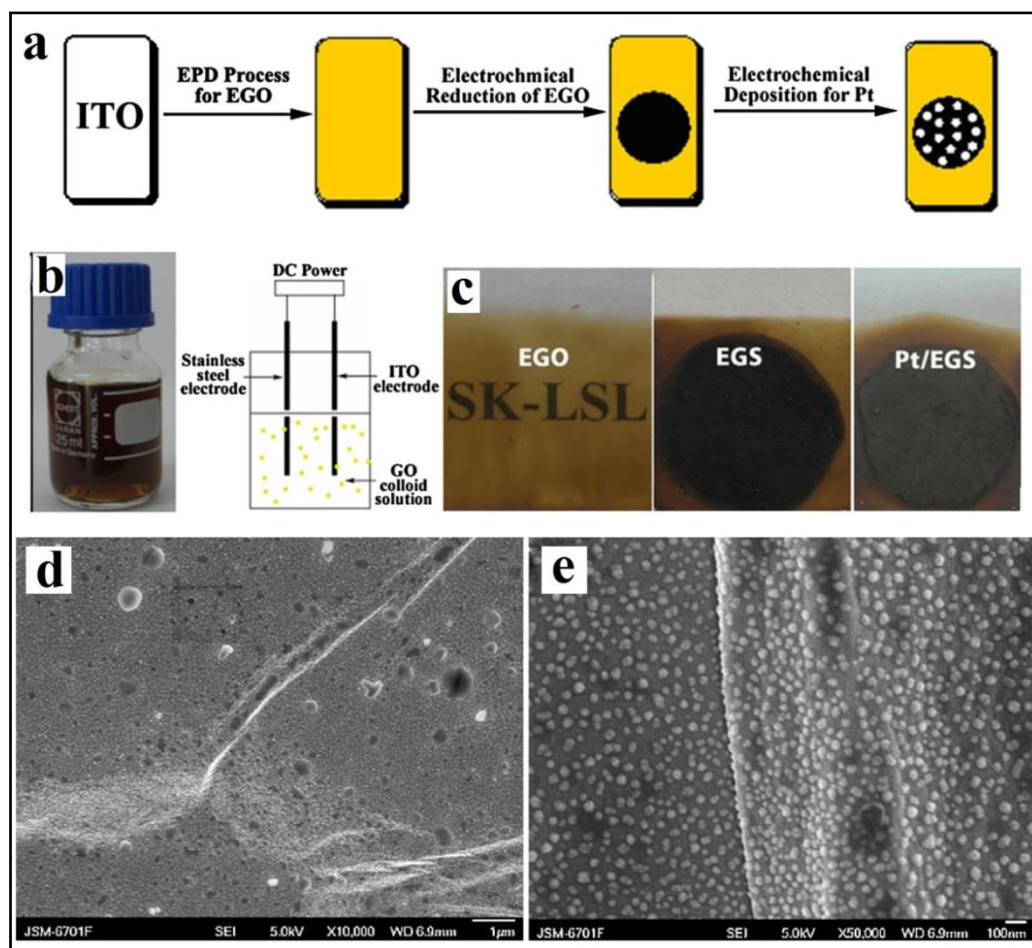


Figure 2.17 (a) Schematic illustration of the fabrication procedures of Pt/EGS nanocomposite film, (b) Photograph of EGO colloid solution and the setup of electrophoretic deposition process, (c) Photograph of the electrodeposited samples of Expandable graphene oxide (EGO), Expandable graphene sheets (EGS) and Pt/EGS, and (d and e) FESEM images of Pt/EGS nanocomposite at increasing magnifications. (Source: Liu et al., 2010c).

In addition to electrodeposition of graphene-metal nanocomposites, electrochemical techniques can be used to fabricate graphene-based metal oxide nanocomposite such as ZnO (Yin et al., 2010, Wu et al., 2010b), Cu<sub>2</sub>O (Wu et al., 2010b, Wu et al., 2011) and MnO<sub>2</sub> (Cheng et al., 2011). For example, Wu et al. had reported the electrodeposition of ZnO nanorods (NRs), as well as n-type and p-type Cu<sub>2</sub>O films on pre-assembled rGO thin film on polyethylene terephthalate (PET) as the substrate (Wu et al., 2010b). For electrodeposition of ZnO NRs, the process includes two steps: 1) the buffer layer growth by applying a constant current of 10  $\mu$ A to the rGO-PET electrode in an oxygen-saturated aqueous solution of ZnCl<sub>2</sub> as an electrolyte at room temperature, and 2) the growth of ZnO NRs by applying a constant potential of



-1.9 V to the resultant electrode at 80 °C, which includes the reduction of O<sub>2</sub> and precipitation of ZnO at the electrode. For electrodeposition of Cu<sub>2</sub>O films, a constant potential of -0.4 V applies to the rGO-PET electrode in the electrolyte contained CuSO<sub>4</sub> and lactic acid, in which the pH of the solution affects the type of the electrodeposited Cu<sub>2</sub>O film.

#### 2.5.2.4 Sonochemical method

Sonochemical method has been proven to be a versatile and promising technique in the synthesis of a variety of nanostructures such as metals (Pol et al., 2002, Tripathy et al., 2013), metal oxides (Khorsand Zak et al., 2013, Geng et al., 2011) and metal sulfides (Geng et al., 2011, Wu et al., 2006). The chemical effects of ultrasound irradiation arise from acoustic cavitation phenomenon. When a liquid is irradiated with ultrasound, bubbles are created, which accumulate the ultrasonic energy while growing. The unstable gas-liquid interface subsequently collapsed, releasing the stored energy within a very short time. These cavitation implosions generate localized hotspots with a high temperature of 5000 K, a pressure of 1000 bar, and a heating and cooling rate of 10<sup>10</sup> K/s (Bang and Suslick, 2010). Different parameters such as ultrasonic irradiation time, frequency, concentration and various organic additives can affect on the shape and size of nanostructures (Khorsand Zak et al., 2013, Okitsu et al., 2005, Caruso et al., 2002). For example, Zak et al. carried out a systematic study on the effect of the ultrasonication time on the formation and shape of the ZnO nanostructures (Khorsand Zak et al., 2013). It is found that during the primary 5 minutes ultrasonic irradiation, Zn(OH)<sub>2</sub> seeds crystals can be nucleated and formed. After this 5 minutes, the ZnO seeds are formed by decomposition of Zn(OH)<sub>2</sub>. By increasing the ultrasonication time to 15 minutes, the ZnO seeds can be incorporated with each other to form ZnO nanorods. Further increasing of the ultrasonication time to 30 minutes causes the formation of flower-like ZnO nanostructures. In recent years, sonochemical strategy has

been used for the synthesis of graphene-based inorganic nanocomposites such as metals (Au (Vinodgopal et al., 2010), Rh (Chandra et al., 2011)), bimetals (Anandan et al., 2012) and metal oxides (ZnO (Luo et al., 2012), TiO<sub>2</sub> (Guo et al., 2011), Mn<sub>3</sub>O<sub>4</sub> (Park et al., 2012), Fe<sub>3</sub>O<sub>4</sub> (Zhu et al., 2013)).

## **2.6 Application of graphene-inorganic nanocomposites**

Functionalization of the intriguing two-dimensional nanosheets is expected not only to enhance the performance of graphene and nanocrystals, but also to display novel advantages resulting from the interaction between the materials. It is found that graphene-based inorganic nanocomposites show enhanced performance in the field of catalysis, energy conversion and storage, sensors, and other interesting applications.

### **2.6.1 Photocatalysis**

In recent years, semiconductor-mediated photocatalysis has attracted tremendous attention for its potential applications such as photocatalytic degradation of organic pollutants and photocatalytic hydrogen generation. In general, when a semiconductor is illuminated with photons, which have energies greater than the band gap of the semiconductor, electrons in the valence band of the semiconductor are excited into the conduction band, resulting the generation of electron-hole pairs. These electron-hole pairs either recombine or migrate to the surface of photocatalyst to initiate a series of photocatalytic reactions and produce hydroxyl radicals,  $\cdot\text{OH}$  and superoxide radical,  $\cdot\text{O}_2^-$  in water, resulting the generation of hydrogen gas and degradation of organic pollutants. The drawback of the most of the photocatalysts such as titanium dioxide (TiO<sub>2</sub>) and zinc oxide (ZnO) is the rapid electron-hole recombination within photocatalysts, which decreases the efficiency of its photocatalytic activity. It is believed that graphene with excellent electrical conductivity and large specific surface area can be used as an electron acceptor and transfer channel for reducing the rate of electron-hole

recombination, which increases the efficiency of photocatalytic activity. In addition, graphene can increase the adsorption of pollutants due to the non-covalent interaction between organic pollutants and the aromatic regions of graphene, and extend the light absorption range of photocatalysts. TiO<sub>2</sub> is well-known as one of the best photocatalyst materials, and several reports have focused on the synthesis and photocatalytic applications of graphene-TiO<sub>2</sub> nanocomposite (Zhang et al., 2009a). For example, Zhang et al. reported the significant enhancement of photocatalytic activity of TiO<sub>2</sub> (P25) for degradation of methylene blue (MB) in water under both visible and ultraviolet (UV) light irradiation by incorporating with graphene (Zhang et al., 2009a). It was found that graphene plays different important roles in the process of photodegradation of MB (Figure 2.18): 1) MB molecules can be adsorbed onto the surface of graphene with offset face-to-face orientation via  $\pi$ - $\pi$  conjugation between MB and the aromatic regions of graphene, which increases the adsorptivity of MB compare to the bare P25, 2) graphene plays as a carbon matrix and the formation of Ti-O-C bond decreases the band gap of P25, which extends the light adsorption range of graphene-P25 compare to the bare P25, and 3) graphene can trap the photogenerated electrons from the conduction band of P25 and transfers them through the its surface, which suppresses the electron-hole recombination.

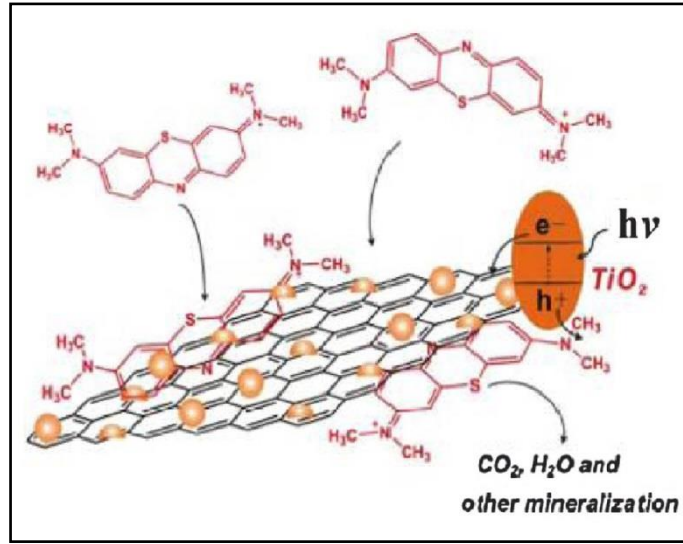
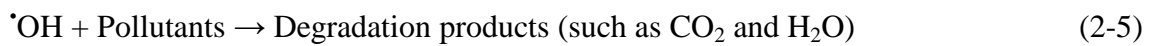
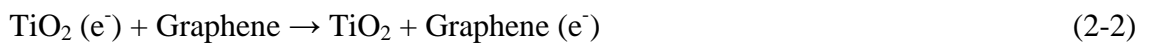


Figure 2.18 Schematic structure of P25-GR and tentative processes of the photodegradation of methylene blue (MB) over P25-GR. (Source: Zhang et al., 2009a).

As mentioned, when a semiconductor such as  $\text{TiO}_2$  is illuminated with photons, the electron-hole pairs are generated. The photogenerated electrons can be trapped by graphene and scavenged by the dissolved oxygen to form superoxide radical ( $\cdot\text{O}_2^-$ ), which facilitates the electron-hole separation. Meanwhile, the holes can either react with adsorb water molecules or surface hydroxyl to form hydroxyl radicals ( $\cdot\text{OH}$ ), or directly oxidize the pollutants. The proposed reactions for this photocatalytic degradation mechanism are summarized by the following equations (Xiang et al., 2012).



Apart from  $\text{TiO}_2$ , graphene has been incorporated with other photocatalysts such as  $\text{ZnO}$  (Li and Cao, 2011),  $\text{SnO}_2$  (Zhang et al., 2011b),  $\text{ZnS}$  (Hu et al., 2011),  $\text{ZnFe}_2\text{O}_4$  (Fu and Wang, 2011),  $\text{Ag/AgCl}$  (Zhang et al., 2011a, Zhu et al., 2011d) and  $\text{Ag/AgBr}$  (Zhu et al., 2011d). Also, the photocatalytic activity of semiconductors can be used for production of hydrogen ( $\text{H}_2$ ). For example, Jia et al. investigated the photocatalytic

hydrogen production activity of N-doped graphene/CdS nanocomposites with different graphene weight percentages from aqueous solutions containing  $\text{Na}_2\text{S}$  and  $\text{Na}_2\text{SO}_3$  under visible-light illumination (Jia et al., 2011). It was found that the photocatalytic hydrogen evolution rate of CdS is significantly enhanced by introducing N-doped graphene, and the optimal amount of N-doped graphene is 2.0 wt%, which gives a hydrogen production rate of  $210 \mu\text{mol/h}$ . As shown in Figure 2.19, the work function of graphene is lower than the conduction band of CdS, on the other hand, higher than the potential reduction of  $\text{H}^+$ , which causes the transferring of the photogenerated electrons from the conduction band of CdS to the graphene nanosheets and the reduction of  $\text{H}^+$ , thus enhancing the photocatalytic hydrogen production activity.

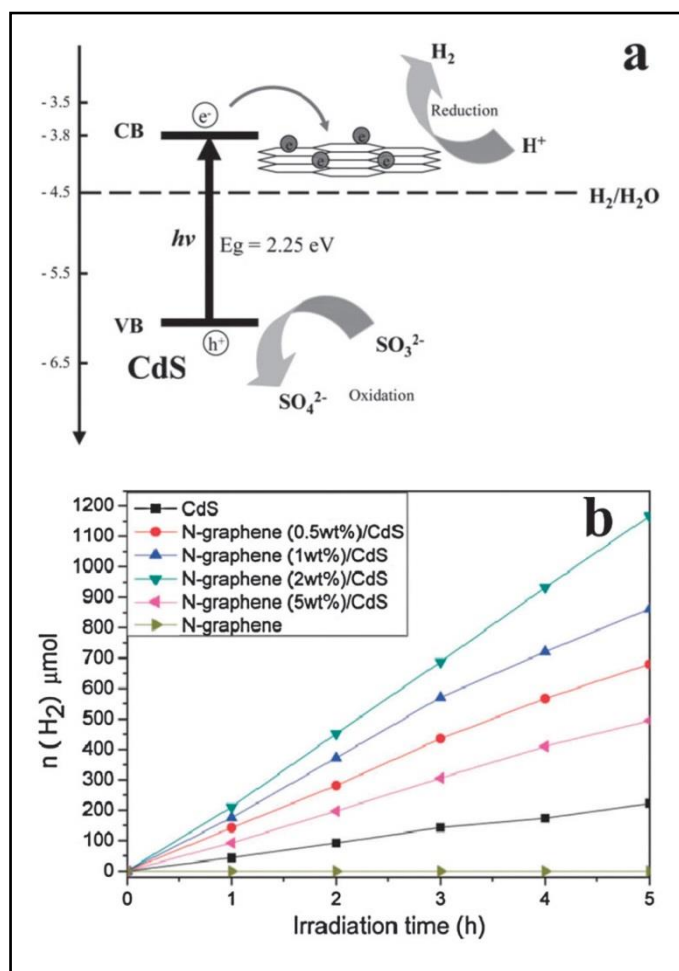


Figure 2.19 (a) The energy level diagram for N-graphene/CdS nanocomposites in relation to the redox potentials for water splitting process in  $\text{Na}_2\text{S}/\text{Na}_2\text{SO}_3$  aqueous solution, and (b)  $\text{H}_2$  evolution of CdS, N-graphene/CdS composites with different contents of N-graphene. (Source: Jia et al., 2011).

## 2.6.2 Energy storage and conversion

The increasing demand for energy in the world and growing interests about environmental pollution have motivated significant efforts to develop the energy conversion and storage devices with high power and high-density energy. Graphene-based nanomaterials have been widely considered as promising alternatives as electrode nanomaterials in energy-related devices, due to their high thermal and electrical conductivities, excellent chemical tolerance, large surface-to-volume ratio, high mechanical strength and wide electrochemical window. Recently, graphene-based inorganic nanocomposites have been investigated for various applications in energy-related devices, such as supercapacitors, lithium-ion batteries, fuel cells, and solar cells.

### 2.6.2.1 Supercapacitors

Supercapacitor is a type of electrochemical energy storage devices with long-cycle life and high-power density. According to the different charge storage mechanism, supercapacitors can be classified into two types. One is the electrochemical double-layer capacitors (EDLCs), in which the energy can be stored *via* an electrostatic process. Another type of supercapacitors is called the pseudo-capacitors, in which the energy storage is based on the rapid redox reactions of the materials present in the electrode. It is reported that the specific capacitance of graphene nanosheets in organic and aqueous electrolytes can reach to the value of 99 F/g and 135 F/g, respectively (Stoller et al., 2008). The agglomeration of graphene nanosheets limits the experimental observation of intrinsically high capacitance of an individual graphene nanosheets. The decoration of graphene nanosheets with metal oxides or hydroxides nanoparticles not only prevents graphene nanosheets from aggregation, which increases the accessible surface area of graphene nanosheets, but also significantly increases the capacitance due to the incorporation of nanoparticles to the additional pseudo-capacitance. Until now, graphene nanosheets have been incorporated with a variety of metal compounds such as

MnO<sub>2</sub> (Zhu et al., 2011a, Cheng et al., 2011, Li et al., 2011e, Yan et al., 2010a), Mn<sub>3</sub>O<sub>4</sub> (Wang et al., 2010a), Co<sub>3</sub>O<sub>4</sub> (Yan et al., 2010b, Zhou et al., 2011d), SnO<sub>2</sub> (Li et al., 2009a, Lu et al., 2010), NiO (Xia et al., 2011, Lv et al., 2011), ZnO (Lu et al., 2010, Zhang et al., 2009b, Chen et al., 2011c), Fe<sub>3</sub>O<sub>4</sub> (Shi et al., 2011, Li et al., 2011a), Ni(OH)<sub>2</sub> (Lee et al., 2011, Wang et al., 2010d) and Co(OH)<sub>2</sub> (Chen et al., 2010b), and explored for supercapacitor electrode materials. All of these nanocomposites exhibited higher capacitance values with better reversible charge and discharge ability.

#### 2.6.2.2 *Lithium-ion batteries*

The growing demand from the modern society to provide low cost, high efficient and green methods for energy conversion and storage devices has stimulated efforts to develop battery systems, especially the rechargeable batteries. Lithium-ion batteries (LIBs) are considered as the most promising storage systems due to its high absolute potential value of -3.04 V versus standard hydrogen electrode and its low equivalent weight ( $M = 6.94 \text{ g/mol}$ ), which leads to the high energy density (Tarascon and Armand, 2001). Besides the traditional insertion-type and alloying-type of electrode materials for insertion/extraction of Li, transition metal compounds ( $M_aX_b$ ,  $M = \text{Co, Ni, Fe, Cu etc.}$ ;  $X = \text{O, S, Se, etc.}$ ) have been studied recently for the conversion-type of electrode materials, in which the Li insertion/extraction facilitate through redox reaction between the ionic and metallic form of the metal.



It has been proven that the nanostructured metal compound electrodes have more advantages if compared to micrometer-sized structure electrodes for LIBs due to short path lengths for both Li ions and electrons, and higher electrode/electrolyte contact area (Sun et al., 2012). However, disadvantages such as poor conductivity and low packing of particles, which reduce volumetric energy density, remain the issues and need continuous development. Graphene has higher lithium storage capacity (theoretical

value of 744 mAh/g for single layer graphene nanosheet) compared to graphite (theoretical value of 372 mAh/g), which is commercially used in LIBs. This is because graphene has higher electrical conductivity and large surface-to-volume ratio, and the lithium ions can also be adsorbed on both sides of the graphene nanosheets. It is expected the incorporation of graphene nanosheets with metal compound nanomaterials enhances the lithium storage capacity of the composite. First of all, the highly conductivity nature of graphene can increase the conductivity of the metal compound based electrodes. For example,  $\text{Mn}_3\text{O}_4$  with a theoretically high capacity value of 936 mAh/g has demonstrated an experimental capacity value of 400 mAh/g due to its low conductivity. By growing the  $\text{Mn}_3\text{O}_4$  nanoparticles on the surface of graphene nanosheets, graphene nanosheets act as good conducting networks. Such  $\text{Mn}_3\text{O}_4$ /graphene hybrid electrode exhibited a specific capacity value up to ~900 mAh/g, which is two times higher than that of pure  $\text{Mn}_3\text{O}_4$  (Wang et al., 2010e). The contribution of graphene nanosheets in composite not only provides an elastic buffer space to limit the volume expansion upon lithium insertion, but also prevents the agglomeration of nanoparticles and cracking or crumbling of the electrode, thus enhances the specific capacity and cycling stability of electrode (Wu et al., 2010c). Moreover, the decoration of graphene sheets with metal compound nanomaterials prevents the graphene nanosheets from aggregation, which increases the accessible surface area of graphene nanosheets and consequently increases the lithium storage capacity of graphene in composite. Therefore, graphene nanosheets have been incorporated with a wide range of inorganic nanomaterials such as metal oxide ( $\text{SnO}_2$  (Zhang et al., 2010a, Wang et al., 2011g),  $\text{Fe}_3\text{O}_4$  (Zhang et al., 2010b, Zhou et al., 2010a),  $\text{Co}_3\text{O}_4$  (Zhu et al., 2011c, Chen and Wang, 2010),  $\text{Mn}_3\text{O}_4$  (Wang et al., 2010e) etc.), metal hydroxides ( $\text{Ni}(\text{OH})_2$  (Li et al., 2011b),  $\text{Co}(\text{OH})_2$  (He et al., 2010b)) and chalcogenides ( $\text{MnS}_2$  (Chang and Chen,



2011a, Chang and Chen, 2011b), SnSe<sub>2</sub> (Choi et al., 2011)) for application as anode electrode materials for LIBs.

#### 2.6.2.3 *Solar cells*

A solar cell device converts the energy of sunlight into electric energy by photovoltaic effect. Due to the fast electron transfer rate and excellent optical transparency of graphene nanosheets, graphene-based inorganic nanocomposites have been investigated for application in solar cell, mainly in the dye-sensitized solar cells (DSSCs) and quantum dot-sensitized solar cells (QDSSCs). A dye-sensitized solar cell consists of a layer of semiconductor material coated on the anode electrode, for example TiO<sub>2</sub>, covered with photo-sensitive dyes, an electrolyte and a counter electrode. Upon light irradiation, the photo-excited dye electrons transfer to the conduction band of semiconductor material, then transfer to the collector electrode, for example ITO. To enhance the efficiency of the DSSCs electrode, the following factors are important: 1) the loading amount of dye molecules, 2) the interface area of dye and electrolyte, and 3) the conductivity of electrode, which decreases the photo-induced electron-hole recombination rate. Therefore, graphene nanosheets have been incorporated with semiconductor materials, such as TiO<sub>2</sub> (Yang et al., 2010, Sun et al., 2010a) and ZnO (Xu et al., 2013b, Khurana et al., 2013), to enhance the above mentioned factors. Incorporated graphene nanosheets can trap the photo-induced electrons from the conduction band of semiconductor. These captured electrons can transport to the collector electrode quickly through graphene bridges (Yang et al., 2010). In addition, graphene nanosheets not only prevent the semiconductor nanoparticles from aggregation to create large particles, which increases the surface area of semiconductor nanoparticles, but also adsorb the dye molecules, for example porphyrin, on their surfaces (Wojcik and Kamat, 2010). These two effects increase the loading amount of dye molecules into the electrode. Moreover, the electrode prepared by using

graphene/semiconductor nanocomposite forms a porous, leading to the large interface area of dye and electrolyte, and increasing the light scattering. For example, Yang et al. reported on the conversion efficiency enhancement of 39% by incorporating the graphene nanosheets with TiO<sub>2</sub> compared to the bare TiO<sub>2</sub> photoanode (Yang et al., 2010).

Another example of the successful incorporation of graphene with inorganic materials for application in solar cell is the development of QDSSCs (Zhu et al., 2011b, Chen et al., 2011a, Zhao et al., 2013b). The configuration of QDSSCs is similar to the DSSCs where the dye molecules are replaced by quantum dots such as CdS and CdSe etc (Nozik, 2002). Similar to DSSCs, it is shown that the introduction of graphene nanosheets can improve the performance of QDSSCs by suppressing electron-hole recombination and back-transport reaction, enhancing the electron transport and increasing the QDs adsorption. For example, a maximum power conversion efficiency value of 1.44% was achieved by using a CdS QDSSC incorporating 0.8% graphene in TiO<sub>2</sub> photoanode, which is 56% higher than that without rGO.

#### 2.6.2.4 Fuel cells

Unlike supercapacitors or batteries, in which the energy can be stored chemically in the electrochemical cell, the fuel cells generate electric energy *via* fuel oxidation at anode and oxygen reduction at cathode, which both electrodes are continuously supplied from external sources. Carbon nanotubes (CNTs) have been used as catalyst supporting materials for application in fuel cells, which have shown improved catalytic activities. Compared to CNTs (1315 m<sup>2</sup>/g), graphene possesses similar conductivity and stable physical properties but larger specific surface area (2630 m<sup>2</sup>/g), which both sides of graphene can be used for anchoring the nanoparticles (Choi et al., 2012, Long et al., 2011). In addition, graphene nanosheets can be produced in large quantities at a much lower cost. Due to these outstanding properties, graphene has attracted attention to be

applied in fuel cells. Therefore, graphene has been incorporated with the catalysts for application in different types of fuel cells, such as graphene/Pt nanocomposite in direct methanol fuel cells (Li et al., 2009e, Zhou et al., 2010c) and proton-exchange membrane fuel cells (PEMFCs) (Seger and Kamat, 2009, Kou et al., 2009), graphene/Pd nanocomposite in direct formic acid fuel cells (Zhao et al., 2011, Yang et al., 2011a), and alloys in PEMFCs (Vinayan and Ramaprabhu, 2013). As an example, Yoo et al. reported a high catalytic activity of graphene/Pt nanocomposite for methanol oxidation, in which the composite exhibits a current density of  $0.12 \text{ mA/cm}^2$  at 0.6 V (vs reference hydrogen electrode), which is about 4 times higher than that obtained with the carbon black/Pt catalyst (Yoo et al., 2009).

### **2.6.3 Sensing**

The development of graphene provides new opportunities for the progress of analytical science. Nowadays, graphene nanosheets with high conductivity and large surface area have been introduced into analytical chemistry and implanted novel functions into analytical sensing systems.

#### *2.6.3.1 Gas sensing*

The toxic gas molecules detection is necessary in many fields due to their toxicity. CNT-based gas sensors have attracted tremendous interest in the last several years due to their promising potential for the selective and rapid detection of various gas molecules. Compared with CNT, graphene has better chemical and physical properties, which suggests that graphene might have advantages in this application. However, using graphene nanosheets alone for high performance sensing is very challenging due to the relatively weak, poor stability and slow. Nevertheless, some groups have shown good sensitivity for the detection of  $\text{H}_2\text{S}$  (Cuong et al., 2010),  $\text{H}_2$  (Kumar et al., 2011, Johnson et al., 2010, Kaniyoor et al., 2009), ethanol (Jiang et al., 2011),  $\text{NO}_2$  (Jeong et

al., 2010), and propanal (Song et al., 2011) molecules by using graphene-based inorganic nanocomposites. Graphene-incorporated noble metals such as Pt (Kaniyoor et al., 2009), Pd (Johnson et al., 2010) and PtPd alloy (Kumar et al., 2011) have been employed for H<sub>2</sub> molecules sensing. In most of them, the detection mechanism of gas molecules is based on the change of resistance of the composites due to decomposition of H<sub>2</sub> molecules into atomic H at the catalytically active noble metal nanoparticles. The high conductivity and large surface area of graphene nanosheets enhance the sensitivity to the change of the resistance during H<sub>2</sub> molecules detection. Recently, graphene nanosheets have been decorated with metal oxide such as SnO<sub>2</sub> (Mao et al., 2012), TiO<sub>2</sub> (Esfandiar et al., 2012), ZnO (Singh et al., 2012), WO<sub>3</sub> (An et al., 2012) and Cu<sub>2</sub>O (Zhou et al., 2013), and have been applied for gas sensing. For example, An et al. reported on the fabrication of WO<sub>3</sub> nanorods on the surface of graphene (An et al., 2012). Compare to the WO<sub>3</sub> nanorods alone, the WO<sub>3</sub>/graphene composite exhibited higher sensitivity and selectivity to NO<sub>2</sub> molecules (Figure 2.20). That such enhancement of NO<sub>2</sub> sensing can be aroused from the improvement of the conductivity, specific electron transferring and increasing the gas molecules adsorption.

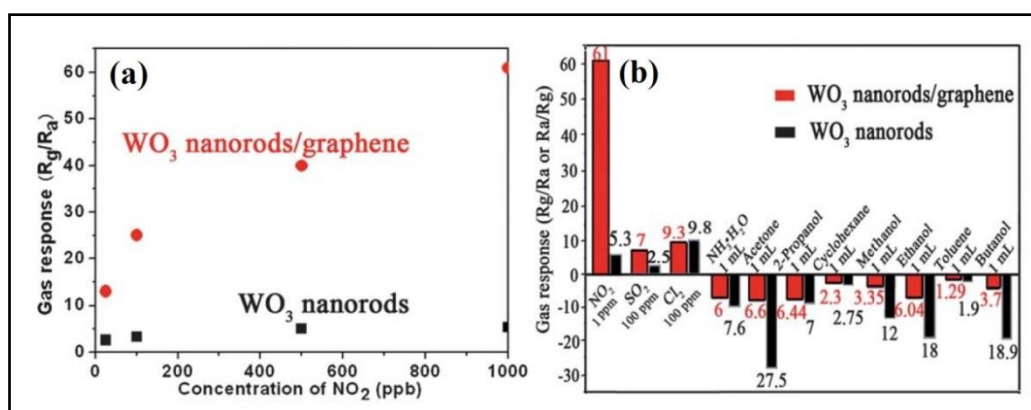


Figure 2.20 (a) Gas response of WO<sub>3</sub> and WO<sub>3</sub> nanorods/graphene versus NO<sub>2</sub> concentration at 300 °C; (b) gas sensing to 1 ppm NO<sub>2</sub>, 100 ppm SO<sub>2</sub>, 100 ppm Cl<sub>2</sub> and 1 mL NH<sub>3</sub>.H<sub>2</sub>O, acetone, propanol, cyclohexane, methanol, ethanol, toluene and butanol. (Source: An et al., 2012).

### 2.6.3.2 *Biosensor*

Graphene-based noble metal nanocomposites have been investigated for detection of various electroactive biomolecules, such as  $\text{H}_2\text{O}_2$  (Liu et al., 2010b, Fang et al., 2010), glucose (Chen et al., 2011d, Lu et al., 2011b), ascorbic acid (Sun et al., 2011, Li et al., 2010a), cholesterol, dopamine (Sun et al., 2011, Li et al., 2010a), uric acid (Sun et al., 2011, Hong et al., 2010), protein (Mao et al., 2010) and DNA (Du et al., 2010). In another case, graphene have been incorporated with various metal compounds such as  $\text{Fe}_3\text{O}_4$  (Zhou et al., 2011c),  $\text{TiO}_2$  (Fan et al., 2011a),  $\text{MnO}_2$  (Li et al., 2010b),  $\text{ZrO}_2$  (Du et al., 2011),  $\text{CdS}$  (Wang et al., 2010h, Wang et al., 2011e) and  $\text{CdSe}$  (Zhang et al., 2011c) for determination of various biology-related molecules, such as  $\text{H}_2\text{O}_2$ , dopamine and glucose. These inorganic nanomaterials (noble metals and metal compounds) can play different roles in the electrochemical sensing system. They can act for immobilizing biomolecules and catalyzing electrochemical reactions, or act as a reactant. Graphene with superior electrical conductivity and large surface area can enhance the electrochemical sensing performance of inorganic nanomaterials by incorporating with these inorganic nanomaterials. Graphene nanosheets assist the growth and dispersion of the nanoparticles on its surface, which prevent the aggregation of the nanoparticles. Thus, the active surface area of nanoparticles increases, which enhances their electrochemical sensing performance. In addition, graphene nanosheets not only can immobilize different target biomolecules, but also effectively enhance the electrical conductivity of the nanocomposite and promote the electron transfer between analyte and electrode. Most of the reports on biosensors are based on an electrochemical strategy using techniques such as cyclic voltammetry, amperometric and electrochemiluminescence (ECL) methods due to its advantages such as high sensitivity, fast detection, good selectivity and low cost. For example, Shan et al. reported an electrochemical biosensor based on AuNPs/graphene nanocomposite for

detection of H<sub>2</sub>O<sub>2</sub> and glucose with high sensitivity and good reproducibility (Shan et al., 2010). The good electrocatalytic activity of the composite might be arisen from the synergetic effect of Au nanoparticles and graphene.

#### **2.6.4 Other applications**

Graphene-based inorganic nanocomposites have also been investigated for the use as a matrix for surface enhanced raman scattering and antibacterial applications. Raman signals of GO and rGO are weak, especially when observing single-layer GO or rGO nanosheets. Surface-enhanced raman scattering (SERS) able to overcome this limitation. Recently, the SERS of graphene was reported by incorporation with Ag (Xu and Wang, 2009, Kumar et al., 2013) and Au (Huang et al., 2010a, Kim et al., 2010). The degree of the enhancement depends on the size (Zhou et al., 2011a), quantity (Xu and Wang, 2009) and nanostructure (Jasuja and Berry, 2009) of the noble metal NPs on the surface of graphene nanosheets. Based on the mechanism of Raman enhancement, the graphene-based metal nanocomposites have been applied as efficient SERS substrates for detecting molecules. Also, graphene-Ag nanocomposites were reported to exhibit excellent antibacterial activity towards bacteria such as *Escherichia coli* and *Pseudomonas aeruginosa* (Das et al., 2011a, Xu et al., 2011a, Shen et al., 2010, Ma et al., 2011). Silver is well known as a natural antibacterial agent for centuries. Graphene can support and stabilize AgNPs on its surface and keep AgNPs well-dispersed in solutions. Meanwhile, graphene can adsorb the bacteria, and graphene and graphene oxide nanosheets also display antibacterial activity themselves. All of these contribute to the excellent antibacterial activity of the nanocomposites.

## CHAPTER III: DESIGN, METHODS AND PROCEDURE

### 3.1 Chemicals and Materials

Graphite flakes (Ashbury Inc. (NJ,USA)) was used to synthesize graphene oxide (GO). Sulphuric acid ( $\text{H}_2\text{SO}_4$ , 98%), potassium permanganate ( $\text{KMnO}_4$ , 99.9%), hydrogen peroxide ( $\text{H}_2\text{O}_2$ , 30%), hydrochloric acid ( $\text{HCl}$ , 37%) and sodium hydroxide ( $\text{NaOH}$ , 99.99%) were purchased from Merck and used as received. Silver nitrate ( $\text{AgNO}_3$ , 99.7%) was purchased from System, Malaysia. Ammonia solution ( $\text{NH}_3$ , 25%), Gelatin (Type B from bovine skin), sulphur powder ( $\text{S}$ , >99.8%), Zinc acetate dehydrate ( $\text{Zn}(\text{CH}_3\text{COO})_2 \cdot 2\text{H}_2\text{O}$ ,  $\geq 98.0\%$ ), Thioacetamide ( $\text{CH}_3\text{CSNH}_2$ ,  $\geq 99.0\%$ ) and ferrous chloride tetrahydrate ( $\text{FeCl}_2 \cdot 4\text{H}_2\text{O}$ ,  $\geq 99.0\%$ ) were purchased from Sigma-Aldrich and used as received. Distilled water was used throughout the sample preparation.

### 3.2 Synthesis of graphene oxide

GO aqueous suspension was synthesized via a simplified Hummers method. 3g of graphite flakes was slowly added into mixture of  $\text{H}_2\text{SO}_4$  and  $\text{H}_3\text{PO}_4$  (9:1) solution. Then, 18 g of  $\text{KMnO}_4$  powder was gradually added into the mixture and left to stir for 3 days for oxidation to occur. The obtained dark green solution was transferred into a beaker containing ice and 27 mL of 30%  $\text{H}_2\text{O}_2$  was added. After addition of  $\text{H}_2\text{O}_2$ , a yellowish brown solution was obtained. The obtained yellowish-brown solution was diluted with 1 M  $\text{HCl}$  solution followed by vigorously mixed. Then it is centrifuged with 6000 rpm for 15 min. after this, it was washed 6 times with deionized water followed by centrifugation (11500 rpm for 45 min). After washing process, a high concentrated brown solution was obtained.

### **3.3 Electrodeposition synthesis of silver-nanoparticle-decorated graphene on indium-tin-oxide for enzymeless hydrogen peroxide detection**

#### **3.3.1 Fabrication of AgNPs-rGO/ITO**

GO was prepared by a simplified Hummers' method (Huang et al., 2011a). The electrodeposition of AgNPs-rGO was conducted in a three-electrode electrochemical cell (Figure 3.1). Silver-ammonia [ $\text{Ag}(\text{NH}_3)_2\text{OH}$ ] solution was prepared by adding ammonia (1 wt%) to silver nitrate solution (50 mM) until complete absence of precipitates was observed. The concentration of the obtained  $\text{Ag}(\text{NH}_3)_2\text{OH}$  was approximately 40 mM. The freshly prepared  $\text{Ag}(\text{NH}_3)_2\text{OH}$  solution was mixed with an aqueous solution of GO (1.0 mg/mL) at GO-to- $\text{Ag}(\text{NH}_3)_2\text{OH}$  volume ratios of 12, 6, and 3 (the samples were labelled as AgNPs-rGO-1, AgNPs-rGO-2 and AgNPs-rGO-3, respectively) and stirred for 2 min to ensure homogeneity. Cyclic voltammetry was performed in the solutions on a potentiostat/galvanostat (Versastat 3 Applied Research Princeton, USA) using a three-electrode system: an ITO (with active area of  $0.25 \text{ cm}^2$ ) as the working electrode, a platinum foil as the counter electrode and a saturated calomel electrode (SCE) as the reference electrode. The scan was performed between  $-1.5$  and  $0 \text{ V}$  at a rate of  $25 \text{ mV s}^{-1}$  while the loading amount of deposits was controlled by five potential cycles. After deposition, the working electrode was washed with double-distilled water (see Figure 4.1). For comparison, AgNPs-rGO-4 was prepared in the same conditions as AgNPs-rGO-1 using  $\text{AgNO}_3$  solution ( $0.04 \text{ M}$ ) instead of  $\text{Ag}(\text{NH}_3)_2\text{OH}$  solution ( $0.04 \text{ M}$ ).



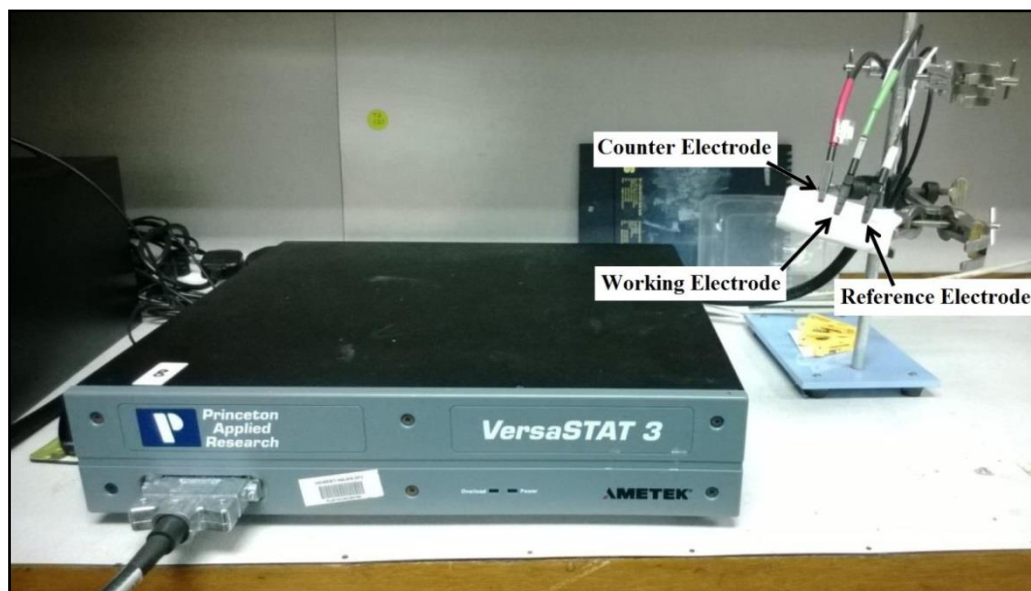


Figure 3.1 Potentiostat/galvanostat (Versastat 3 Applied Research Princeton, USA).

### 3.3.2 Electrochemical sensing measurements

As a proof-of-concept demonstration of the enzymeless electrochemical sensing application of AgNPs-rGO electrodeposited on ITO, CV of bare ITO and AgNPs-rGO/ITO electrodes (as the working electrode) was conducted in a 0.2 M phosphate buffer solution (PBS) at pH 6.5 in the presence of 1 mM  $\text{H}_2\text{O}_2$  on a potentiostat/galvanostat (Versastat 3 Applied Research Princeton, USA) using a three-electrode system: a platinum wire as the counter electrode and a saturated calomel electrode (SCE) as the reference electrode. The scan was performed between  $-0.8$  and  $0$  V at a rate of  $20 \text{ mV s}^{-1}$ . The amperometric response of the AgNPs-rGO-2/ITO electrode was conducted at  $-0.3$  V in  $\text{N}_2$ -saturated 0.2 M PBS buffer (pH: 6.5) upon a successive step change of  $\text{H}_2\text{O}_2$  concentrations.

### **3.4 One-pot sonochemical synthesis of reduced graphene oxide uniformly decorated with ultrafine silver nanoparticles for non-enzymatic detection of H<sub>2</sub>O<sub>2</sub> and optical detection of mercury ions**

#### **3.4.1 Preparation of Ag-rGO composite**

GO was prepared by a simplified Hummers' method. Silver–ammonia [Ag(NH<sub>3</sub>)<sub>2</sub>OH] solution was prepared by adding ammonia (1 w/v %) to silver nitrate solution (50 mM) until complete absence of precipitates was observed. The concentration of the obtained Ag(NH<sub>3</sub>)<sub>2</sub>OH was approximately 40 mM. The freshly prepared Ag(NH<sub>3</sub>)<sub>2</sub>OH solution was mixed with an aqueous solution of GO (1.0 mg/mL) at GO-to-Ag(NH<sub>3</sub>)<sub>2</sub>OH volume ratios of 8, 4, and 2 (the samples were labelled as AgNPs-rGO-1, AgNPs-rGO-2 and AgNPs-rGO-3, respectively) and stirred for 5 min to ensure homogeneity. The resulting solution was exposed to acoustic cavitation by using ultrasonic horn (Misonix Sonicator S-4000, USA, 20 kHz) immersed directly into the solution at 60 % amplitude for 5 min with 3 s pulse and 5 s relaxation cycle (Figure 3.2). The inset of Figure 4.11 shows the corresponding photograph of the solution of Ag(NH<sub>3</sub>)<sub>2</sub>OH and GO before and after ultrasonic irradiation treatment, which the color changed from yellow brown to black. The products were centrifuged and washed with distilled water three times and were finally redispersed in water. To investigate the effect of the ultrasonic irradiation time, AgNPs-rGO-4 and AgNPs-rGO-5 were prepared by using 15 and 30 min ultrasonic irradiation times for the same solution as AgNPs-rGO-2, respectively. The ultrasonic reaction was conducted without cooling, thus the temperature of about 65, 75 and 80 °C were achieved at the end of the 5, 15 and 30 min reaction, respectively. For comparison, AgNPs-rGO-6 was prepared at the same conditions as AgNPs-rGO-2 using AgNO<sub>3</sub> solution (0.04 M) instead of Ag(NH<sub>3</sub>)<sub>2</sub>OH solution (0.04 M).



Figure 3.2 Photograph of Misonix Sonicator S-4000, USA, 20 kHz.

### 3.4.2 Preparation of modified electrode

A glassy carbon electrode (GCE) was polished using 1.0- and 0.3- $\mu\text{m}$  alumina powders and then sonicated in ethanol and distilled water for 1 min each. Finally, the electrode was dried in a stream of nitrogen, and 5  $\mu\text{L}$  of a suspension of the AgNPs/rGO composite was dropped onto the pre-cleaned GCE and allowed to dry in air at room temperature. An electrochemical sensing application of AgNPs-rGO was conducted on a potentiostat/galvanostat (Versastat 3 Applied Research Princeton, USA) using a three-electrode system, with a modified GCE (with an active area of 0.07  $\text{cm}^2$ ) as the working electrode, a platinum wire as the counter electrode and a saturated calomel electrode (SCE) as the reference electrode.

### 3.4.3 Spectral detection of $\text{Hg}^{2+}$ ions

The spectral detection of  $\text{Hg}^{2+}$  ions using the AgNPs/rGO composite was performed using a UV–visible spectrometer (Thermo Scientific Evolution). The absorption spectra of the AgNPs/rGO composite were recorded after adding different concentrations of  $\text{Hg}^{2+}$  ions from 0.1 to 100  $\mu\text{M}$ . To monitor the absorption spectra, a freshly prepared solution of  $\text{Hg}^{2+}$  ions was added to 4 mL of the AgNPs/rGO composite, shaken well, and allowed a constant resting time (8 min). For selective detection, 100  $\mu\text{M}$  of the analyte ( $\text{Hg}^{2+}$ ,  $\text{Fe}^{2+}$ ,  $\text{K}^+$ ,  $\text{Mn}^{2+}$ ,  $\text{Pb}^{2+}$ ,  $\text{Zn}^{2+}$ ,  $\text{Cd}^{2+}$ ,  $\text{Cu}^{2+}$  and  $\text{Ni}^{2+}$  ions) was added to the AgNPs/rGO composite, and the changes in the absorption spectra were recorded. The limits of detection (LODs) for both hydrogen peroxide and mercury ions were calculated using the following equation:

$$\text{LOD}=3S/b \quad (3-1)$$

where S is the standard deviation of the blank, and b is the slope of the calibrated curve.

## 3.5 One-pot hydrothermal synthesis and characterization of $\text{FeS}_2$

### (Pyrite)/Graphene nanocomposite

#### 3.5.1 Preparation of $\text{FeS}_2$ (pyrite)

The mass of gelatin of 0.54 g was dissolved in 30 mL of distilled water and stirred to obtain a homogenous solution. Then, 0.3 g of  $\text{FeCl}_2 \cdot 4\text{H}_2\text{O}$  was dissolved in 5 mL of distilled water and added in a drop-wise fashion to the gelatin solution while stirring to achieve a homogenous solution. The pH of the mixture was adjusted to 11 by NaOH. Finally, 30 mg of sulphur powder (S) was added to the solution under magnetic stirring for 1 h. The concentration of gelatin was about 1.5% wt/v. The mixture was placed and sealed in a Teflon-lined stainless steel autoclave (80% filled) (Figure 3.3), and maintained at 200 °C for 24 h, before being cooled to room temperature. The product,  $\text{FeS}_2$  (pyrite), was obtained by centrifugation and washed with distilled water

and ethanol several times to remove the excess polymer and ions, and finally dried at 60 °C for 24 h in a vacuum oven. To optimize the experimental conditions for the preparation of pure FeS<sub>2</sub> (pyrite), a number of samples with different parameters were synthesized, as shown in Table 3.1.



Figure 3.3 Photograph of stainless steel autoclave and its teflon used for hydrothermal reaction.

Table 3.1 Experimental conditions for the preparation of FeS<sub>2</sub>.

Sample	Temperature (°C)	Time (h)	pH	Gelatin (% wt/v)
A	180	12	11	1.5
B	180	24	11	1.5
C	180	36	11	1.5
D	200	12	11	1.5
E	200	24	11	1.5
F	200	36	11	1.5
G	200	24	10	1.5
H	200	24	12	1.5
I	200	24	11	0
J	200	24	11	0.8
K	200	24	11	2

### 3.5.2 Preparation of FeS<sub>2</sub> (pyrite)/graphene nanocomposite

GO was prepared by a simplified Hummers' method (Lim HN, 2011 ). To prepare the nanocomposite, 0.3 g of FeCl<sub>2</sub>·4H<sub>2</sub>O was dissolved in 5 mL of distilled water and added in a drop-wise fashion to 20 mL of GO solution (with different concentrations of 0.5, 1 and 2 mg/mL) and stirred for 2 h. Subsequently, 0.54 g of gelatin was dissolved in 10 mL of distilled water and added to the solution under constant stirring to form a homogeneous solution. The pH of the solution was adjusted to a pH of 11 using NaOH. Finally, 30 mg of sulphur powder (S) was added to the solution under magnetic stirring for 1 h. The following steps are similar to the description in Section 3.5.1, Preparation of FeS<sub>2</sub> (pyrite).

### 3.5.3 Photocurrent measurement

For the preparation of the working electrodes, FeS<sub>2</sub> particles or FeS<sub>2</sub> (pyrite)/graphene nanocomposites with different concentrations of GO were dispersed

in chitosan solution (0.5% wt/v) to form a 10 mg/mL solution and ultrasonicated for 5 min. 0.1 mL of colloidal solution was dropped on the cleaned ITO surface ( $1 \times 1 \text{ cm}^2$ ) and allowed to dry overnight at room temperature. The photocurrent generation was measured between the working electrodes (prepared with  $\text{FeS}_2$  particles and  $\text{FeS}_2$  (pyrite)/graphene nanocomposites) and a counter electrode (gold sputtered ITO glass). A drop of electrolyte solution (propylene carbonate solution containing 0.03 mol/L  $\text{I}_2$  and 0.3 mol/L KI) was introduced into the cell between two electrodes using syringe. Photocurrent intensities were measured using a potentiostat/galvanostat (versastat 3 Applied Research Princeton, USA) with 0 V bias potential. A xenon lamp (with AM 1.5G filter and  $100 \text{ mW/cm}^2$ ) was employed as an excitation source (Figure 3.4).

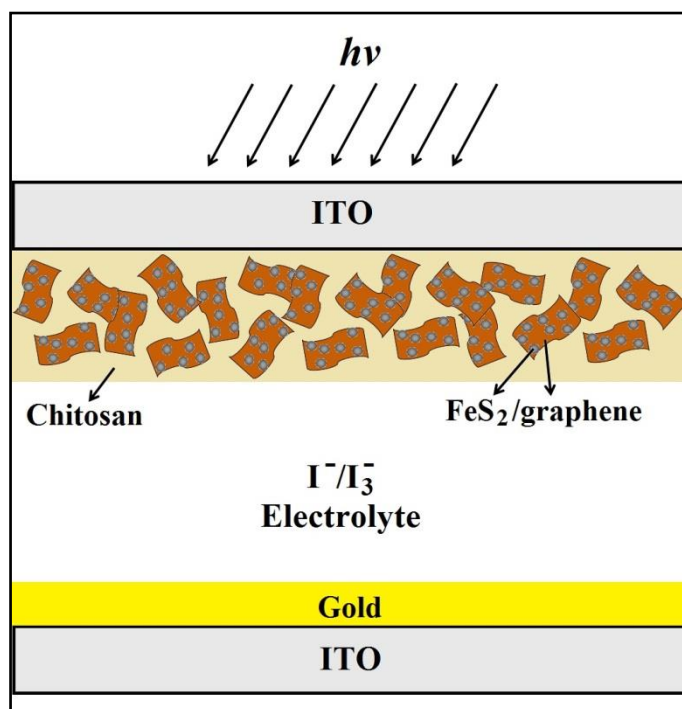


Figure 3.4 Schematic illustration of the sandwich-type device for photocurrent measurements.

### 3.5.4 EIS measurement

Electrochemical measurement were performed in a three-electrode cell system with 0.1 mM  $\text{K}_3[\text{Fe}(\text{CN})_6]/\text{K}_4[\text{Fe}(\text{CN})_6]$  (1:1) mixture as a redox probe in 0.1 M KCl solution as electrolyte. The impedance spectra were obtained over a frequency range of 100 kHz–0.1 Hz, with acquisition of 10 points per decade and a signal with amplitude

of 5 mV around the open circuit potential. A potentiostat/galvanostat model PGSTAT-302N from Autolab, controlled by a USB IF030 (Metrohm Autolab) inter-face and the FRA.EXE software (Distributor: Metrohm Malaysia, Version: 409.007) that has been installed onto a PC computer were used to perform these experiments. Analysis of the impedance spectra was performed by fitting the experimental results to equivalent circuits using the nonlinear least-squares fitting procedure. The impedance spectra were further analyzed by using ZSimpWin V3.10 software. The quality of fitting to the equivalent circuit was first evaluated based on the chi-squared ( $\chi^2$ ) value (the sum of the square of the difference between the theoretical and experimental value) and secondly by limiting the relative error in the value of each element in the equivalent circuit to 5%.

### **3.6 Sonochemical synthesis of reduced graphene oxide decorated with hierarchical ZnS nanospheres**

#### **3.6.1 Preparation of ZnS-rGO nanocomposite**

GO was prepared by a simplified Hummers' method. In order to prepare the nanocomposite, 0.4, 0.8, 1.2 and 1.6 mM of an aqueous solution of zinc acetate dihydrate was added by drop-wise fashion to 10 mL of an aqueous solution of GO (1.0 mg/mL) and stirred (or overnight) for 16 h to ensure the adsorption of the zinc ions to the surface of GO sheets. Then, 0.4, 0.8, 1.2 and 1.6 mM of an aqueous solution of thioacetamide was added to the above mixture and adjusted to the final volume of 20 mL with distilled water and stirred for 5 min to ensure homogeneity. The resulting solution was exposed to acoustic cavitation by using ultrasonic horn (Misonix Sonicator S-4000, USA, 20 kHz) immersed directly into the solution at 80 % amplitude for 15 min with 3 s pulse and 3 s relaxation cycle (Figure 3.2). The products were centrifuged and washed with distilled water and ethanol several times, and finally dried at 60 °C for 24 h in a vacuum oven. The ultrasonic reaction was applied without any cooling, so that the



temperature of about 80 °C was reached at the end of the reactions for 15 min. For comparison, free ZnS particles were also synthesized using the same procedure with the solution of zinc acetate dihydrate and the solution of thioacetamide without GO.

### **3.6.2 Photocatalytic measurements**

The photocatalytic degradation of methylene blue (MB) was carried out in order to evaluate the photocatalytic activity of the as prepared ZnS/rGO nanocomposites. 10 mg of as-prepared ZnS/rGO nanocomposite powder was dispersed in 50 mL of an aqueous solution of MB with an initial concentration of 10 mg/L. The above mixture was first stirred for 60 min in the dark to ensure that the adsorption-desorption equilibrium was reached. Then, the photocatalytic degradation reaction was carried out under the irradiation of a UV lamp (CL-1000 ultraviolet crosslinker UVP, 256 nm, 40 W). At a given time interval during UV irradiation, 3 mL of the suspension was collected and subsequently centrifuged. UV-vis absorption spectra of the degraded solution supernatants was measured using a UV-visible spectrometer (Thermo Scientific Evolution) and the characteristic absorption peak of methylene blue (MB) solution at 663 nm was monitored.

## **3.7 Characterization**

### **3.7.1 X-Ray Diffraction**

X-ray diffraction is a primary, nondestructive and powerful technique for analysis of the material with the arranged atoms in regular planes and forming a crystalline lattice. The XRD analysis gives the information of material such as lattice strain, crystallite size, chemical composition and the orientation of crystal. The fundamental principle of XRD analysis is based on Bragg's law ( $n\lambda=2d\sin\theta$ ). When the beams of X-ray with a wavelength of  $\lambda$  are incident at an angle of  $\theta$  on a crystal lattice, a part of these beams will be scattered in different directions. According to the Bragg's

law, scattered waves originating from each atom of different planes can be in phase with each other by satisfying the Bragg's equation. These in phase waves interfere constructively and produce a peak. During scanning, the characteristic set of the  $d$  spacing and their intensity gives the unique “fingerprint” of different phases, which the material/sample contains. So we can interpret these peaks/value obtain from the “fingerprint” by comparing them to the standard reference pattern and measurement.

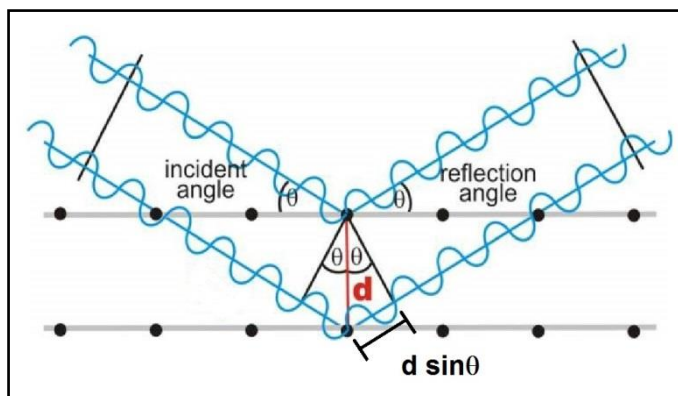


Figure 3.5 Schematic illustration of the X-ray diffraction by parallel atomic planes in a crystallite material.

Powder x-ray diffraction (XRD) of GO and rGO-based nanocomposites were conducted by a Siemens D5000 XRD Diffractometer. The diffraction patterns were collected using a fixed wavelength of CuK $\alpha$  radiation ( $\lambda = 1.54056 \text{ \AA}$ ) over the range of  $5^\circ$  to  $80^\circ$  in  $0.1^\circ$  or  $0.05^\circ$  intervals.

### 3.7.2 Fourier transform infrared spectroscopy

Fourier Transform Infrared is abbreviated as FTIR; it is used for infrared spectroscopy. In this method IR radiations are passes through the sample and the results show in the form of fingerprint of the absorbed and the transmitted infrared light by the molecules (Figure 3.6).

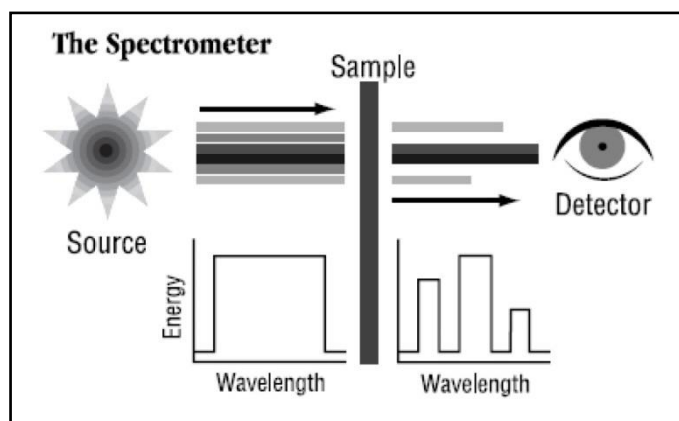


Figure 3.6 Schematic diagram of the FTIR machine.

The infrared spectrum of two unique molecular structures cannot be the same like fingerprints. This is the characteristic of INFRARED spectroscopy which make it useful for several types of analysis. This technique is useful for identifying the chemical bonds on the surface of graphene oxide and reduced graphene oxide. When graphite flakes are oxidized by using strong oxidizing agents, the carbon atom's layer of graphite is decorated by oxygen-containing groups. These oxygen-containing groups can be identified by FTIR spectroscopy. Graphene oxide has usually the absorption peaks at around  $3400\text{ cm}^{-1}$ ,  $1735\text{ cm}^{-1}$ ,  $1620\text{ cm}^{-1}$ ,  $1381\text{ cm}^{-1}$ ,  $1225\text{ cm}^{-1}$ , and  $1169\text{ cm}^{-1}$  and  $1046\text{ cm}^{-1}$ , which can be assigned to the O-H stretching vibrations, C=O stretching,  $sp^2$ -hybridized C=C group and O-H bending, C-OH stretching, C-O-C stretching, and C-O vibration of epoxy or alkoxy groups, respectively. For reduced graphene oxide, some of these absorption peaks are absence or the intensity of them is decreased, which confirm the reduction of graphene oxide. FTIR spectroscopy of GO and rGO-based nanocomposites were conducted by a Fourier transform infrared spectrometer (FTIR; Perkin Elmer System 2000 series spectrophotometer, USA).

### 3.7.3 Raman spectroscopy

When the light falls on the surface of the matter various phenomenon will occur such as absorption, scattering and emission. When the monochromatic laser is striking surface of sample, light are scattered with the same wavelength or the incident

frequency ( $\nu_0$ ). This phenomenon is known as Rayleigh scattering (Figure 3.7). However, when the laser light with the energy of  $h\nu_0$ , where  $h$  is the Planck's constant and  $\nu_0$  is the frequency of the laser beam, falls on the surface of the material, shifting of the incoming laser light wavelength (or frequency) to other wavelength (or frequency) can occur. This re-emitted frequency of light above or below of  $\nu_0$  is called Raman scattering. As shown in Figure 3.7, the molecule can be excited by the laser beam from ground state to the virtual state. After relaxation, molecule emits a photon and returns to the different vibrational or rotational state. The molecule can gain or lose energy of  $\Delta E$ .

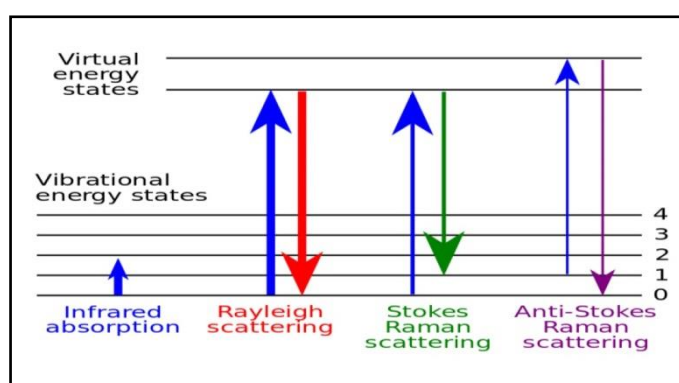


Figure 3.7 Energy-level diagram shows the states involved in Raman signal. The thickness of lines is proportional to the strength of signal from the different transitions.

If the molecule gain energy of  $\Delta E$  then the laser light will be scattered with the energy of  $h\nu_0 - \Delta E$  which causes a peak known as stoke line and it has the energy less than the energy of incident laser light energy. Opposite to this phenomenon when molecules make a transition from excited state (temporary state) to ground state then it releases the energy of  $\Delta E$ , so the laser light will be scattered with energy of  $h\nu_0 + \Delta E$ , higher than the energy of the incident laser light  $h\nu_0$ . Therefore, the anti-stock lines appear in the Raman spectrum and the intensity of the anti-stock lines is usually much less than the intensity of the stoke lines as shown in Figure 3.8.

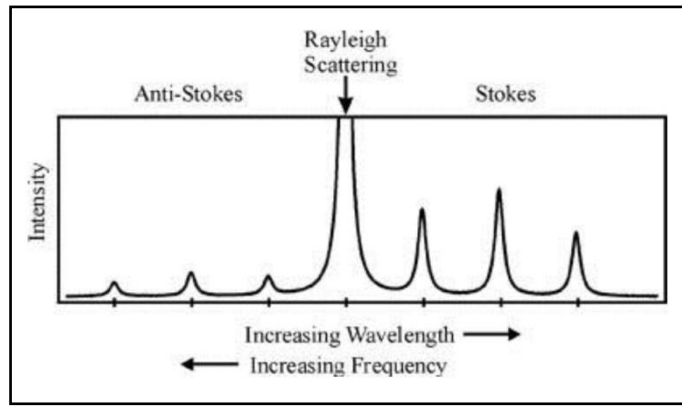


Figure 3.8 The resulting raman lines from different transitions.

Raman spectroscopy is a versatile technique for characterization of graphene. Graphene has three characteristic peaks of G, 2D and D. The *G* peak, which is located at  $\sim 1580 \text{ cm}^{-1}$ , is assigned to the  $E_{2g}$  mode of  $sp^2$ -bonded carbon atoms. The 2D peak at  $\sim 2700 \text{ cm}^{-1}$  corresponds to the second order of zone boundary phonons at the K and  $\Delta$ k points in the Brillouin zone, which has unique signatures distinguishing layer number. While monolayer graphene represents a single-component 2D peak, the 2D peak of bilayer graphene is compound of four peaks. The intensity ratio of the G and 2D peak ( $I_G/I_{2D}$ ) was found to increase almost linearly with the increase of the number of layers from one to four. The D band is assigned to the breathing mode of  $A_{1g}$  symmetry involving phonons near the K zone boundary, which is forbidden in perfect graphitic structure and only can be activated in the presence of disorder and defects.

#### 3.7.4 Field emission scanning electron microscope

Scanning electron microscopy (SEM) is a versatile and well-known technique, which based on the scanning of a sample with a beam of high-energy electrons to observe surface topography, crystalline structure, chemical composition and orientation.

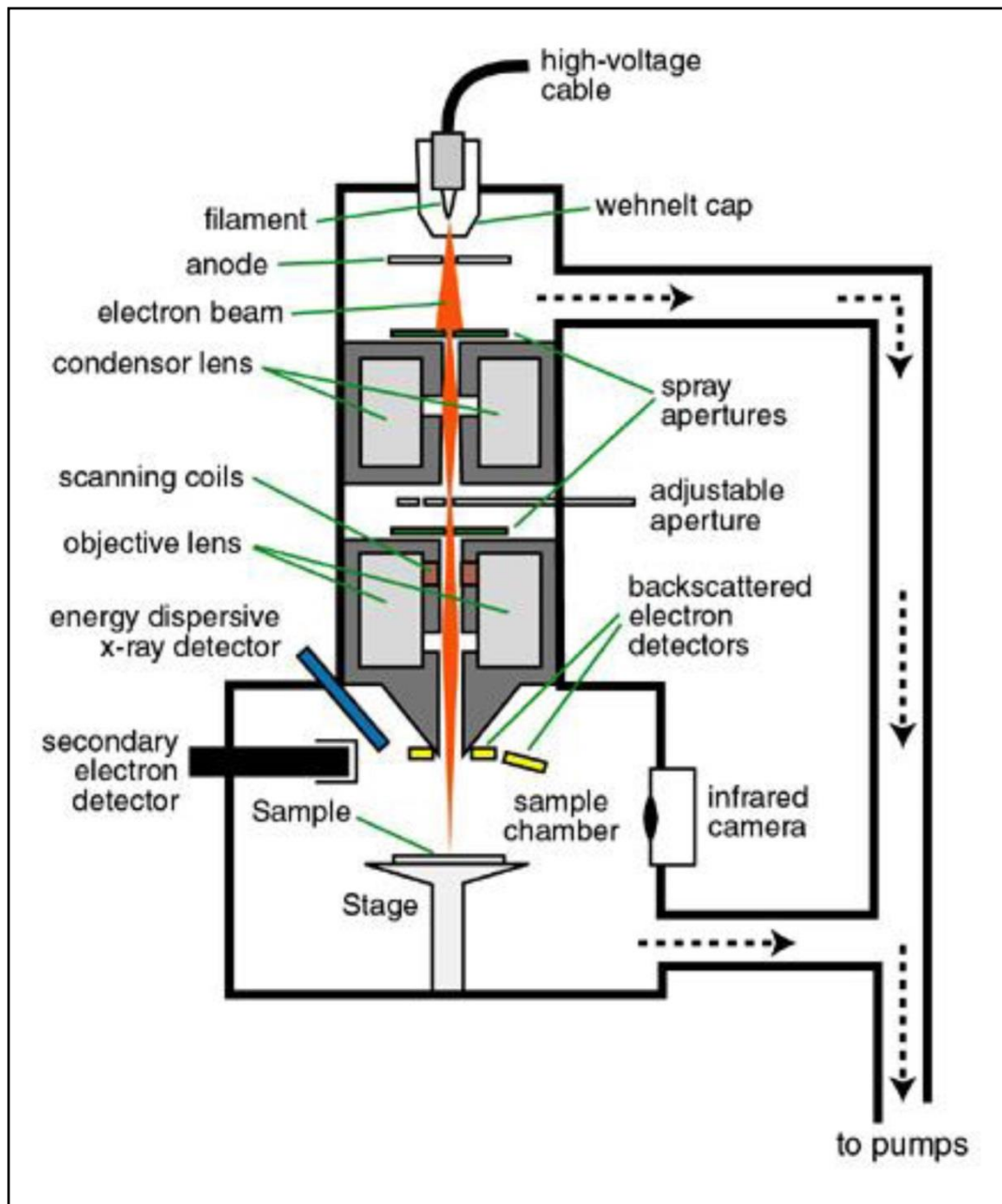


Figure 3.9 Schematic illustration of Scanning electron microscope.

Figure 3.9 shows a typical setup for SEM. The electron beam is emitted from an electron gun and focused by a series of condenser lens to deflect in the x and y axes so that it scans the surface of the sample. In general, the beam of electrons interacts with the sample to generate secondary electrons (SE), back-scattered electrons (BSE) and characteristic X-rays; in which all these signals are detected by special detectors. While back-scattered electrons display contrasts in composition of multi-phase samples and secondary electrons construct three dimensional image of the samples, X-rays could be

used for elemental analysis. In this thesis, a field emission scanning electron microscope (FESEM; FEI Nova Nano-SEM 400 operated at 10.0 kV) was used to study morphology of the samples.

### **3.7.5 High resolution transmission electron microscope**

HRTEM is a technique used to study the morphology of the materials. This is a tool that produce the two dimensional image of the desired sample. In this technique a focused beam of electrons is projected and interact with the sample. This interaction causes the scattering of electrons. So by this way a final image is taken from the incident and diffracted beam. The working principle of the HRTEM is similar to a simple microscope. The projection lenses are used for the illumination of the sample, and so the image of the sample is being projected on a screen. In HRTEM, the electromagnetic lenses are used to give the pathway or to guide the beam of electrons while in a simple microscope the glass lenses are used. In this thesis, Hitachi H-7100 and JEOL JEM-2100F TEM are used. In order to prepare sample for TEM, one or two drops of the sample dispersed in water or ethanol followed by dropcasting onto carbon coated copper grid. The copper grid is placed in an oven to evaporate the excess solvent.

## CHAPTER IV: RESULTS AND DISCUSSIONS

### 4.1 One-step electrodeposition synthesis of silver-nanoparticle-decorated graphene on indium-tin-oxide for enzymeless hydrogen peroxide detection

In this study, silver-nanoparticles-decorated reduced graphene oxide (rGO) was electrodeposited on indium tin oxide (ITO) substrate by a cyclic voltammetry method. The results of X-ray diffraction, Fourier-transform infrared transmission spectroscopy and Raman spectroscopy confirmed the simultaneous formation of cubic phase silver nanoparticles and reduction of GO through electrodeposition process. Field emission scanning electron microscope images showed a uniform distribution of nanometer-sized silver nanoparticles with a narrow size distribution on the RGO sheets, which could only be achieved using silver ammonia complex instead of silver nitrate as precursor. The composite deposited on ITO exhibited notable electrocatalytic activity for the reduction of  $\text{H}_2\text{O}_2$ , leading to an enzymeless electrochemical sensor with a fast amperometric response time of less than 2 s. The corresponding calibration curve of the current response showed a linear detection range of 0.1 mM to 100 mM ( $R^2 = 0.9992$ ) while the limit of detection was estimated to be 5  $\mu\text{M}$ .

#### 4.1.1 Electrodeposition of AgNPs-rGO on ITO via cyclic voltammetry technique

Figure 4.1 shows that the electrodeposition method gives rise to brown and uniform thin films on ITO after five potential cycles. The CV analysis proved the presence of Ag and rGO on ITO, implying the formation of AgNPs/rGO composites. The CV profiles of  $\text{GO:Ag}(\text{NH}_3)_2\text{OH}$  show three cathodic peaks in the negative scan of the first cycle regardless of the volume ratio (Figure 4.2). The first peak (I) may be identified with the reduction of electrochemically active oxygen-containing groups on the graphene planes (Chen et al., 2011b). The second peak (II) is attributed to the reduction of  $\text{Ag}^+$  to form metallic Ag (Sharma et al., 2011, Kaniyankandy et al., 2007).



The third cathodic peak (III), which started at around 0.9 V is attributed to the irreversible electrochemical reduction of GO (Chen et al., 2011b, Guo et al., 2009). Moreover, the reduction current increases with the increase of  $[\text{Ag}(\text{NH}_3)_2]^+$  ions indicating the presence of an increasing amount of loading material on the surface of the ITO. The inset of Figure 4.2 compares the CV profile of the solutions containing  $\text{Ag}(\text{NH}_3)_2\text{OH}$  and  $\text{AgNO}_3$ . The reduction peak of  $\text{Ag}^+$  ions shifted to positive direction in relation to that of  $[\text{Ag}(\text{NH}_3)_2]^+$  since  $[\text{Ag}(\text{NH}_3)_2]^+$  had a higher stability and therefore resisted the reduction of the complex ions (Kaniyankandy et al., 2007).

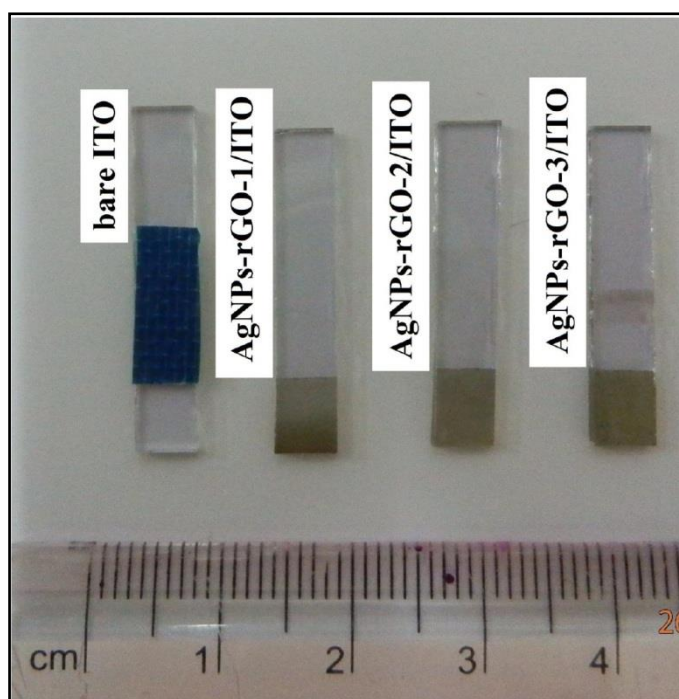


Figure 4.1 Photo image of AgNPs/rGO composites on ITO with different volume ratios of GO (1.0 mg/mL) to  $\text{Ag}(\text{NH}_3)_2\text{OH}$  (0.04 M): 12 (AgNPs-rGO-1), 6 (AgNPs-rGO-2) and 3 (AgNPs-rGO-3).

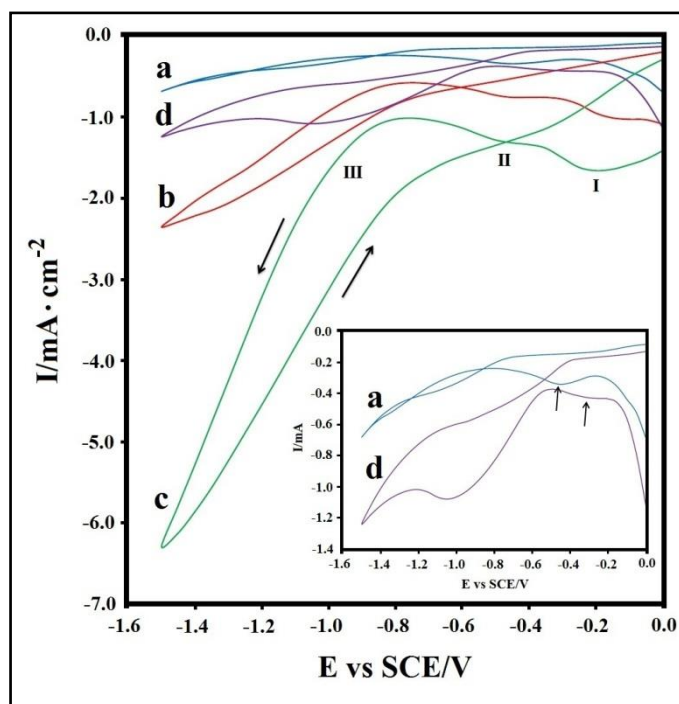


Figure 4.2 The first cycle of the CV profile of ITO in the solution of GO (1.0 mg/mL) and  $\text{Ag}(\text{NH}_3)_2\text{OH}$  (0.04 M) with different volume ratios of 12, 6, and 3 (a–c), respectively, and in the solution of GO (1.0 mg/mL) and  $\text{AgNO}_3$  (0.04 M) with a volume ratio of 12 (d). The inset highlights the CV profile of the solutions containing  $\text{Ag}(\text{NH}_3)_2\text{OH}$  (a) and  $\text{AgNO}_3$  (d).

#### 4.1.2 X-ray diffraction analysis

Figure 4.3 shows the XRD patterns of pristine GO (a), ITO (b), AgNPs-rGO deposited on ITO with different volume ratios of GO (1.0 mg/mL) to  $\text{Ag}(\text{NH}_3)_2\text{OH}$  (0.04 M) (c–e) (12, 6 and 3, respectively). Pristine GO has a sharp peak at  $10.8^\circ$  which is assigned to the (002) inter-planar spacing of 0.82 nm (Xie et al., 2012). All the electrodeposited AgNPs-rGO exhibit some peaks associated with ITO. AgNPs-rGO-1 exhibits a relatively marginal peak at  $38.1^\circ$ . As the amount of  $\text{Ag}(\text{NH}_3)_2\text{OH}$  increases, new peaks appeared at  $44.3^\circ$ ,  $64.4^\circ$ , and  $77.4^\circ$ . The peaks at  $38.1^\circ$ ,  $44.3^\circ$ ,  $64.4^\circ$ , and  $77.4^\circ$  can be indexed to the cubic phase of Ag (PDF card no: 00-001-1167). The increased intensity of the peaks is in agreement with the enhanced signals of the CV profiles. Meanwhile, the (002) peak of GO disappeared after the electrodeposition process. This is attributed to the growth of AgNPs on the surface of rGO nanosheets which prevents the restacking of rGO nanosheets (Xie et al., 2012, Teo et al., 2012).

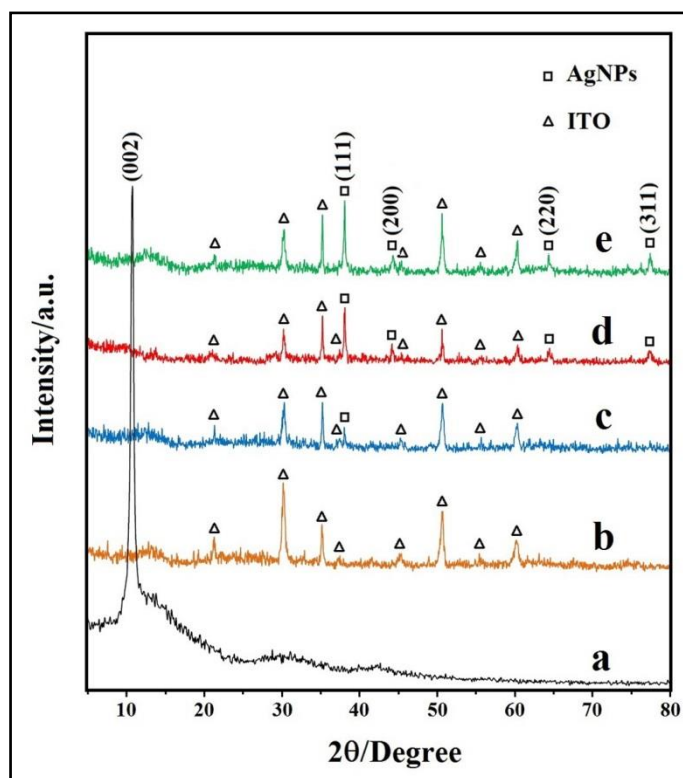


Figure 4.3 XRD patterns of pristine GO (a), ITO (b), and AgNPs-rGO deposited on ITO that prepared by using the solution with different volume ratios of GO (1.0 mg/mL) to  $\text{Ag}(\text{NH}_3)_2\text{OH}$  (0.04 M) of 12, 6, and 3, respectively (c–e).

#### 4.1.3 FTIR spectroscopy

Figures 4.4a and 4.4b show the FTIR spectra of pristine GO and AgNPs-rGO composite, respectively. For GO, the broad peak centred at  $3227\text{ cm}^{-1}$  is attributed to the O-H stretching vibrations while the peaks at  $1734\text{ cm}^{-1}$ ,  $1622\text{ cm}^{-1}$ ,  $1367\text{ cm}^{-1}$ , and  $1225\text{ cm}^{-1}$  are assigned to C=O stretching,  $sp^2$ -hybridized C=C group and O-H bending, C-OH stretching and C-O-C stretching, respectively (Cheng et al., 2013). In addition, the peaks at  $1161\text{ cm}^{-1}$  and  $1041\text{ cm}^{-1}$  can be attributed to C-O vibration of epoxy or alkoxy groups (Pham et al., 2011). For the AgNPs-rGO composite, the peaks at  $1642\text{ cm}^{-1}$ ,  $1418\text{ cm}^{-1}$ ,  $2853\text{ cm}^{-1}$ , and  $2925\text{ cm}^{-1}$  are assigned to the  $sp^2$ -hybridized C=C group and O-H bending, O-H deformation, as well as symmetric and asymmetric stretching vibration of  $\text{CH}_2$  groups, respectively (Cheng et al., 2013). The peak at  $1734\text{ cm}^{-1}$  for GO is absent for AgNPs-rGO, which indicates that the carbonyl group was removed upon the electrochemical reduction (Guo et al., 2009). The noticeable decrease in the

intensity of the peak at  $1642\text{ cm}^{-1}$  implies that a large fraction of the O-H groups was removed (Pham et al., 2011). The broad peak at  $3300\text{ cm}^{-1}$  for AgNPs-rGO composite might be attributed to the O-H stretching vibration of absorbed water molecules.

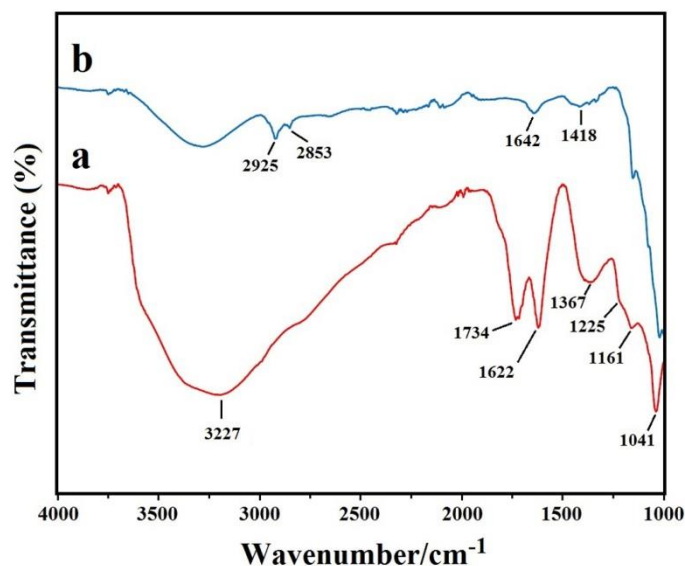


Figure 4.4 FTIR spectra of pristine GO (a) and AgNPs-rGO composite using the solution with the volume ratio of GO (1.0 mg/mL) to  $\text{Ag}(\text{NH}_3)_2\text{OH}$  (0.04 M) of 6 (b).

#### 4.1.4 Raman spectroscopy

Figures 4.5a and 4.5b show the Raman spectra for pristine GO and the AgNPs-rGO composites, respectively. The Raman spectra of GO shows two peaks at  $1349\text{ cm}^{-1}$  and  $1600\text{ cm}^{-1}$ , which correspond to the D and G bands, respectively. The D band is assigned to the breathing mode of  $A_{1g}$  symmetry involving phonons near the K zone boundary. Meanwhile, the G band is assigned to the  $E_{2g}$  mode of  $sp^2$ -bonded carbon atoms (Ferrari and Robertson, 2000). In comparison to the GO, the Raman spectrum of AgNPs-rGO indicates that the D and G bands shifted to lower wavenumbers at  $1347\text{ cm}^{-1}$  and  $1596\text{ cm}^{-1}$ , respectively. This is due to the reduction of GO during the electrodeposition process (Lambert et al., 2009, Liu et al., 2012). In addition, the Raman spectrum of AgNPs-rGO showed a slightly greater  $I(\text{D})/I(\text{G})$  intensity ratio than that of GO, indicating smaller average size but more numerous of the in-plane  $sp^2$  domain. Moreover, the intensity peaks of the D and G bands were enhanced in the case of

AgNPs-rGO due to the surface-enhanced Raman scattering effect of AgNPs, which is about 1700% greater than that of GO (Xu et al., 2011b).

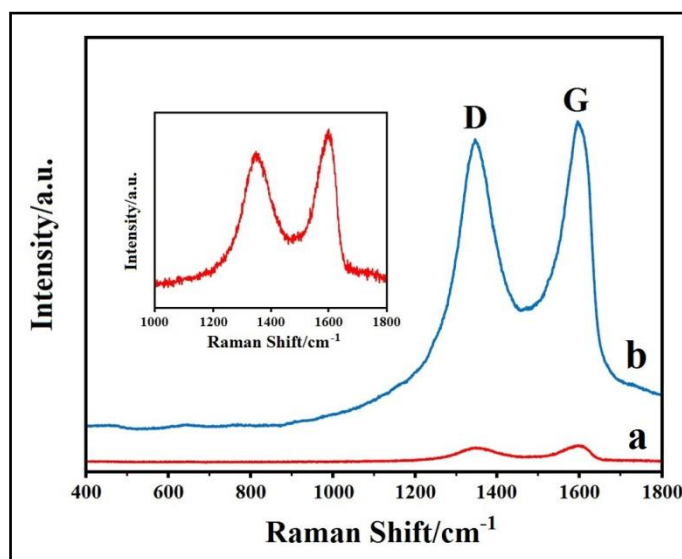


Figure 4.5 Raman spectra of pristine GO (a) and the AgNPs-rGO composites using the solution with the volume ratio of GO (1.0 mg/mL) to  $\text{Ag}(\text{NH}_3)_2\text{OH}$  (0.04 M) of 6 (b). The inset highlights the peaks of pristine GO.

#### 4.1.5 Morphology

Figure 4.6 shows the typical FESEM images and size distribution diagram of AgNPs-rGO prepared by using the solution with GO (1.0 mg/mL) to  $\text{Ag}(\text{NH}_3)_2\text{OH}$  (0.04 M) volume ratio of 12 (a and b), 6 (c and d), 3 (e and f) as well as the solution with GO (1.0 mg/mL) to  $\text{AgNO}_3$  (0.04 M) volume ratio of 12 (g and h). As shown in Figures 4.6a and 4.6b, the silver nanoparticles with a mean size of 20 nm and a narrow size distribution have been anchored and well distributed on the surface of rGO nanosheet. As can be seen in Figures 4.6 (c-f), as the concentration of  $\text{Ag}(\text{NH}_3)_2\text{OH}$  increased, the mean size and number of particles also increased, and the size distribution broadened. The types of Ag precursors appear to affect the size and coverage density of nanoparticles on the rGO surface. When  $\text{AgNO}_3$  was used as precursor of Ag, the mean particle size increased to 48 nm and the size distribution widened, as shown in Figures 4.6g and 4.6h. The two plausible reasons are that: 1) the negatively charged GO are enhanced through neutralization by the alkaline  $\text{Ag}(\text{NH}_3)_2\text{OH}$  to attract more

$[\text{Ag}(\text{NH}_3)_2]^+$  ions than  $\text{AgNO}_3$ , leading to creation of more initial nucleation sites (Zhang et al., 2012b), and 2)  $\text{Ag}(\text{NH}_3)_2\text{OH}$  has a higher stability than  $\text{AgNO}_3$  and resists reduction, hindering the growth of Ag into large particles (Figure 4.2) (Kaniyankandy et al., 2007)].

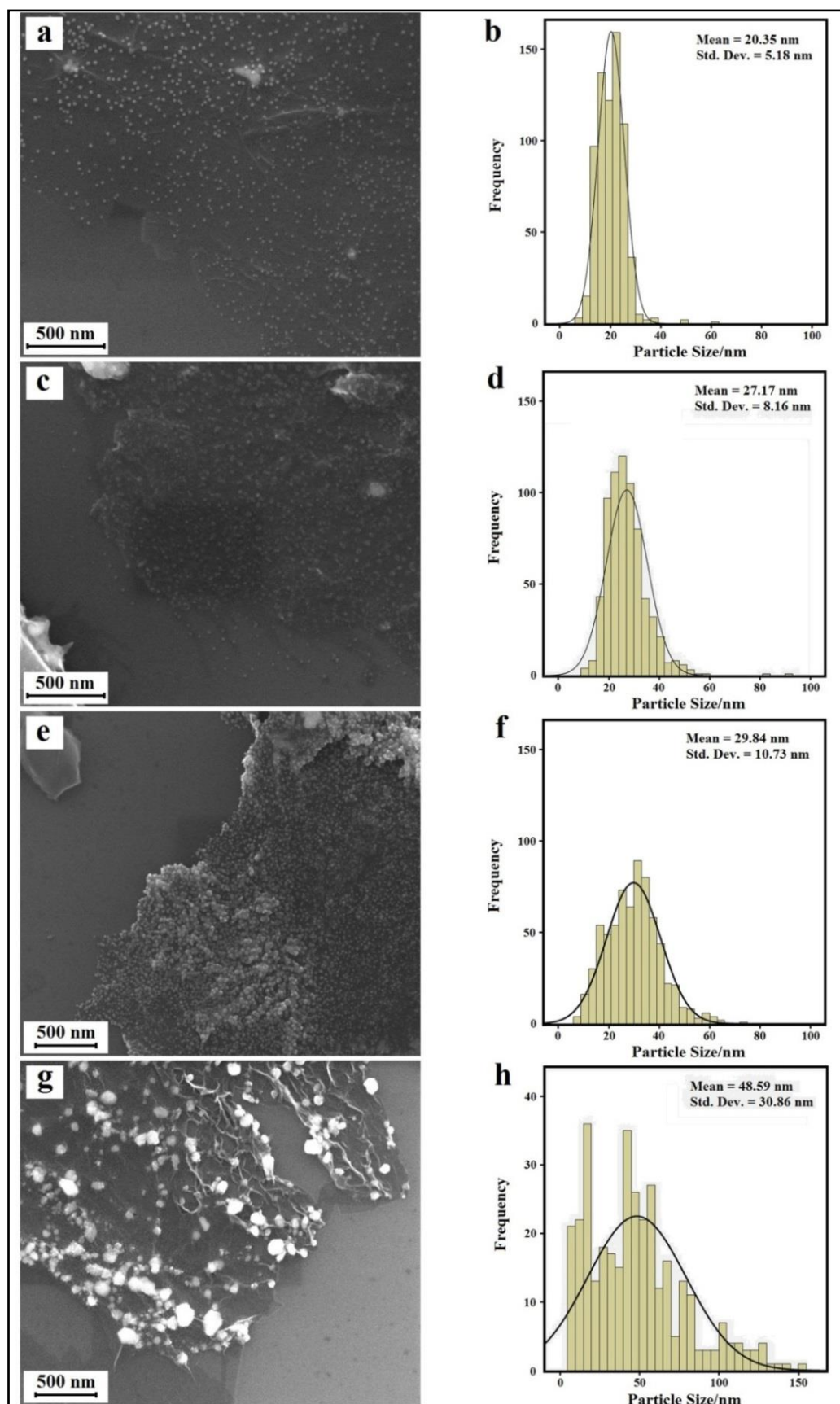


Figure 4.6 FESEM images and size distribution diagram of AgNPs-rGO prepared by using the solution with GO (1.0 mg/mL) to  $\text{Ag}(\text{NH}_3)_2\text{OH}$  (0.04 M) volume ratios of 12 (a and b), 6 (c and d), and 3 (e and f) and using the solution with a GO (1.0 mg/mL) to  $\text{AgNO}_3$  (0.04 M) volume ratio of 12 (g and h).



#### 4.1.6 Formation mechanism

The formation mechanism of AgNPs-rGO *via* electrodeposition is shown in Figure 4.7. Dispersed GO sheets in water are negatively-charged due to the ionization of carboxyl and hydroxyl groups on the surface of GO (Li et al., 2008) (Figure 4.7a). This causes the positively-charged  $[\text{Ag}(\text{NH}_3)_2]^+$  ions to be adsorbed on the negatively-charged GO sheets by electrostatic attraction (Figure 4.7b). The GO nanosheets with the adsorbed  $[\text{Ag}(\text{NH}_3)_2]^+$  ions are deposited on the surface of ITO and reduced to graphene nanosheets and AgNPs by applying a negative potential. Simultaneously, the  $[\text{Ag}(\text{NH}_3)_2]^+$  ions in the aqueous solution are deposited and reduced on the formed AgNPs or on the surface of rGO nanosheets, which lead to the growth of the initially formed AgNPs or nucleation of new AgNPs. This explains the reason behind the increased density of AgNPs on the rGO sheets when the concentration of  $[\text{Ag}(\text{NH}_3)_2]^+$  ions multiplied.

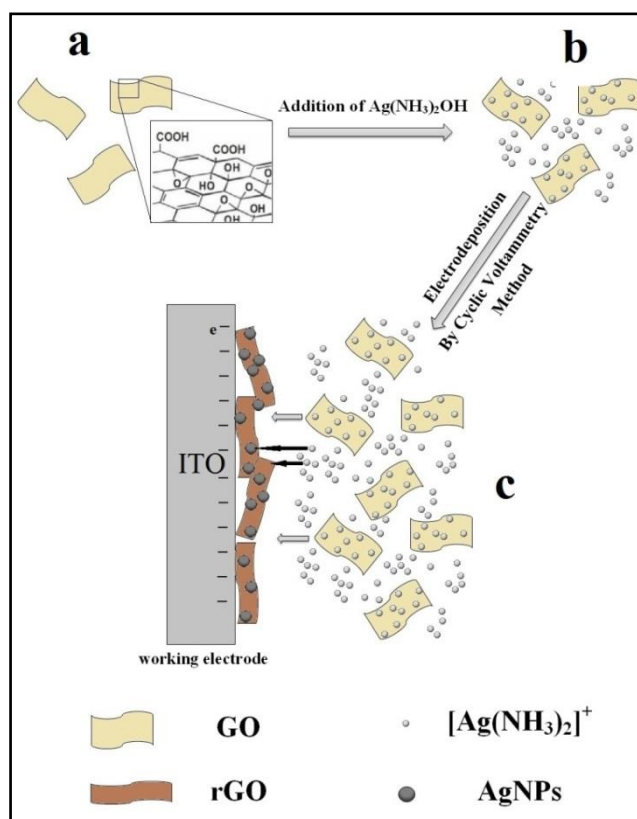


Figure 4.7 Schematic illustration of the formation mechanism of AgNPs-rGO via electrodeposition.



#### 4.1.7 Electrochemical sensing of $\text{H}_2\text{O}_2$

AgNPs are typically known to exhibit high catalytic activity for the reduction of hydrogen peroxide. As a proof-of-concept demonstration of the enzymeless electrochemical sensing application of AgNPs-rGO electrodeposited on ITO, CV of bare ITO and AgNPs-rGO/ITO electrodes was conducted in a 0.2 M phosphate buffer solution (PBS) at pH 6.5 in the presence of 1 mM  $\text{H}_2\text{O}_2$ . As shown in Figure 4.8, all the AgNPs-rGO/ITO electrodes exhibit a notable cathodic peak for the reduction of  $\text{H}_2\text{O}_2$  in comparison to the bare ITO. Figures 4.8b and 4.8e show the comparison between the catalytic activities of AgNPs-rGO-1/ITO and AgNPs-rGO-4/ITO electrodes prepared under similar conditions using different precursors,  $\text{Ag}(\text{NH}_3)_2\text{OH}$  and  $\text{AgNO}_3$ , respectively. The reduction activity of the AgNPs-rGO-1/ITO electrode is markedly better than that of the AgNPs-rGO-4/ITO electrode. A plausible reason is that AgNPs-rGO-1 consists of smaller AgNPs formed on the surface of rGO nanosheets, which results in higher surface area and higher catalytic activity. Among all the AgNPs-rGO/ITO electrodes prepared by using  $\text{Ag}(\text{NH}_3)_2\text{OH}$  complex, the AgNPs-rGO-2/ITO electrode demonstrates the highest catalytic activity. The plausible reason is that the AgNPs-rGO-2/ITO electrode has higher particle density than AgNPs-rGO-1/ITO electrode and although it has lower particle density than AgNPs-rGO-3/ITO electrode, but it consists of smaller AgNPs. These results are in consistent with previous study which implies that electrocatalytic activity of silver nanoparticles decreases with increasing particle size and increases with increasing particle density (Yu et al., 2012). The reduction peak of all the AgNPs-rGO/ITO electrodes increases in current and shifts to the positive potential as the size and density of AgNPs are increased (Campbell et al., 2009, Yu et al., 2012). Therefore, the CV profiles corroborate the observations from the above FESEM images.

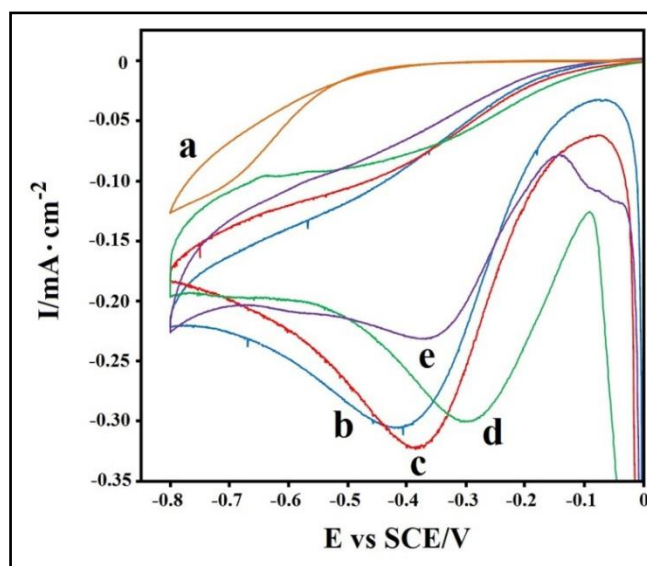


Figure 4.8 CVs of various electrodes in 0.2 M PBS (pH 6.5) in the presence of 1.0 mM  $\text{H}_2\text{O}_2$ : bare ITO (a), AgNPs-rGO/ITO prepared by using different volume ratios of GO (1.0 mg/mL) to  $\text{Ag}(\text{NH}_3)_2\text{OH}$  (0.04 M) of 12, 6, and 3, respectively (b–d), and AgNPs-rGO/ITO prepared by using the solution with GO (1.0 mg/mL) to  $\text{AgNO}_3$  (0.04 M) volume ratio of 12 (e).

Figure 4.9 shows the amperometric response of the AgNPs-rGO-2/ITO electrode at  $-0.3$  V in  $\text{N}_2$ -saturated 0.2 M PBS buffer (pH: 6.5) upon a successive step change of  $\text{H}_2\text{O}_2$  concentrations. When an aliquot of  $\text{H}_2\text{O}_2$  is added, the reduction current changes rapidly to attain a steady-state value and achieve 95% of steady-state current within 2 s, indicating a fast amperometric response behaviour. The inset shows the corresponding calibration curve of the AgNPs-rGO-2/ITO electrode. The current response of the AgNPs-rGO-2/ITO electrode is estimated to be linear within the  $\text{H}_2\text{O}_2$  concentration range from 0.1 to 100 mM ( $R^2 = 0.9992$ ) while the limit of detection is estimated to be 5  $\mu\text{M}$  based on a signal-to-noise ratio of 3. The electrode-to-electrode reproducibility is approximated to be in the presence of 1.0 mM  $\text{H}_2\text{O}_2$  in 0.2 M PBS (pH 6.5) at four electrodes (AgNPs-rGO-2/ITO) prepared in the same conditions, which yields a relative standard deviation (RSD) of 4.5%. Based on the comparative analysis between different types of electrodes shown in Table 4.1, the present AgNPs-rGO/ITO electrode is capable of affording favorable detection limit and linear range for sensing of  $\text{H}_2\text{O}_2$ .

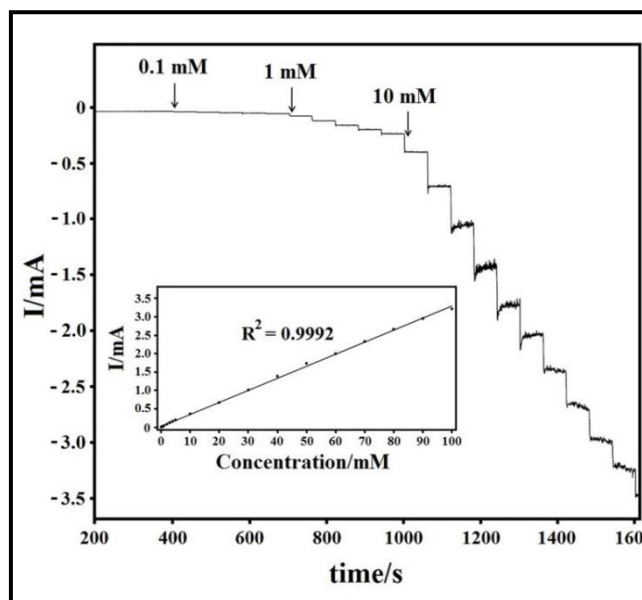


Figure 4.9 Steady-state response of the AgNPs-rGO-2/ITO electrode to successive injection of  $\text{H}_2\text{O}_2$  into the stirred 0.2 M PBS (pH 6.5) with an applied potential of  $-0.3$  V. The inset is the corresponding calibration curve.

Table 4.1 A comparison of this work with works in the literature regarding the performance of the  $\text{H}_2\text{O}_2$  assays.

Type of electrode	Limit of detection (mM)	Linear range (mM)	References
Ag NPs-NFs/GCE	62	0.1–80	(Tian et al., 2010)
Ag NPs-GN-R/GCE	28	0.1–40	(Liu et al., 2010b)
AgNPs-MWCNT/Au	0.5	0.05–17	(Zhao et al., 2009)
AgNPs/collagen/GCE	0.7	0.005–40.6	(Song et al., 2009)
AgNP/rGO-benzylamine/GCE	31.3	0.1–100	(Liu et al., 2011d)
AgNP/GO/ssDNA/Au	1.9	0.1–20	(Lu et al., 2011c)
AgNP-PMPD/GCE	4.7	0.1–30	(Tian et al., 2011)
PQ11-AgNPs/GCE	33.9	0.1–180	(Lu et al., 2011d)
ERGO-Ag/GCE	1.6	0.1–3	(Zhao et al., 2013a)
AgNPs-rGO/ITO	5	0.1–100	This work

## **4.2 One-pot sonochemical synthesis of reduced graphene oxide uniformly decorated with ultrafine silver nanoparticles for non-enzymatic detection of H<sub>2</sub>O<sub>2</sub> and optical detection of mercury ions**

In this work, reduced graphene oxide (rGO) uniformly decorated with silver nanoparticles (AgNPs) is synthesized through a simple ultrasonic irradiation of the aqueous solution containing silver ammonia complex (Ag(NH<sub>3</sub>)<sub>2</sub>OH) and graphene oxide (GO). The results of X-ray diffraction, Fourier-transform infrared transmission spectroscopy, X-ray photoelectron spectroscopy and Raman spectroscopy confirmed the simultaneous formation of cubic-phase AgNPs and the reduction of GO through the ultrasonication process. The size of the nanoparticles could be tuned by adjusting the volume ratio of the precursors and the ultrasonic irradiation time. Transmission electron microscope images show a uniform distribution of ultrafine spherical AgNPs with a narrow size distribution on the rGO sheets, which could only be achieved by using silver ammonia complex instead of silver nitrate as the precursor. The average particle size of silver with the narrowest size distribution is 4.57 nm. The prepared AgNPs-rGO modified glassy carbon electrode exhibited notable electrocatalytic activity toward the non-enzymatic detection of H<sub>2</sub>O<sub>2</sub> with a wide linear range of 0.1–70 mM ( $R^2 = 0.9984$ ) and a detection limit of 4.3  $\mu$ M. Furthermore, the prepared AgNPs-rGO composite was employed for the spectral detection of Hg<sup>2+</sup> ions and showed a detection limit of 20 nM.

### **4.2.1 X-ray diffraction analysis**

Figure 4.10 shows the XRD patterns of pristine GO (a), a sample holder (b) and AgNPs-rGO prepared at different reaction times (c–e) (5, 15 and 30 min, respectively). Pristine GO has a sharp peak at 10.8° which is assigned to the (002) inter-planar spacing of 0.82 nm (Xie et al., 2012). Meanwhile, the XRD pattern of the sample holder has a broad peak at about  $2\theta = 13^\circ$ , which is observed in the XRD patterns of all the samples. As shown in Figure 4.10 (c–e), the XRD pattern of AgNPs-rGO composites exhibits

broad peaks at  $38.1^\circ$ ,  $44.3^\circ$ ,  $64.2^\circ$  and  $77.6^\circ$ , which can be indexed to the (111), (200), (220) and (311) planes of the cubic Ag crystal (PDF card no: 00-004-0783). The calculated lattice spaces of the (111), (200), (220) and (311) planes are 2.36, 2.05, 1.44 and 1.23 Å, respectively. The average crystallite sizes of the AgNPs-rGO composites prepared at 5, 15 and 30 min, calculated by using the size strain plot method, are 5.6, 6.6 and 8.3 nm, respectively. As the ultrasonic irradiation time increases, the intensity of the peaks and the average crystallite size increases, indicating the formation of AgNPs with a larger average size. Meanwhile, the (002) peak of GO disappeared after the sonication process. This is attributed to the growth of AgNPs on the surface of the rGO sheets, which prevents the restacking of the rGO sheets (Xie et al., 2012, Teo et al., 2012).

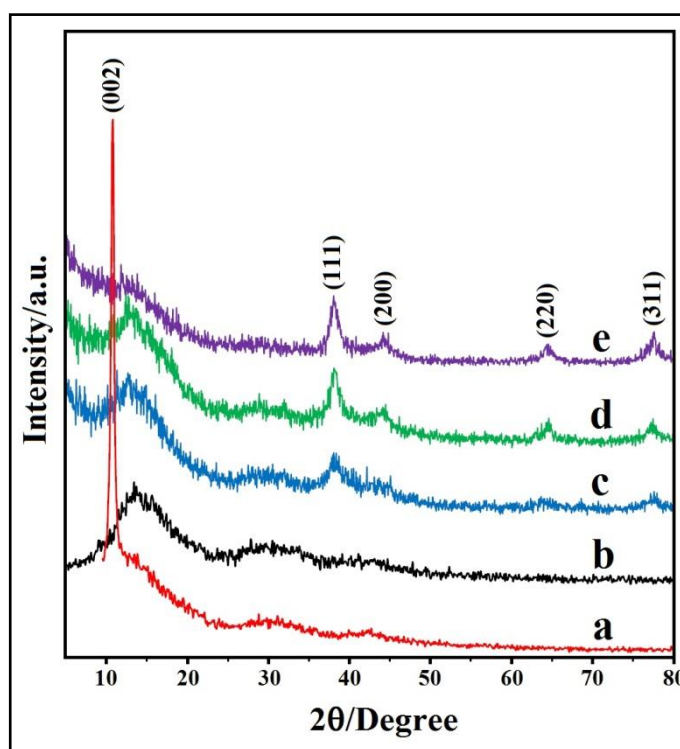


Figure 4.10 XRD patterns of pristine GO (a), sample holder (b), and AgNPs-rGO that were prepared at different ultrasonic irradiation time: 5 min (c), 15 min (d) and 30 min (e).

#### 4.2.2 UV-Vis absorption spectra

Figure 4.11A shows the UV-Vis absorption spectra of GO and AgNPs-rGO. In the UV-Vis spectrum of GO, two characteristic peaks can be observed at 229 and 304

nm, which are attributed respectively to  $\pi - \pi^*$  transitions of aromatic C=C bonds and  $n - \pi^*$  transitions of C=O bonds (Paredes et al., 2008). After ultrasonic irradiation of the  $\text{Ag}(\text{NH}_3)_2\text{OH}$  and GO solution, those peaks disappeared and two new peaks appeared at 251 and 396 nm, which correspond to the reduction in GO and the surface plasmon resonance (SPR) of the spherical AgNPs, respectively (Su et al., 2011, Abdel-Mohsen et al., 2012). The inset of Figure 4.11A shows the corresponding photograph of the solution of  $\text{Ag}(\text{NH}_3)_2\text{OH}$  and GO before and after ultrasonic irradiation treatment, in which the colour changes from yellow brown to black. Figure 4.11B (a–d) shows the effect of the ultrasonic irradiation time on the formation of AgNPs-rGO composites. After 5 min of ultrasonic irradiation, a slight absorption band at 396 nm appears. Meanwhile, the peak can be clearly observed at 15 min, indicating the presence of spherical AgNPs. A further increase in the reaction time induced increasing the peak intensity at 396 nm and broadening the peak. The enhanced peak intensity and broadness imply the increased concentration of silver, which is attributed to the increased amount and size of AgNPs, as proven in the subsequent discussion on the morphology of the composite observed using the HRTEM.

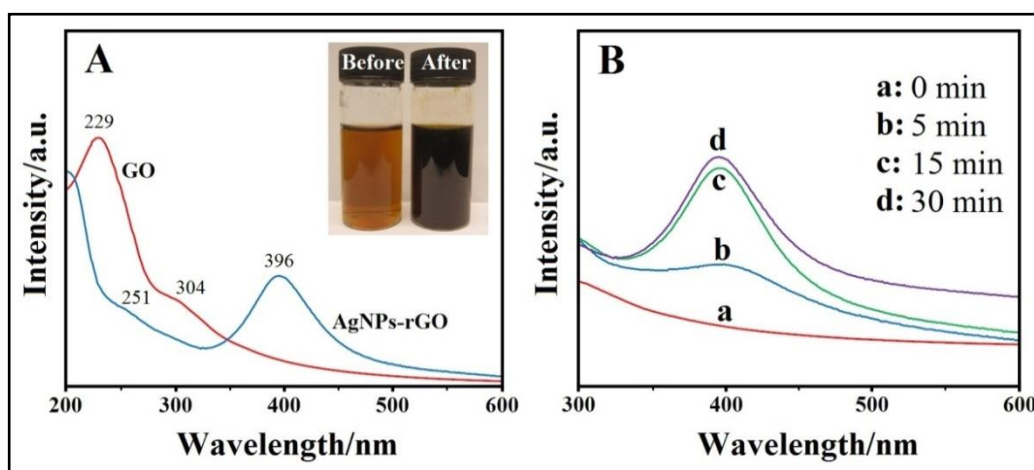


Figure 4.11 (A) UV-vis absorption spectra of GO and AgNPs-rGO (the inset shows the photograph of the solution of GO and  $\text{Ag}(\text{NH}_3)_2\text{OH}$  before and after ultrasonic irradiation), (B) time evolution of UV-vis absorption spectra of AgNPs-rGO.

### 4.2.3 FTIR spectroscopy

Figure 4.12 shows the FTIR spectra of pristine GO (a) and AgNPs-rGO composites that were prepared at different ultrasonic irradiation times (b–d) (5, 15 and 30 min, respectively). For GO, the broad peak centred at  $3227\text{ cm}^{-1}$  is attributed to the O-H stretching vibrations while the peaks at  $1735\text{ cm}^{-1}$ ,  $1626\text{ cm}^{-1}$ ,  $1381\text{ cm}^{-1}$ , and  $1225\text{ cm}^{-1}$  are assigned to C=O stretching,  $sp^2$ -hybridized C=C group and O-H bending, C-OH stretching and C-O-C stretching, respectively (Cheng et al., 2013). Meanwhile, the peaks at  $1169\text{ cm}^{-1}$  and  $1046\text{ cm}^{-1}$  can be attributed to the C-O vibration of epoxy or alkoxy groups (Pham et al., 2011). For the AgNPs-rGO composites, the peak at  $1597\text{ cm}^{-1}$  is assigned to the  $sp^2$ -hybridized C=C group. The peak at  $1169\text{ cm}^{-1}$  for GO is absent for AgNPs-rGO composites and the intensity of the peaks, related to the oxygen-containing groups, decreases for AgNPs-rGO composites, indicating the reduction of GO during the ultrasonic irradiation process. In addition, Figure 4.12 shows that the peak intensity of oxygen-containing groups decreases gradually with the increase in ultrasonic irradiation time, which indicates the stepwise removal of oxygen-containing groups.

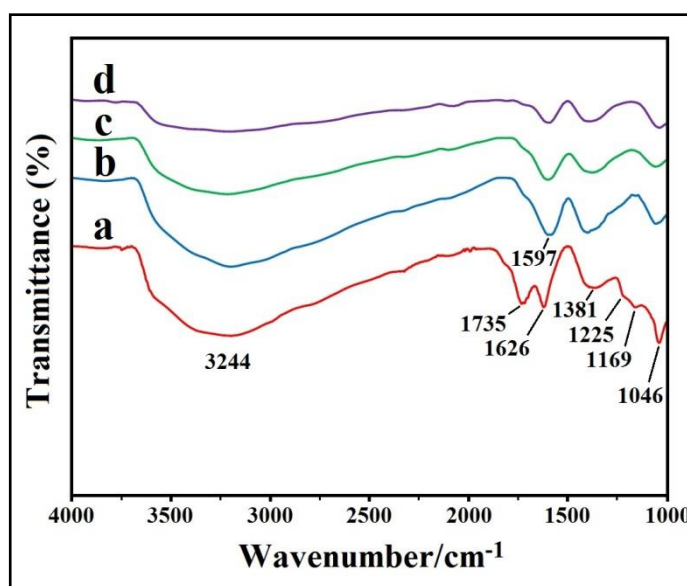


Figure 4.12 FTIR spectra of pristine GO (a), and AgNPs-rGO that were prepared at different ultrasonic irradiation time: 5 min (b), 15 min (c) and 30 min (d).

#### 4.2.4 X-ray photoelectron spectroscopy

XPS spectra further proved the reduction of GO after ultrasonic treatment. As shown in Figure 4.13a, the C1 band of pristine GO can be fitted to four deconvoluted components, centred at 284.5, 286.2, 287.8 and 289 eV, which are assigned to the non-oxygenated ring C, the C in C-O, the C in C=O, and the C in C(O)O, respectively (Dreyer et al., 2010, Pei et al., 2010). In comparison to the pristine GO, the C1 band of the AgNPs-rGO composites shows that the peak intensity of the oxygenated carbonaceous bands decreased, indicating the reduction of GO after ultrasonic treatment. In addition, the peak intensity of the oxygenated carbonaceous bands decreases gradually with the increase in ultrasonic irradiation time, which is consistent with the FTIR results.

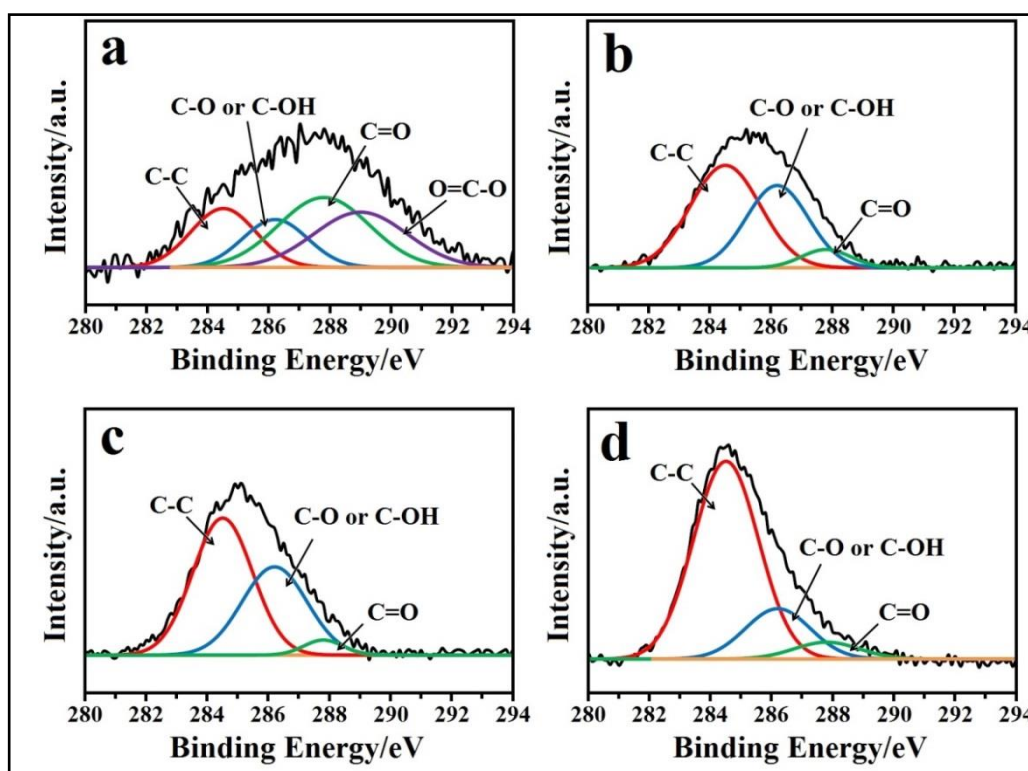


Figure 4.13 XPS spectra of pristine GO (a), and AgNPs-rGO that were prepared at different ultrasonic irradiation time: 5 min (b), 15 min (c) and 30 min (d).

#### 4.2.5 Raman spectroscopy

Figure 4.14 shows the Raman spectra for pristine GO (a) and the AgNPs-rGO composites with different ultrasonic irradiation times (b–d) (5, 15 and 30 min,



respectively). The raman spectrum of GO shows two peaks at 1350 and 1603  $\text{cm}^{-1}$ , which correspond to the well-known D and G bands, respectively. The D band is ascribed to the breathing mode of  $A_{1g}$  symmetry involving phonons near the K zone boundary. Meanwhile, the G band is assigned to the  $E_{2g}$  mode of  $sp^2$ -bonded carbon atoms (Ferrari and Robertson, 2000). The D and G band positions and intensity ratios of  $I(D)/I(G)$  for the GO and AgNPs-rGO composites, prepared at different ultrasound irradiation times, are summarized in Table 4.2. In comparison to the pristine GO, the raman spectra of the AgNPs-rGO composites show that the G band shifted to lower wavenumbers, which can be attributed to the reduction in GO during the ultrasonic irradiation process (Lambert et al., 2009, Liu et al., 2012). In addition, the intensity ratio of  $I(D)/I(G)$  for AgNPs-rGO composite decreases with the increase in the ultrasonic irradiation time to 15 min compared to that of GO, which can be attributed to the formation of  $sp^2$  bonds during the ultrasonic irradiation process (Shi et al., 2012). By further increasing the ultrasonic irradiation time to 30 min, the intensity ratio of  $I(D)/I(G)$  increased to the slightly higher value of 0.95 than that of GO (0.91), which can be assigned to the formation of further defects in the rGO sheets. A possible explanation is that the prolonged reaction time is conducive to the increased formation of AgNPs on the rGO, thus overriding the  $sp^2$  hybridized carbon. Moreover, the intensity peaks of the D and G bands were enhanced in the case of AgNPs-rGO due to the SERS effect of AgNPs. As shown in Figure 4.14, the intensity peaks of the D and G bands for AgNPs-rGO composite increased from 1.3 to 4 times compared to that of GO with the increase in ultrasonic irradiation time, which indicates the increase of AgNPs on the surface of the rGO nanosheets as the ultrasonic irradiation time increased (Xu et al., 2011b).

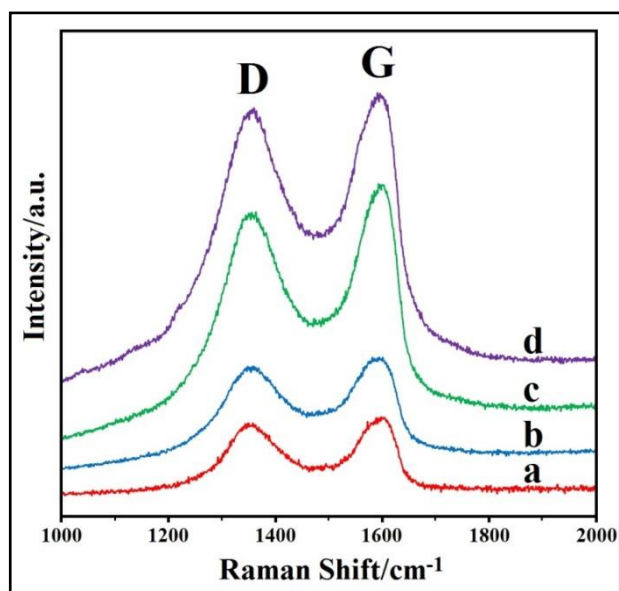


Figure 4.14 Raman spectra of pristine GO (a), and AgNPs-rGO that were prepared at different ultrasonic irradiation time: 5 min (b), 15 min (c) and 30 min (d).

Table 4.2 D and G peak positions, and intensity ratio of I (D) /I (G) (obtained by Raman analysis) of GO and AgNPs-rGO composites that were prepared at different ultrasonic irradiation times.

	GO	AgNPs-rGO (5 min)	AgNPs-rGO (15 min)	AgNPs-rGO (30 min)
<b>D band (cm<sup>-1</sup>)</b>	1350	1360	1363	1360
<b>G band (cm<sup>-1</sup>)</b>	1603	1594	1593	1591
<b>I(D)/I(G)</b>	0.91	0.88	0.87	0.95

#### 4.2.6 Morphology

Figure 4.15 shows the typical TEM images and size distribution histograms of AgNPs-rGO prepared by using the solution with GO (1.0 mg/mL) to Ag(NH<sub>3</sub>)<sub>2</sub>OH (0.04 M) volume ratios of 8 (a and b), 4 (c and d), 2 (e and f) as well as the solution with a GO (1.0 mg/mL) to AgNO<sub>3</sub> (0.04 M) volume ratio of 4 (g and h) at the ultrasonic irradiation time of 5 min. As shown in Figures 4.15a and 4.15b, the ultrafine spherical AgNPs with a mean size of 4.56 nm and a narrow size distribution have been anchored and well distributed on the surface of the rGO sheets. Figures 4.15(c–f) illustrate that the increased amount of Ag(NH<sub>3</sub>)<sub>2</sub>OH is commensurate with the mean size and size

distribution. The types of Ag precursor appear to affect the size and coverage density of the nanoparticles on the surface of the rGO. When  $\text{AgNO}_3$  was used as a precursor of Ag, the mean particle size increased to 9.96 nm and the size distribution as widened, as shown in Figures 4.15g and 4.15h. Moreover, the density of the particles is reduced tremendously as compared to those prepared by using  $\text{Ag}(\text{NH}_3)_2\text{OH}$  as the precursor of Ag, caused by the clumping of nanoparticles. This implies that the ammonia molecules somewhat act as a template for the nucleation and growth of AgNPs at a constraint geometry. The ammonia molecules critically control the particle size and size distribution of AgNPs.

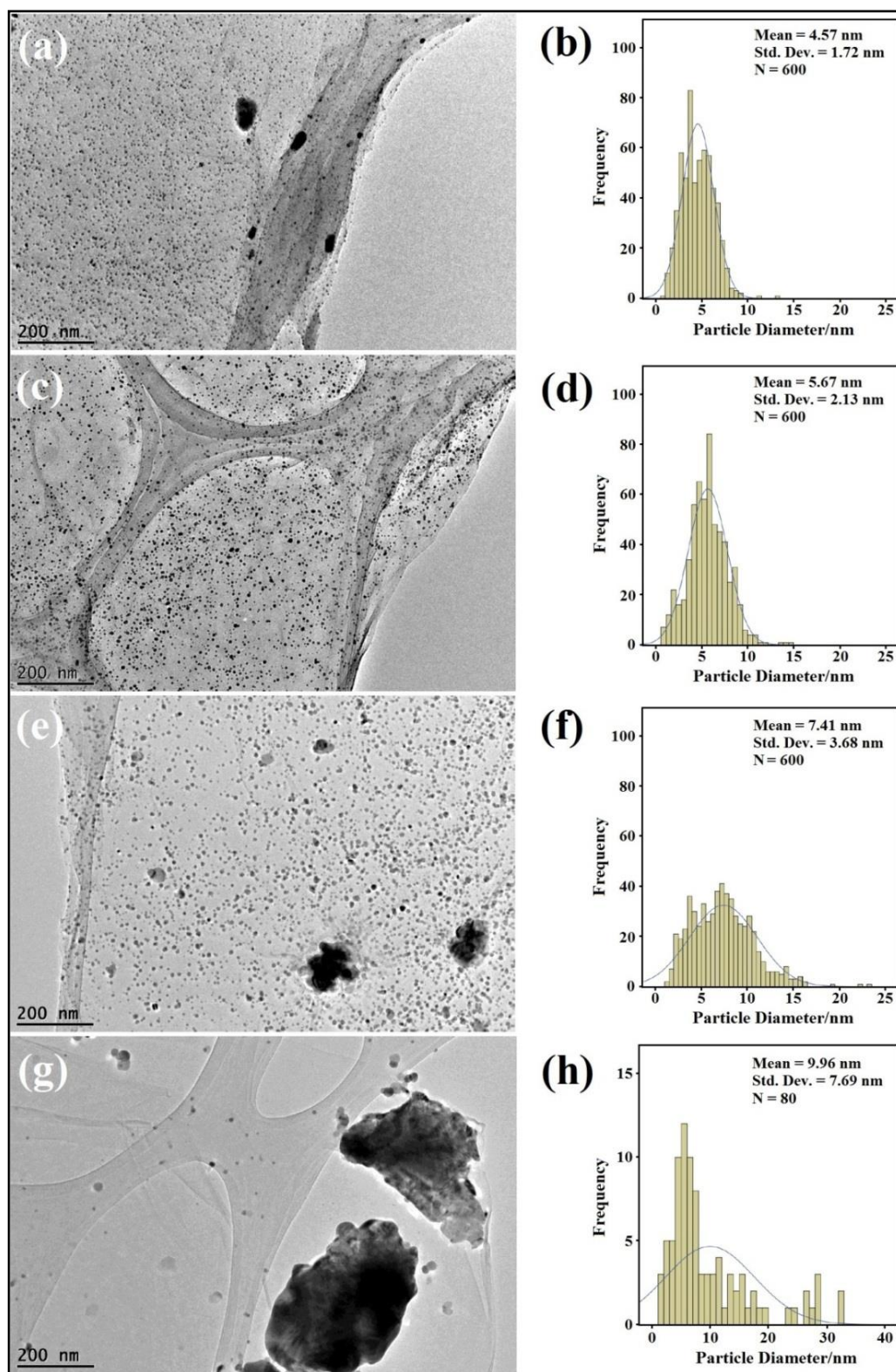


Figure 4.15 TEM images and size distribution diagrams of AgNPs-rGO prepared by using the solution with GO (1.0 mg/mL) to Ag(NH<sub>3</sub>)<sub>2</sub>OH (0.04 M) volume ratio of 8 (a and b), 4 (c and d), 2 (e and f) as well as the solution with GO (1.0 mg/mL) to AgNO<sub>3</sub> (0.04 M) volume ratio of 4 (g and h) with the same ultrasonic irradiation time of 5 min.

Figure 4.16 shows the typical TEM images and size distribution diagrams of AgNPs-rGO prepared by using the solution with the GO (1.0 mg/mL) to Ag(NH<sub>3</sub>)<sub>2</sub>OH

(0.04 M) volume ratio of 4 at different ultrasonic irradiation times 15 min (a and b) and 30 min (c and d), respectively. As shown in Figure 4.16, as the ultrasonic irradiation time increased from 5 min to 15 and 30 min, the mean size increased from 5.67 nm to 7.82 and 12.68 nm, respectively and the size distribution broadened. Figure 4.16e shows the HRTEM image of AgNPs anchored on the surface of the rGO sheet. The measured lattice fringe spaces of 0.23 and 0.20 nm are attributed to the (111) and (200) planes of silver crystal, respectively. In retrospect, the planes are in agreement with the XRD results.

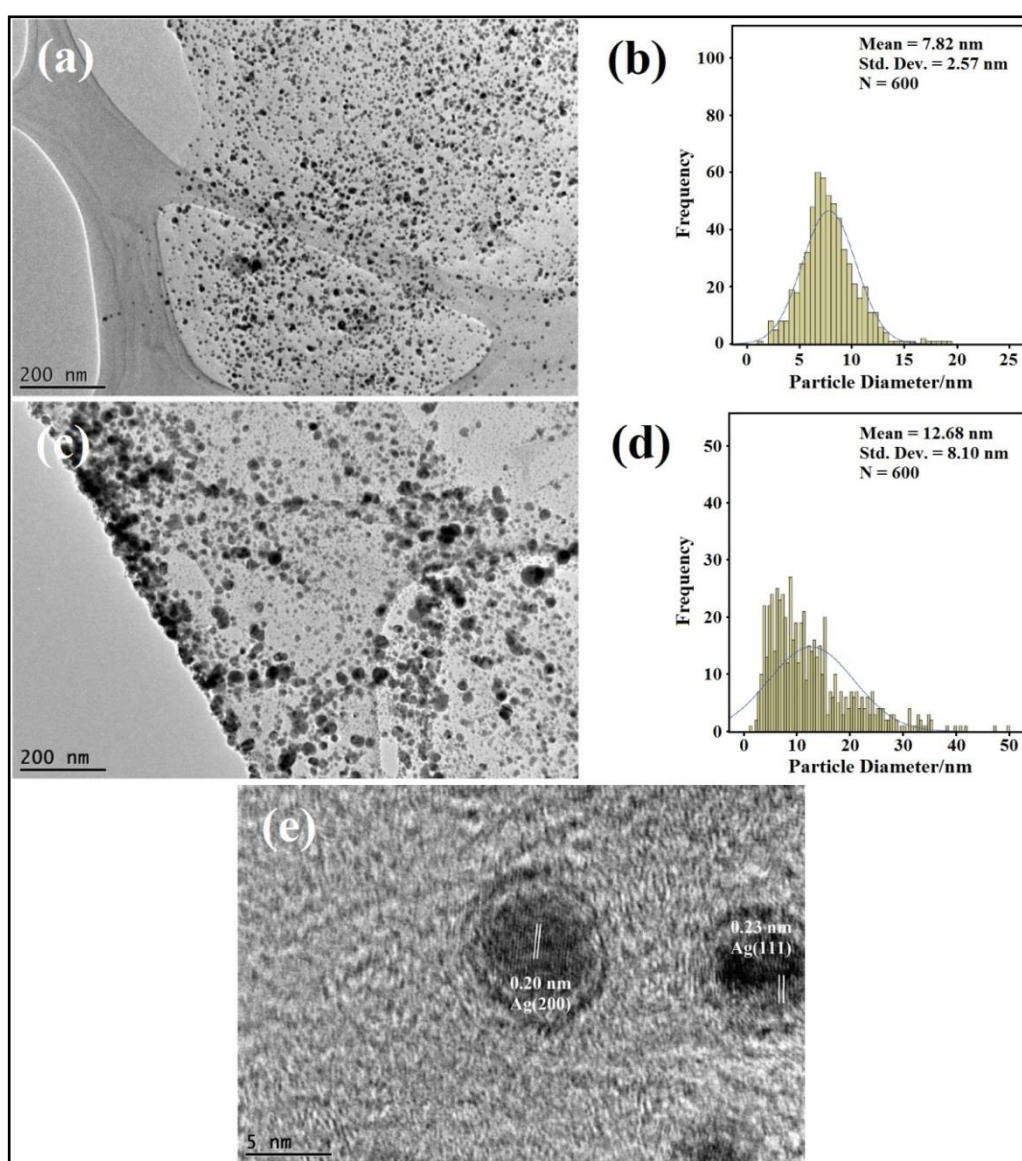


Figure 4.16 TEM images and size distribution diagrams of AgNPs-rGO prepared by using the solution with GO (1.0 mg/mL) to  $\text{Ag}(\text{NH}_3)_2\text{OH}$  (0.04 M) volume ratio of 4 at different ultrasonic irradiation times 15 min (a and b) and 30 min (c and d), and HRTEM image of silver nanoparticles anchored on the surface of rGO sheet (e).

#### 4.2.7 Formation mechanism

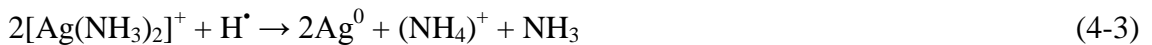
The formation mechanism of AgNPs-rGO *via* sonochemical reaction is shown in Figure 4.17. Dispersed GO sheets in water are negatively charged due to the ionization of carboxyl and hydroxyl groups on the surface of the GO (Li et al., 2008) (Figure 4.17a). This causes the positively charged  $[\text{Ag}(\text{NH}_3)_2]^+$  ions to be adsorbed on the negatively charged GO sheets by electrostatic attraction (Figure 4.17b). When an aqueous solution is irradiated with ultrasound, bubbles are created and accumulate ultrasonic energy while growing. When the bubbles collapse rapidly, this leads to the creation of localized hotspots with a high temperature of 5000 K, a pressure of 1000 bar, and a heating and cooling rate of  $10^{10}$  K/s. In these conditions, highly reactive H and OH radicals can be generated by the pyrolysis of water molecules (Pol et al., 2002).



$\text{H}^\bullet$  radicals act as reducing species, resulting in reduction mechanisms (Pol et al., 2002, Vinodgopal et al., 2010):



or



and



The GO and adsorbed  $[\text{Ag}(\text{NH}_3)_2]^+$  or  $\text{Ag}^+$  ions are reduced to graphene and AgNPs simultaneously by the ultrasonic irradiation process (Figure 4.17c). In addition, GO is a thermally unstable material above 200 °C. Hence, the high temperature, generated during ultrasonic irradiation, could reduce GO into graphene (Krishnamoorthy et al., 2012, Krishnamoorthy et al., 2013). When the concentration of  $[\text{Ag}(\text{NH}_3)_2]^+$  ions or the ultrasonic irradiation time increased, the free  $[\text{Ag}(\text{NH}_3)_2]^+$  or  $\text{Ag}^+$  ions in the aqueous solution continue to grow on the previously formed AgNPs as



well as nucleating on the rGO sheets, which explains the increased particle size and density on the rGO sheets. As can be seen in Figure 4.15, the sonochemical reaction can be enhanced by using silver ammonia complex instead of silver nitrate. The two plausible reasons are that: 1) the negatively-charged GO is enhanced through neutralization by the alkaline  $\text{Ag}(\text{NH}_3)_2\text{OH}$  to attract more  $[\text{Ag}(\text{NH}_3)_2]^+$  ions than  $\text{AgNO}_3$ , leading to the creation of more initial nucleation sites (Zhang et al., 2012b), and 2) The ammonia would scavenge the OH radicals which are produced from pyrolysis to provide a reducing condition (Huang et al., 2008).

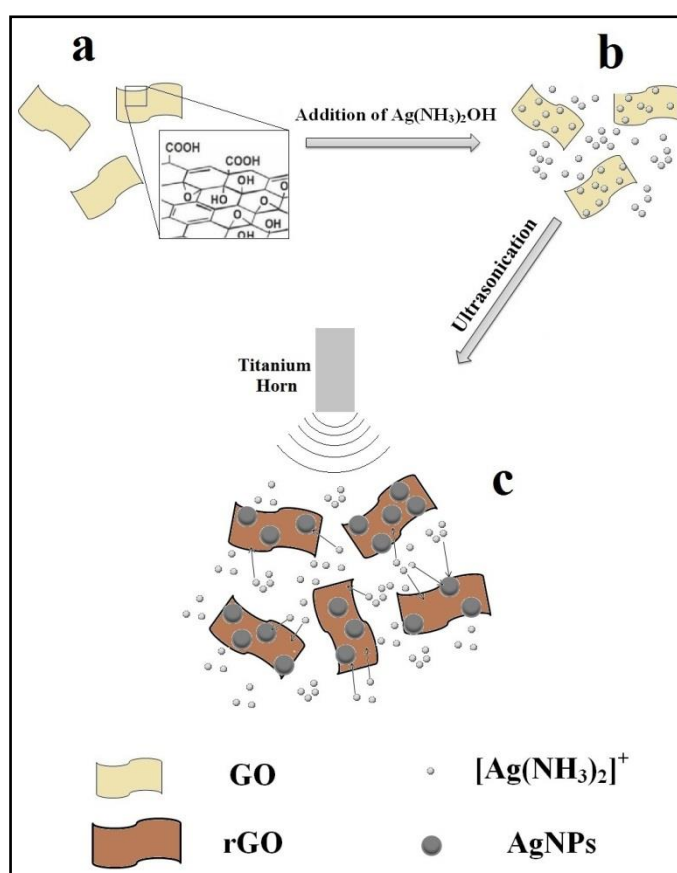


Figure 4.17 Schematic illustration of the formation mechanism of AgNPs-rGO composite via ultrasonic irradiation.

#### 4.2.8 Electrochemical sensing of $\text{H}_2\text{O}_2$

AgNPs are typically known to exhibit high catalytic activity for the reduction of hydrogen peroxide. To investigate the effect of the ultrasonication time on the electrocatalytic activity of the AgNPs-rGO towards hydrogen peroxide reduction, cyclic

voltammetry (CV) measurements of the AgNPs-rGO/GCE electrodes prepared at different ultrasonication times were conducted in a 0.2 M phosphate buffer solution (PBS) at pH 6.5 in the presence of 1 mM H<sub>2</sub>O<sub>2</sub>. As shown in Figure 4.18, all the AgNPs-rGO/GCE electrodes exhibited a notable cathodic peak for the reduction of H<sub>2</sub>O<sub>2</sub> in comparison to the bare GCE. As can be seen in Figure 4.18, the catalytic activity of the AgNPs-rGO/GCE electrode was enhanced by an increase in the ultrasonication time used to prepare the composite from 5 min to 15 min. A plausible reason is that a higher-density of AgNPs could be achieved on the surface of rGO by increasing the ultrasonication time, which enhanced the electrocatalytic activity of the composite. In addition, a further increase in the ultrasonication time to 30 min decreased the electrocatalytic activity of the composite towards the reduction of H<sub>2</sub>O<sub>2</sub>. A plausible reason is that, although a higher density of AgNPs could be achieved on the surface of the rGO, it consisted of larger AgNPs. These results are consistent with those of a previous study (Yu et al., 2012), which implied that the electrocatalytic activity of silver nanoparticles decreased with increasing particle size and increased with increasing particle density. The reduction peak of all the AgNPs-rGO/GCE electrodes shifted to a positive potential as the size and density of the AgNPs increased (Yu et al., 2012, Campbell et al., 2009).



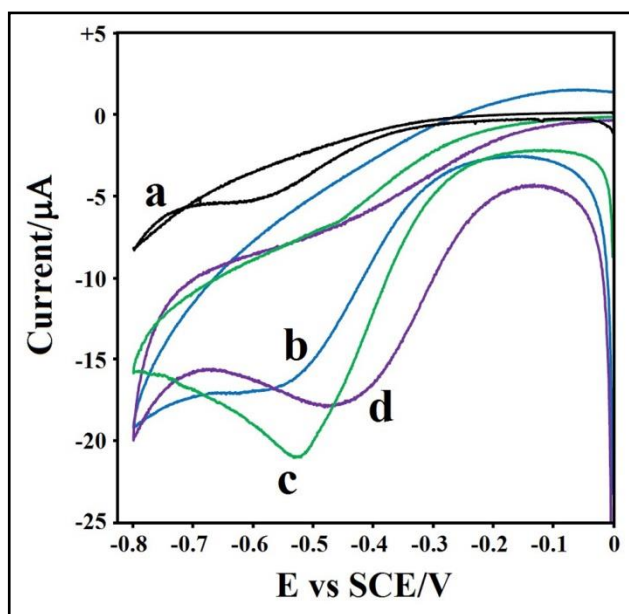


Figure 4.18 CV values of various electrodes in 0.2 M PBS (pH 6.5) in presence of 1.0 mM  $\text{H}_2\text{O}_2$ : (a) bare GCE and AgNPs-rGO/GCE prepared by using different ultrasonication times of (b) 5 min, (c) 15 min and (d) 30 min.

Figure 4.19 shows the amperometric current–time response of the AgNPs-rGO-4/GCE electrode (prepared by using the solution with GO (1.0 mg/mL) to  $\text{Ag}(\text{NH}_3)_2\text{OH}$  (0.04 M) volume ratio of 4 at ultrasonic irradiation time of 15 min) at  $-0.4$  V in an  $\text{N}_2$ -saturated 0.2 M PBS buffer (pH: 6.5) upon successive step changes in the  $\text{H}_2\text{O}_2$  concentration. When an aliquot of  $\text{H}_2\text{O}_2$  was injected in the stirring PBS solution, the reduction current rapidly changed to reach a steady-state value within 3 s, indicating fast amperometric response behaviour. The inset shows the corresponding calibration curve of the AgNPs-rGO-4/GCE electrode. The current response of the AgNPs-rGO-4/GCE electrode is estimated to be linear within the  $\text{H}_2\text{O}_2$  concentration range of 0.1 to 70 mM ( $R^2 = 0.9984$ ), whereas the limit of detection is estimated to be 4.3  $\mu\text{M}$ , based on a signal-to-noise ratio of three. The relative standard deviation (RSD) of the current response to 5 mM  $\text{H}_2\text{O}_2$  at  $-0.4$  V is 5.6% for five successive measurements. Based on the results of a comparative analysis of different types of electrodes listed in Table 4.3, the present AgNPs-rGO/GCE electrode is demonstrated to be capable of affording a favourable detection limit and linear range for sensing  $\text{H}_2\text{O}_2$ .

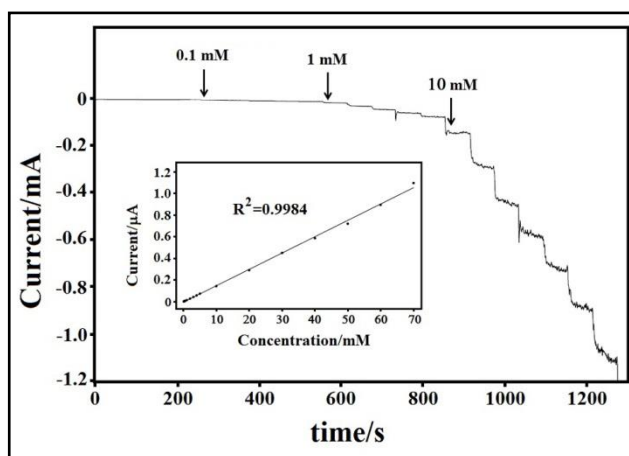


Figure 4.19 Steady-state response of AgNPs-rGO-4/GCE to successive injections of  $\text{H}_2\text{O}_2$  into stirred 0.2 M PBS (pH 6.5) with applied potential of -0.4 V. The inset is the corresponding calibration curve.

Table 4.3 Comparison of results from this work and literature regarding performance of  $\text{H}_2\text{O}_2$  assays.

Type of electrode	Detection limit ( $\mu\text{M}$ )	Linear range (mM)	References
AgNPs-MWCNT/Au electrode	0.5	0.05-17	(Zhao et al., 2009)
Ag NPs-GN-R/GCE	28	0.1-40	(Liu et al., 2010b)
AgNP-PMPD/GCE	4.7	0.1-30	(Tian et al., 2011)
$\text{MnO}_2\text{NWs-Ag/GCE}$	0.24	0.1-4	(Han et al., 2014)
AgNP/GO/ssDNA/Au	1.9	0.1-20	(Lu et al., 2011c)
GN-AgNWs/GCE	9.3	0.02-5.34	(Chandra et al., 2011)
Ag NPs-NFs/GCE	62	0.1-80	(Tian et al., 2010)
AgNPs-rGO/ITO	5	0.1-100	(Moradi Golsheikh et al., 2013)
AgNP/rGO-benzylamine/GCE	31.3	0.1-100	(Liu et al., 2011d)
PDDA-rGO/AgNPs/GCE	35	0.1-41	(Liu et al., 2013)
Ag NPs/3DG	14.9	0.03-16.21	(Zhan et al., 2014)
AgNPs/rGO/GCE	4.3	0.1-70	This work

#### 4.2.9 Optical detection of $\text{Hg}^{2+}$ ions

In order to evaluate the sensitivity and application of the AgNPs-rGO composite to the determination of  $\text{Hg}^{2+}$  ions, the UV-vis absorbance peak related to the surface plasmon resonance (SPR) of silver nanoparticles was monitored during the addition of

different concentrations of an aqueous solution of  $\text{Hg}^{2+}$  ions at room temperature. As shown in the inset of Figure 4.20a, the colour of AgNPs/rGO gradually changes from brown-yellow to colourless with the increase in the  $\text{Hg}^{2+}$  ion concentrations. Figure 4.20a shows the UV-vis absorbance values for the AgNPs-rGO composite in the absence and presence of different concentrations of  $\text{Hg}^{2+}$  ions, where the intensity of the absorbance peak decreases with an increasing concentration of  $\text{Hg}^{2+}$  ions. Accompanied by the extinction intensity of the peak, the SPR peak position shifts toward shorter wavelengths. This phenomenon can be explained by the redox reaction between the  $\text{Hg}^{2+}$  ions and Ag atoms. Because the redox potential of the  $\text{Hg}^{2+}/\text{Hg}^0$  (0.85 V) is higher than that of the  $\text{Ag}^+/\text{Ag}^0$  (0.8 V),  $\text{Hg}^{2+}$  ions oxidize the metallic Ag atoms, which produces metallic Hg atoms and  $\text{Ag}^+$  ions. According to the previous reports, the blue shift in the SPR peak can be related to the adsorption of Hg onto Ag NPs (Henglein and Brancewicz, 1997, Morris et al., 2002). Figure 4.20b shows a calibration curve related to the difference in the absorbance peak of the AgNPs-rGO composite, which is subject to the concentration of  $\text{Hg}^{2+}$  ions. The intensity of the absorbance peak rapidly decreases with an increase in the concentration of  $\text{Hg}^{2+}$  ions up to 10  $\mu\text{M}$ . Above this concentration, the intensity of the absorbance peak slowly decreases with good linearity. A plausible reason for the two linear ranges is that with the increase in the  $\text{Hg}^{2+}$  ion concentration above 10  $\mu\text{M}$ , the formation of a metallic Hg layer around the Ag nanoparticles may occur, which decreases the sensitivity and produces the second linear range (Morris et al., 2002). The estimated limit of detection is 20 nM, based on a signal-to-noise ratio of three. Further experiments were carried out to investigate the selective sensing of  $\text{Hg}^{2+}$  ions by AgNPs-rGO in the presence of other environmentally relevant metal ions ( $\text{Fe}^{2+}$ ,  $\text{K}^+$ ,  $\text{Mn}^{2+}$ ,  $\text{Pb}^{2+}$ ,  $\text{Zn}^{2+}$ ,  $\text{Cd}^{2+}$ ,  $\text{Cu}^{2+}$  and  $\text{Ni}^{2+}$ ). As shown in Figure 4.20c, the SPR peak of AgNPs/rGO was dramatically quenched only by the addition of  $\text{Hg}^{2+}$ , and no significant changes in the SPR peak were observed by the addition of other

metal ions, which demonstrated the selective sensing ability of the prepared AgNPs/rGO composite toward  $\text{Hg}^{2+}$  ions.

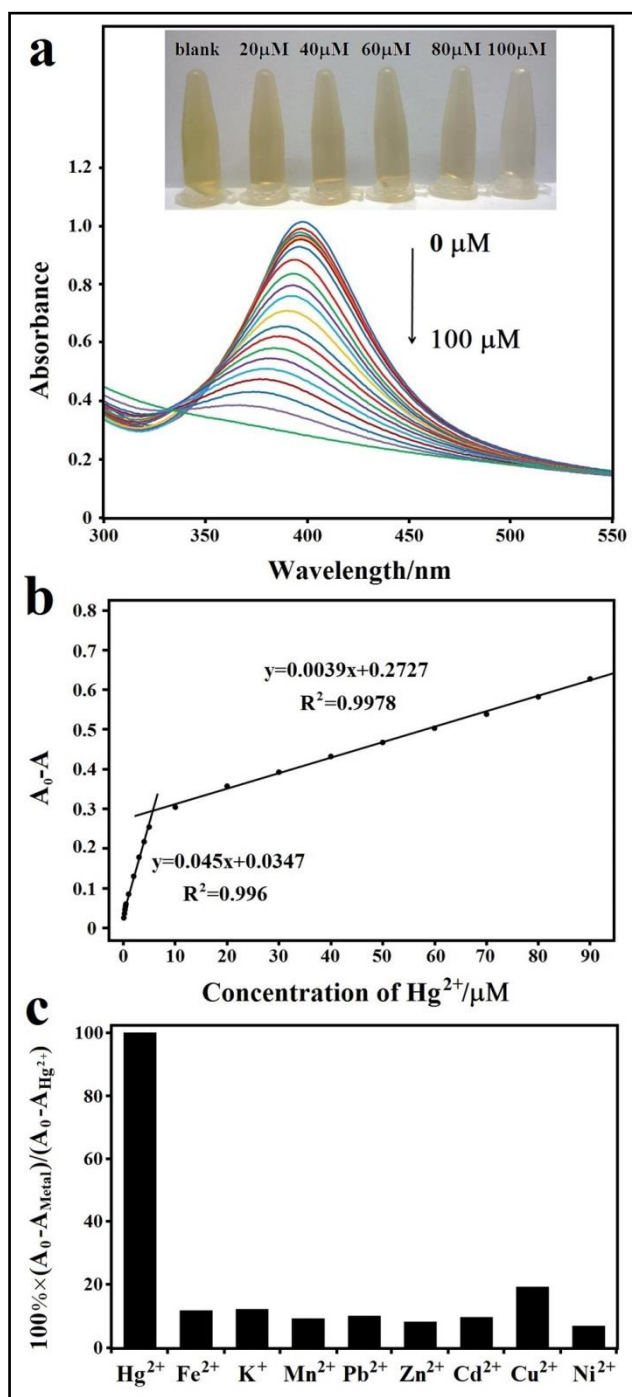


Figure 4.20 (a) Absorbance responses of AgNPs-rGO composite for different concentrations of  $\text{Hg}^{2+}$  ions from 0.1 to 100  $\mu\text{M}$ . The inset shows the gradual colour change of the AgNPs-rGO solution with the increase in the  $\text{Hg}^{2+}$  ion concentration. (b) The corresponding calibration curve for the  $\text{Hg}^{2+}$  ion detection. (c) The relative absorbance change in AgNPs-rGO in the presence of  $\text{Hg}^{2+}$  ions and some other common metal ions.

### **4.3 One-pot hydrothermal synthesis and characterization of FeS<sub>2</sub> (Pyrite)/Graphene nanocomposite**

This work reports on the investigation of temperature, reaction time, pH, concentration of graphene oxide (GO) and the effect of gelatin on the synthesis of pyrite structured FeS<sub>2</sub> nanoparticles assembled on rGO nanosheets using a simple ‘one-pot’ hydrothermal method. The results of X-ray diffraction, Fourier transform infrared transmission spectroscopy, Raman spectroscopy and electron microscopy confirmed the simultaneous formation of pyrite structured FeS<sub>2</sub> and the reduction of GO, yielding a nanocomposite of the materials, through the hydrothermal process. The systematic investigation shows that the nanocomposite, comprising a uniform distribution of nanoparticles on the surface of the rGO sheets, is easily synthesized, providing that certain reaction criteria are achieved. The condition warrants that the reaction is carried out in the presence of gelatin with concentration of 1.5% wt/v and occurred in a pH of 11 at 200 °C for 24 h. At the optimum concentration of GO (1 mg/mL), a photocurrent intensity of about 1.01  $\mu$ A is obtained, which is about 2.6 time higher than that obtained on the pure FeS<sub>2</sub> electrode.

#### **4.3.1 Optimization of the hydrothermal conditions**

Figure 4.21 (a–c) shows the XRD pattern of samples A, B, and C that were prepared at different reaction times (12, 24 and 36 h, respectively) under the same reaction temperature of 180 °C. In addition to the peaks associated with the FeS<sub>2</sub> (pyrite), the XRD pattern of sample A has some peaks attributed to impurities such as FeS<sub>2</sub> (marcasite), FeS, and Fe<sub>2</sub>O<sub>3</sub>. As the reaction time increased to 24 h and 36 h, FeS<sub>2</sub> (pyrite) became the main phase although there are some remaining impurities. The XRD results show that the pure pyrite phase of FeS<sub>2</sub> could not be achieved at 180 °C.

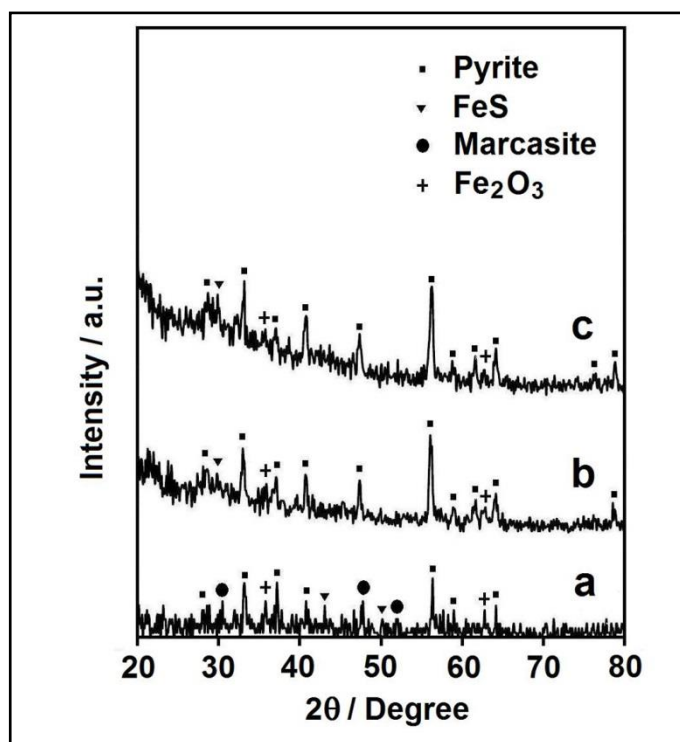


Figure 4.21 XRD patterns of samples A, B and C prepared at 180 °C with different reaction times; (a) 12 h, (b) 24 h and (c) 36 h.

Figure 4.22 (a–c) shows the XRD patterns of samples D, E, and F that were prepared at an elevated temperature of 200 °C at different reaction times (12, 24 and 36 h, respectively). As shown in Figures 4.21a and 4.22a, although the intensity of the FeS<sub>2</sub> (pyrite) peaks increases with the increase in reaction temperature, some impurity peaks can be observed in the XRD pattern of sample D if the reaction time is unaltered. As can be seen in Figure 4.22, the peaks associated with impurities weakened with the increase in reaction time, indicating that the amount of the impurities is decreasing or the amount of FeS<sub>2</sub> (pyrite) is increasing in the product. The XRD results show that the optimum temperature and reaction time to produce pure pyrite are 200 °C and 24 h, respectively.

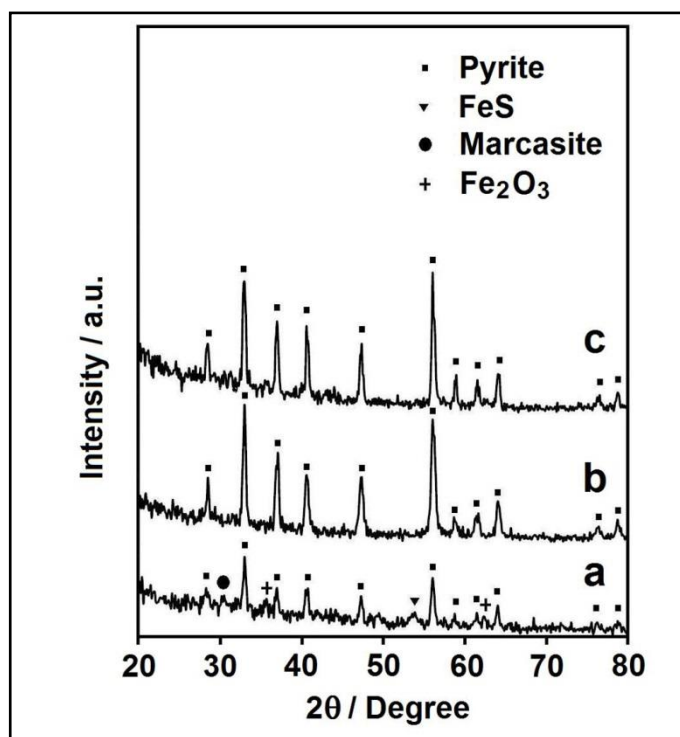


Figure 4.22 XRD patterns of samples D, E and F prepared at 200 °C with different reaction times; (a) 12 h, (b) 24 h and (c) 36 h.

Figure 4.23 (a–c) shows the XRD patterns of samples G, E, and H that were prepared at 200 °C for 24 h with different pH (10, 11 and 12, respectively). The XRD pattern of sample G includes peaks attributed to both the pyrite and marcasite structured  $\text{FeS}_2$ ,  $\text{FeS}$  and  $\text{Fe}_2\text{O}_3$ , indicating that pure pyrite could not be formed at pH 10 (Figure 4.23a). As shown in Figures 4.23b and 4.23c, pure pyrite could be achieved at a high alkaline condition, which is favourable for the formation of the pyrite phase rather than marcasite phase of  $\text{FeS}_2$  (Wang et al., 2010c). The average crystallite size of the samples prepared at pH 11 and 12, calculated using size strain plots method (Tagliente and Massaro, 2008), is  $15 \pm 2$  and  $23 \pm 2$  nm, respectively. The XRD results show that the average crystallite size of the samples increases with the increase in pH.

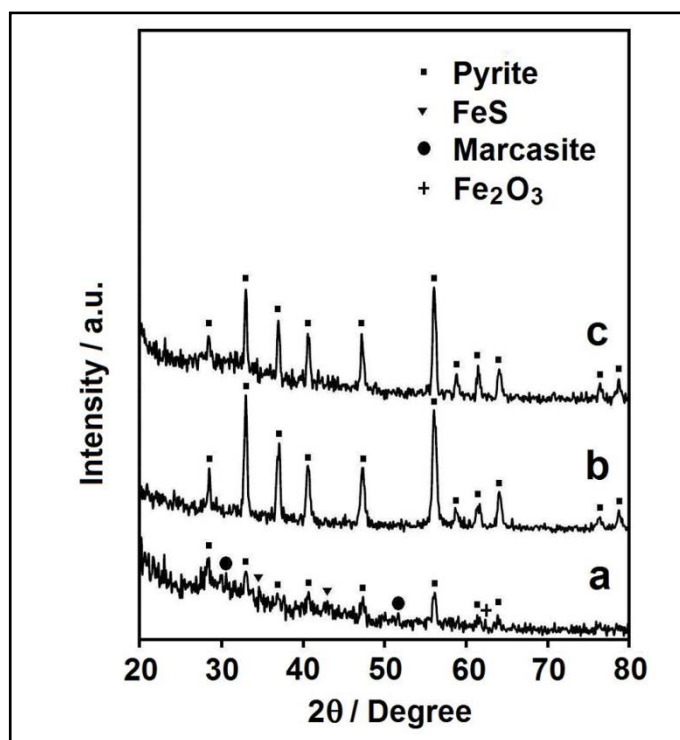


Figure 4.23 XRD patterns of samples G, E and H prepared at 200 °C for 24 h under different pH conditions; (a) 10, (b) 11 and (c) 12.

Figure 4.24 shows the FESEM images of samples prepared at pH 11 (a) and 12 (b). The FESEM images show that the average particle size increases with the increase in pH. Hence, the optimum pH to obtain pure pyrite was 11.

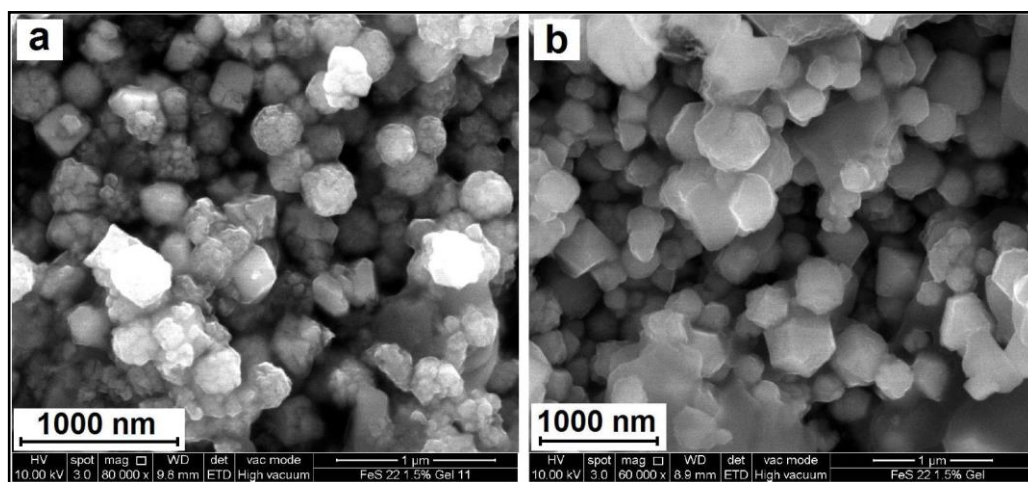


Figure 4.24 FESEM images of samples E and H prepared at 200 °C for 24 h under different pH conditions; (a) 11, (b) 12.

To investigate the effect of gelatin, samples I, J, E and K were prepared at 200 °C for 24 h at a pH of 11 with different concentrations of gelatin (0, 0.8, 1.5 and 2% wt/v,



respectively). As shown in Figure 4.25, the concentration of gelatin affects the shape and size of the particles. The FeS<sub>2</sub> particles, prepared in the low concentration of gelatin (0 and 0.8% wt/v ), are large with an average dimension of more than 1  $\mu\text{m}$  (Figures 4.25a and 4.25b). They are cubic and octahedral in shape. As the concentration of gelatin increased, the particles became spherical while the average size dramatically decreased (Figures 4.25c and 4.25d). This is because gelatin is adsorbed onto the surface of Fe(OH)<sub>2</sub>, which acts as a capping agent, whilst the nucleation of FeS and FeS<sub>2</sub> into seeds occurs. The layer of gelatin limits the diffusion of S<sup>2-</sup> ions, sulphur and H<sub>2</sub>S to the surface of the seeds, thus constraining the growth of FeS<sub>2</sub> within the geometry of the gelatin micelles, resulting in well-formed nanoparticles (Sugimoto et al., 1995, Muramatsu and Sugimoto, 1997).

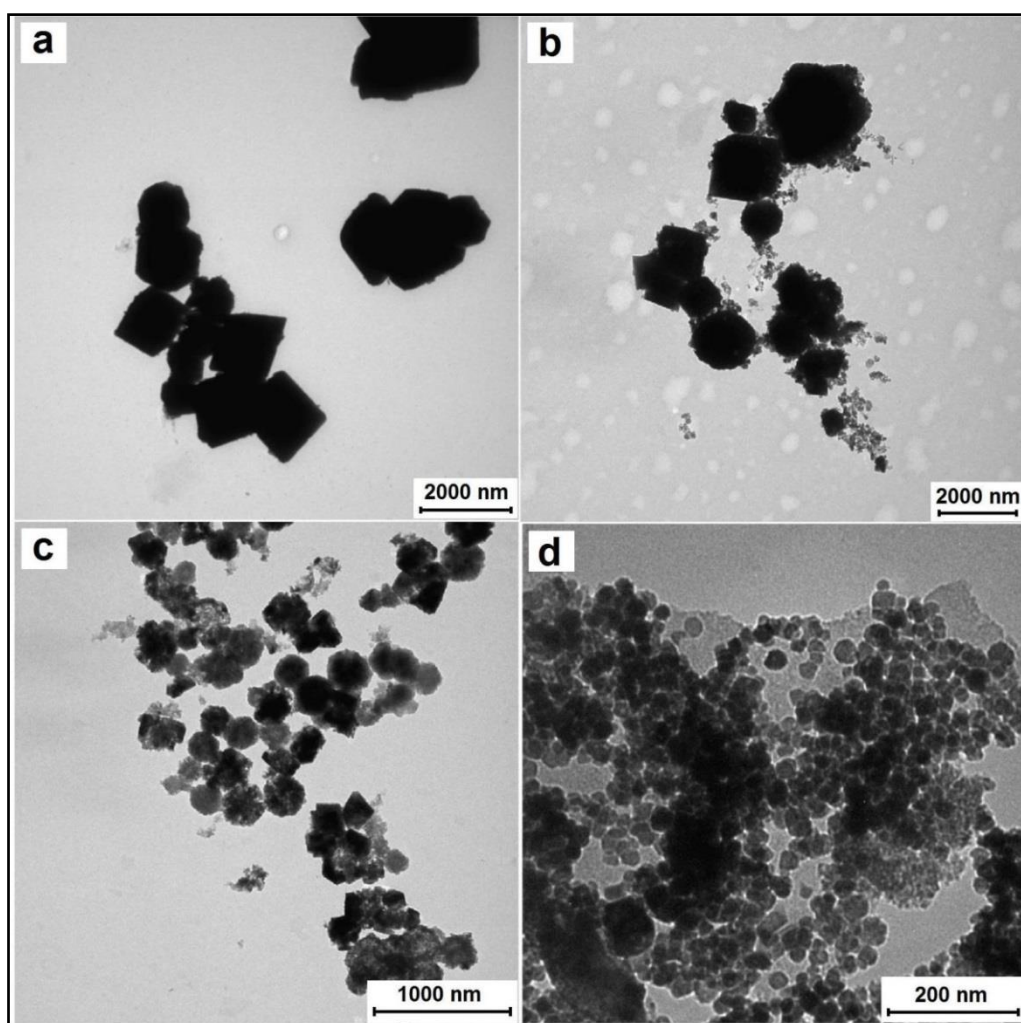


Figure 4.25 TEM images of samples I, J, E and K prepared with different concentrations of gelatin; (a) 0, (b) 0.8, (c) 1.5 and (d) 2% wt/v.

Figure 4.26 shows the XRD pattern of FeS<sub>2</sub> particles with different concentration of gelatin. The XRD results show the peaks related to the FeS<sub>2</sub> (pyrite) were broadened with the increase of gelatin concentration. The average crystallite size of the samples I (without gelatin), J (0.8 % wt/v) and E (1.5 % wt/v), calculated using size strain plot method, is 24±2, 18±2 and 15±2 nm, respectively. The results show that the average crystallite size of the particles is decreased with the increase of gelatin concentration. At a higher concentration of gelatin (>1.5 %wt/v), the XRD pattern of sample K (2.0 % wt/v) did not reflect a pure pyrite structured FeS<sub>2</sub> (Figure 4.26d), even though the reaction happened at the optimized conditions. This is because a high concentration of gelatin restricts the diffusion of S<sup>2-</sup> ions, sulfure and H<sub>2</sub>S to the surface of Fe(OH)<sub>2</sub>, consequently retarding the growth of the FeS and FeS<sub>2</sub> seeds.

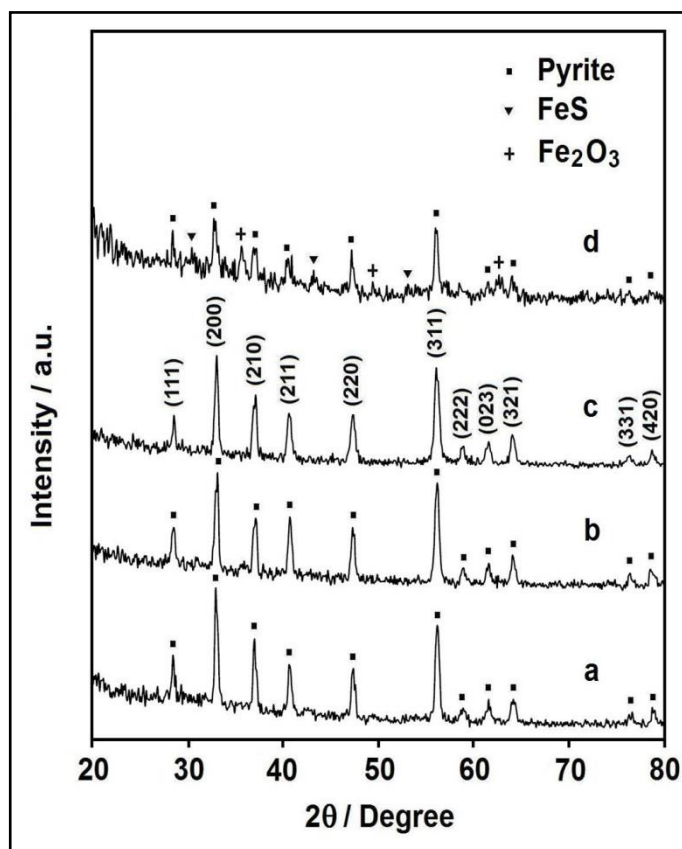


Figure 4.26 XRD pattern of samples I, J, E and K prepared with different concentrations of gelatin; (a) 0, (b) 0.8, (c) 1.5 and (d) 2% wt/v.

### 4.3.2 X-ray diffraction

For the preparation of FeS<sub>2</sub>/rGO nanocomposites, we have utilized the optimum hydrothermal parameters: reaction temperature (200 °C), reaction time (24 h), pH (11) and concentration of gelatin (1.5 wt%). Figure 4.27 shows a comparison of the XRD pattern of pristine GO (a), sample holder of XRD (b), FeS<sub>2</sub> particles (c) and FeS<sub>2</sub> (pyrite)/rGO nanocomposites with different concentrations of GO (d-f). As can be seen in Figure 4.27a, pristine GO has a sharp peak at 10.8° which is related to the (002) interplanar spacing of 0.82 nm. As shown in Figure 4.27b, the XRD pattern of sample holder has a broad hump peak at about 2θ=13°, which can be seen in the XRD pattern of the all samples. The XRD pattern of FeS<sub>2</sub> particles has peaks associated to cubic FeS<sub>2</sub> pyrite (PDF card no: 01-071-0053). As shown in Figure 4.27 (d-f), XRD pattern of the all nanocomposites have peaks associated to cubic FeS<sub>2</sub> pyrite. In addition, the peak related to the GO sheets is disappeared after hydrothermal treatment and a weak peak is appeared at 2θ= 25.8°, which is attributed to the (002) plane of rGO (Wang et al., 2010b, Wang et al., 2011b, Wang et al., 2011a). The plausible reasons are that during hydrothermal process some oxygen-containing functional groups of GO are removed that causes the rGO peak to shift to 2θ= 25.8° and anchored FeS<sub>2</sub> particles can prevent to restacking of rGO nanosheets that causes the intensity of rGO peak to weaken (Willemse et al., 2011, Shen et al., 2011c, Xie et al., 2012).

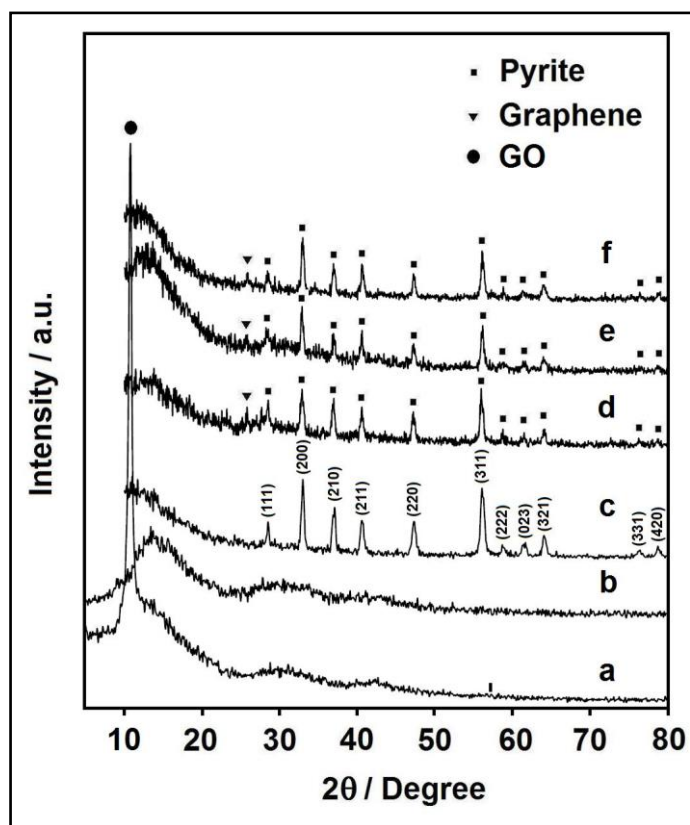


Figure 4.27 XRD pattern of (a) pristine GO, (b) sample holder and samples prepared with different concentrations of GO: (c) without GO (sample E), (d) 0.5, (e) 1 and (f) 2 mg/mL.

### 4.3.3 FTIR spectroscopy

Figures 4.28a and 4.28b show the FTIR spectra of pristine GO and FeS<sub>2</sub> (pyrite)/rGO nanocomposite, respectively. In the FTIR spectrum of GO, the broad peak centered at 3396 cm<sup>-1</sup> is attributed to the O-H stretching vibrations and the peaks at 1731 cm<sup>-1</sup>, 1625 cm<sup>-1</sup>, 1424 cm<sup>-1</sup>, 1218 cm<sup>-1</sup> and 1051 cm<sup>-1</sup> are assigned to C=O stretching, the *sp*<sup>2</sup>-hybridized C=C group, O-H deformation, C-OH stretching and the C-O stretching, respectively (Shen et al., 2011c). In contrast, the peaks at 1731 cm<sup>-1</sup> and 1424 cm<sup>-1</sup> in the FTIR spectrum of FeS<sub>2</sub> (pyrite)/rGO nanocomposite are missing, which indicates the reduction of GO (Ren et al., 2011, Zou et al., 2011b). The broad peak at 3418 cm<sup>-1</sup> in the FTIR spectrum of FeS<sub>2</sub> (pyrite)/rGO nanocomposite might be attributed to the O-H stretching vibration of absorbed water molecules.

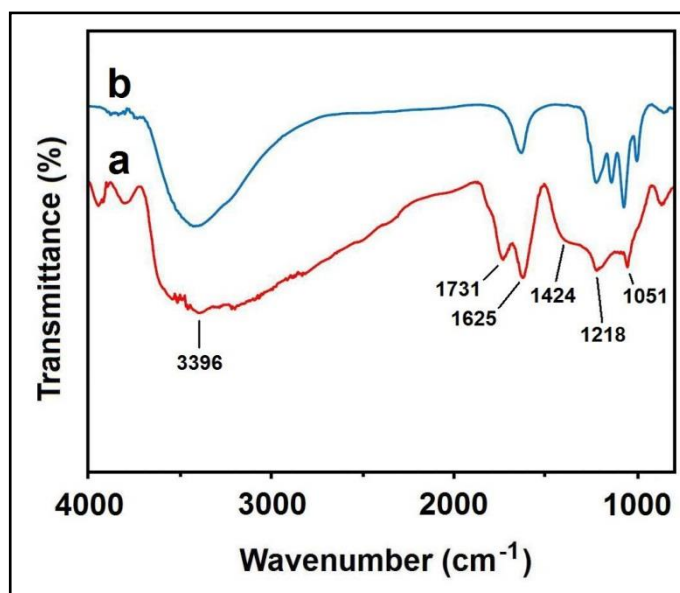


Figure 4.28 FTIR spectra of (a) pristine GO and (b) FeS<sub>2</sub>/rGO nanocomposite (with 1 mg/mL of GO concentration).

#### 4.3.4 Raman spectroscopy

Figures 4.29a and 4.29b show the Raman spectra of pristine GO and the FeS<sub>2</sub> (pyrite)/rGO nanocomposite, respectively. The Raman spectra of GO shows two peaks at 1361 cm<sup>-1</sup> and 1604 cm<sup>-1</sup>, which correspond to the well-known D and G band, respectively. The D band is ascribed to the breathing mode of A<sub>1g</sub> symmetry, involving phonons near the K zone boundary. Meanwhile, the G band is assigned to the E<sub>2g</sub> mode of *sp*<sup>2</sup>-bonded carbon atoms (Ferrari and Robertson, 2000). In comparison to the pristine GO, the Raman spectra of the FeS<sub>2</sub> (pyrite)/rGO nanocomposite shows that the D and G band shifted to lower wave numbers at 1352 cm<sup>-1</sup> and 1583 cm<sup>-1</sup>, respectively. This is because of the reduction of GO after the hydrothermal process (Lambert et al., 2009, Pan et al., 2011, Liu et al., 2012). Moreover, the intensity ratio of I(D)/I(G) for GO and FeS<sub>2</sub> (pyrite)/rGO nanocomposite is 0.95 and 0.71, respectively. Decreasing the I(D)/I(G) intensity ratio of FeS<sub>2</sub> (pyrite)/rGO nanocomposite compare to that of GO can be attributed to the further formation of *sp*<sup>2</sup> bonds and decreasing the defects during the hydrothermal process (Shi et al., 2012, Li et al., 2012b). In addition to the peaks associated with the D and G band of rGO, the Raman spectra of the FeS<sub>2</sub> (pyrite)/rGO

nanocomposite has two sharp peaks at  $341\text{ cm}^{-1}$  and  $376\text{ cm}^{-1}$  and a small peak at  $427\text{ cm}^{-1}$  which are attributed to the  $E_g$ ,  $A_g$ , and  $T_g$  mode of  $\text{FeS}_2$  (pyrite), respectively (inset of Figure 4.29). The  $E_g$  mode corresponds to the vibration of sulphur atoms perpendicular to the dimer axes, whereas the  $A_g$  mode corresponds to the S-S in phase stretching. The  $T_g$  mode is assigned to coupled libration and stretching (Toniazzi et al., 1999, Yuan et al., 2012). Based on the Raman spectroscopy results, we confirm that the  $\text{FeS}_2$  (pyrite)/rGO nanocomposite is composed of rGO nanosheets and pure  $\text{FeS}_2$  (pyrite).

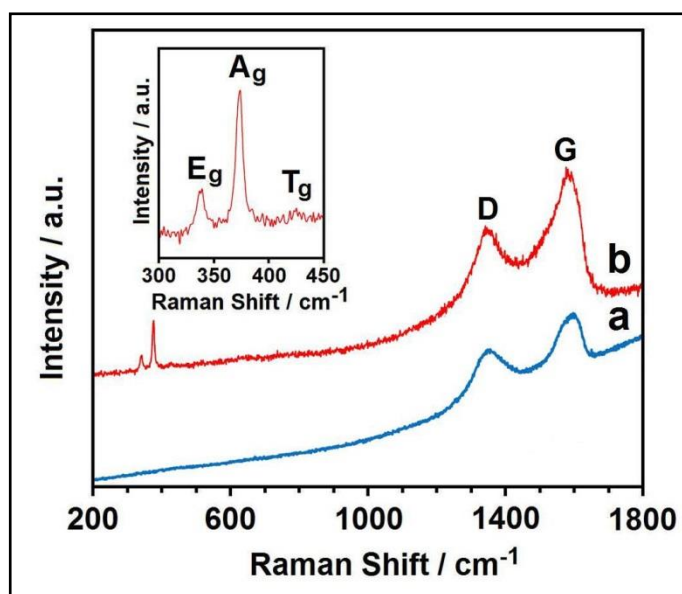


Figure 4.29 Raman spectra of (a) pristine GO and (b)  $\text{FeS}_2$ /rGO nanocomposite (with 1 mg/mL of GO concentration). The inset highlights the miniature peaks of the nanocomposite.

### 4.3.5 Morphology

Figure 4.30 shows the FESEM images of  $\text{FeS}_2$  particles, prepared at the optimum conditions (200 °C, 24 h, pH 11 and gelatin concentration 1.5% wt/v), in the absence and presence of GO. Figure 4.30a shows that the spherical  $\text{FeS}_2$  particles (diameter  $\sim 250\text{ nm}$ ) are made up of many nanoparticles aggregated with one another. Figures 4.30b–4.30d show the FESEM images of  $\text{FeS}_2$  (pyrite)/rGO nanocomposite prepared at different concentrations of GO (0.5, 1 and 2 mg/mL). When the concentration of GO was 0.5 mg/mL (Figure 4.30b), the morphology of the  $\text{FeS}_2$

particles attached to the creased rGO sheets are similar to that of the lone FeS<sub>2</sub> particles (Figure 4.30a). As the GO concentration increased to 1 mg/mL, the number of nanoparticles forming on the surface of rGO increased tremendously while the size of the nanoparticles decreased fivefold (~ 50 nm, as shown in Figure 4.31). One plausible reason is that the surface active sites increased with the increase in the GO concentration, leading to a higher number of nucleation sites. Therefore, the aggregation of nanoparticles into large spherical particles is successfully prohibited. A further increase of the GO concentration to 2 mg/mL gives rise to more uniformly distributed FeS<sub>2</sub> nanoparticles with an average particle size of around 50 nm (Figure 4.30d) and narrow size distribution (Figure 4.31). Without gelatin, large octahedral shaped particles with dimensions in the range of 500 nm are formed alongside the composites (Figure 4.30e). The absence of gelatin leads to two kinetically competing reactions; one is the formation of particles on the surface of the rGO sheets and the other is the formation of particles in the liquid phase. Although 2 mg/mL of GO was used during the synthesis, the particles were largely grown in the liquid phase as there was no encapsulation by the gelatin. This confirms that gelatin plays a decisive role in controlling the size of the nanoparticles as well as stabilizing them on the surface of the rGO sheets.



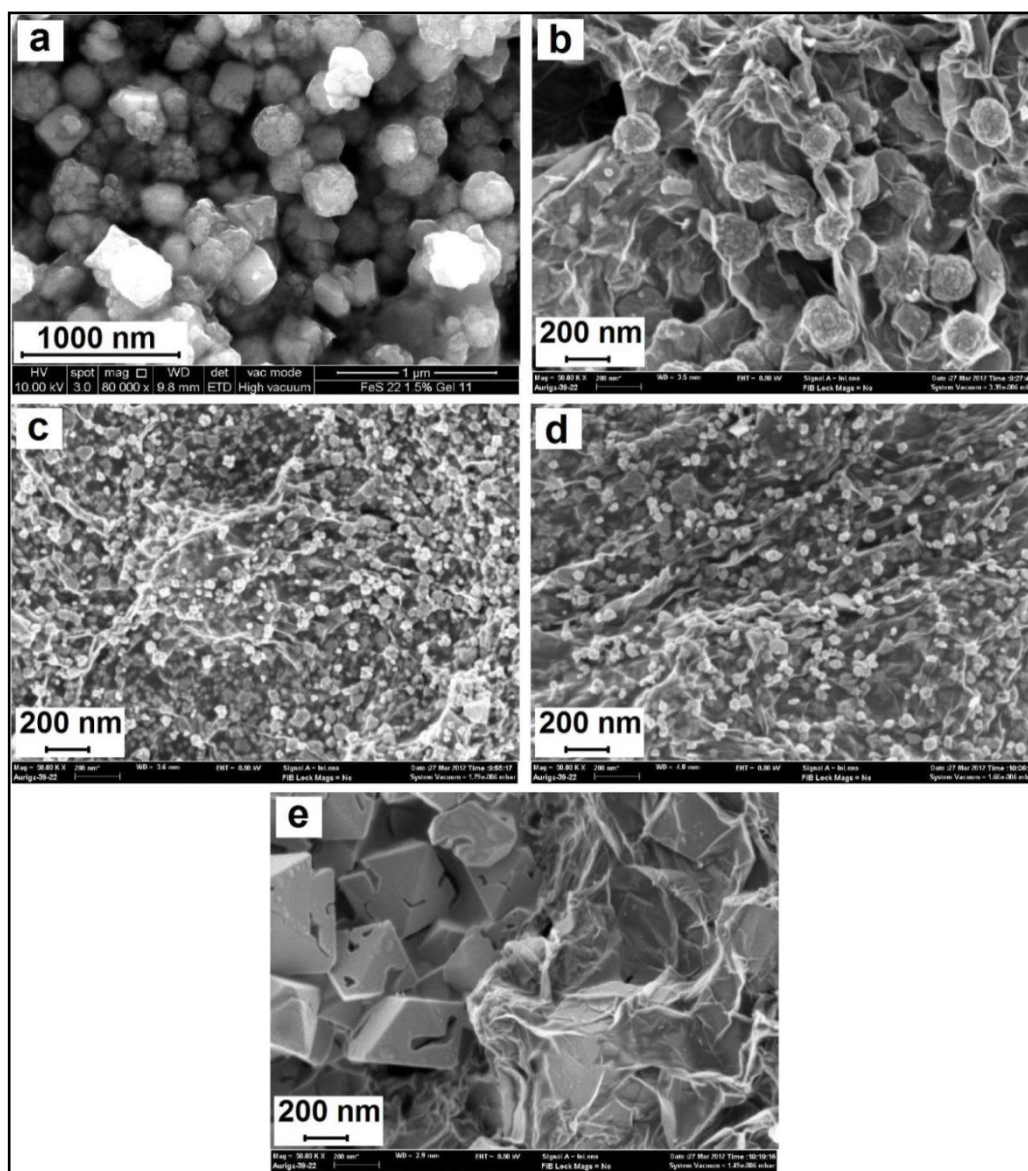


Figure 4.30 FESEM images of samples prepared at the optimum hydrothermal conditions with different concentrations of GO: (a) without GO (sample E), (b) 0.5, (c) 1 and (d) 2 mg/mL. (e) FESEM image of sample prepared at 200 °C for 24 h under pH 11 with 2 mg/mL of GO concentration in the absence of gelatin.

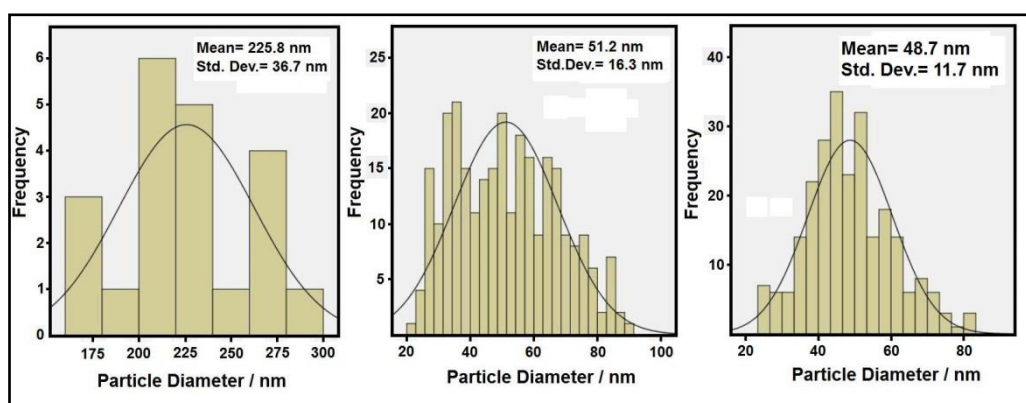
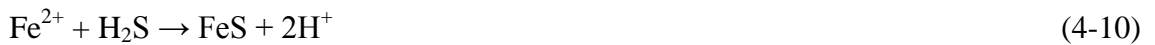


Figure 4.31 Size distribution diagram of  $\text{FeS}_2/\text{rGO}$  nanocomposites with different concentration of GO: (a) 0.5, (b) 1 and (c) 2 mg/mL.



#### 4.3.6 Formation mechanism

The formation mechanism of the FeS<sub>2</sub> (pyrite)/rGO nanocomposite is shown in Figure 4.32. It is well known that dispersed GO sheets in water are highly negatively charged due to the ionization of carboxyl and hydroxyl groups on the surface of GO (Li et al., 2008) (Figure 4.32a). This causes the positively charged Fe<sup>2+</sup> ions to be adsorbed on the negatively charged GO sheets by electrostatic attraction (Figure 4.32b). Then, Fe(OH)<sub>2</sub> particles are formed on the surface of the GO sheets by the presence of NaOH. Finally, the GO and Fe(OH)<sub>2</sub> particles are reduced to graphene and FeS<sub>2</sub> simultaneously by the hydrothermal process (Zhou et al., 2009c) (Figure 4.32c). Moreover the reducing process can be supported by gelatin as the reducing, capping and stabilizing agent (Liu et al., 2011c). The formation of FeS<sub>2</sub> can be proposed based on the reaction of ferrous iron, H<sub>2</sub>O, OH<sup>-</sup> and S as follows (Wang et al., 2010c):



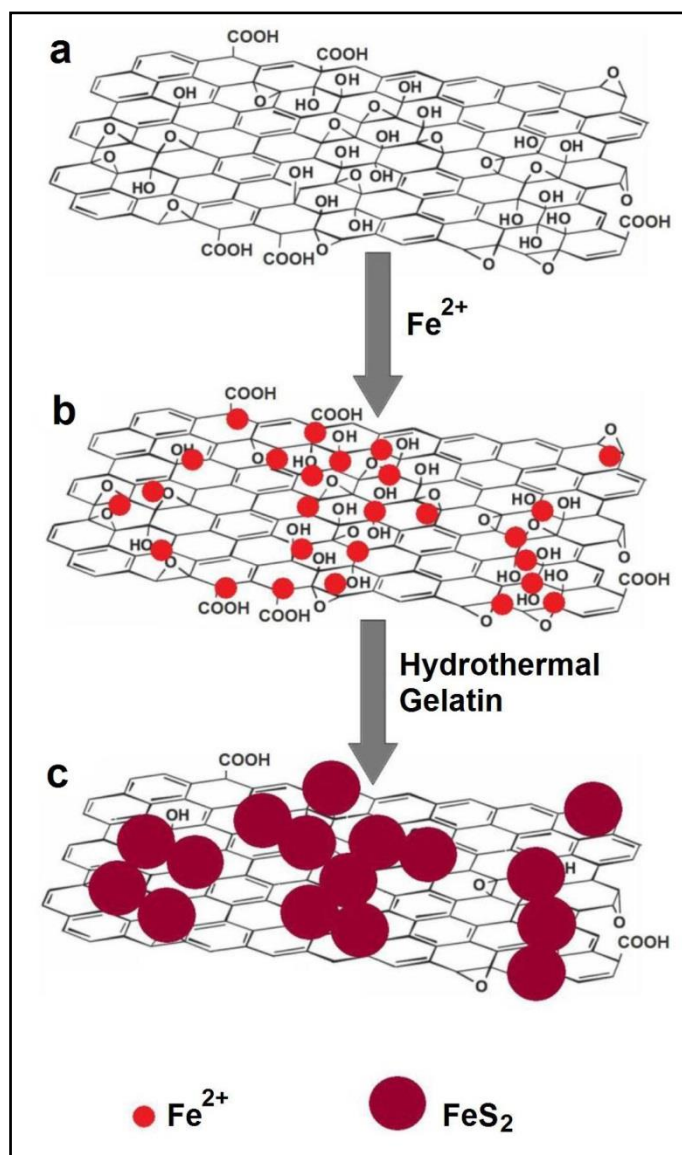


Figure 4.32 Schematic illustration of the formation mechanism of FeS<sub>2</sub>/rGO nanocomposite.

#### 4.3.7 EIS measurment

The capability of electron transfer on the surface of electrodes was investigated using electrochemical impedance spectroscopy. Figure 4.33 shows the Nyquist plots of different electrodes: FeS<sub>2</sub> (a), FeS<sub>2</sub>/rGO nanocompoaites with different GO concentrations consisted of (b) 0.5, (c) 1, (d) 2 mg/mL and together (e) in a 0.1 M KCl containing 1 mM Fe(CN)<sub>6</sub><sup>3-/4-</sup> (1:1). As shown in Figure 4.33, the charge transfer resistance decreases with the introduction of rGO and increasing the amount of rGO. This is because rGO has high electric conductivity and high charge mobility.

The ZSimpWin software is used in the simulations to understand the EIS parameters of electrode/solution interface. Figure 4.34 shows the Bode plots and an excellent agreement between experimental results and the parameters obtained from two equivalent circuit models where the chi-squared ( $\chi^2$ ) is minimised at  $10^{-4}$ . The  $R_s$  ( $R_{ct}C_p$ ) and  $R_s$  [ $Q$  ( $R_{ct}W$ )] equivalent circuit models were used in the simulation of the impedance behaviour of the electrolyte/FeS<sub>2</sub>/ITO and electrolyte/FeS<sub>2</sub>-rGO composites/ITO, from the experimentally obtained impedance data. The  $R_s$  and  $R_{ct}$ , in both equivalent circuits, are the bulk solution resistance of the electrolyte and the charge transfer resistance of the electrodes, respectively. The  $C_p$ ,  $Q$  and  $W$  are pseudocapacitive element, constant phase element (CPE) to account for double-layer capacitance and Warburg element from diffusion impedance, respectively. As can be seen in Figure 4.34 (2), a constant phase element (CPE), instead of a pure capacitor, and a Warburg element ( $W$ ) were introduced during the fitting procedure to obtain a good correlation between the simulated and experimental data. The constant phase element may arise from: (1) distribution of relaxation times as a result of inhomogeneities existing at the electrode/electrolyte interface; (2) porosity; (3) the nature of the electrode; (4) dynamic disorder associated with diffusion. The double layer capacitance of electrode/electrolyte interface can be calculated according to the equation:

$$C = R^{(1-n)/n} Q^{1/n} \quad (4-13)$$

where,  $R$  is the resistance,  $Q$  is the combination of properties related to both the surface and the electroactive species independent of frequency and  $n$  is related to the slope of the  $\log |Z|$  vs.  $\log f$  in the Bode plot. Table 4.4 shows the summary of EIS parameter in the equivalent circuit models for the all of electrodes. The Table 4.4 shows the double layer capacitance increases with the increasing amount of rGO sheets in the composite. The plausible reason is that the inhomogeneities at the electrode/electrolyte interface and dynamic disorder associated with diffusion are increased due to the wrinkles on the

surface of rGO nanosheets. In addition, the Table 4.4 shows W (Warburg element) increases with increasing the amount of rGO. This is because rGO has high permeability for diffusion of active species (Mahmoudian et al., 2012).

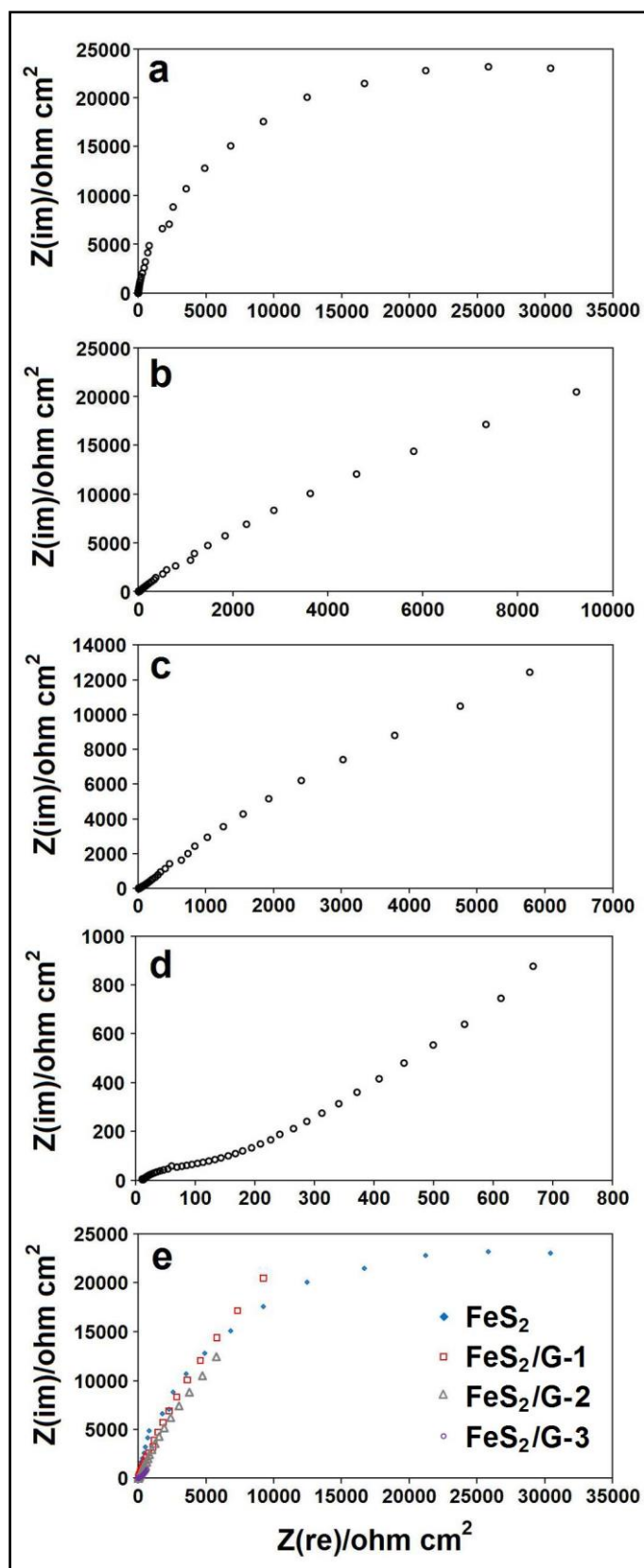


Figure 4.33 Nyquist plots of different electrodes:  $\text{FeS}_2$  (a),  $\text{FeS}_2/\text{rGO}$  nanocomposites with different GO concentrations; (b) 0.5, (c) 1, (d) 2 mg/mL and together (e) in a 0.1 M KCl containing 1 mM  $\text{Fe}(\text{CN})_6^{3-/4-}$  (1:1).

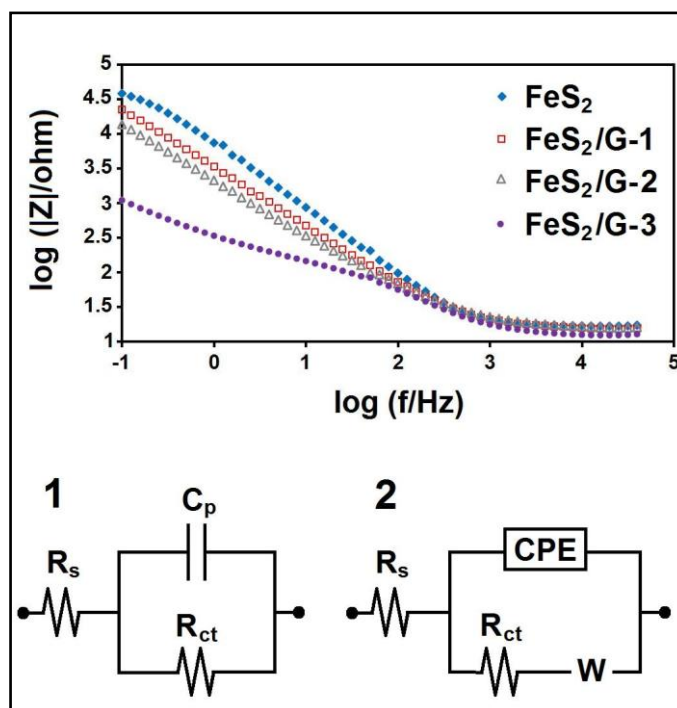


Figure 4.34 Bode plots of different electrodes and the equivalent circuit models of the electrodes that prepared using: (1) FeS<sub>2</sub> particles and (2) FeS<sub>2</sub>/rGO nanocompoaites with different GO concentrations; 0.5, 1, and 2 mg/mL where the chi-squared ( $\chi^2$ ) is minimised at  $10^{-4}$ .

Table 4.4 Electrochemical parameters obtained by simulation of the EIS results of FeS<sub>2</sub> particles and FeS<sub>2</sub>/rGO nanocompoaites with different GO concentrations; 0.5, 1, and 2 mg/mL in 0.1 M KCl solution containing 1 mM Fe(CN)<sub>6</sub><sup>3-/4-</sup> (1:1).

electrode	R <sub>s</sub> (ohm)	R <sub>ct</sub> (kohm)	C <sub>p</sub> (μF)	Q (μF)	C (μF)	W (mSs <sup>1/2</sup> )	n
FeS <sub>2</sub> /ITO	17.22	42.1	18.76	-		-	-
FeS <sub>2</sub> /G-1/ITO	17.1	1.74	-	0.6611e-4	43.7	0.4460e-8	0.8394
FeS <sub>2</sub> /G-2/ITO	16.28	1.74	-	0.1125e-3	71.3	0.4934e-8	0.7816
FeS <sub>2</sub> /G-3/ITO	16.31	0.293	-	0.1525e-2	1051	0.989e-3	0.6843

### 4.3.8 Photocurrent measurement

Figure 4.35 shows the photocurrent response of FeS<sub>2</sub> particles (a) and FeS<sub>2</sub> (pyrite)/rGO nanocomposites with different concentrations of GO (b-d). As can be seen in Figure 4.35, the photocurrent generation is increased with the introduction of rGO nanosheets. The plausible reason is that the photogenerated electrons on the conduction band of FeS<sub>2</sub> particles are trapped by the rGO nanosheets, which can prevent the photogenerated electrons and holes from recombination (Zou et al., 2011a). In addition,

the photocurrent generation of FeS<sub>2</sub> (pyrite)/rGO nanocomposite increases with the increase in the concentration of GO from 0.5 to 1 mg/mL. Further increase in the concentration of GO to 2 mg/mL leads to a decrease in the photocurrent generation. The reason may be that the amount of FeS<sub>2</sub> decreases in the composite, which leads to decrease the photogenerated electrons and holes. Hence, the optimum concentration of GO is 1 mg/mL for the nanocomposite with photocurrent intensity of 1.01  $\mu$ A, which is about 2.6 times higher than that obtained on the pure FeS<sub>2</sub> electrode.

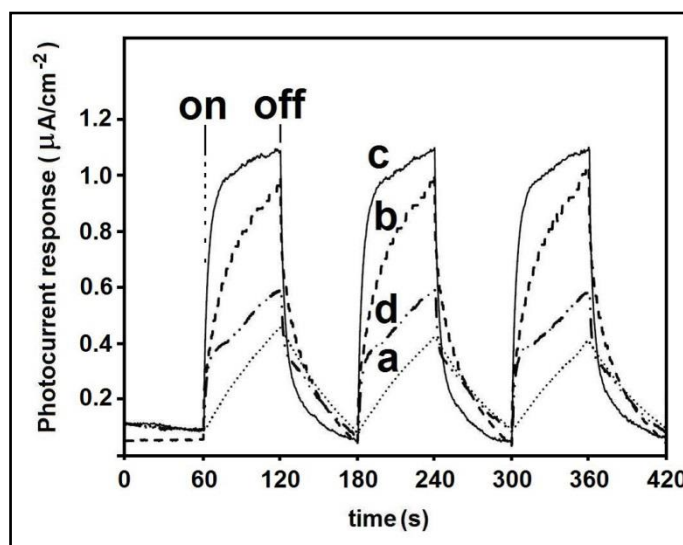


Figure 4.35 Photocurrent response of FeS<sub>2</sub> particles (a) and FeS<sub>2</sub>/rGO nanocomposites with different concentration of GO: (b) 0.5, (c) 1 and (d) 2 mg/mL.

#### 4.4 Sonochemical synthesis of reduced graphene oxide decorated with hierarchical ZnS nanoparticles

In this work, reduced graphene oxide (rGO) decorated with zinc sulphide nanoparticles (ZnSNPs) is synthesized through a simple ultrasonic irradiation of the aqueous solution containing zinc acetate dihydrate ( $\text{Zn}(\text{O}_2\text{CCH}_3)_2(\text{H}_2\text{O})_2$ ), thioacetamide ( $\text{C}_2\text{H}_5\text{NS}$ ) and graphene oxide (GO). The results of X-ray diffraction, Fourier-transform infrared transmission spectroscopy and Raman spectroscopy confirmed the simultaneous formation of cubic-phase ZnSNPs and the reduction of GO through the ultrasonic irradiation process. Field emission scanning electron microscope images showed the size and number density of the nanoparticles could be tuned by

adjusting the amount of the precursors. Transmission electron microscope images show that the spherical ZnS nanoparticles are comprised of small nanoparticles with the average size of ~5 nm aggregated with one another. The result of photoluminescence spectroscopy demonstrated that the incorporation of reduced graphene oxide (rGO) sheets with ZnSNPs suppresses the electron-hole recombination. Hence, a significant enhancement in the photocatalytic degradation of methylene blue (MB) was observed with ZnS/rGO nanocomposite, compare to the bare ZnS particles.

#### 4.4.1 X-ray diffraction analysis

Figure 4.36 shows the XRD patterns of pristine GO (a), sample holder (b) and ZnSNPs-rGO nanocomposites that were prepared by using 2 mL of the solution of zinc acetate dihydrate (2M) at different ultrasonic irradiation times (c–e) (5, 15 and 30 min, respectively). Pristine GO has a sharp peak at  $10.8^{\circ}$  which is assigned to the (002) interplanar spacing of 0.82 nm (Xie et al., 2012). Meanwhile, the XRD pattern of the sample holder has a broad peak at about  $2\theta$  of about  $13^{\circ}$ , which is observed in the XRD patterns of all the samples. As shown in Figure 4.36c, after 5 min of ultrasonic irradiation, a broad peak appears at  $28.85^{\circ}$ , which indicates the formation of ZnS particles in the composite. When the ultrasonic irradiation time increases to 15 minutes, besides the broad peak at  $28.85^{\circ}$ , two small broad peaks appear at  $48.1^{\circ}$  and  $56.75^{\circ}$  which indicates the crystal growth of ZnS particles. All peaks at  $28.85^{\circ}$ ,  $48.1^{\circ}$  and  $56.75^{\circ}$  can be indexed to the (111), (220) and (311) planes of the cubic ZnS (PDF card no: 00-065-0309). The calculated lattice spaces of the (111), (220), and (311) planes are 3.09, 1.89 and 1.62 Å, respectively. By further increasing the ultrasonic irradiation time to 30 min, the intensity of peaks does not change significantly.



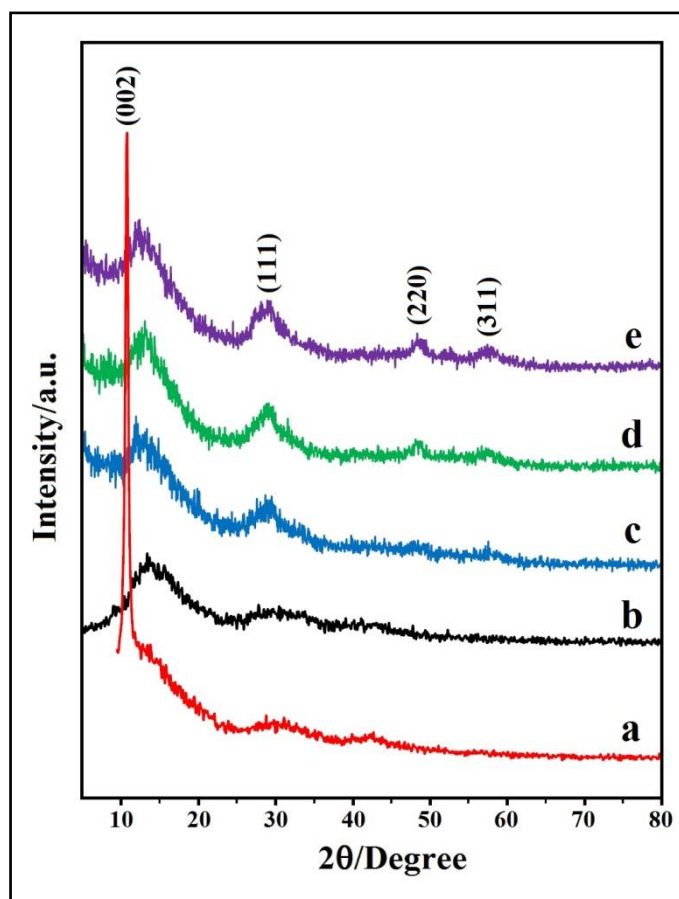


Figure 4.36 XRD patterns of pristine GO (a), sample holder (b), and ZnS/rGO nanocomposites that prepared at different ultrasonic irradiation time: 5 min (c), 15 min (d) and 30 min (e).

Meanwhile, the (002) peak of GO disappeared after the sonication process. This is attributed to the growth of ZnS particles on the surface of the rGO sheets, which prevents the restacking of the rGO sheets (Xie et al., 2012, Teo et al., 2012).

#### 4.4.2 FTIR spectroscopy

Figure 4.37 shows the FTIR spectra of pristine GO (a) and ZnS/rGO nanocomposite (b). For GO, the broad peak centred at  $3233\text{ cm}^{-1}$  is attributed to the O-H stretching vibrations while the peaks at  $1739\text{ cm}^{-1}$ ,  $1627\text{ cm}^{-1}$ ,  $1395\text{ cm}^{-1}$ , and  $1226\text{ cm}^{-1}$  are assigned to C=O stretching,  $sp^2$ -hybridized C=C group and O-H bending, C-OH stretching and C-O-C stretching, respectively (Cheng et al., 2013). In addition, the peaks at  $1170\text{ cm}^{-1}$  and  $1047\text{ cm}^{-1}$  can be attributed to C-O vibration of epoxy or alkoxy groups (Pham et al., 2011). For the ZnS/rGO nanocomposite, the peak at  $1556\text{ cm}^{-1}$  is

assigned to the  $sp^2$ -hybridized C=C group. The peak at  $1739\text{ cm}^{-1}$  for GO is absent for ZnS/rGO nanocomposite and the intensity of the peaks, related to the oxygen-containing groups, decreases for ZnS/rGO composites, which indicates the reduction of GO during the ultrasonic irradiation process.

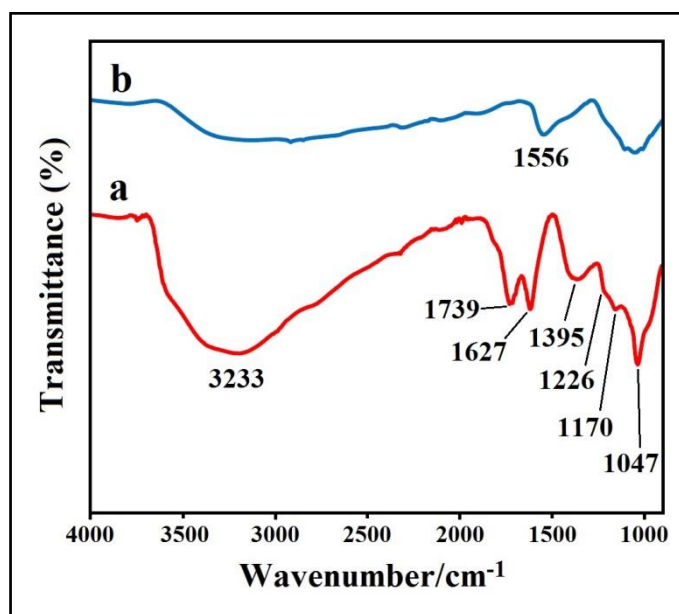


Figure 4.37 FTIR spectra of pristine GO (a), and ZnS/rGO nanocomposite (b).

#### 4.4.3 Raman spectroscopy

Figure 4.38 shows the Raman spectra for pristine GO (a) and the ZnS/rGO nanocomposite (b). The Raman spectra of GO shows two peaks at  $1350$  and  $1608\text{ cm}^{-1}$ , which correspond to the well-known D and G band, respectively. The D band is assigned to the breathing mode of  $A_{1g}$  symmetry involving phonons near the K zone boundary. Meanwhile, the G band is assigned to the  $E_{2g}$  mode of  $sp^2$ -bonded carbon atoms (Ferrari and Robertson, 2000). In comparison to the pristine GO, the Raman spectra of the ZnS/rGO nanocomposite shows that the D and G band shifted to lower wave numbers at  $1344$  and  $1600\text{ cm}^{-1}$ , respectively. This is because of the reduction of GO during ultrasonic irradiation process (Lambert et al., 2009, Liu et al., 2012). Moreover, Figure 4.38 shows the intensity ratio of  $I(D)/I(G)$  of ZnS/rGO nanocomposite increased to a slightly higher value of 1.04 than that of GO (0.92),

which indicates the formation of more numerous of the in-plane  $sp^2$  domains with a smaller average size.

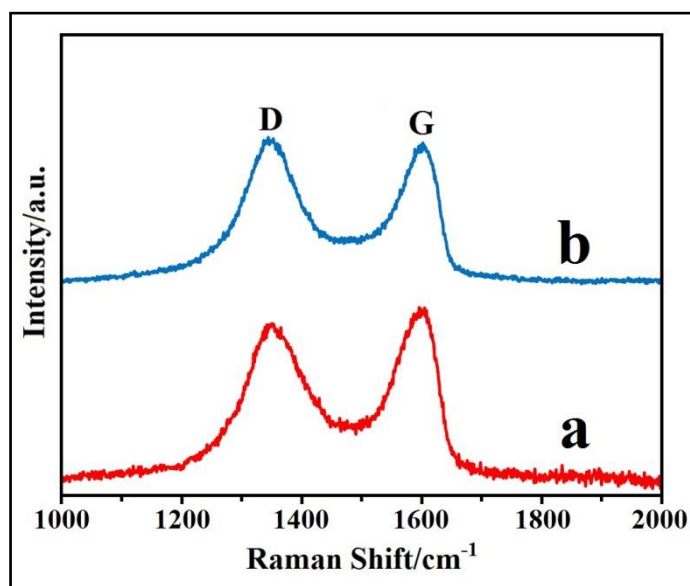


Figure 4.38 Raman spectra of pristine GO (a), and ZnS/rGO nanocomposite (b).

#### 4.4.4 Morphology study

Figure 4.39 illustrates the representative FESEM images and size distribution diagrams of ZnS/rGO nanocomposites prepared by using the solution with GO (1.0 mg/mL) and different amount of zinc acetate dihydrate 0.4 mM (a and b), 0.8 mM (c and d), 1.2 mM (e and f) and 1.6 mM (g and h), and ZnS particles (i and j). When zinc acetate with the amount of 0.4 mM used for preparation of the nanocomposite, as shown in Figure 4.39a and 4.39b, ZnS nanoparticles with the mean size of 33.3 nm and low number density were generated on the surface of reduced graphene oxide due to plenty of residual oxygen containing groups on the surface of GO. In addition, Figure 4.39a illustrates that some ZnS nanoparticles were out of focus, meaning that the ZnS nanoparticles were located on the both sides of rGO sheets and the rGO sheets were rough with wrinkles, or on the surface of bottom layer rGO sheets. As shown in Figure 4.39, when the amount of zinc acetate increases from 0.4 mM to 1.2 mM, the mean size of ZnS nanoparticles is slightly increased from 33.3 nm to 40.5 nm, but the number density of ZnS nanoparticles is increased significantly. This is because the  $Zn^{2+}$  ions

prefer to adsorb onto the surface of GO and produce the new initial nucleation sites due to enough residual oxygen containing groups on the surface of GO nanosheets, instead of absorption to the preformed ZnS nanoparticles to form larger ZnS nanoparticles. By further increase of zinc acetate to 1.6 mM, the average size of ZnS nanoparticles is increased significantly, which indicates the absorption of the excess  $\text{Zn}^{2+}$  ions to the preformed ZnS nanoparticles to form larger nanoparticles due to less free residual oxygen containing groups. As shown in Figure 4.39i and 4.39j, the ZnS particles with the mean size of 142.4 nm were obtained and stacked randomly with together in the absence of GO. This indicates the rGO nanosheets play an important role to assist the growth and dispersion of ZnS nanoparticles on its surface, which prevents the aggregation of the ZnS nanoparticles.

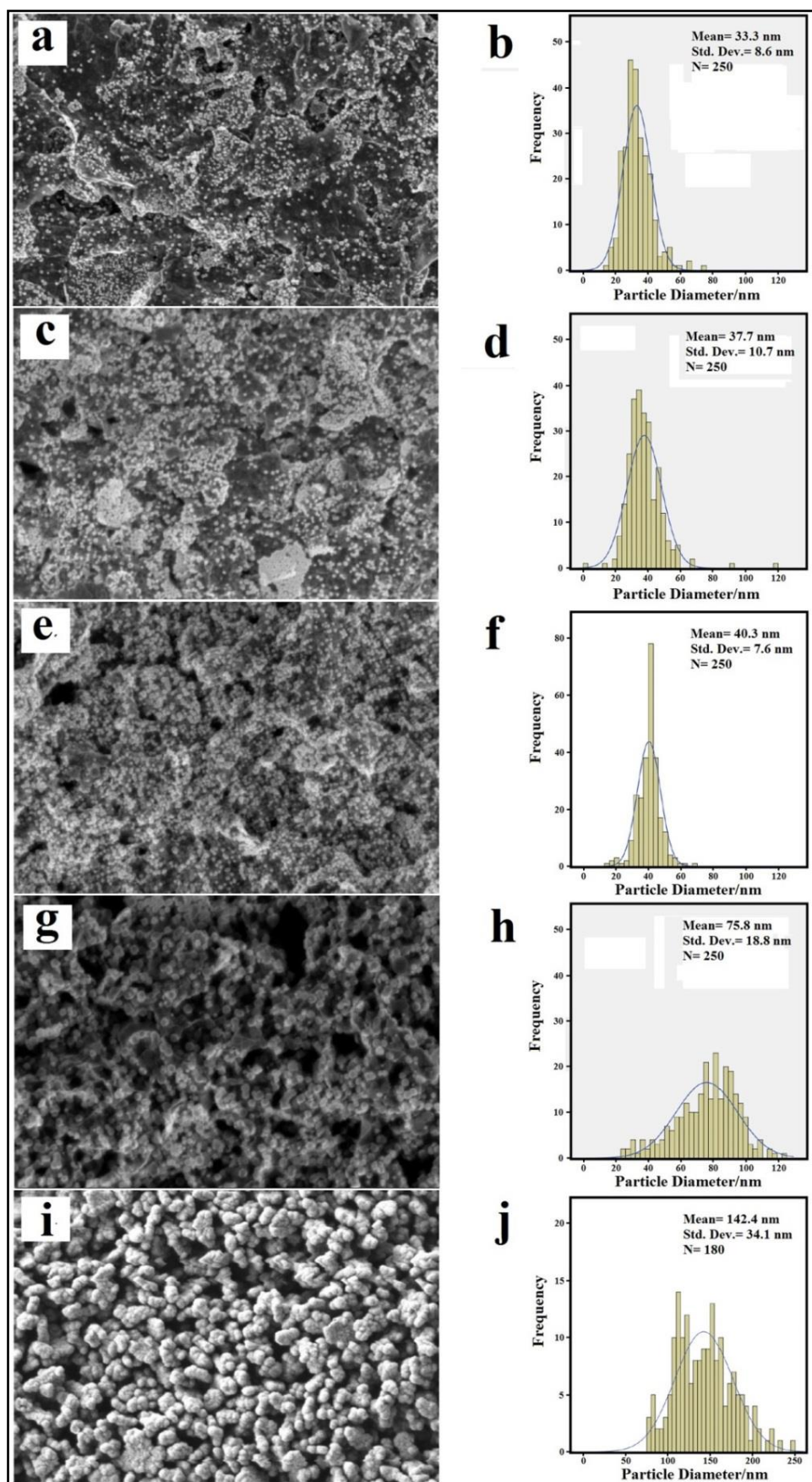


Figure 4.39 FESEM images and size distribution diagrams of ZnS/rGO nanocomposites prepared by using the solution with GO (1.0 mg/mL) and different amount of zinc acetate dehydrate 0.4 mM (a and b), 0.8 mM (c and d), 1.2 mM (e and f) and 1.6 mM (g and h), and ZnS particles (i and j).



The structure of ZnS/rGO nanocomposite was further analyzed by HRTEM. Figure 4.40 shows low and high resolution TEM images of ZnS/rGO nanocomposite. A rGO sheet can be clearly observed with typical wrinkles, which the ZnS nanoparticles with the spherical shape anchor on its surface. Figure 4.40 b shows that the spherical ZnS nanoparticles are comprised of many small nanoparticles with the average size of ~5 nm aggregated with one another. Figure 4.40c shows the HRTEM image of a ZnS nanoparticle anchored on the surface of rGO sheet. The measured lattice fringe spaces of 0.31 and 0.19 nm are attributed to the (111) and (220) planes of ZnS, respectively, which are in agreement to the cubic ZnS (PDF card no: 00-065-0309).

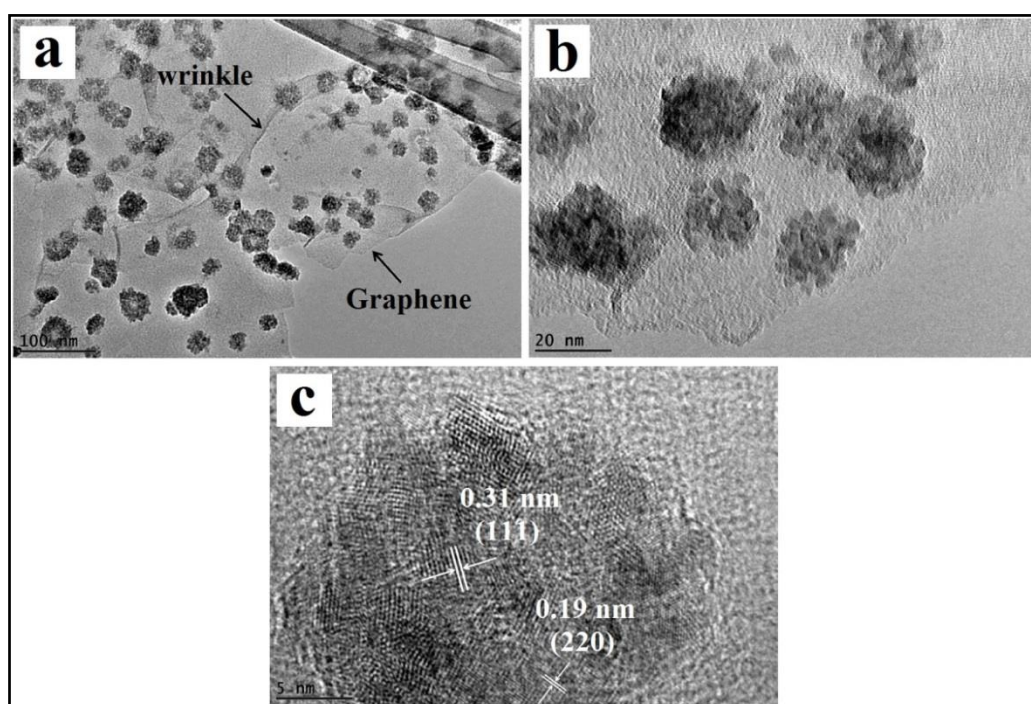


Figure 4.40 TEM mages of ZnS/rGO nanocomposite at different magnifications.

#### 4.4.5 Photoluminescence study

Figure 4.41 shows the room temperature photoluminescence spectrum of ZnS particles (a) and ZnS/rGO nanocomposite (b). The photoluminescence spectrum of ZnS particles exhibits weak shoulders around 416 nm and 445 nm, and broad peaks at 540 nm and 575 nm. These shoulders and peaks may be related to the point defects, which can serve as luminescent sites. The point defects, which can be presented in ZnS

particles, are sulphur vacancies, zinc vacancies, interstitial sulphur atoms and interstitial zinc atoms. The blue emission shoulders at 416 nm and 445 nm are attributed to transition from conduction band to the energy level of interstitial sulphur atoms and zinc vacancies, respectively (Denzler et al., 1998). The green emission peak at 540 nm can be attributed to transition between the energy level of sulphur vacancies and interstitial sulphur atoms (Wang et al., 2011f). The orange emission peak at 575 nm could be associated with transition between the energy level of interstitial zinc atoms and zinc vacancies. The photoluminescence spectrum of ZnS/rGO nanocomposite demonstrates that after the incorporation of ZnS nanoparticles with rGO sheets, the photoluminescence emission of ZnS nanoparticles was significantly quenched. This indicates that after the incorporation, the photogenerated electron-hole pairs in ZnS nanoparticles could be efficiently separated through the transfer of electrons from the conduction band of ZnS nanoparticles (-3.65 eV vs. vacuum) to rGO sheets (with work function of about -4.5 eV vs. vacuum) and thus suppresses the electron-hole recombination (Kumar et al., 2011).

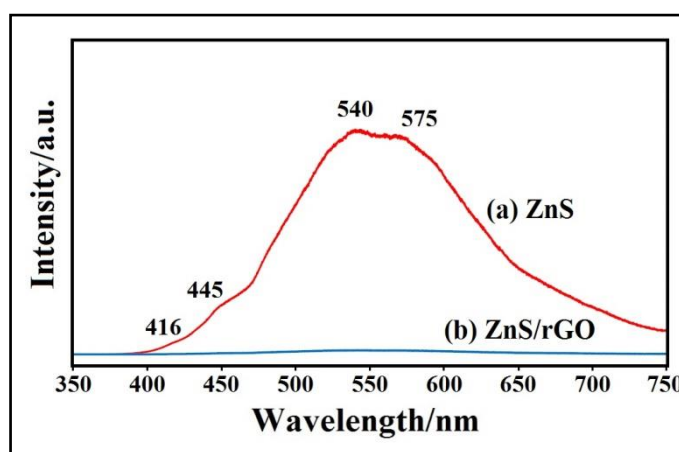


Figure 4.41 Room temperature photoluminescence spectra of pure ZnS (a), and ZnS/rGO nanocomposite (b).

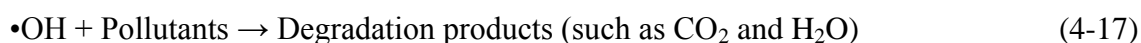
#### 4.4.6 Photocatalytic activity

The photocatalytic activity of ZnS particles and the ZnS/rGO nanocomposites was measured by liquid-phase degradation of methylene blue (MB) under ultraviolet

light (UV) irradiation at ambient temperature. Figure 4.42a illustrates the absorption spectra of MB aqueous solution in the presence of ZnS/rGO-1.2 nanocomposite under UV light irradiation for different interval times. It can be easily observed that the intensity of the absorption peak of MB at 663 nm decreases with the increase of UV light irradiation time, which indicates the degradation of MB molecules by the photocatalytic phenomena. Figure 4.42b shows comparison of photocatalytic activity of pure ZnS particles and ZnS/rGO nanocomposites that prepared with different amount of zinc acetate dehydrate as precursor of zinc ions. As can be seen in Figure 4.42b, pure ZnS particles has low photocatalytic activity in comparison with the ZnS/rGO nanocomposites. The high photocatalytic activity of the composites could be explained by the following causes. MB molecules can be adsorbed onto the surface of rGO with offset face-to-face orientation *via*  $\pi$ - $\pi$  conjugation between MB and the aromatic regions of rGO, which increases the adsorptivity of MB compare to the bare ZnS and it is an important prerequisite to obtain a good photocatalytic activity (Zhang et al., 2009a). To show the effect of the rGO on the adsorption of MB in composite, the UV-vis absorption spectra of MB in dark condition was monitored, as shown in Figure 4.43. It can be easily seen after equilibrium in the dark for 15 min, most MB molecules (ca. 90%) remained in the solution with pure ZnS as catalyst, whereas a large amount of MB molecules was adsorbed on the surface of ZnS/rGO nanocomposites. Meanwhile, Figure 4.43 shows the adsorption of MB molecules increases with the increase of rGO in the composite. In general, when a semiconductor is illuminated with photons electrons in the valance band of the semiconductor are excited into the conduction band, resulting the generation of electron-hole pairs. These electron-hole pairs either recombine or migrate to the surface of photocatalyst to initiate a series of photocatalytic reactions and produce hydroxyl radicals,  $\bullet\text{OH}$  and superoxide radicals,  $\bullet\text{O}_2^-$  in water, resulting the



generation of hydrogen gas and degradation of organic pollutants, which is summarized by the following equations (Xiang et al., 2012).



The drawback of the most of the photocatalysts such as ZnS is the rapid electron-hole recombination within photocatalysts, which decreases the efficiency of their photocatalytic activity. As discussed in photoluminescence study, rGO can trap the photogenerated electrons from the conduction band of ZnS and transfers them through its surface, which suppresses the electron-hole recombination and thus enhances the photocatalytic activity of the ZnS/rGO nanocomposite. Finally, the size of ZnS particles in the composites is smaller than the pure ZnS particles, leading to the higher surface area of photocatalyst and thus improves the photocatalytic activity of the ZnS/rGO nanocomposite.

In addition, the photocatalytic activity of the ZnS/rGO nanocomposite increases with the increase in the initial amount of zinc acetate dehydrate, which uses as precursor of zinc ions, from 0.4 to 1.2 mM. The plausible reason is that the amount of ZnS increased in the composite, resulting in the increase of photogenerated electron-hole pairs. Further increase in the initial amount of zinc acetate dehydrates to 1.6 mM leads to a decrease in the photocatalytic activity of the ZnS/rGO nanocomposite. The reason may be due to the fact that the size of the ZnS nanoparticles increased, which decreases the active surface area of the nanoparticles and therefore, decreases the photocatalytic activity.

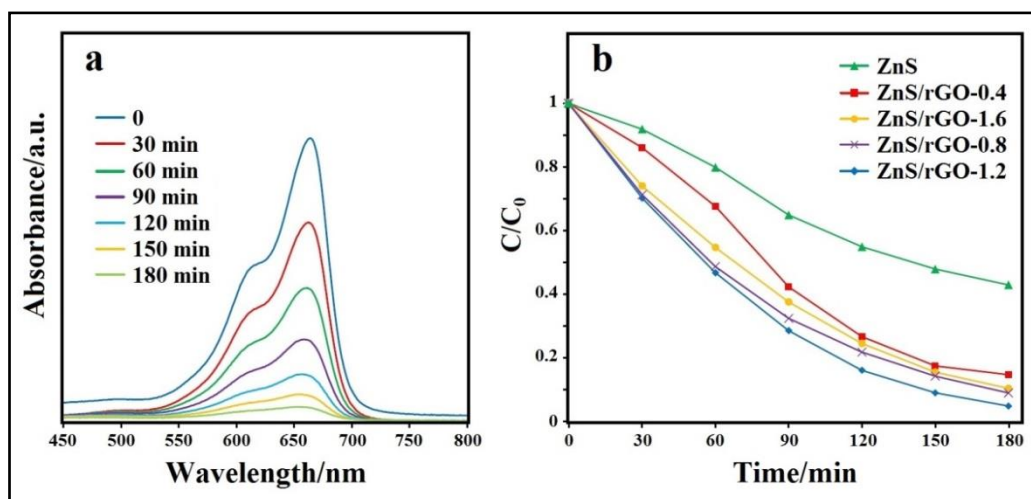


Figure 4.42 Photocatalytic activity: (a) UV-vis absorption spectra of MB aqueous solution at different time in the presence of ZnS/rGO-1.2 as photocatalyst and (b) photodegradation rate of MB at different interval times in the presence of various photocatalysts.

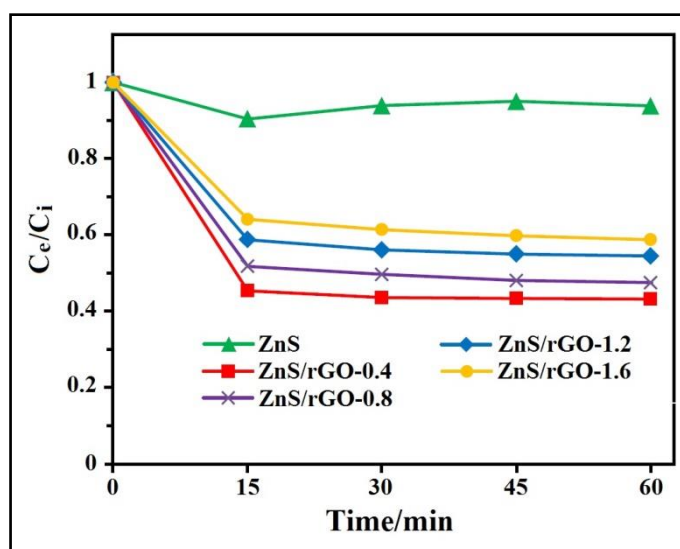


Figure 4.43 Adsorption-desorption equilibrium rate of MB in dark condition versus time in the presence of various photocatalysts.

## CHAPTER V: CONCLUSIONS

In this thesis, electrochemical deposition, hydrothermal and sonochemical methods have been used and developed as low cost, simple, environmentally-friendly without using toxic stabilizing, capping or reducing agents to synthesize different rGO-based nanocomposites, includes Ag/rGO/ITO, Ag/rGO, FeS<sub>2</sub>/rGO and ZnS/rGO for different potential applications. Several conclusions can be drawn from these works.

Silver-nanoparticle (AgNP)-decorated reduced graphene oxide (rGO) was successfully electrodeposited on ITO coated glass slides by a CV method without using any reducing agent. It was established that the silver ammonia complex was the key component to achieving well-distributed AgNPs with small and narrow size distribution decorated on reduced graphene oxide sheets. The as prepared electrode exhibited notable electrocatalytic activity for the reduction of H<sub>2</sub>O<sub>2</sub>, leading to an enzymeless electrochemical sensor with a linear detection range of 0.1 mM to 100 mM (with regression value of  $R^2 = 0.9992$ ) while the limit of detection was estimated to be 5  $\mu$ M. Our method essentially provides an easy, one-step, environmentally-friendly and cost-effective fabrication of AgNPs-rGO/ITO electrodes as an enzymeless electrochemical sensor of hydrogen peroxide.

Ultrasonic irradiation of the aqueous solution containing silver ammonia complex (Ag(NH<sub>3</sub>)<sub>2</sub>OH) and graphene oxide (GO) is a simple strategy in producing rGO uniformly decorated with ultrafine AgNPs of narrow size distribution and does not require the use of any stabilizing or reducing agents. It is established that the silver ammonia complex is the key to the successful synthesis of well-formed composites. The particle size of AgNPs embedded on the rGO sheets can be easily tuned by adjusting the ultrasonic radiation time. The modified glassy carbon electrode by using resultant composite exhibited electrocatalytic activity for the reduction of H<sub>2</sub>O<sub>2</sub>, leading to an enzymeless electrochemical sensor with a linear detection range of 0.1 mM to 70 mM

(with regression value of  $R^2 = 0.9992$ ) while the limit of detection was estimated to be 4.3  $\mu\text{M}$ . Furthermore, the prepared AgNPs-rGO composite was employed for the spectral detection of  $\text{Hg}^{2+}$  ions and showed a detection limit of 20 nM.

$\text{FeS}_2$  (pyrite)/rGO nanocomposite was successfully synthesized using a facile ‘one-pot’ hydrothermal method at the optimum conditions of 200  $^\circ\text{C}$ , 24 h, pH 11, 1.5% wt/v of gelatin and 2 mg/mL of GO concentration. The gelatin is an important ingredient in the preparation of the  $\text{FeS}_2$  (pyrite)/rGO nanocomposites. With the increase in the GO concentration, the size of the  $\text{FeS}_2$  particles decreased fivefold to  $\sim 50$  nm and the nanoparticles were uniformly distributed on the surface of the rGO sheets. The  $\text{FeS}_2$ /rGO nanocomposites serve as a highly potential material for the conversion of solar energy based on the enhanced photocurrent response.

Reduced graphene oxide (rGO) decorated with zinc sulphide nanoparticles (ZnSNPs) was successfully synthesized by using a one-pot sonochemical synthesis method without using any stabilizing, capping or reducing agents. The particle size and number density of ZnSNPs anchored on the surface of rGO sheets can be easily tuned by adjusting the amount of the precursors. It is established that the reduced graphene oxide sheets play important roles in different ways to enhance the photocatalytic efficiency of the ZnS/rGO nanocomposite as compared to the bare ZnS, which can be explained by the following reasons: 1) the prevention of the ZnSNPs agglomeration, leading the growth of small nanoparticles on its surface and achieving the higher active surface area, 2) the increasing of the adsorption of MB molecules, and 3) the suppression of electron-hole recombination.

## REFERENCES

- ABDEL-MOHSEN, A. M., HRDINA, R., BURGERT, L., KRYLOVÁ, G., ABDEL-RAHMAN, R. M., KREJČOVÁ, A., STEINHART, M. & BENEŠ, L. 2012. Green synthesis of hyaluronan fibers with silver nanoparticles. *Carbohydrate Polymers*, 89, 411-422.
- AN, S. J., ZHU, Y., LEE, S. H., STOLLER, M. D., EMILSSON, T., PARK, S., VELAMAKANNI, A., AN, J. & RUOFF, R. S. 2010. Thin Film Fabrication and Simultaneous Anodic Reduction of Deposited Graphene Oxide Platelets by Electrophoretic Deposition. *The Journal of Physical Chemistry Letters*, 1, 1259-1263.
- AN, X., YU, J. C., WANG, Y., HU, Y., YU, X. & ZHANG, G. 2012. WO<sub>3</sub> nanorods/graphene nanocomposites for high-efficiency visible-light-driven photocatalysis and NO<sub>2</sub> gas sensing. *Journal of Materials Chemistry*, 22, 8525-8531.
- ANANDAN, S., MANIVEL, A. & ASHOKKUMAR, M. 2012. One-Step Sonochemical Synthesis of Reduced Graphene Oxide/Pt/Sn Hybrid Materials and Their Electrochemical Properties. *Fuel Cells*, 12, 956-962.
- B, K. A. 2001. Electronic transport properties of conducting polymers and carbon nanotubes. *Reports on Progress in Physics*, 64, 1.
- BAE, S., KIM, H., LEE, Y., XU, X., PARK, J.-S., ZHENG, Y., BALAKRISHNAN, J., LEI, T., RI KIM, H., SONG, Y. I., KIM, Y.-J., KIM, K. S., OZYILMAZ, B., AHN, J.-H., HONG, B. H. & IJIMA, S. 2010. Roll-to-roll production of 30-inch graphene films for transparent electrodes. *Nat Nano*, 5, 574-578.
- BAI, S. & SHEN, X. 2012. Graphene-inorganic nanocomposites. *RSC Advances*, 2, 64-98.
- BAI, S., SHEN, X., ZHU, G., XU, Z. & LIU, Y. 2011. Reversible phase transfer of graphene oxide and its use in the synthesis of graphene-based hybrid materials. *Carbon*, 49, 4563-4570.
- BALANDIN, A. A., GHOSH, S., BAO, W., CALIZO, I., TEWELDEBRHAN, D., MIAO, F. & LAU, C. N. 2008. Superior Thermal Conductivity of Single-Layer Graphene. *Nano Letters*, 8, 902-907.
- BANG, J. H. & SUSLICK, K. S. 2010. Applications of Ultrasound to the Synthesis of Nanostructured Materials. *Advanced Materials*, 22, 1039-1059.
- BECERRIL, H. A., MAO, J., LIU, Z., STOLTENBERG, R. M., BAO, Z. & CHEN, Y. 2008. Evaluation of Solution-Processed Reduced Graphene Oxide Films as Transparent Conductors. *ACS Nano*, 2, 463-470.
- BERGER, C., SONG, Z., LI, X., WU, X., BROWN, N., NAUD, C., MAYOU, D., LI, T., HASS, J., MARCHENKOV, A. N., CONRAD, E. H., FIRST, P. N. & DE HEER, W. A. 2006. Electronic Confinement and Coherence in Patterned Epitaxial Graphene. *Science*, 312, 1191-1196.

- BIN, X., CHEN, J., CAO, H., CHEN, L. & YUAN, J. 2009. Preparation of graphene encapsulated copper nanoparticles from CuCl<sub>2</sub>-GIC. *Journal of Physics and Chemistry of Solids*, 70, 1-7.
- BLAKE, P., BRIMICOMBE, P. D., NAIR, R. R., BOOTH, T. J., JIANG, D., SCHEDIN, F., PONOMARENKO, L. A., MOROZOV, S. V., GLEESON, H. F., HILL, E. W., GEIM, A. K. & NOVOSELOV, K. S. 2008. Graphene-Based Liquid Crystal Device. *Nano Letters*, 8, 1704-1708.
- BOURLINOS, A. B., GOURNIS, D., PETRIDIS, D., SZABÓ, T., SZERI, A. & DÉKÁNY, I. 2003. Graphite Oxide: Chemical Reduction to Graphite and Surface Modification with Primary Aliphatic Amines and Amino Acids. *Langmuir*, 19, 6050-6055.
- BRODIE, B. C. 1859. On the Atomic Weight of Graphite. *Philosophical Transactions of the Royal Society of London*, 149, 249-259.
- CAMPBELL, F. W., BELDING, S. R., BARON, R., XIAO, L. & COMPTON, R. G. 2009. Hydrogen Peroxide Electroreduction at a Silver-Nanoparticle Array: Investigating Nanoparticle Size and Coverage Effects. *The Journal of Physical Chemistry C*, 113, 9053-9062.
- CAO, A., LIU, Z., CHU, S., WU, M., YE, Z., CAI, Z., CHANG, Y., WANG, S., GONG, Q. & LIU, Y. 2010. A Facile One-step Method to Produce Graphene-CdS Quantum Dot Nanocomposites as Promising Optoelectronic Materials. *Advanced Materials*, 22, 103-106.
- CAO, Y., LI, X., AKSAY, I. A., LEMMON, J., NIE, Z., YANG, Z. & LIU, J. 2011. Sandwich-type functionalized graphene sheet-sulfur nanocomposite for rechargeable lithium batteries. *Physical Chemistry Chemical Physics*, 13, 7660-7665.
- CARUSO, R. A., ASHOKKUMAR, M. & GRIESER, F. 2002. Sonochemical Formation of Gold Sols. *Langmuir*, 18, 7831-7836.
- CHANDRA, S., BAG, S., BHAR, R. & PRAMANIK, P. 2011. Sonochemical synthesis and application of rhodium-graphene nanocomposite. *Journal of Nanoparticle Research*, 13, 2769-2777.
- CHANG, K. & CHEN, W. 2011a. In situ synthesis of MoS<sub>2</sub>/graphene nanosheet composites with extraordinarily high electrochemical performance for lithium ion batteries. *Chemical Communications*, 47, 4252-4254.
- CHANG, K. & CHEN, W. 2011b. l-Cysteine-Assisted Synthesis of Layered MoS<sub>2</sub>/Graphene Composites with Excellent Electrochemical Performances for Lithium Ion Batteries. *ACS Nano*, 5, 4720-4728.
- CHEN, J., LI, C., EDA, G., ZHANG, Y., LEI, W., CHHOWALLA, M., MILNE, W. I. & DENG, W.-Q. 2011a. Incorporation of graphene in quantum dot sensitized solar cells based on ZnO nanorods. *Chemical Communications*, 47, 6084-6086.
- CHEN, L., TANG, Y., WANG, K., LIU, C. & LUO, S. 2011b. Direct electrodeposition of reduced graphene oxide on glassy carbon electrode and its electrochemical application. *Electrochemistry Communications*, 13, 133-137.

- CHEN, S., ZHU, J., HUANG, H., ZENG, G., NIE, F. & WANG, X. 2010a. Facile solvothermal synthesis of graphene–MnOOH nanocomposites. *Journal of Solid State Chemistry*, 183, 2552-2557.
- CHEN, S., ZHU, J. & WANG, X. 2010b. One-Step Synthesis of Graphene–Cobalt Hydroxide Nanocomposites and Their Electrochemical Properties. *The Journal of Physical Chemistry C*, 114, 11829-11834.
- CHEN, S. Q. & WANG, Y. 2010. Microwave-assisted synthesis of a Co<sub>3</sub>O<sub>4</sub>-graphene sheet-on-sheet nanocomposite as a superior anode material for Li-ion batteries. *Journal of Materials Chemistry*, 20, 9735-9739.
- CHEN, Y.-L., HU, Z.-A., CHANG, Y.-Q., WANG, H.-W., ZHANG, Z.-Y., YANG, Y.-Y. & WU, H.-Y. 2011c. Zinc Oxide/Reduced Graphene Oxide Composites and Electrochemical Capacitance Enhanced by Homogeneous Incorporation of Reduced Graphene Oxide Sheets in Zinc Oxide Matrix. *The Journal of Physical Chemistry C*, 115, 2563-2571.
- CHEN, Y., LI, Y., SUN, D., TIAN, D., ZHANG, J. & ZHU, J.-J. 2011d. Fabrication of gold nanoparticles on bilayer graphene for glucose electrochemical biosensing. *Journal of Materials Chemistry*, 21, 7604-7611.
- CHENG, C., NIE, S., LI, S., PENG, H., YANG, H., MA, L., SUN, S. & ZHAO, C. 2013. Biopolymer functionalized reduced graphene oxide with enhanced biocompatibility via mussel inspired coatings/anchors. *Journal of Materials Chemistry B*.
- CHENG, Q., TANG, J., MA, J., ZHANG, H., SHINYA, N. & QIN, L.-C. 2011. Graphene and nanostructured MnO<sub>2</sub> composite electrodes for supercapacitors. *Carbon*, 49, 2917-2925.
- CHOI, H.-J., JUNG, S.-M., SEO, J.-M., CHANG, D. W., DAI, L. & BAEK, J.-B. 2012. Graphene for energy conversion and storage in fuel cells and supercapacitors. *Nano Energy*, 1, 534-551.
- CHOI, J., JIN, J., JUNG, I. G., KIM, J. M., KIM, H. J. & SON, S. U. 2011. SnSe<sub>2</sub> nanoplate-graphene composites as anode materials for lithium ion batteries. *Chemical Communications*, 47, 5241-5243.
- CHOU, S.-L., WANG, J.-Z., CHOUCAIR, M., LIU, H.-K., STRIDE, J. A. & DOU, S.-X. 2010. Enhanced reversible lithium storage in a nanosize silicon/graphene composite. *Electrochemistry Communications*, 12, 303-306.
- CUONG, T. V., PHAM, V. H., CHUNG, J. S., SHIN, E. W., YOO, D. H., HAHN, S. H., HUH, J. S., RUE, G. H., KIM, E. J., HUR, S. H. & KOHL, P. A. 2010. Solution-processed ZnO-chemically converted graphene gas sensor. *Materials Letters*, 64, 2479-2482.
- DAS, M. R., SARMA, R. K., SAIKIA, R., KALE, V. S., SHELKE, M. V. & SENGUPTA, P. 2011a. Synthesis of silver nanoparticles in an aqueous suspension of graphene oxide sheets and its antimicrobial activity. *Colloids and Surfaces B: Biointerfaces*, 83, 16-22.

- DAS, S., SEELABOYINA, R., VERMA, V., LAHIRI, I., HWANG, J. Y., BANERJEE, R. & CHOI, W. 2011b. Synthesis and characterization of self-organized multilayered graphene-carbon nanotube hybrid films. *Journal of Materials Chemistry*, 21, 7289-7295.
- DE HEER, W. A., BERGER, C., WU, X., FIRST, P. N., CONRAD, E. H., LI, X., LI, T., SPRINKLE, M., HASS, J., SADOWSKI, M. L., POTEMSKI, M. & MARTINEZ, G. 2007. Epitaxial graphene. *Solid State Communications*, 143, 92-100.
- DENZLER, D., OLSCHESKI, M. & SATTLER, K. 1998. Luminescence studies of localized gap states in colloidal ZnS nanocrystals. *Journal of Applied Physics*, 84, 2841-2845.
- DONG, L., CHEN, Z., YANG, D. & LU, H. 2013. Hierarchically structured graphene-based supercapacitor electrodes. *RSC Advances*, 3, 21183-21191.
- DONG, X., LI, B., WEI, A., CAO, X., CHAN-PARK, M. B., ZHANG, H., LI, L.-J., HUANG, W. & CHEN, P. 2011. One-step growth of graphene-carbon nanotube hybrid materials by chemical vapor deposition. *Carbon*, 49, 2944-2949.
- DREYER, D. R., PARK, S., BIELAWSKI, C. W. & RUOFF, R. S. 2010. The chemistry of graphene oxide. *Chemical Society Reviews*, 39, 228-240.
- DU, D., LIU, J., ZHANG, X., CUI, X. & LIN, Y. 2011. One-step electrochemical deposition of a graphene-ZrO<sub>2</sub> nanocomposite: Preparation, characterization and application for detection of organophosphorus agents. *Journal of Materials Chemistry*, 21, 8032-8037.
- DU, M., YANG, T. & JIAO, K. 2010. Immobilization-free direct electrochemical detection for DNA specific sequences based on electrochemically converted gold nanoparticles/graphene composite film. *Journal of Materials Chemistry*, 20, 9253-9260.
- DU, X., SKACHKO, I., BARKER, A. & ANDREI, E. Y. 2008. Approaching ballistic transport in suspended graphene. *Nature Nanotechnology*, 3, 491-495.
- EIZENBERG, M. & BLAKELY, J. M. 1979. Carbon monolayer phase condensation on Ni(111). *Surface Science*, 82, 228-236.
- EMTSEV, K. V., BOSTWICK, A., HORN, K., JOBST, J., KELLOGG, G. L., LEY, L., MCCHESENEY, J. L., OHTA, T., RESHANOV, S. A., ROHRL, J., ROTENBERG, E., SCHMID, A. K., WALDMANN, D., WEBER, H. B. & SEYLLER, T. 2009. Towards wafer-size graphene layers by atmospheric pressure graphitization of silicon carbide. *Nat Mater*, 8, 203-207.
- ESFANDIAR, A., GHASEMI, S., IRAJIZAD, A., AKHAVAN, O. & GHOLAMI, M. R. 2012. The decoration of TiO<sub>2</sub>/reduced graphene oxide by Pd and Pt nanoparticles for hydrogen gas sensing. *International Journal of Hydrogen Energy*, 37, 15423-15432.
- FAN, Y., LU, H.-T., LIU, J.-H., YANG, C.-P., JING, Q.-S., ZHANG, Y.-X., YANG, X.-K. & HUANG, K.-J. 2011a. Hydrothermal preparation and electrochemical



sensing properties of TiO<sub>2</sub>–graphene nanocomposite. *Colloids and Surfaces B: Biointerfaces*, 83, 78-82.

- FAN, Z.-J., YAN, J., WEI, T., NING, G.-Q., ZHI, L.-J., LIU, J.-C., CAO, D.-X., WANG, G.-L. & WEI, F. 2011b. Nanographene-Constructed Carbon Nanofibers Grown on Graphene Sheets by Chemical Vapor Deposition: High-Performance Anode Materials for Lithium Ion Batteries. *ACS Nano*, 5, 2787-2794.
- FANG, Y., GUO, S., ZHU, C., ZHAI, Y. & WANG, E. 2010. Self-Assembly of Cationic Polyelectrolyte-Functionalized Graphene Nanosheets and Gold Nanoparticles: A Two-Dimensional Heterostructure for Hydrogen Peroxide Sensing. *Langmuir*, 26, 11277-11282.
- FERNÁNDEZ-MERINO, M. J., GUARDIA, L., PAREDES, J. I., VILLAR-RODIL, S., SOLÍS-FERNÁNDEZ, P., MARTÍNEZ-ALONSO, A. & TASCÓN, J. M. D. 2010. Vitamin C Is an Ideal Substitute for Hydrazine in the Reduction of Graphene Oxide Suspensions. *The Journal of Physical Chemistry C*, 114, 6426-6432.
- FERRARI, A. C. & ROBERTSON, J. 2000. Interpretation of Raman spectra of disordered and amorphous carbon. *Physical Review B*, 61, 14095-14107.
- FU, C., KUANG, Y., HUANG, Z., WANG, X., DU, N., CHEN, J. & ZHOU, H. 2010. Electrochemical co-reduction synthesis of graphene/Au nanocomposites in ionic liquid and their electrochemical activity. *Chemical Physics Letters*, 499, 250-253.
- FU, Y. & WANG, X. 2011. Magnetically Separable ZnFe<sub>2</sub>O<sub>4</sub>–Graphene Catalyst and its High Photocatalytic Performance under Visible Light Irradiation. *Industrial & Engineering Chemistry Research*, 50, 7210-7218.
- GAO, W., ALEMANY, L. B., CI, L. & AJAYAN, P. M. 2009. New insights into the structure and reduction of graphite oxide. *Nat Chem*, 1, 403-408.
- GEIM, A. K. & NOVOSELOV, K. S. 2007. The rise of graphene. *Nature Materials*, 6, 183-191.
- GENG, J., JIA, X.-D. & ZHU, J.-J. 2011. Sonochemical selective synthesis of ZnO/CdS core/shell nanostructures and their optical properties. *CrystEngComm*, 13, 193-198.
- GILJE, S., HAN, S., WANG, M., WANG, K. L. & KANER, R. B. 2007. A Chemical Route to Graphene for Device Applications. *Nano Letters*, 7, 3394-3398.
- GÓMEZ-NAVARRO, C., WEITZ, R. T., BITTNER, A. M., SCOLARI, M., MEWS, A., BURGHARD, M. & KERN, K. 2007. Electronic Transport Properties of Individual Chemically Reduced Graphene Oxide Sheets. *Nano Letters*, 7, 3499-3503.
- GUO, H.-L., WANG, X.-F., QIAN, Q.-Y., WANG, F.-B. & XIA, X.-H. 2009. A Green Approach to the Synthesis of Graphene Nanosheets. *ACS Nano*, 3, 2653-2659.

- GUO, J., ZHU, S., CHEN, Z., LI, Y., YU, Z., LIU, Q., LI, J., FENG, C. & ZHANG, D. 2011. Sonochemical synthesis of TiO<sub>2</sub> nanoparticles on graphene for use as photocatalyst. *Ultrasonics Sonochemistry*, 18, 1082-1090.
- HAN, Q., NI, P., LIU, Z., DONG, X., WANG, Y., LI, Z. & LIU, Z. 2014. Enhanced hydrogen peroxide sensing by incorporating manganese dioxide nanowire with silver nanoparticles. *Electrochemistry Communications*, 38, 110-113.
- HASS, J., HEER, W. A. D. & CONRAD, E. H. 2008. The growth and morphology of epitaxial multilayer graphene. *Journal of Physics: Condensed Matter*, 20, 323202.
- HE, F., FAN, J., MA, D., ZHANG, L., LEUNG, C. & CHAN, H. L. 2010a. The attachment of Fe<sub>3</sub>O<sub>4</sub> nanoparticles to graphene oxide by covalent bonding. *Carbon*, 48, 3139-3144.
- HE, Y.-S., BAI, D.-W., YANG, X., CHEN, J., LIAO, X.-Z. & MA, Z.-F. 2010b. A Co(OH)<sub>2</sub>-graphene nanosheets composite as a high performance anode material for rechargeable lithium batteries. *Electrochemistry Communications*, 12, 570-573.
- HENGLEIN, A. & BRANCEWICZ, C. 1997. Absorption Spectra and Reactions of Colloidal Bimetallic Nanoparticles Containing Mercury. *Chemistry of Materials*, 9, 2164-2167.
- HONG, W., BAI, H., XU, Y., YAO, Z., GU, Z. & SHI, G. 2010. Preparation of Gold Nanoparticle/Graphene Composites with Controlled Weight Contents and Their Application in Biosensors. *The Journal of Physical Chemistry C*, 114, 1822-1826.
- HU, H., WANG, X., LIU, F., WANG, J. & XU, C. 2011. Rapid microwave-assisted synthesis of graphene nanosheets-zinc sulfide nanocomposites: Optical and photocatalytic properties. *Synthetic Metals*, 161, 404-410.
- HU, Y., JIN, J., WU, P., ZHANG, H. & CAI, C. 2010. Graphene-gold nanostructure composites fabricated by electrodeposition and their electrocatalytic activity toward the oxygen reduction and glucose oxidation. *Electrochimica Acta*, 56, 491-500.
- HUANG, G. B., ZHANG, C. C., LONG, Y., WYNN, J., LIU, Y., WANG, W. & GAO, J. P. 2013. Low temperature preparation of alpha-FeOOH/reduced graphene oxide and its catalytic activity for the photodegradation of an organic dye. *Nanotechnology*, 24.
- HUANG, J., ZHANG, L., CHEN, B., JI, N., CHEN, F., ZHANG, Y. & ZHANG, Z. 2010a. Nanocomposites of size-controlled gold nanoparticles and graphene oxide: Formation and applications in SERS and catalysis. *Nanoscale*, 2, 2733-2738.
- HUANG, L., LI, L., DONG, W., LIU, Y. & HOU, H. 2008. Removal of Ammonia by OH Radical in Aqueous Phase. *Environmental Science & Technology*, 42, 8070-8075.

- HUANG, N. M., LIM, H. N., CHIA, C. H., YARMO, M. A. & MUHAMAD, M. R. 2011a. Simple room-temperature preparation of high-yield large-area graphene oxide. *Int J Nanomedicine*, 6, 3443-8.
- HUANG, X., ZHOU, X., WU, S., WEI, Y., QI, X., ZHANG, J., BOEY, F. & ZHANG, H. 2010b. Reduced Graphene Oxide-Templated Photochemical Synthesis and in situ Assembly of Au Nanodots to Orderly Patterned Au Nanodot Chains. *Small*, 6, 513-516.
- HUANG, X., ZHOU, X., ZHOU, L., QIAN, K., WANG, Y., LIU, Z. & YU, C. 2011b. A Facile One-Step Solvothermal Synthesis of SnO<sub>2</sub>/Graphene Nanocomposite and Its Application as an Anode Material for Lithium-Ion Batteries. *ChemPhysChem*, 12, 278-281.
- HUANG, Y., LIANG, J. & CHEN, Y. 2012. An Overview of the Applications of Graphene-Based Materials in Supercapacitors. *Small*, 8, 1805-1834.
- HUMMERS, W. S. & OFFEMAN, R. E. 1958. Preparation of Graphitic Oxide. *Journal of the American Chemical Society*, 80, 1339-1339.
- JASUJA, K. & BERRY, V. 2009. Implantation and Growth of Dendritic Gold Nanostructures on Graphene Derivatives: Electrical Property Tailoring and Raman Enhancement. *ACS Nano*, 3, 2358-2366.
- JEONG, H. Y., LEE, D.-S., CHOI, H. K., LEE, D. H., KIM, J.-E., LEE, J. Y., LEE, W. J., KIM, S. O. & CHOI, S.-Y. 2010. Flexible room-temperature NO<sub>2</sub> gas sensors based on carbon nanotubes/reduced graphene hybrid films. *Applied Physics Letters*, 96, -.
- JIA, F., LI, Y.-L., FENG, J.-M., SU, D., WEN, Y.-Y., FENG, Y. & HOU, F. 2009. Electrochemical performance of graphene nanosheets and ceramic composites as anodes for lithium batteries. *Journal of Materials Chemistry*, 19, 9063-9067.
- JIA, L., WANG, D.-H., HUANG, Y.-X., XU, A.-W. & YU, H.-Q. 2011. Highly Durable N-Doped Graphene/CdS Nanocomposites with Enhanced Photocatalytic Hydrogen Evolution from Water under Visible Light Irradiation. *The Journal of Physical Chemistry C*, 115, 11466-11473.
- JIANG, Z., WANG, J., MENG, L., HUANG, Y. & LIU, L. 2011. A highly efficient chemical sensor material for ethanol: Al<sub>2</sub>O<sub>3</sub>/Graphene nanocomposites fabricated from graphene oxide. *Chemical Communications*, 47, 6350-6352.
- JOHNSON, J. L., BEHNAM, A., PEARTON, S. J. & URAL, A. 2010. Hydrogen Sensing Using Pd-Functionalized Multi-Layer Graphene Nanoribbon Networks. *Advanced Materials*, 22, 4877-4880.
- JUANG, Z.-Y., WU, C.-Y., LO, C.-W., CHEN, W.-Y., HUANG, C.-F., HWANG, J.-C., CHEN, F.-R., LEOU, K.-C. & TSAI, C.-H. 2009. Synthesis of graphene on silicon carbide substrates at low temperature. *Carbon*, 47, 2026-2031.
- KANIYANKANDY, S., NUWAD, J., THINAHARAN, C., DEY, G. K. & PILLAI, C. G. S. 2007. Electrodeposition of silver nanodendrites. *Nanotechnology*, 18, 125610.

- KANIYOOR, A., IMRAN JAFRI, R., AROCKIADOSS, T. & RAMAPRABHU, S. 2009. Nanostructured Pt decorated graphene and multi walled carbon nanotube based room temperature hydrogen gas sensor. *Nanoscale*, 1, 382-386.
- KEDZIERSKI, J., PEI-LAN, H., HEALEY, P., WYATT, P. W., KEAST, C. L., SPRINKLE, M., BERGER, C. & DE HEER, W. A. 2008. Epitaxial Graphene Transistors on SiC Substrates. *Electron Devices, IEEE Transactions on*, 55, 2078-2085.
- KHORSAND ZAK, A., MAJID, W. H. A., WANG, H. Z., YOUSEFI, R., MORADI GOLSHEIKH, A. & REN, Z. F. 2013. Sonochemical synthesis of hierarchical ZnO nanostructures. *Ultrasonics Sonochemistry*, 20, 395-400.
- KHURANA, G., SAHOO, S., BARIK, S. K. & KATIYAR, R. S. 2013. Improved photovoltaic performance of dye sensitized solar cell using ZnO-graphene nano-composites. *Journal of Alloys and Compounds*, 578, 257-260.
- KIM, K. S., ZHAO, Y., JANG, H., LEE, S. Y., KIM, J. M., KIM, K. S., AHN, J.-H., KIM, P., CHOI, J.-Y. & HONG, B. H. 2009. Large-scale pattern growth of graphene films for stretchable transparent electrodes. *Nature*, 457, 706-710.
- KIM, Y.-K., NA, H.-K., LEE, Y. W., JANG, H., HAN, S. W. & MIN, D.-H. 2010. The direct growth of gold rods on graphene thin films. *Chemical Communications*, 46, 3185-3187.
- KOPELEVICH, Y. & ESQUINAZI, P. 2007. Graphene Physics in Graphite. *Advanced Materials*, 19, 4559-4563.
- KOU, L. & GAO, C. 2011. Making silica nanoparticle-covered graphene oxide nanohybrids as general building blocks for large-area superhydrophilic coatings. *Nanoscale*, 3, 519-528.
- KOU, R., SHAO, Y., WANG, D., ENGELHARD, M. H., KWAK, J. H., WANG, J., VISWANATHAN, V. V., WANG, C., LIN, Y., WANG, Y., AKSAY, I. A. & LIU, J. 2009. Enhanced activity and stability of Pt catalysts on functionalized graphene sheets for electrocatalytic oxygen reduction. *Electrochemistry Communications*, 11, 954-957.
- KRISHNAMOORTHY, K., KIM, G.-S. & KIM, S. J. 2013. Graphene nanosheets: Ultrasound assisted synthesis and characterization. *Ultrasonics Sonochemistry*, 20, 644-649.
- KRISHNAMOORTHY, K., VEERAPANDIAN, M., MOHAN, R. & KIM, S.-J. 2012. Investigation of Raman and photoluminescence studies of reduced graphene oxide sheets. *Applied Physics A*, 106, 501-506.
- KUDIN, K. N., OZBAS, B., SCHNIEPP, H. C., PRUD'HOMME, R. K., AKSAY, I. A. & CAR, R. 2007. Raman Spectra of Graphite Oxide and Functionalized Graphene Sheets. *Nano Letters*, 8, 36-41.
- KUMAR, R., VARANDANI, D., MEHTA, B. R., SINGH, V. N., WEN, Z., FENG, X. & MÜLLEN, K. 2011. Fast response and recovery of hydrogen sensing in Pd-Pt nanoparticle-graphene composite layers. *Nanotechnology*, 22, 275719.

- KUMAR, S. V., HUANG, N. M., LIM, H. N., ZAINY, M., HARRISON, I. & CHIA, C. H. 2013. Preparation of highly water dispersible functional graphene/silver nanocomposite for the detection of melamine. *Sensors and Actuators B: Chemical*, 181, 885-893.
- LAMBERT, T. N., CHAVEZ, C. A., HERNANDEZ-SANCHEZ, B., LU, P., BELL, N. S., AMBROSINI, A., FRIEDMAN, T., BOYLE, T. J., WHEELER, D. R. & HUBER, D. L. 2009. Synthesis and Characterization of Titania–Graphene Nanocomposites. *The Journal of Physical Chemistry C*, 113, 19812-19823.
- LEE, C., WEI, X., KYSAR, J. W. & HONE, J. 2008. Measurement of the elastic properties and intrinsic strength of monolayer graphene. *Science*, 321, 385-388.
- LEE, J. W., AHN, T., SOUNDARARAJAN, D., KO, J. M. & KIM, J.-D. 2011. Non-aqueous approach to the preparation of reduced graphene oxide/[small alpha]-Ni(OH)<sub>2</sub> hybrid composites and their high capacitance behavior. *Chemical Communications*, 47, 6305-6307.
- LEI, Z., CHRISTOV, N. & ZHAO, X. S. 2011. Intercalation of mesoporous carbon spheres between reduced graphene oxide sheets for preparing high-rate supercapacitor electrodes. *Energy & Environmental Science*, 4, 1866-1873.
- LERF, A., HE, H., FORSTER, M. & KLINOWSKI, J. 1998. Structure of Graphite Oxide Revisited. *The Journal of Physical Chemistry B*, 102, 4477-4482.
- LI, B. & CAO, H. 2011. ZnO@graphene composite with enhanced performance for the removal of dye from water. *Journal of Materials Chemistry*, 21, 3346-3349.
- LI, B., CAO, H., SHAO, J., QU, M. & WARNER, J. H. 2011a. Superparamagnetic Fe<sub>3</sub>O<sub>4</sub> nanocrystals@graphene composites for energy storage devices. *Journal of Materials Chemistry*, 21, 5069-5075.
- LI, B., CAO, H., SHAO, J., ZHENG, H., LU, Y., YIN, J. & QU, M. 2011b. Improved performances of [small beta]-Ni(OH)<sub>2</sub>@reduced-graphene-oxide in Ni-MH and Li-ion batteries. *Chemical Communications*, 47, 3159-3161.
- LI, D., MULLER, M. B., GILJE, S., KANER, R. B. & WALLACE, G. G. 2008. Processable aqueous dispersions of graphene nanosheets. *Nat Nano*, 3, 101-105.
- LI, F., CHAI, J., YANG, H., HAN, D. & NIU, L. 2010a. Synthesis of Pt/ionic liquid/graphene nanocomposite and its simultaneous determination of ascorbic acid and dopamine. *Talanta*, 81, 1063-1068.
- LI, F., SONG, J., YANG, H., GAN, S., ZHANG, Q., HAN, D., IVASKA, A. & NIU, L. 2009a. One-step synthesis of graphene / SnO<sub>2</sub> nanocomposites and its application in electrochemical supercapacitors. *Nanotechnology*, 20, 455602.
- LI, J. & LIU, C.-Y. 2010. Ag/Graphene Heterostructures: Synthesis, Characterization and Optical Properties. *European Journal of Inorganic Chemistry*, 2010, 1244-1248.
- LI, J., LIU, C.-Y. & LIU, Y. 2012a. Au/graphene hydrogel: synthesis, characterization and its use for catalytic reduction of 4-nitrophenol. *Journal of Materials Chemistry*, 22, 8426-8430.

- LI, L., DU, Z., LIU, S., HAO, Q., WANG, Y., LI, Q. & WANG, T. 2010b. A novel nonenzymatic hydrogen peroxide sensor based on MnO<sub>2</sub>/graphene oxide nanocomposite. *Talanta*, 82, 1637-1641.
- LI, X.-H., CHEN, J.-S., WANG, X., SUN, J. & ANTONIETTI, M. 2011c. Metal-Free Activation of Dioxygen by Graphene/g-C<sub>3</sub>N<sub>4</sub> Nanocomposites: Functional Dyads for Selective Oxidation of Saturated Hydrocarbons. *Journal of the American Chemical Society*, 133, 8074-8077.
- LI, X., CAI, W., AN, J., KIM, S., NAH, J., YANG, D., PINER, R., VELAMAKANNI, A., JUNG, I., TUTUC, E., BANERJEE, S. K., COLOMBO, L. & RUOFF, R. S. 2009b. Large-Area Synthesis of High-Quality and Uniform Graphene Films on Copper Foils. *Science*, 324, 1312-1314.
- LI, X., CAI, W., COLOMBO, L. & RUOFF, R. S. 2009c. Evolution of Graphene Growth on Ni and Cu by Carbon Isotope Labeling. *Nano Letters*, 9, 4268-4272.
- LI, X., WANG, H., ROBINSON, J. T., SANCHEZ, H., DIANKOV, G. & DAI, H. 2009d. Simultaneous Nitrogen Doping and Reduction of Graphene Oxide. *Journal of the American Chemical Society*, 131, 15939-15944.
- LI, Y., GAO, W., CI, L., WANG, C. & AJAYAN, P. M. 2010c. Catalytic performance of Pt nanoparticles on reduced graphene oxide for methanol electro-oxidation. *Carbon*, 48, 1124-1130.
- LI, Y., TANG, L. & LI, J. 2009e. Preparation and electrochemical performance for methanol oxidation of pt/graphene nanocomposites. *Electrochemistry Communications*, 11, 846-849.
- LI, Y., WANG, H., XIE, L., LIANG, Y., HONG, G. & DAI, H. 2011d. MoS<sub>2</sub> Nanoparticles Grown on Graphene: An Advanced Catalyst for the Hydrogen Evolution Reaction. *Journal of the American Chemical Society*, 133, 7296-7299.
- LI, Z., CHEN, Y., DU, Y., WANG, X., YANG, P. & ZHENG, J. 2012b. Triphenylamine-functionalized graphene decorated with Pt nanoparticles and its application in photocatalytic hydrogen production. *International Journal of Hydrogen Energy*, 37, 4880-4888.
- LI, Z., WANG, J., LIU, X., LIU, S., OU, J. & YANG, S. 2011e. Electrostatic layer-by-layer self-assembly multilayer films based on graphene and manganese dioxide sheets as novel electrode materials for supercapacitors. *Journal of Materials Chemistry*, 21, 3397-3403.
- LI, Z., WU, S., DING, H., ZHENG, D., HU, J., WANG, X., HUO, Q., GUAN, J. & KAN, Q. 2013a. Immobilized Cu(ii) and Co(ii) salen complexes on graphene oxide and their catalytic activity for aerobic epoxidation of styrene. *New Journal of Chemistry*, 37, 1561-1568.
- LI, Z. J., YANG, B. C., YUN, G. Q., ZHANG, S. R., ZHANG, M. & ZHAO, M. X. 2013b. Synthesis of Sn nanoparticle decorated graphene sheets for enhanced field emission properties. *Journal of Alloys and Compounds*, 550, 353-357.
- LIM HN, H. N., LIM SS, HARRISON I, CHIA CH 2011 Fabrication and characterization of graphene hydrogel via hydrothermal approach as a scaffold

for preliminary study of cell growth *International Journal of Nanomedicine*, 6 1817-1823

- LIM, S. P., HUANG, N. M. & LIM, H. N. 2013. Solvothermal synthesis of SnO<sub>2</sub>/graphene nanocomposites for supercapacitor application. *Ceramics International*, 39, 6647-6655.
- LIU, C., WANG, K., LUO, S., TANG, Y. & CHEN, L. 2011a. Direct Electrodeposition of Graphene Enabling the One-Step Synthesis of Graphene–Metal Nanocomposite Films. *Small*, 7, 1203-1206.
- LIU, C., YU, Z., NEFF, D., ZHAMU, A. & JANG, B. Z. 2010a. Graphene-Based Supercapacitor with an Ultrahigh Energy Density. *Nano Letters*, 10, 4863-4868.
- LIU, K., ZHANG, J.-J., CHENG, F.-F., ZHENG, T.-T., WANG, C. & ZHU, J.-J. 2011b. Green and facile synthesis of highly biocompatible graphene nanosheets and its application for cellular imaging and drug delivery. *Journal of Materials Chemistry*, 21, 12034-12040.
- LIU, K., ZHANG, J.-J., CHENG, F.-F., ZHENG, T.-T., WANG, C. & ZHU, J.-J. 2011c. Green and facile synthesis of highly biocompatible graphene nanosheets and its application for cellular imaging and drug delivery. *Journal of Materials Chemistry*, 21.
- LIU, S., TIAN, J., WANG, L., LI, H., ZHANG, Y. & SUN, X. 2010b. Stable Aqueous Dispersion of Graphene Nanosheets: Noncovalent Functionalization by a Polymeric Reducing Agent and Their Subsequent Decoration with Ag Nanoparticles for Enzymeless Hydrogen Peroxide Detection. *Macromolecules*, 43, 10078-10083.
- LIU, S., TIAN, J., WANG, L. & SUN, X. 2011d. A method for the production of reduced graphene oxide using benzylamine as a reducing and stabilizing agent and its subsequent decoration with Ag nanoparticles for enzymeless hydrogen peroxide detection. *Carbon*, 49, 3158-3164.
- LIU, S., WANG, J., ZENG, J., OU, J., LI, Z., LIU, X. & YANG, S. 2010c. “Green” electrochemical synthesis of Pt/graphene sheet nanocomposite film and its electrocatalytic property. *Journal of Power Sources*, 195, 4628-4633.
- LIU, X., PAN, L., ZHAO, Q., LV, T., ZHU, G., CHEN, T., LU, T., SUN, Z. & SUN, C. 2012. UV-assisted photocatalytic synthesis of ZnO–reduced graphene oxide composites with enhanced photocatalytic activity in reduction of Cr(VI). *Chemical Engineering Journal*, 183, 238-243.
- LIU, X., XU, X., ZHU, H. & YANG, X. 2013. Synthesis of graphene nanosheets with incorporated silver nanoparticles for enzymeless hydrogen peroxide detection. *Analytical Methods*, 5, 2298-2304.
- LONG, D., LI, W., QIAO, W., MIYAWAKI, J., YOON, S.-H., MOCHIDA, I. & LING, L. 2011. Partially unzipped carbon nanotubes as a superior catalyst support for PEM fuel cells. *Chemical Communications*, 47, 9429-9431.
- LU, G., LI, H., LIUSMAN, C., YIN, Z., WU, S. & ZHANG, H. 2011a. Surface enhanced Raman scattering of Ag or Au nanoparticle-decorated reduced

- graphene oxide for detection of aromatic molecules. *Chemical Science*, 2, 1817-1821.
- LU, L.-M., LI, H.-B., QU, F., ZHANG, X.-B., SHEN, G.-L. & YU, R.-Q. 2011b. In situ synthesis of palladium nanoparticle–graphene nanohybrids and their application in nonenzymatic glucose biosensors. *Biosensors and Bioelectronics*, 26, 3500-3504.
- LU, T., ZHANG, Y., LI, H., PAN, L., LI, Y. & SUN, Z. 2010. Electrochemical behaviors of graphene–ZnO and graphene–SnO<sub>2</sub> composite films for supercapacitors. *Electrochimica Acta*, 55, 4170-4173.
- LU, W., CHANG, G., LUO, Y., LIAO, F. & SUN, X. 2011c. Method for effective immobilization of Ag nanoparticles/graphene oxide composites on single-stranded DNA modified gold electrode for enzymeless H<sub>2</sub>O<sub>2</sub> detection. *Journal of Materials Science*, 46, 5260-5266.
- LU, W., LIAO, F., LUO, Y., CHANG, G. & SUN, X. 2011d. Hydrothermal synthesis of well-stable silver nanoparticles and their application for enzymeless hydrogen peroxide detection. *Electrochimica Acta*, 56, 2295-2298.
- LU, Z., GUO, C. X., YANG, H. B., QIAO, Y., GUO, J. & LI, C. M. 2011e. One-step aqueous synthesis of graphene–CdTe quantum dot-composed nanosheet and its enhanced photoresponses. *Journal of Colloid and Interface Science*, 353, 588-592.
- LUECHINGER, N. A., ATHANASSIOU, E. K. & STARK, W. J. 2008. Graphene-stabilized copper nanoparticles as an air-stable substitute for silver and gold in low-cost ink-jet printable electronics. *Nanotechnology*, 19, 445201.
- LUO, Q.-P., YU, X.-Y., LEI, B.-X., CHEN, H.-Y., KUANG, D.-B. & SU, C.-Y. 2012. Reduced Graphene Oxide-Hierarchical ZnO Hollow Sphere Composites with Enhanced Photocurrent and Photocatalytic Activity. *The Journal of Physical Chemistry C*, 116, 8111-8117.
- LV, W., SUN, F., TANG, D.-M., FANG, H.-T., LIU, C., YANG, Q.-H. & CHENG, H.-M. 2011. A sandwich structure of graphene and nickel oxide with excellent supercapacitive performance. *Journal of Materials Chemistry*, 21, 9014-9019.
- MA, J., ZHANG, J., XIONG, Z., YONG, Y. & ZHAO, X. S. 2011. Preparation, characterization and antibacterial properties of silver-modified graphene oxide. *Journal of Materials Chemistry*, 21, 3350-3352.
- MAHMOUDIAN, M. R., ALIAS, Y. & BASIRUN, W. J. 2012. The electrical properties of a sandwich of electrodeposited polypyrrole nanofibers between two layers of reduced graphene oxide nanosheets. *Electrochimica Acta*, 72, 53-60.
- MAO, S., CUI, S., LU, G., YU, K., WEN, Z. & CHEN, J. 2012. Tuning gas-sensing properties of reduced graphene oxide using tin oxide nanocrystals. *Journal of Materials Chemistry*, 22, 11009-11013.
- MAO, S., LU, G., YU, K., BO, Z. & CHEN, J. 2010. Specific Protein Detection Using Thermally Reduced Graphene Oxide Sheet Decorated with Gold Nanoparticle-Antibody Conjugates. *Advanced Materials*, 22, 3521-3526.



- MARCANO, D. C., KOSYNKIN, D. V., BERLIN, J. M., SINITSKII, A., SUN, Z., SLESAREV, A., ALEMANY, L. B., LU, W. & TOUR, J. M. 2010. Improved Synthesis of Graphene Oxide. *ACS Nano*, 4, 4806-4814.
- MARLINDA, A. R., HUANG, N. M., MUHAMAD, M. R., AN'AMT, M. N., CHANG, B. Y. S., YUSOFF, N., HARRISON, I., LIM, H. N., CHIA, C. H. & KUMAR, S. V. 2012. Highly efficient preparation of ZnO nanorods decorated reduced graphene oxide nanocomposites. *Materials Letters*, 80, 9-12.
- MAY, J. W. 1969. Platinum surface LEED rings. *Surface Science*, 17, 267-270.
- MCALLISTER, M. J., LI, J.-L., ADAMSON, D. H., SCHNIEPP, H. C., ABDALA, A. A., LIU, J., HERRERA-ALONSO, M., MILIUS, D. L., CAR, R., PRUD'HOMME, R. K. & AKSAY, I. A. 2007. Single Sheet Functionalized Graphene by Oxidation and Thermal Expansion of Graphite. *Chemistry of Materials*, 19, 4396-4404.
- MOON, I. K., LEE, J., RUOFF, R. S. & LEE, H. 2010. Reduced graphene oxide by chemical graphitization. *Nat Commun*, 1, 73.
- MORADI GOLSHEIKH, A., HUANG, N. M., LIM, H. N., ZAKARIA, R. & YIN, C.-Y. 2013. One-step electrodeposition synthesis of silver-nanoparticle-decorated graphene on indium-tin-oxide for enzymeless hydrogen peroxide detection. *Carbon*, 62, 405-412.
- MORRIS, T., COPELAND, H., MCLINDEN, E., WILSON, S. & SZULCZEWSKI, G. 2002. The Effects of Mercury Adsorption on the Optical Response of Size-Selected Gold and Silver Nanoparticles. *Langmuir*, 18, 7261-7264.
- MURAMATSU, A. & SUGIMOTO, T. 1997. Synthesis of Uniform Spherical Cu<sub>2</sub>O Particles from Condensed CuO Suspensions. *Journal of Colloid and Interface Science*, 189, 167-173.
- NAGASHIO, K., NISHIMURA, T., KITA, K. & TORIUMI, A. 2009. Mobility Variations in Mono- and Multi-Layer Graphene Films. *Applied Physics Express*, 2, 025003.
- NAIR, R. R., BLAKE, P., GRIGORENKO, A. N., NOVOSELOV, K. S., BOOTH, T. J., STAUBER, T., PERES, N. M. R. & GEIM, A. K. 2008. Fine Structure Constant Defines Visual Transparency of Graphene. *Science*, 320, 1308.
- NOVOSELOV, K. S., GEIM, A. K., MOROZOV, S. V., JIANG, D., ZHANG, Y., DUBONOS, S. V., GRIGORIEVA, I. V. & FIRSOV, A. A. 2004. Electric Field Effect in Atomically Thin Carbon Films. *Science*, 306, 666-669.
- NOZIK, A. J. 2002. Quantum dot solar cells. *Physica E: Low-dimensional Systems and Nanostructures*, 14, 115-120.
- OKITSU, K., ASHOKKUMAR, M. & GRIESER, F. 2005. Sonochemical Synthesis of Gold Nanoparticles: Effects of Ultrasound Frequency. *The Journal of Physical Chemistry B*, 109, 20673-20675.

- PAN, S., LIU, X. & WANG, X. 2011. Preparation of Ag<sub>2</sub>S–Graphene nanocomposite from a single source precursor and its surface-enhanced Raman scattering and photoluminescent activity. *Materials Characterization*, 62, 1094-1101.
- PAREDES, J. I., VILLAR-RODIL, S., MARTÍNEZ-ALONSO, A. & TASCÓN, J. M. D. 2008. Graphene Oxide Dispersions in Organic Solvents. *Langmuir*, 24, 10560-10564.
- PARK, G., BARTOLOME, L., LEE, K. G., LEE, S. J., KIM, D. H. & PARK, T. J. 2012. One-step sonochemical synthesis of a graphene oxide-manganese oxide nanocomposite for catalytic glycolysis of poly(ethylene terephthalate). *Nanoscale*, 4, 3879-3885.
- PASRICHA, R., GUPTA, S. & SRIVASTAVA, A. K. 2009. A Facile and Novel Synthesis of Ag–Graphene-Based Nanocomposites. *Small*, 5, 2253-2259.
- PEI, S., ZHAO, J., DU, J., REN, W. & CHENG, H.-M. 2010. Direct reduction of graphene oxide films into highly conductive and flexible graphene films by hydrohalic acids. *Carbon*, 48, 4466-4474.
- PENG, T., LV, H., HE, D., PAN, M. & MU, S. 2013. Direct Transformation of Amorphous Silicon Carbide into Graphene under Low Temperature and Ambient Pressure. *Sci. Rep.*, 3.
- PHAM, V. H., CUONG, T. V., HUR, S. H., OH, E., KIM, E. J., SHIN, E. W. & CHUNG, J. S. 2011. Chemical functionalization of graphene sheets by solvothermal reduction of a graphene oxide suspension in N-methyl-2-pyrrolidone. *Journal of Materials Chemistry*, 21, 3371-3377.
- POL, V. G., SRIVASTAVA, D. N., PALCHIK, O., PALCHIK, V., SLIFKIN, M. A., WEISS, A. M. & GEDANKEN, A. 2002. Sonochemical Deposition of Silver Nanoparticles on Silica Spheres. *Langmuir*, 18, 3352-3357.
- POTTS, J. R., DREYER, D. R., BIELAWSKI, C. W. & RUOFF, R. S. 2011. Graphene-based polymer nanocomposites. *Polymer*, 52, 5-25.
- QIN, Z., LI, Z. J., ZHANG, M., YANG, B. C. & OUTLAW, R. A. 2012. Sn nanoparticles grown on graphene for enhanced electrochemical properties. *Journal of Power Sources*, 217, 303-308.
- QUAN, H., ZHANG, B.-Q., ZHAO, Q., YUEN, R. K. K. & LI, R. K. Y. 2009. Facile preparation and thermal degradation studies of graphite nanoplatelets (GNPs) filled thermoplastic polyurethane (TPU) nanocomposites. *Composites Part A: Applied Science and Manufacturing*, 40, 1506-1513.
- RAMANATHANT, ABDALA, A. A., STANKOVICH, DIKIN, D. A., HERRERA ALONSO, M., PINER, R. D., ADAMSON, D. H., SCHNIEPP, H. C., CHENX, RUOFF, R. S., NGUYEN, S. T., AKSAY, I. A., PRUD'HOMME, R. K. & BRINSON, L. C. 2008. Functionalized graphene sheets for polymer nanocomposites. *Nat Nano*, 3, 327-331.
- RAMESHA, G. K. & SAMPATH, S. 2009. Electrochemical Reduction of Oriented Graphene Oxide Films: An in Situ Raman Spectroelectrochemical Study. *The Journal of Physical Chemistry C*, 113, 7985-7989.

- RAO, C. N. R., SOOD, A. K., SUBRAHMANYAM, K. S. & GOVINDARAJ, A. 2009. Graphene: The New Two-Dimensional Nanomaterial. *Angewandte Chemie International Edition*, 48, 7752-7777.
- REINA, A., JIA, X., HO, J., NEZICH, D., SON, H., BULOVIC, V., DRESSELHAUS, M. S. & KONG, J. 2008. Large Area, Few-Layer Graphene Films on Arbitrary Substrates by Chemical Vapor Deposition. *Nano Letters*, 9, 30-35.
- REN, P.-G., YAN, D.-X., JI, X., CHEN, T. & LI, Z.-M. 2011. Temperature dependence of graphene oxide reduced by hydrazine hydrate. *Nanotechnology*, 22, 055705.
- SCHNIEPP, H. C., LI, J.-L., MCALLISTER, M. J., SAI, H., HERRERA-ALONSO, M., ADAMSON, D. H., PRUD'HOMME, R. K., CAR, R., SAVILLE, D. A. & AKSAY, I. A. 2006. Functionalized Single Graphene Sheets Derived from Splitting Graphite Oxide. *The Journal of Physical Chemistry B*, 110, 8535-8539.
- SEGER, B. & KAMAT, P. V. 2009. Electrocatalytically Active Graphene-Platinum Nanocomposites. Role of 2-D Carbon Support in PEM Fuel Cells. *The Journal of Physical Chemistry C*, 113, 7990-7995.
- SHAN, C., YANG, H., HAN, D., ZHANG, Q., IVASKA, A. & NIU, L. 2010. Graphene/AuNPs/chitosan nanocomposites film for glucose biosensing. *Biosensors and Bioelectronics*, 25, 1070-1074.
- SHARMA, B. K. & AHN, J.-H. 2013. Graphene based field effect transistors: Efforts made towards flexible electronics. *Solid-State Electronics*, 89, 177-188.
- SHARMA, D. K., OTT, A., O'MULLANE, A. P. & BHARGAVA, S. K. 2011. The facile formation of silver dendritic structures in the absence of surfactants and their electrochemical and SERS properties. *Colloids and Surfaces A: Physicochemical and Engineering Aspects*, 386, 98-106.
- SHELTON, J. C., PATIL, H. R. & BLAKELY, J. M. 1974. Equilibrium segregation of carbon to a nickel (111) surface: A surface phase transition. *Surface Science*, 43, 493-520.
- SHEN, J., SHI, M., LI, N., YAN, B., MA, H., HU, Y. & YE, M. 2010. Facile synthesis and application of Ag-chemically converted graphene nanocomposite. *Nano Research*, 3, 339-349.
- SHEN, J., SHI, M., YAN, B., MA, H., LI, N. & YE, M. 2011a. Ionic liquid-assisted one-step hydrothermal synthesis of TiO<sub>2</sub>-reduced graphene oxide composites. *Nano Research*, 4, 795-806.
- SHEN, J., SHI, M., YAN, B., MA, H., LI, N. & YE, M. 2011b. One-pot hydrothermal synthesis of Ag-reduced graphene oxide composite with ionic liquid. *Journal of Materials Chemistry*, 21, 7795-7801.
- SHEN, J., YAN, B., SHI, M., MA, H., LI, N. & YE, M. 2011c. One step hydrothermal synthesis of TiO<sub>2</sub>-reduced graphene oxide sheets. *Journal of Materials Chemistry*, 21, 3415-3421.
- SHI, M., SHEN, J., MA, H., LI, Z., LU, X., LI, N. & YE, M. 2012. Preparation of graphene-TiO<sub>2</sub> composite by hydrothermal method from peroxotitanium acid

and its photocatalytic properties. *Colloids and Surfaces A: Physicochemical and Engineering Aspects*, 405, 30-37.

- SHI, W., ZHU, J., SIM, D. H., TAY, Y. Y., LU, Z., ZHANG, X., SHARMA, Y., SRINIVASAN, M., ZHANG, H., HNG, H. H. & YAN, Q. 2011. Achieving high specific charge capacitances in Fe<sub>3</sub>O<sub>4</sub>/reduced graphene oxide nanocomposites. *Journal of Materials Chemistry*, 21, 3422-3427.
- SHIN, H.-J., KIM, K. K., BENAYAD, A., YOON, S.-M., PARK, H. K., JUNG, I.-S., JIN, M. H., JEONG, H.-K., KIM, J. M., CHOI, J.-Y. & LEE, Y. H. 2009. Efficient Reduction of Graphite Oxide by Sodium Borohydride and Its Effect on Electrical Conductance. *Advanced Functional Materials*, 19, 1987-1992.
- SINGH, G., CHOUDHARY, A., HARANATH, D., JOSHI, A. G., SINGH, N., SINGH, S. & PASRICHA, R. 2012. ZnO decorated luminescent graphene as a potential gas sensor at room temperature. *Carbon*, 50, 385-394.
- SONG, H., ZHANG, L., HE, C., QU, Y., TIAN, Y. & LV, Y. 2011. Graphene sheets decorated with SnO<sub>2</sub> nanoparticles: in situ synthesis and highly efficient materials for cataluminescence gas sensors. *Journal of Materials Chemistry*, 21, 5972-5977.
- SONG, Y., CUI, K., WANG, L. & CHEN, S. 2009. The electrodeposition of Ag nanoparticles on a type I collagen-modified glassy carbon electrode and their applications as a hydrogen peroxide sensor. *Nanotechnology*, 20, 105501.
- STANKOVICH, S., DIKIN, D. A., DOMMETT, G. H. B., KOHLHAAS, K. M., ZIMNEY, E. J., STACH, E. A., PINER, R. D., NGUYEN, S. T. & RUOFF, R. S. 2006a. Graphene-based composite materials. *Nature*, 442, 282-286.
- STANKOVICH, S., DIKIN, D. A., PINER, R. D., KOHLHAAS, K. A., KLEINHAMMES, A., JIA, Y., WU, Y., NGUYEN, S. T. & RUOFF, R. S. 2007. Synthesis of graphene-based nanosheets via chemical reduction of exfoliated graphite oxide. *Carbon*, 45, 1558-1565.
- STANKOVICH, S., PINER, R. D., CHEN, X., WU, N., NGUYEN, S. T. & RUOFF, R. S. 2006b. Stable aqueous dispersions of graphitic nanoplatelets via the reduction of exfoliated graphite oxide in the presence of poly(sodium 4-styrenesulfonate). *Journal of Materials Chemistry*, 16, 155-158.
- STAUDENMAIER, L. 1898. Verfahren zur Darstellung der Graphitsäure. *Berichte der deutschen chemischen Gesellschaft*, 31, 1481-1487.
- STOLLER, M. D., PARK, S., ZHU, Y., AN, J. & RUOFF, R. S. 2008. Graphene-Based Ultracapacitors. *Nano Letters*, 8, 3498-3502.
- SU, B., TANG, D., LI, Q., TANG, J. & CHEN, G. 2011. Gold–silver–graphene hybrid nanosheets-based sensors for sensitive amperometric immunoassay of alpha-fetoprotein using nanogold-enclosed titania nanoparticles as labels. *Analytica Chimica Acta*, 692, 116-124.
- SUGIMOTO, T., DIRIGE, G. E. & MURAMATSU, A. 1995. Synthesis of Uniform CdS Particles from Condensed Cd(OH)<sub>2</sub> Suspension. *Journal of Colloid and Interface Science*, 173, 257-259.

- SUN, C.-L., LEE, H.-H., YANG, J.-M. & WU, C.-C. 2011. The simultaneous electrochemical detection of ascorbic acid, dopamine, and uric acid using graphene/size-selected Pt nanocomposites. *Biosensors and Bioelectronics*, 26, 3450-3455.
- SUN, S., GAO, L. & LIU, Y. 2010a. Enhanced dye-sensitized solar cell using graphene-TiO<sub>2</sub> photoanode prepared by heterogeneous coagulation. *Applied Physics Letters*, 96, -.
- SUN, Y.-K., CHEN, Z., NOH, H.-J., LEE, D.-J., JUNG, H.-G., REN, Y., WANG, S., YOON, C. S., MYUNG, S.-T. & AMINE, K. 2012. Nanostructured high-energy cathode materials for advanced lithium batteries. *Nat Mater*, 11, 942-947.
- SUN, Y., LI, C., XU, Y., BAI, H., YAO, Z. & SHI, G. 2010b. Chemically converted graphene as substrate for immobilizing and enhancing the activity of a polymeric catalyst. *Chemical Communications*, 46, 4740-4742.
- TAGLIENTE, M. A. & MASSARO, M. 2008. Strain-driven (0 0 2) preferred orientation of ZnO nanoparticles in ion-implanted silica. *Nuclear Instruments and Methods in Physics Research Section B: Beam Interactions with Materials and Atoms*, 266, 1055-1061.
- TARASCON, J. M. & ARMAND, M. 2001. Issues and challenges facing rechargeable lithium batteries. *Nature*, 414, 359-367.
- TEO, P. S., LIM, H. N., HUANG, N. M., CHIA, C. H. & HARRISON, I. 2012. Room temperature in situ chemical synthesis of Fe<sub>3</sub>O<sub>4</sub>/graphene. *Ceramics International*, 38, 6411-6416.
- TIAN, J., LI, H., LU, W., LUO, Y., WANG, L. & SUN, X. 2011. Preparation of Ag nanoparticle-decorated poly(m-phenylenediamine) microparticles and their application for hydrogen peroxide detection. *Analyst*, 136, 1806-1809.
- TIAN, J., LIU, S. & SUN, X. 2010. Supramolecular Microfibrils of o-Phenylenediamine Dimers: Oxidation-Induced Morphology Change and the Spontaneous Formation of Ag Nanoparticle Decorated Nanofibers. *Langmuir*, 26, 15112-15116.
- TIEN, H.-W., HUANG, Y.-L., YANG, S.-Y., WANG, J.-Y. & MA, C.-C. M. 2011. The production of graphene nanosheets decorated with silver nanoparticles for use in transparent, conductive films. *Carbon*, 49, 1550-1560.
- TONIAZZO, V., MUSTIN, C., PORTAL, J. M., HUMBERT, B., BENOIT, R. & ERRE, R. 1999. Elemental sulfur at the pyrite surfaces: speciation and quantification. *Applied Surface Science*, 143, 229-237.
- TRIPATHY, S. K., MISHRA, A., JHA, S. K., WAHAB, R. & AL-KHEDHAIRY, A. A. 2013. Synthesis of thermally stable monodispersed Au@SnO<sub>2</sub> core-shell structure nanoparticles by a sonochemical technique for detection and degradation of acetaldehyde. *Analytical Methods*, 5, 1456-1462.
- VAN BOMMEL, A. J., CROMBEEN, J. E. & VAN TOOREN, A. 1975. LEED and Auger electron observations of the SiC(0001) surface. *Surface Science*, 48, 463-472.

- VAN NOORDEN, R. 2012. Production: Beyond sticky tape. *Nature*, 483, S32-S33.
- VIJAY KUMAR, S., HUANG, N. M., LIM, H. N., MARLINDA, A. R., HARRISON, I. & CHIA, C. H. 2013. One-step size-controlled synthesis of functional graphene oxide/silver nanocomposites at room temperature. *Chemical Engineering Journal*, 219, 217-224.
- VINAYAN, B. P. & RAMAPRABHU, S. 2013. Platinum-TM (TM = Fe, Co) alloy nanoparticles dispersed nitrogen doped (reduced graphene oxide-multiwalled carbon nanotube) hybrid structure cathode electrocatalysts for high performance PEMFC applications. *Nanoscale*, 5, 5109-5118.
- VINODGOPAL, K., NEPPOLIAN, B., LIGHTCAP, I. V., GRIESER, F., ASHOKKUMAR, M. & KAMAT, P. V. 2010. Sonolytic Design of Graphene–Au Nanocomposites. Simultaneous and Sequential Reduction of Graphene Oxide and Au(III). *The Journal of Physical Chemistry Letters*, 1, 1987-1993.
- WALKER, L. S., MAROTTO, V. R., RAFIEE, M. A., KORATKAR, N. & CORRAL, E. L. 2011. Toughening in Graphene Ceramic Composites. *ACS Nano*, 5, 3182-3190.
- WANG, B., PARK, J., WANG, C., AHN, H. & WANG, G. 2010a. Mn<sub>3</sub>O<sub>4</sub> nanoparticles embedded into graphene nanosheets: Preparation, characterization, and electrochemical properties for supercapacitors. *Electrochimica Acta*, 55, 6812-6817.
- WANG, B., WU, X.-L., SHU, C.-Y., GUO, Y.-G. & WANG, C.-R. 2010b. Synthesis of CuO/graphene nanocomposite as a high-performance anode material for lithium-ion batteries. *Journal of Materials Chemistry*, 20, 10661-10664.
- WANG, C., FENG, C., GAO, Y., MA, X., WU, Q. & WANG, Z. 2011a. Preparation of a graphene-based magnetic nanocomposite for the removal of an organic dye from aqueous solution. *Chemical Engineering Journal*, 173, 92-97.
- WANG, C., LI, Y., CHUI, Y.-S., WU, Q.-H., CHEN, X. & ZHANG, W. 2013a. Three-dimensional Sn-graphene anode for high-performance lithium-ion batteries. *Nanoscale*, 5, 10599-10604.
- WANG, D., WANG, Q. & WANG, T. 2010c. Shape controlled growth of pyrite FeS<sub>2</sub> crystallites via a polymer-assisted hydrothermal route. *CrystEngComm*, 12.
- WANG, G., LIU, T., LUO, Y., ZHAO, Y., REN, Z., BAI, J. & WANG, H. 2011b. Preparation of Fe<sub>2</sub>O<sub>3</sub>/graphene composite and its electrochemical performance as an anode material for lithium ion batteries. *Journal of Alloys and Compounds*, 509, L216-L220.
- WANG, G., WANG, B., WANG, X., PARK, J., DOU, S., AHN, H. & KIM, K. 2009a. Sn/graphene nanocomposite with 3D architecture for enhanced reversible lithium storage in lithium ion batteries. *Journal of Materials Chemistry*, 19, 8378-8384.

- WANG, H., CASALONGUE, H. S., LIANG, Y. & DAI, H. 2010d. Ni(OH)<sub>2</sub> Nanoplates Grown on Graphene as Advanced Electrochemical Pseudocapacitor Materials. *Journal of the American Chemical Society*, 132, 7472-7477.
- WANG, H., CUI, L.-F., YANG, Y., SANCHEZ CASALONGUE, H., ROBINSON, J. T., LIANG, Y., CUI, Y. & DAI, H. 2010e. Mn<sub>3</sub>O<sub>4</sub>-Graphene Hybrid as a High-Capacity Anode Material for Lithium Ion Batteries. *Journal of the American Chemical Society*, 132, 13978-13980.
- WANG, H., ROBINSON, J. T., DIANKOV, G. & DAI, H. 2010f. Nanocrystal Growth on Graphene with Various Degrees of Oxidation. *Journal of the American Chemical Society*, 132, 3270-3271.
- WANG, H., YANG, Y., LIANG, Y., ROBINSON, J. T., LI, Y., JACKSON, A., CUI, Y. & DAI, H. 2011c. Graphene-Wrapped Sulfur Particles as a Rechargeable Lithium-Sulfur Battery Cathode Material with High Capacity and Cycling Stability. *Nano Letters*, 11, 2644-2647.
- WANG, J.-Z., ZHONG, C., CHOU, S.-L. & LIU, H.-K. 2010g. Flexible free-standing graphene-silicon composite film for lithium-ion batteries. *Electrochemistry Communications*, 12, 1467-1470.
- WANG, J.-Z., ZHONG, C., WEXLER, D., IDRIS, N. H., WANG, Z.-X., CHEN, L.-Q. & LIU, H.-K. 2011d. Graphene-Encapsulated Fe<sub>3</sub>O<sub>4</sub> Nanoparticles with 3D Laminated Structure as Superior Anode in Lithium Ion Batteries. *Chemistry – A European Journal*, 17, 661-667.
- WANG, K., LIU, Q., GUAN, Q.-M., WU, J., LI, H.-N. & YAN, J.-J. 2011e. Enhanced direct electrochemistry of glucose oxidase and biosensing for glucose via synergy effect of graphene and CdS nanocrystals. *Biosensors and Bioelectronics*, 26, 2252-2257.
- WANG, K., LIU, Q., WU, X.-Y., GUAN, Q.-M. & LI, H.-N. 2010h. Graphene enhanced electrochemiluminescence of CdS nanocrystal for H<sub>2</sub>O<sub>2</sub> sensing. *Talanta*, 82, 372-376.
- WANG, P., JIANG, T., ZHU, C., ZHAI, Y., WANG, D. & DONG, S. 2010i. One-step, solvothermal synthesis of graphene-CdS and graphene-ZnS quantum dot nanocomposites and their interesting photovoltaic properties. *Nano Research*, 3, 794-799.
- WANG, X., SHI, J., FENG, Z., LI, M. & LI, C. 2011f. Visible emission characteristics from different defects of ZnS nanocrystals. *Physical Chemistry Chemical Physics*, 13, 4715-4723.
- WANG, X., ZHI, L. & MULLEN, K. 2007. Transparent, Conductive Graphene Electrodes for Dye-Sensitized Solar Cells. *Nano Letters*, 8, 323-327.
- WANG, X., ZHOU, X., YAO, K., ZHANG, J. & LIU, Z. 2011g. A SnO<sub>2</sub>/graphene composite as a high stability electrode for lithium ion batteries. *Carbon*, 49, 133-139.
- WANG, Y., YAO, H.-B., WANG, X.-H. & YU, S.-H. 2011h. One-pot facile decoration of CdSe quantum dots on graphene nanosheets: novel graphene-CdSe

- nanocomposites with tunable fluorescent properties. *Journal of Materials Chemistry*, 21, 562-566.
- WANG, Z., DU, Y., ZHANG, F., ZHENG, Z., ZHANG, Y. & WANG, C. 2013b. High electrocatalytic activity of non-noble Ni-Co/graphene catalyst for direct ethanol fuel cells. *Journal of Solid State Electrochemistry*, 17, 99-107.
- WANG, Z., ZHOU, X., ZHANG, J., BOEY, F. & ZHANG, H. 2009b. Direct Electrochemical Reduction of Single-Layer Graphene Oxide and Subsequent Functionalization with Glucose Oxidase. *The Journal of Physical Chemistry C*, 113, 14071-14075.
- WARNER, J. H., RÜMMELI, M. H., BACHMATIUK, A., WILSON, M. & BÜCHNER, B. 2009. Examining Co-Based Nanocrystals on Graphene Using Low-Voltage Aberration-Corrected Transmission Electron Microscopy. *ACS Nano*, 4, 470-476.
- WASSEI, J. K., CHA, K. C., TUNG, V. C., YANG, Y. & KANER, R. B. 2011. The effects of thionyl chloride on the properties of graphene and graphene-carbon nanotube composites. *Journal of Materials Chemistry*, 21, 3391-3396.
- WILLEMSE, C. M., TLHOMELANG, K., JAHED, N., BAKER, P. G. & IWUOHA, E. I. 2011. Metallo-Graphene nanocomposite electrocatalytic platform for the determination of toxic metal ions. *Sensors*, 11, 3970-3987.
- WOJCIK, A. & KAMAT, P. V. 2010. Reduced Graphene Oxide and Porphyrin. An Interactive Affair in 2-D. *ACS Nano*, 4, 6697-6706.
- WU, J., SHEN, X., JIANG, L., WANG, K. & CHEN, K. 2010a. Solvothermal synthesis and characterization of sandwich-like graphene/ZnO nanocomposites. *Applied Surface Science*, 256, 2826-2830.
- WU, S., HE, Q., TAN, C., WANG, Y. & ZHANG, H. 2013. Graphene-Based Electrochemical Sensors. *Small*, 9, 1160-1172.
- WU, S., YIN, Z., HE, Q., HUANG, X., ZHOU, X. & ZHANG, H. 2010b. Electrochemical Deposition of Semiconductor Oxides on Reduced Graphene Oxide-Based Flexible, Transparent, and Conductive Electrodes. *The Journal of Physical Chemistry C*, 114, 11816-11821.
- WU, S., YIN, Z., HE, Q., LU, G., ZHOU, X. & ZHANG, H. 2011. Electrochemical deposition of Cl-doped n-type Cu<sub>2</sub>O on reduced graphene oxide electrodes. *Journal of Materials Chemistry*, 21, 3467-3470.
- WU, Y., HAO, X., YANG, J., TIAN, F. & JIANG, M. 2006. Ultrasound-assisted synthesis of nanocrystalline ZnS in the ionic liquid [BMIM]·BF<sub>4</sub>. *Materials Letters*, 60, 2764-2766.
- WU, Z.-S., REN, W., GAO, L., LIU, B., JIANG, C. & CHENG, H.-M. 2009a. Synthesis of high-quality graphene with a pre-determined number of layers. *Carbon*, 47, 493-499.
- WU, Z.-S., REN, W., GAO, L., ZHAO, J., CHEN, Z., LIU, B., TANG, D., YU, B., JIANG, C. & CHENG, H.-M. 2009b. Synthesis of Graphene Sheets with High



Electrical Conductivity and Good Thermal Stability by Hydrogen Arc Discharge Exfoliation. *ACS Nano*, 3, 411-417.

- WU, Z.-S., REN, W., WEN, L., GAO, L., ZHAO, J., CHEN, Z., ZHOU, G., LI, F. & CHENG, H.-M. 2010c. Graphene Anchored with Co<sub>3</sub>O<sub>4</sub> Nanoparticles as Anode of Lithium Ion Batteries with Enhanced Reversible Capacity and Cyclic Performance. *ACS Nano*, 4, 3187-3194.
- XIA, X., TU, J., MAI, Y., CHEN, R., WANG, X., GU, C. & ZHAO, X. 2011. Graphene Sheet/Porous NiO Hybrid Film for Supercapacitor Applications. *Chemistry – A European Journal*, 17, 10898-10905.
- XIANG, Q., YU, J. & JARONIEC, M. 2011. Preparation and Enhanced Visible-Light Photocatalytic H<sub>2</sub>-Production Activity of Graphene/C<sub>3</sub>N<sub>4</sub> Composites. *The Journal of Physical Chemistry C*, 115, 7355-7363.
- XIANG, Q., YU, J. & JARONIEC, M. 2012. Graphene-based semiconductor photocatalysts. *Chemical Society Reviews*, 41, 782-796.
- XIE, G., CHENG, J., LI, Y., XI, P., CHEN, F., LIU, H., HOU, F., SHI, Y., HUANG, L., XU, Z., BAI, D. & ZENG, Z. 2012. Fluorescent graphene oxide composites synthesis and its biocompatibility study. *Journal of Materials Chemistry*, 22, 9308-9314.
- XU, C. & WANG, X. 2009. Fabrication of Flexible Metal-Nanoparticle Films Using Graphene Oxide Sheets as Substrates. *Small*, 5, 2212-2217.
- XU, C., XU, B., GU, Y., XIONG, Z., SUN, J. & ZHAO, X. S. 2013a. Graphene-based electrodes for electrochemical energy storage. *Energy & Environmental Science*, 6, 1388-1414.
- XU, F., CHEN, J., WU, X., ZHANG, Y., WANG, Y., SUN, J., BI, H., LEI, W., NI, Y. & SUN, L. 2013b. Graphene Scaffolds Enhanced Photogenerated Electron Transport in ZnO Photoanodes for High-Efficiency Dye-Sensitized Solar Cells. *The Journal of Physical Chemistry C*, 117, 8619-8627.
- XU, W.-P., ZHANG, L.-C., LI, J.-P., LU, Y., LI, H.-H., MA, Y.-N., WANG, W.-D. & YU, S.-H. 2011a. Facile synthesis of silver@graphene oxide nanocomposites and their enhanced antibacterial properties. *Journal of Materials Chemistry*, 21, 4593-4597.
- XU, Y., WANG, Y., LIANG, J., HUANG, Y., MA, Y., WAN, X. & CHEN, Y. 2009. A hybrid material of graphene and poly (3,4-ethyldioxythiophene) with high conductivity, flexibility, and transparency. *Nano Research*, 2, 343-348.
- XU, Z., GAO, H. & GUOXIN, H. 2011b. Solution-based synthesis and characterization of a silver nanoparticle–graphene hybrid film. *Carbon*, 49, 4731-4738.
- XUE, L., SHEN, C., ZHENG, M., LU, H., LI, N., JI, G., PAN, L. & CAO, J. 2011. Hydrothermal synthesis of graphene–ZnS quantum dot nanocomposites. *Materials Letters*, 65, 198-200.

- YAN, J., FAN, Z., WEI, T., QIAN, W., ZHANG, M. & WEI, F. 2010a. Fast and reversible surface redox reaction of graphene–MnO<sub>2</sub> composites as supercapacitor electrodes. *Carbon*, 48, 3825-3833.
- YAN, J., WEI, T., QIAO, W., SHAO, B., ZHAO, Q., ZHANG, L. & FAN, Z. 2010b. Rapid microwave-assisted synthesis of graphene nanosheet/Co<sub>3</sub>O<sub>4</sub> composite for supercapacitors. *Electrochimica Acta*, 55, 6973-6978.
- YAN, J., WEI, T., SHAO, B., MA, F., FAN, Z., ZHANG, M., ZHENG, C., SHANG, Y., QIAN, W. & WEI, F. 2010c. Electrochemical properties of graphene nanosheet/carbon black composites as electrodes for supercapacitors. *Carbon*, 48, 1731-1737.
- YANG, J., TIAN, C., WANG, L. & FU, H. 2011a. An effective strategy for small-sized and highly-dispersed palladium nanoparticles supported on graphene with excellent performance for formic acid oxidation. *Journal of Materials Chemistry*, 21, 3384-3390.
- YANG, N., ZHAI, J., WANG, D., CHEN, Y. & JIANG, L. 2010. Two-Dimensional Graphene Bridges Enhanced Photoinduced Charge Transport in Dye-Sensitized Solar Cells. *ACS Nano*, 4, 887-894.
- YANG, S., FENG, X., WANG, X. & MÜLLEN, K. 2011b. Graphene-Based Carbon Nitride Nanosheets as Efficient Metal-Free Electrocatalysts for Oxygen Reduction Reactions. *Angewandte Chemie International Edition*, 50, 5339-5343.
- YANG, X., XU, M., QIU, W., CHEN, X., DENG, M., ZHANG, J., IWAI, H., WATANABE, E. & CHEN, H. 2011c. Graphene uniformly decorated with gold nanodots: in situ synthesis, enhanced dispersibility and applications. *Journal of Materials Chemistry*, 21, 8096-8103.
- YAVARI, F. & KORATKAR, N. 2012. Graphene-Based Chemical Sensors. *The Journal of Physical Chemistry Letters*, 3, 1746-1753.
- YIN, Z., WU, S., ZHOU, X., HUANG, X., ZHANG, Q., BOEY, F. & ZHANG, H. 2010. Electrochemical Deposition of ZnO Nanorods on Transparent Reduced Graphene Oxide Electrodes for Hybrid Solar Cells. *Small*, 6, 307-312.
- YOO, E., OKATA, T., AKITA, T., KOHYAMA, M., NAKAMURA, J. & HONMA, I. 2009. Enhanced Electrocatalytic Activity of Pt Subnanoclusters on Graphene Nanosheet Surface. *Nano Letters*, 9, 2255-2259.
- YU, A., RAMESH, P., ITKIS, M. E., BEKYAROVA, E. & HADDON, R. C. 2007. Graphite Nanoplatelet–Epoxy Composite Thermal Interface Materials. *The Journal of Physical Chemistry C*, 111, 7565-7569.
- YU, A., WANG, Q., YONG, J., MAHON, P. J., MALHERBE, F., WANG, F., ZHANG, H. & WANG, J. 2012. Silver nanoparticle–carbon nanotube hybrid films: Preparation and electrochemical sensing. *Electrochimica Acta*, 74, 111-116.
- YU, D., PARK, K., DURSTOCK, M. & DAI, L. 2011. Fullerene-Grafted Graphene for Efficient Bulk Heterojunction Polymer Photovoltaic Devices. *The Journal of Physical Chemistry Letters*, 2, 1113-1118.

- YU, Q., LIAN, J., SIRIPONGLERT, S., LI, H., CHEN, Y. P. & PEI, S.-S. 2008. Graphene segregated on Ni surfaces and transferred to insulators. *Applied Physics Letters*, 93, -.
- YUAN, B., LUAN, W. & TU, S.-T. 2012. One-step synthesis of cubic FeS<sub>2</sub> and flower-like FeSe<sub>2</sub> particles by a solvothermal reduction process. *Dalton Transactions*, 41.
- YUAN, W. & SHI, G. 2013. Graphene-based gas sensors. *Journal of Materials Chemistry A*, 1, 10078-10091.
- YUNG, K. C., WU, W. M., PIERPOINT, M. P. & KUSMARTSEV, F. V. 2013. Introduction to graphene electronics – a new era of digital transistors and devices. *Contemporary Physics*, 1-19.
- ZHAN, B., LIU, C., SHI, H., LI, C., WANG, L., HUANG, W. & DONG, X. 2014. A hydrogen peroxide electrochemical sensor based on silver nanoparticles decorated three-dimensional graphene. *Applied Physics Letters*, 104, -.
- ZHANG, D., GAN, L., CAO, Y., WANG, Q., QI, L. & GUO, X. 2012a. Understanding Charge Transfer at PbS-Decorated Graphene Surfaces toward a Tunable Photosensor. *Advanced Materials*, 24, 2715-2720.
- ZHANG, H., FAN, X., QUAN, X., CHEN, S. & YU, H. 2011a. Graphene Sheets Grafted Ag@AgCl Hybrid with Enhanced Plasmonic Photocatalytic Activity under Visible Light. *Environmental Science & Technology*, 45, 5731-5736.
- ZHANG, H., LV, X., LI, Y., WANG, Y. & LI, J. 2009a. P25-Graphene Composite as a High Performance Photocatalyst. *ACS Nano*, 4, 380-386.
- ZHANG, J., XIONG, Z. & ZHAO, X. S. 2011b. Graphene-metal-oxide composites for the degradation of dyes under visible light irradiation. *Journal of Materials Chemistry*, 21, 3634-3640.
- ZHANG, L.-S., JIANG, L.-Y., YAN, H.-J., WANG, W. D., WANG, W., SONG, W.-G., GUO, Y.-G. & WAN, L.-J. 2010a. Mono dispersed SnO<sub>2</sub> nanoparticles on both sides of single layer graphene sheets as anode materials in Li-ion batteries. *Journal of Materials Chemistry*, 20, 5462-5467.
- ZHANG, M., LEI, D., YIN, X., CHEN, L., LI, Q., WANG, Y. & WANG, T. 2010b. Magnetite/graphene composites: microwave irradiation synthesis and enhanced cycling and rate performances for lithium ion batteries. *Journal of Materials Chemistry*, 20, 5538-5543.
- ZHANG, X., LI, S., JIN, X. & ZHANG, S. 2011c. A new photoelectrochemical aptasensor for the detection of thrombin based on functionalized graphene and CdSe nanoparticles multilayers. *Chemical Communications*, 47, 4929-4931.
- ZHANG, Y., CHEN, B., ZHANG, L., HUANG, J., CHEN, F., YANG, Z., YAO, J. & ZHANG, Z. 2011d. Controlled assembly of Fe<sub>3</sub>O<sub>4</sub> magnetic nanoparticles on graphene oxide. *Nanoscale*, 3, 1446-1450.

- ZHANG, Y., LI, H., PAN, L., LU, T. & SUN, Z. 2009b. Capacitive behavior of graphene–ZnO composite film for supercapacitors. *Journal of Electroanalytical Chemistry*, 634, 68-71.
- ZHANG, Y., LIU, S., LU, W., WANG, L., TIAN, J. & SUN, X. 2011e. In situ green synthesis of Au nanostructures on graphene oxide and their application for catalytic reduction of 4-nitrophenol. *Catalysis Science & Technology*, 1, 1142-1144.
- ZHANG, Y., YUAN, X., WANG, Y. & CHEN, Y. 2012b. One-pot photochemical synthesis of graphene composites uniformly deposited with silver nanoparticles and their high catalytic activity towards the reduction of 2-nitroaniline. *Journal of Materials Chemistry*, 22, 7245-7251.
- ZHANG, Y., ZHANG, N., TANG, Z.-R. & XU, Y.-J. 2012c. Graphene Transforms Wide Band Gap ZnS to a Visible Light Photocatalyst. The New Role of Graphene as a Macromolecular Photosensitizer. *ACS Nano*, 6, 9777-9789.
- ZHANG, Z., XU, F., YANG, W., GUO, M., WANG, X., ZHANG, B. & TANG, J. 2011f. A facile one-pot method to high-quality Ag-graphene composite nanosheets for efficient surface-enhanced Raman scattering. *Chemical Communications*, 47, 6440-6442.
- ZHAO, B., LIU, Z., FU, W. & YANG, H. 2013a. Construction of 3D electrochemically reduced graphene oxide–silver nanocomposite film and application as nonenzymatic hydrogen peroxide sensor. *Electrochemistry Communications*, 27, 1-4.
- ZHAO, H., YANG, J., WANG, L., TIAN, C., JIANG, B. & FU, H. 2011. Fabrication of a palladium nanoparticle/graphene nanosheet hybrid via sacrifice of a copper template and its application in catalytic oxidation of formic acid. *Chemical Communications*, 47, 2014-2016.
- ZHAO, J., WU, J., YU, F., ZHANG, X., LAN, Z. & LIN, J. 2013b. Improving the photovoltaic performance of cadmium sulfide quantum dots-sensitized solar cell by graphene/titania photoanode. *Electrochimica Acta*, 96, 110-116.
- ZHAO, W., WANG, H., QIN, X., WANG, X., ZHAO, Z., MIAO, Z., CHEN, L., SHAN, M., FANG, Y. & CHEN, Q. 2009. A novel nonenzymatic hydrogen peroxide sensor based on multi-wall carbon nanotube/silver nanoparticle nanohybrids modified gold electrode. *Talanta*, 80, 1029-1033.
- ZHOU, G., WANG, D.-W., LI, F., ZHANG, L., LI, N., WU, Z.-S., WEN, L., LU, G. Q. & CHENG, H.-M. 2010a. Graphene-Wrapped Fe<sub>3</sub>O<sub>4</sub> Anode Material with Improved Reversible Capacity and Cyclic Stability for Lithium Ion Batteries. *Chemistry of Materials*, 22, 5306-5313.
- ZHOU, H., QIU, C., YU, F., YANG, H., CHEN, M., HU, L. & SUN, L. 2011a. Thickness-Dependent Morphologies and Surface-Enhanced Raman Scattering of Ag Deposited on n-Layer Graphenes. *The Journal of Physical Chemistry C*, 115, 11348-11354.

- ZHOU, K., ZHU, Y., YANG, X., JIANG, X. & LI, C. 2011b. Preparation of graphene-TiO<sub>2</sub> composites with enhanced photocatalytic activity. *New Journal of Chemistry*, 35, 353-359.
- ZHOU, K., ZHU, Y., YANG, X. & LI, C. 2011c. Preparation and Application of Mediator-Free H<sub>2</sub>O<sub>2</sub> Biosensors of Graphene-Fe<sub>3</sub>O<sub>4</sub> Composites. *Electroanalysis*, 23, 862-869.
- ZHOU, K., ZHU, Y., YANG, X., LUO, J., LI, C. & LUAN, S. 2010b. A novel hydrogen peroxide biosensor based on Au-graphene-HRP-chitosan biocomposites. *Electrochimica Acta*, 55, 3055-3060.
- ZHOU, L., SHEN, F., TIAN, X., WANG, D., ZHANG, T. & CHEN, W. 2013. Stable Cu<sub>2</sub>O nanocrystals grown on functionalized graphene sheets and room temperature H<sub>2</sub>S gas sensing with ultrahigh sensitivity. *Nanoscale*, 5, 1564-1569.
- ZHOU, M., WANG, Y., ZHAI, Y., ZHAI, J., REN, W., WANG, F. & DONG, S. 2009a. Controlled Synthesis of Large-Area and Patterned Electrochemically Reduced Graphene Oxide Films. *Chemistry – A European Journal*, 15, 6116-6120.
- ZHOU, M., ZHAI, Y. & DONG, S. 2009b. Electrochemical Sensing and Biosensing Platform Based on Chemically Reduced Graphene Oxide. *Analytical Chemistry*, 81, 5603-5613.
- ZHOU, W., LIU, J., CHEN, T., TAN, K. S., JIA, X., LUO, Z., CONG, C., YANG, H., LI, C. M. & YU, T. 2011d. Fabrication of Co<sub>3</sub>O<sub>4</sub>-reduced graphene oxide scrolls for high-performance supercapacitor electrodes. *Physical Chemistry Chemical Physics*, 13, 14462-14465.
- ZHOU, Y.-G., CHEN, J.-J., WANG, F.-B., SHENG, Z.-H. & XIA, X.-H. 2010c. A facile approach to the synthesis of highly electroactive Pt nanoparticles on graphene as an anode catalyst for direct methanol fuel cells. *Chemical Communications*, 46, 5951-5953.
- ZHOU, Y., BAO, Q., TANG, L. A. L., ZHONG, Y. & LOH, K. P. 2009c. Hydrothermal Dehydration for the “Green” Reduction of Exfoliated Graphene Oxide to Graphene and Demonstration of Tunable Optical Limiting Properties. *Chemistry of Materials*, 21, 2950-2956.
- ZHU, C., GUO, S., FANG, Y. & DONG, S. 2010a. Reducing Sugar: New Functional Molecules for the Green Synthesis of Graphene Nanosheets. *ACS Nano*, 4, 2429-2437.
- ZHU, C., GUO, S., FANG, Y., HAN, L., WANG, E. & DONG, S. 2011a. One-step electrochemical approach to the synthesis of Graphene/MnO<sub>2</sub> nanowall hybrids. *Nano Research*, 4, 648-657.
- ZHU, G., LIU, Y., XU, Z., JIANG, T., ZHANG, C., LI, X. & QI, G. 2010b. Flexible Magnetic Nanoparticles-Reduced Graphene Oxide Composite Membranes Formed by Self-Assembly in Solution. *ChemPhysChem*, 11, 2432-2437.

- ZHU, G., XU, T., LV, T., PAN, L., ZHAO, Q. & SUN, Z. 2011b. Graphene-incorporated nanocrystalline TiO<sub>2</sub> films for CdS quantum dot-sensitized solar cells. *Journal of Electroanalytical Chemistry*, 650, 248-251.
- ZHU, J., SHARMA, Y. K., ZENG, Z., ZHANG, X., SRINIVASAN, M., MHAISALKAR, S., ZHANG, H., HNG, H. H. & YAN, Q. 2011c. Cobalt Oxide Nanowall Arrays on Reduced Graphene Oxide Sheets with Controlled Phase, Grain Size, and Porosity for Li-Ion Battery Electrodes. *The Journal of Physical Chemistry C*, 115, 8400-8406.
- ZHU, M., CHEN, P. & LIU, M. 2011d. Graphene Oxide Enwrapped Ag/AgX (X = Br, Cl) Nanocomposite as a Highly Efficient Visible-Light Plasmonic Photocatalyst. *ACS Nano*, 5, 4529-4536.
- ZHU, S., GUO, J., DONG, J., CUI, Z., LU, T., ZHU, C., ZHANG, D. & MA, J. 2013. Sonochemical fabrication of Fe<sub>3</sub>O<sub>4</sub> nanoparticles on reduced graphene oxide for biosensors. *Ultrasonics Sonochemistry*, 20, 872-880.
- ZOU, F., YU, Y., CAO, N., WU, L. & ZHI, J. 2011a. A novel approach for synthesis of TiO<sub>2</sub>-graphene nanocomposites and their photoelectrical properties. *Scripta Materialia*, 64, 621-624.
- ZOU, W., ZHU, J., SUN, Y. & WANG, X. 2011b. Depositing ZnO nanoparticles onto graphene in a polyol system. *Materials Chemistry and Physics*, 125, 617-620.